

MAGNETOM Flash

Issue Number 85 · 3/2023
RSNA Edition

magnetomworld.siemens-healthineers.com

Page 3

Editorial Comment Leading Through Change

Ulrike Attenberger

Page 8

Clinical User Perspective of Deep Resolve for Improved MRI Capabilities

Trina V. Gulay, et al.

Page 41

Whole-Body MRI at 1.5T in the Era of Deep Resolve

Will McGuire, et al.

Page 50

MR Elastography Using the Gravitational Transducer

Ralph Sinkus, et al.

Page 79

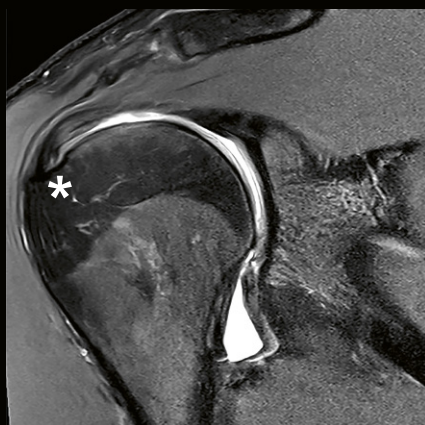
Optimizing Brachial Plexus MR Neurography at 3T

Darryl Sneag, et al.

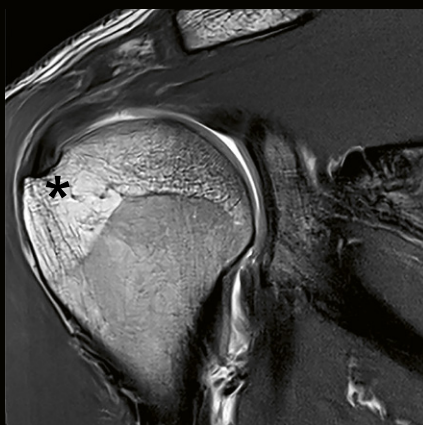
Page 95

MR-Guided Thermoablation for Hepatic Malignancies in Clinical Routine

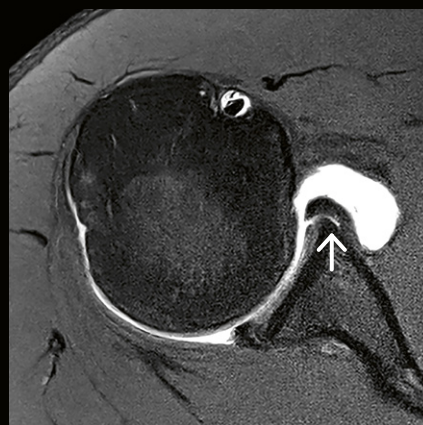
Rüdiger Hoffmann, et al.



$0.2 \times 0.2 \times 2.0 \text{ mm}^3$, 2:38 min



$0.2 \times 0.2 \times 3.0 \text{ mm}^3$, 2:03 min



$0.2 \times 0.2 \times 2.0 \text{ mm}^3$, 2:47 min

The entire editorial staff at University Hospital Bonn, Germany, and at Siemens Healthineers extends their appreciation to all the radiologists, technologists, physicists, experts, and scholars who donate their time and energy – without payment – in order to share their expertise with the readers of MAGNETOM Flash.

MAGNETOM Flash – Imprint

© 2023 by Siemens Healthineers AG,
All Rights Reserved

Publisher:

Siemens Healthineers AG
Magnetic Resonance,
Karl-Schall-Str. 6, D-91052 Erlangen, Germany

Editor-in-chief:

Antje Hellwich
(antje.hellwich@siemens-healthineers.com)

Guest Editor:

Professor Ulrike Attenberger, M.D.
Chair of the Clinic for Diagnostic and Interventional
Radiology at University Hospital Bonn, Germany

Editorial Board:

Katie Grant, Ph.D.; Kathrin El Nemer, M.D.;
Heiko Meyer, Ph.D.; Rebecca Ramb, Ph.D.;
Wellesley Were

Review Board:

Gaia Banks, Ph.D.; André Fischer, Ph.D.; Daniel Fischer;
Felix Müller-Witt; Gregor Thörmer, Ph.D.

Copy Editing:

Sheila Regan, Jen Metcalf, UNIWORKS,
www.uni-works.org
(with special thanks to Kylie Martin)

Layout:

Agentur Baumgärtner,
Friedrichstr. 4, D-90762 Fürth, Germany,
www.agentur-baumgaertner.com

PrePress and Image Editing, Production:

Clemens Ulrich, Paul Linssen,
Siemens Healthineers AG

Printer:

Schmidl & Rotaplan Druck GmbH,
Hofer Str. 1, D-93057 Regensburg, Germany

Note in accordance with § 33 Para.1 of the German Federal Data Protection Law: Despatch is made using an address file which is maintained with the aid of an automated data processing system.

MAGNETOM Flash is sent free of charge to Siemens Healthineers MR customers, qualified physicians, technologists, physicists and radiology departments throughout the world. It includes reports in the English language on magnetic resonance: diagnostic and therapeutic methods and their application as well as results and experience gained with corresponding systems and solutions. It introduces from case to case new principles and procedures and discusses their clinical potential. The statements and views of the authors in the individual contributions do not necessarily reflect the opinion of the publisher.

The information presented in these articles and case reports is for illustration only and is not intended to be relied upon by the reader for instruction as to the practice of medicine. Any health care practitioner reading this information is reminded that they must use their own learning, training and expertise in dealing with their individual patients. This material does not substitute for that duty and is not intended by Siemens Healthcare to be used for any purpose in that regard. The drugs and doses mentioned herein are consistent with the approval labeling for uses and/or indications of the drug. The treating physician bears the sole responsibility for the diagnosis and treatment of patients, including drugs and doses prescribed in connection with such use. The Operating Instructions must always be strictly followed when operating the MR system. The sources for the technical data are the corresponding data sheets. Results may vary.

Partial reproduction in printed form of individual contributions is permitted, provided the customary bibliographical data such as author's name and title of the contribution as well as year, issue number and pages of MAGNETOM Flash are named, but the editors request that two copies be sent to them. The written consent of the authors and publisher is required for the complete reprinting of an article.

We welcome your questions and comments about the editorial content of MAGNETOM Flash. Please contact us at
magnetomworld.team@siemens-healthineers.com

Manuscripts as well as suggestions, proposals and information are always welcome; they are carefully examined and submitted to the editorial board for attention. MAGNETOM Flash is not responsible for loss, damage, or any other injury to unsolicited manuscripts or other materials. We reserve the right to edit for clarity, accuracy, and space. Include your name, address, and phone number and send to the editors, address above.

MAGNETOM Flash is also available online:

www.magnetomworld.siemens-healthineers.com



Photo Universitätsklinikum Bonn (UKB),
Katharina Wislsperger

Professor Ulrike Attenberger, M.D., is Chair of the Clinic for Diagnostic and Interventional Radiology at University Hospital Bonn in Germany, and Head of the KI.NRW flagship project, Innovative Secure Medical Campus UKB.

Dr. Attenberger was a resident at the Institute of Clinical Radiology at University Hospital Munich (LMU) Grosshadern, Germany, between 2005 and 2008. She then spent a year as a resident at the Institute for Clinical Radiology and Nuclear Medicine, which is part of Medical Faculty Mannheim at Heidelberg University, Germany. After her residency, she remained at the institute, taking a position as Senior Physician for the MRI Division. This was also the year she qualified as a radiologist. In January 2011, Dr. Attenberger became Senior Physician and Section Chief of the Preventive Diagnostics Division at the institute. In January 2013, she became Section Chief of the Oncological and Preventive Diagnostics Division. In March 2013, Dr. Attenberger was appointed Vice Chair of Clinical Operations. She took up her current position at University Hospital Bonn in December 2019.

In addition to these roles, Dr. Attenberger holds an adjunct professorship at the Medical University Vienna, Austria. Between 2012 and 2015 she was visiting professor at the A. Martinos Center for Biomedical Imaging and Massachusetts General Hospital, Harvard Medical School, Boston, MA, USA; in Zurich, Switzerland, and in Vienna, Austria. She has also received several awards, including the Fellow Award of the Radiological Society of North America in 2010 and the Walter Friedrich Prize, awarded by the German Society of Radiology, in 2012. In her work today, Dr. Attenberger seeks to improve diagnosis and treatment for patients. With this goal in mind, she primarily focuses on using artificial intelligence to characterize diseases and tailor therapies to individual patient needs.

Leading through change

Point of departure

Healthcare today must address a number of significant challenges: Demographic change is leading to a steady rise in the number of multimorbid patients with complex diseases that require a high level of care and therapy, but the number of specialists available to treat them is comparatively low. At the same time, the innovation cycles of medical technologies are becoming shorter. Combined with the (demographically driven) fact that fewer people are actively paying into health insurance funds, this is creating palpable cost pressure in the system. Despite this strained situation, providers still need to maintain access to care for all with the guarantee of a quality-assured, patient-centric healthcare system.

Digitalization and artificial intelligence appear to be the most powerful methods of alleviating the strain. Digitalization is crucial to creating more efficient processes in daily clinical workflows by optimizing the way in which existing resources are used. It is also the foundation for developing AI algorithms. Without digital data, we cannot continue using AI.

Transformation of healthcare

What is more, the healthcare system itself is on the brink of a transformation. It is moving away from a model where a single expert studies and cognitively merges individual

data, toward precision medicine where AI methods are used to achieve a fully integrated assessment of all data (lab, genomic, imaging, and clinical) gathered in the treatment context. The aim of this model is to do more than simply detect diseases; it is about characterizing, or rather phenotyping them more accurately in order to predict therapy response and outcome. A 2019 analysis by Roland Berger identified digital monitoring and AI diagnostics as the two leading technologies that would have a significant impact on diagnosis and therapy by 2025 [1].

PwC goes a step further and predicts that the next decade will see a shift from real-time, outcome-based care driven by wearables, big data, and healthcare analytics, to preventive care founded on robotics, AI, and augmented reality [2].

If we were to put a ruler against these developments, some of which are already underway, and hypothetically extrapolate them, the outcome would show that we will probably all be part of an AI continuum in future. All our clinical, lab, imaging, and genetic data will be integrated into multisource data models, on which disease pathways and clinical decision support systems will be developed. When a person falls ill, their individual situation will be compared with global databases to identify the best possible therapy for the individual and their pathology. Perhaps our digital twin will one day remind us that it is time to make an appointment with our primary care physician.

Before that day comes, we need to find comprehensive answers to the data-protection, legal, and ethical questions. We must also address the challenges of structured data storage (in data lakes, data repositories) and interoperability, including across national borders.

Advancements in imaging technology

One major issue in multisource data models is imaging. Image data are a major input for multisource data models. It is therefore more relevant than ever that we continue to advance imaging technology in terms of the robustness and speed of data acquisition and its ability to generate multiparametric, morphological, and functional information for improved disease characterization. Major technologies of recent years include photon-counting technology, which we expect to deliver optimized tissue characterization, among other things. Then there is high-gradient imaging technology (MAGNETOM Cima.X), which lays the technical groundwork for gaining a more detailed view of the microstructure of tissues by using linear multiscale modeling [3], for instance, and makes this available for clinical as well as purely research applications. In addition, smart AI-based reconstruction algorithms like Deep Resolve Boost can significantly reduce image acquisition time, even for time-consuming exams such as whole-body diffusion MRI, without any loss in image quality. Achieving standardized high image quality is an essential requirement for AI imaging models, especially in MRI.

Yet, in view of the urgent healthcare challenges that I outlined at the start, it is not (or no longer) sufficient to use high-end imaging technologies as a stand-alone solution, or to solely optimize radiological workflows and processes. The healthcare system of the future requires a holistic approach that goes far beyond individual technologies and incorporates a broad range of blended solutions – although imaging will undisputedly still play a leading role.

Digitalization and AI in hospital operations

To maintain the quality of medical care at its current high level while also continuing to refine it to meet the requirements of precision medicine, all data must be fully digitalized. This requires a seamless exchange of treatment-related patient information both inside hospitals and with external referring hospitals or medical practices. It will guarantee optimal data availability, which in itself will improve processes and raise efficiency, simply because it will save staff time by removing the need to search for information. Another significant aspect in this context is the use of AI to optimize internal hospital processes for diagnostics and therapy to enable efficient use of expensive large equipment and OR infrastructure, as well as

efficient shift planning for staff, particularly those who are highly specialized. Solutions include systems for AI-based patient routing and staff shift planning, remote scanning, and remote surgery technologies that can cover gaps in staffing, and robotic systems that can provide care and lift patients to relieve the burden on radiology technologists and nursing staff. From a radiological perspective, this must also include simplifying complex examinations such as cardiac imaging. The 3D Whole Heart collaboration initiative is testing interesting approaches to optimize workflows in this context. This can achieve efficiencies that lead to better scanner utilization and therefore a reduction in waiting times.

Communication and collaboration

Communication processes, such as those within full-service university hospitals, also need to be improved to save time that can then be invested in patient care. Patient dashboards and Google communication tools, for instance, could enable more efficient and targeted communication. One potential area of application would be ad-hoc tumor boards.

Building structured databases makes it possible to develop AI-supported clinical-decision support systems. This provides the foundation for data-based treatment of even extremely ill patients or those with complex diseases. These data are also the basis for developing digital twin models that enable AI-based simulations of possible therapies. When combined with real-time collaboration in extended reality environments, digital twins will also provide many benefits when it comes to planning and carrying out surgeries. They will also support patient communication by helping patients understand complex syndromes or therapies. The visual clarity provided by virtual reality means the technology could be used to improve training for students, physicians, radiology technologists, and nurses. When used in the OR or the interventional suite, virtual and extended realities can also optimize navigation to enable greater therapeutic precision.

Cybersecurity and patient education

With all this said, we must not lose sight of two key aspects: As healthcare becomes more digital, it will increasingly become a target for cyberattacks. Sensitive and personal data must only be accessible to people who genuinely need to see this information. To achieve this, the data will be stored in extremely secure environments and monitored to protect them from potential threats. This is why it is crucial to consider and implement cybersecurity from the outset – for instance, by setting up special cyber-defense centers that can monitor healthcare facilities worldwide to identify cyberattacks in real time.

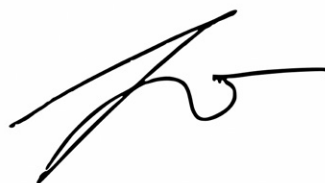
In addition, patients must be fully informed. Achieving broad acceptance for digitalization and AI relies on patients being able to develop a deep understanding of the advantages and possible risks of the technology. There are doubtless major differences on this matter worldwide. Within Europe, it is definitely a topic that still requires a great deal of public attention and education.

Future outlook

However fascinating the potential of digitalization and AI in healthcare may be, we must keep in mind that all stakeholders – full-service university hospitals, regular-service hospitals, medical practices, care facilities, and patient associations – must pull together to make this vision a reality.

Full-service university hospitals can surely play a pioneering role here by testing new approaches and developing proof-of-principle concepts for the extent to which digitalization and AI can really provide tangible relief for hospital staff. They can trial a shared database with maximum interoperability for all participating facilities, and they can ensure that patients are included in digital processes. We would expect this to lead to a better use of staff and equipment capacities, which could address the shortages of specialists. We would also expect a reduction in waiting times and the duration of hospital stays

through AI-based coordinated scheduling for patients and an optimized flow of information within the facility and externally with stakeholders such as referrers. Ultimately, success depends on the willingness to collaborate and on everyone involved sharing a common goal.



Ulrike Attenberger

References

- 1 Roland Berger. Future of health: An industry goes digital – faster than expected. October 2019. Accessed on October 16, 2023. https://content.rolandberger.com/hubfs/Roland-Berger_Future-of-health.pdf
- 2 PwC. Sherlock in Health: How artificial intelligence may improve quality and efficiency, whilst reducing healthcare costs in Europe. June 2017. Accessed on October 16, 2023. <https://www.pwc.de/de/gesundheitswesen-und-pharma/studie-sherlock-in-health.pdf>
- 3 Wichtmann BD, Fan Q, Eskandarian L, Witzel T, Attenberger UI, Pieper CC, et al. Linear multi-scale modeling of diffusion MRI data: A framework for characterization of oriented structures across length scales. Hum Brain Mapp. 2023;44(4):1496–1514.

We appreciate your comments.

Please contact us at magnetomworld.team@siemens-healthineers.com

Editorial Board



Antje Hellwich
Editor-in-chief



Rebecca Ramb, Ph.D.
Vice President of MR
Research & Clinical Translation



Kathrin El Nemer, M.D.
MR Medical Officer



Wellesley Were
MR Business Development
Manager Australia and
New Zealand



Katie Grant, Ph.D.
Vice President of MR
Malvern, PA, USA



Heiko Meyer, Ph.D.
Head of Neurovascular
Applications

Review Board

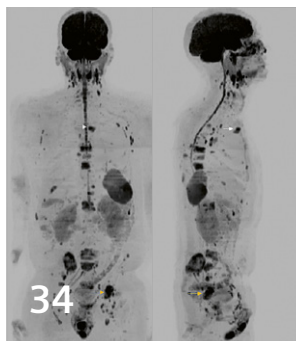
Gaia Banks, Ph.D.
Global Segment Manager
Cardiovascular and Pediatric MRI

André Fischer, Ph.D.
Global Segment Manager Neurology

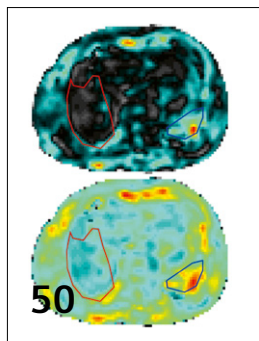
Daniel Fischer
Head of Clinical and
Scientific Marketing

Felix Müller-Witt
Global Head of Product Marketing

Gregor Thörmer, Ph.D.
Head of Oncological Applications



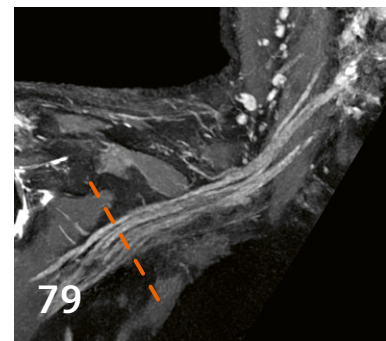
34 Whole-body b900 3D MIP (inverted scale)



50 3D Wave-encoded MRE results in the liver



64 3D volume-rendered non-contrast CMRA



79 0.8 mm Deep Resolve SPACE-STIR¹

Editorial Comment

3 Leading Through Change

Ulrike Attenberger

Clinic for Diagnostic and Interventional Radiology,
University Hospital Bonn, Germany

Deep Resolve

8 Clinical User Perspective of Deep Learning Image Reconstruction Techniques (Deep Resolve) for Improved MRI Capabilities

Trina V. Gulay, Brent Carson, et al.

Nanaimo Regional General Hospital, Island Health,
Nanaimo, BC, Canada

34 Initial Experiences Using Deep Resolve Boost to Accelerate Whole-Body Diffusion MRI¹

Anwar Padhani, et al.

Paul Strickland Scanner Centre, Mount Vernon Cancer
Centre, Northwood, Middlesex, UK

41 How-I-do-it: Whole-Body MRI at 1.5T in the Era of Deep Resolve

Will McGuire, et al.

Paul Strickland Scanner Centre, Mount Vernon Cancer
Centre, Northwood, Middlesex, UK

Abdominal Imaging

50 MR Elastography Using the Gravitational Transducer

Ralph Sinkus, et al.

School of Biomedical Engineering and Imaging,
King's College London, UK

Cardiovascular Imaging

62 Expert Insights: The Trigger Delay Parameter

Khaled Khames

Siemens Healthineers, Cairo, Egypt

64 3D Whole-Heart Imaging: An Innovative Collaborative Solution

Michaela Schmidt, Karl P. Kunze, et al.

Siemens Healthineers, Erlangen, Germany

70 Free-Breathing Cardiac Cine MRI with Compressed Sensing Real-Time Acquisition and Respiratory Motion Correction: Initial Clinical Experience at a Single Pediatric Center²

Prakash M. Masand, et al.

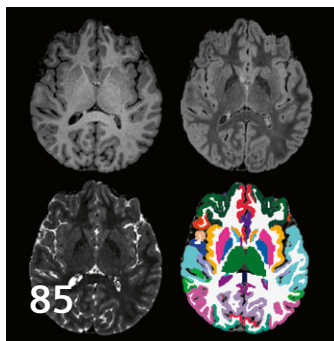
Texas Children's Hospital, Houston, TX, USA

Neurography

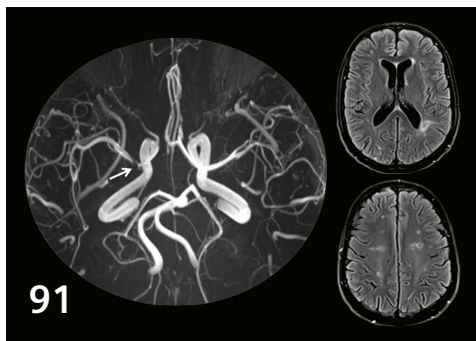
79 Optimizing Brachial Plexus MR Neurography at 3T

Darryl Sneag, et al.

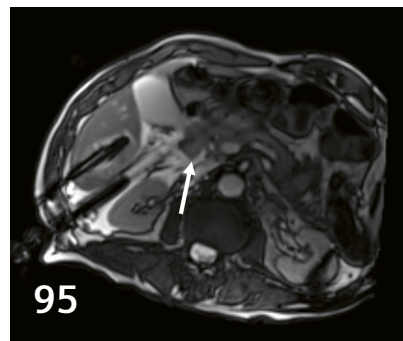
Hospital for Special Surgery, New York, NY, US



BTO structural protocol and post-processed results



Intracranial vessel wall MRI



MRI-guided thermoablation

Neurologic Imaging

85 Advancing Clinical and Neuroscientific Research Through Accessible and Optimized Protocol Design at 3T

Sriranga Kashyap and Kâmil Uludağ
University Health Network, Toronto, ON, Canada

91 How-I-do-it: Intracranial Vessel Wall MRI

Luigi Cirillo, et al.
University of Bologna, Italy

Interventional MRI

95 MR-Guided Thermoablation for Hepatic Malignancies in Clinical Routine

Rüdiger Hoffmann, et al.
University Hospital Tübingen, Germany

Spotlight

101 Celebrating 20 Years of MAGNETOM Avanto

Euan Stokes
Siemens Healthineers, Erlangen, Germany

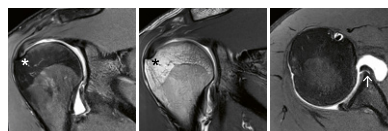
Meet Siemens Healthineers

105 Introducing HyunSoo Lee

MR research collaboration scientist,
Seoul, Republic of Korea

106 Introducing DongYeob Han

Onsite MR scientist, Seoul, Republic of Korea



Cover images courtesy of Dr. Julian A. Luetkens (Clinic for Diagnostic and Interventional Radiology at University Hospital Bonn, Germany). Acquired on MAGNETOM Cima.X

Deep Resolve PD TSE FS

$0.2 \times 0.2 \times 2.0 \text{ mm}^3$, 2:38 min
TR 3600 ms, TE 33 ms

Deep Resolve T1 TSE

$0.2 \times 0.2 \times 3.0 \text{ mm}^3$, 2:03 min
TR 700 ms, TE 70 ms

Deep Resolve T1 TSE FS

$0.2 \times 0.2 \times 2.0 \text{ mm}^3$, 2:47 min
TR 802 ms, TE 11 ms

Dx: Hill-Sachs defect (asterisk) with anterior labral tear (Bankart lesion, arrow)

¹Work in progress. The product is still under development and not commercially available. Its future availability cannot be ensured.

²MR scanning has not been established as safe for imaging fetuses and infants less than two years of age. The responsible physician must evaluate the benefits of the MR examination compared to those of other imaging procedures.

Clinical User Perspective of Deep Learning Image Reconstruction Techniques (Deep Resolve) for Improved MRI Capabilities

Brent Carson, M.D.; Patricia Maile; Jim Sielicki; Trina V. Gulay

Nanaimo Regional General Hospital, Island Health, Nanaimo, BC, Canada

Abstract

Decreased acquisition time and increased image quality during magnetic resonance imaging (MRI) exams are important diagnostic imaging considerations. MRI scan times are highly variable depending on the body area being imaged, patient compliance, and the radiologist's preferred imaging protocols. Attempts to reduce imaging time and increase resolution are becoming increasingly important, due to the time required to complete a high-quality MRI exam while keeping patient comfort in mind. Advanced imaging methods using deep learning (DL) algorithms offer unique advantages for demonstrating human anatomy, physiology, and pathology in a variety of ways.

In this paper, we review initial user experience with a combination of the DL algorithms Deep Resolve Boost (DRB) and Deep Resolve Sharp (DRS). Deep Resolve Boost is a denoising algorithm applied after collection of k -space data. How does it work? Deep Resolve Boost uses raw data from a data-reduced fast scan and applies an iterative process which uses multiple applications of a deep neural network to produce a final image with significantly reduced noise and a high apparent signal-to-noise ratio (SNR) in a shortened acquisition time. In the remainder of this manuscript, we will refer to the simultaneous application of Deep Resolve Boost and Deep Resolve Sharp simply as "Deep Resolve" since the combined application of both DL tools leads to the best results.

Introduction

Increasing demand for diagnostic testing, specifically MRI, has outpaced the provincial capacity in British Columbia. Wait lists for access to MRI technology are long, and attempts to increase capacity and streamline patient flow are required to ensure future sustainability. Patient flow through the MRI department can be improved by using quick imaging protocols that are standardized and optimized. Vendors are supporting frontline users by developing methods to improve imaging quality and reduce scan time through the use of deep learning algorithms. To build

capacity and improve access to magnetic resonance imaging (MRI), artificial intelligence (AI) and machine learning (ML) technology can be advantageous in reducing MRI scan times. Deep learning (DL) methods with new algorithms for gathering high-quality data in shorter acquisition times are now routinely being employed in medical imaging departments in Canada. Deep learning can optimize and streamline imaging protocols by reducing the time spent acquiring image data, or it can be used to improve resolution and enhance image quality.

Background

AI and deep neural networks or DL are rapidly expanding in medical imaging departments. Several factors that are under direct control of the MR technologist can determine quality in MR imaging. The quality tradeoffs aim to balance scan time, image resolution, and signal-to-noise ratio (SNR) while minimizing image artifacts. The focus is to reduce the amount of time spent in the MR system while contributing to patient comfort and tolerance. In an ideal MRI world, images would be acquired with short acquisition times, high spatial resolution, and adequate SNR to produce a high-quality image. If DL algorithms can accurately improve image quality, MRI departments can make steady gains in decreasing the time the patient spends in the scanner.

Siemens Healthineers has introduced advanced DL imaging technologies to denoise images and increase sharpness. These DL reconstruction techniques allow for improved resolution and increased SNR while potentially decreasing acquisition times. Currently Deep Resolve Boost can be applied to TSE sequences. Nanaimo Regional General Hospital (NRGH) is a test site for the new Deep Resolve reconstruction algorithm and was granted a trial license in 2023.

Methods

Clinical applications of Deep Resolve

NRGH opted to assess the Deep Resolve technology in a variety of body areas that relied heavily on TSE acquisitions. Between February and August 2023, frontline user input was compiled, and clinical examples were shared with Siemens Healthineers in an early review of the technology. The body areas where we tested Deep Resolve technology include:

- Knee and shoulder, including arthrogram
- Wrist and ankle
- Brain, pituitary gland
- Cervical, thoracic, and lumbar spine
- Pelvis (prostate, female pelvis, rectum)
- Heart

This is by no means an exhaustive list, but we felt these were the most important areas to focus on for our site. Additionally, routine protocols for areas such as the internal auditory canal (IAC) and musculoskeletal (MSK) mass protocols, might be more easily implemented if imaging protocols are TSE-based. NRGH uses 3D SPACE and MPRAGE sequences for IAC protocols, and Dixon for orbit and small-part mass protocols.

Assessments and measures

In early discussions, it was felt that NRGH would attempt to use Deep Resolve in both small and large MSK studies. Small field-of-view (FOV) MSK imaging can be prone to signal loss due to the size of the FOV, especially in finger and wrist imaging, where the FOV ranges from 80 to 100 mm. Deep Resolve was used in a variety of ways to ensure the technology directly aided protocol optimization. The intent was to gather data about the technology in use and then observe the resultant images to ensure no major differences existed in the final image quality, such as loss of contrast or an increase in image artifacts or noise. Several of our MRI technologists were involved in using the technology and were consulted on patient response to scan time, patient movement, and the protocols best suited to Deep Resolve. The radiologists visually assessed the images for contrast and spatial differentiation and clinical significance. The technology was implemented into existing imaging protocols using a triangulated assessment approach in the following categories:

- Pure comparative analysis
- Optimized Deep Resolve pulse sequence
- Resolution enhancement
- Speed enhancement

Comparative analysis

Comparative analysis was performed when the Deep Resolve option was rerun as a second acquisition with identical parameters, or as close to identical parameters as possible. When Deep Resolve is applied in the resolution card, interpolation and generalized autocalibrating partially parallel acquisition (GRAPPA) with a parallel acquisition technique (PAT) factor of 2 is automatically applied to the sequence in the k -space domain. No change in time is noted when Deep Resolve is applied, but significant inherent signal is gained from the technology. Our site used the inherent signal gain in a variety of ways while preserving or improving image quality.

Deep Resolve was initially applied in the knee and shoulder trials. The department did not purchase new coils for the Deep Resolve technology: We used our 15-channel transmit/receive knee coil and our single (large) 16-channel receive shoulder coil. If the original sequence did not have parallel imaging, the k -space-based GRAPPA with a PAT factor of 2 was automatically applied with Deep Resolve. Depending on the number of averages in the original sequence, and if GRAPPA was selected, we used this as a starting point to either increase the PAT factor, decrease averages, or decrease acquired resolution.

Initial consultations from the radiologists indicated which exams/sequences required higher resolution or when faster scanning was acceptable. When the department first started using Deep Resolve, our approach was overly aggressive: We increased two resolution steps, increased the PAT factor, and decreased an average without adding any oversampling. While the approach seemed to work for most small adults, the images could be signal-starved on large or bariatric subjects. With time and experience, we developed a nuanced approach. We learned we could be quite aggressive with PAT factors and resolution, as long as sufficient phase oversampling was present.

Optimized Deep Resolve pulse sequence

Optimized Deep Resolve versions of pulse sequences, with several modified parameters, were created to compare with NRGH's standard sequences. This will be discussed in detail in the individual clinical examples with an accompanying image to demonstrate the potential benefits. Parameter changes include TR, TE, concatenation, base matrix, bandwidth, echo train length, motion compensation, slice thickness, gap, phase oversampling and direction, number of signal averages, and FOV. Some of the current standard spine sequences employ simultaneous multi-slice (SMS), and despite the thinner slices, an optimized Deep Resolve acquisition only with in-plane parallel imaging is felt to be superior in image quality. Overall, we found removing SMS and using Deep Resolve with in-plane parallel imaging provided better image quality in most applications. The combination of changes will be looked at when continuing to develop new protocols for NRGH.

Resolution enhancement

With new advances in Deep Resolve, the primary two foci are resolution or speed enhancement. Resolution enhancement was the early focus at NRGH for specific protocols. Attempts were made to keep the pixel aspect ratio as close to square as possible to optimize resolution, or at least to keep the ratio at 80% of the base matrix or higher, e.g., 80% of 256, 320, or 384. This equates to 204 × 256, 256 × 320, and 307 × 384 matrices. For most MSK areas, we found the optimal resolution/time balance was between 80% and 85% phase resolution. Clinical decisions were made to reduce the phase resolution for certain sequences (i.e., anatomic information), while higher resolution was applied to critical 'money-shot' sequences.

Resolution enhancement can also be performed in the slice direction with a reduction in slice thickness. In brain imaging, the standard seems to traditionally be 5 mm slice thickness. However with the continued advances in pulse sequences, sites can strive for thicknesses of 3 to 4 mm. Spinal imaging also seems to be in the 3 to 4 mm range. At NRGH, the slice gap is consistently above 20%, and attempts to reduce this below 10% were employed, especially when covering neurological and musculoskeletal anatomy. We found an increased susceptibility to artifacts in areas which are subject to motion, such as the bowel (peristalsis) which can be explained by the fact that Deep Resolve protocols usually contain less averages and may be balanced by increasing the number of averages to benefit from motion averaging (of course giving up on some of the scan time reduction gained with Deep Resolve).

Speed enhancement

With the paucity of MR resources in Canada, doing more scans in less time is an important focus. NRGH decided that quick imaging attempts and scans at very low base matrix settings of 256 or below might also be an interesting way to use Deep Resolve. Reducing the cycle time of a patient through the system, without altering the diagnostic quality of the final image, has the potential to drastically improve access to limited MR resources in Canada. There are several applications where a quick scan is beneficial, namely in patients who are:

- Claustrophobic
- In extreme pain
- Pediatric
- Geriatric
- Unable to hold still for long periods of time
- High risk (patients under sedation or ICU patients)
- Fitted with implants¹ requiring restrictive SAR deposition, e.g., neurostimulators

The method employed was to drop the base matrix, e.g., 256 or lower in cardiac or pelvic TSE imaging, and reduce a signal average. This typically shortens the time drastically by a factor of 2, which can be useful when imaging patients in the aforementioned categories. The image findings (outlined below) are very exciting and potentially far reaching for one of the traditional challenges in MR: total imaging time.

¹The MRI restrictions (if any) of the metal implant must be considered prior to patient undergoing MRI exam. MR imaging of patients with metallic implants brings specific risks. However, certain implants are approved by the governing regulatory bodies to be MR conditionally safe. For such implants, the previously mentioned warning may not be applicable. Please contact the implant manufacturer for the specific conditional information. The conditions for MR safety are the responsibility of the implant manufacturer, not of Siemens Healthineers.

Musculoskeletal imaging focus

Wrist imaging

Prior to Deep Resolve, the wrist protocol was run with an FOV between 90 and 100 mm, depending on slice orientation, and took 12.5 minutes. The wrist protocol has been converted to Deep Resolve and is now 8 minutes with significantly better resolution, including an overall smaller FOV between 80 and 85 mm. The 16-channel hand/wrist coil is used for routine image acquisition. For the routine wrist protocol, NRGH runs the following Deep Resolve TSE sequences:

Sequence	Slice thickness (mm)	Gap (mm)	Time (min:s)
ax Deep Resolve PD FS TSE	2.5	0.25	2:11
cor Deep Resolve T1 TSE	2.0	0.2	2:00
cor Deep Resolve PD FS TSE	2.0	0.2	2:00
sag Deep Resolve PD FS TSE	2.5	0.25	2:25

Table 1: Wrist imaging

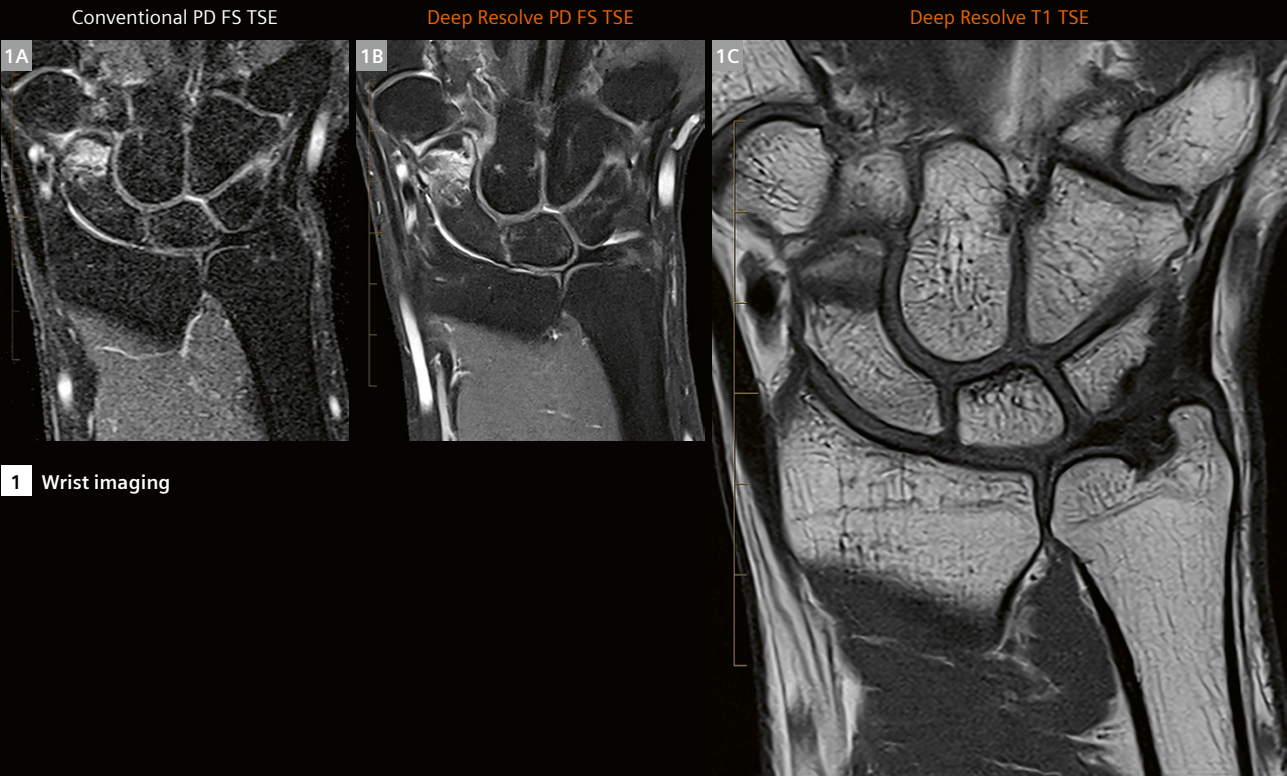
Coronal wrist (Figure 1)

(1A) is the standard coronal PD FS TSE wrist image with a base matrix of 230×288, a FOV of 100 mm, and was acquired in 3:03 minutes. Two averages were used with a GRAPPA acceleration of 2.

(1B) is the Deep Resolve sequence, with an acquisition time of 2:48 minutes, a base matrix of 220×256, and a FOV of 85 mm. Three averages were used with a PAT acceleration factor of 4.

(1B) shows a significant improvement in image quality with Deep Resolve for the coronal PD FS TSE sequence. It improves the depiction of articular cartilage, scaphoid edema, and the triangular fibrocartilage complex (TFCC). Also note the improved assessment of the scapholunate ligament.

(1C) is the Deep Resolve T1 TSE sequence with a base matrix of 216×288, a FOV of 85 mm, acquired in 2:04 minutes. Three averages were used with a PAT acceleration factor of 4. The acquired voxel size is 0.39×0.29×2.0 mm³, compared to the reconstructed voxel size of 0.15×0.15×2.0 mm³. The coronal Deep Resolve T1 TSE demonstrates excellent cortical and trabecular detail.



Knee imaging

At NRGH, the knee protocol is run with a FOV of around 150 mm, depending on slice orientation, with a 15-channel transmit/receive coil. We have adopted Deep Resolve for our routine knee protocol, as imaging time has decreased to 9 minutes from 15 minutes with an overall improvement in image resolution.

Coronal knee (Figure 2)

(2A) and (2B) demonstrate a displaced osteochondral fragment within the medial compartment. Image quality is almost equivalent between conventional and Deep Resolve imaging, with slightly better edge sharpness of the menisci and articular cartilage definition on the Deep Resolve image. The acquisition time and parameters of (2A) are: 4:15 minutes, matrix 246×352 , SMS 2, GRAPPA acceleration 2, and 3 averages, compared to (2B) with an acquisition time of 1:55 minute. Sequence time is less than half the original due to lower base resolution, an SMS acceleration factor of 3, and dropping the averages to 2. Figures (2C) and (2D) demonstrate improved delineation of menisci and articular cartilage using Deep Resolve. Scan time: 4:15 minutes vs. 1:55 minute.

Elbow imaging

The current elbow protocol at NRGH includes coronal and axial T1 with axial, sagittal, and coronal PD FS. We have converted our elbow protocol to Deep Resolve and while our time has remained relatively constant (9:50 compared to 9:00 minutes with Deep Resolve), image quality has significantly improved. Due to positioning requirements, patients with elbow pathology often have difficulty remaining motionless as a result of pain. In patients who have difficulty with positioning, the excellent SNR with Deep Resolve means NRGH could have sacrificed resolution to allow for shorter scan times. However, as our previous elbow routine was already short, we were able to significantly improve image quality while still decreasing overall scan time.

Coronal and axial elbow (Figure 3)

(3A) and (3B) show a significantly improved depiction of cortical bone, trabecular pattern, and articular cartilage using Deep Resolve. Scan time is 1:42 minute (conventional) compared to 1:29 minute (Deep Resolve). Both sequences have 1 average, but the conventional sequence uses SMS acceleration 3 and the Deep Resolve sequence uses GRAPPA 4.

In (3C) and (3D), DL allows for improved contrast, sharpness, and resolution. Scan time: conventional 2:34 minutes, Deep Resolve 2:29 minutes. The recon-

structed voxel size was $0.51 \times 0.51 \times 2.5 \text{ mm}^3$ on the conventional scan, and decreased to $0.18 \times 0.18 \times 2.5 \text{ mm}^3$ using Deep Resolve. Both sequences use 1 average but (3C) uses SMS acceleration 2 while (3D) uses GRAPPA 4.

Hand imaging

Imaging of the fingers can be challenging due to the small anatomic structures. This necessitates thinner slices, which increases scan time. Our current finger protocol consists of the following sequences, and acquisition time has decreased from 15 minutes to 9 minutes:

Sequence	Slice thickness (mm)	Gap (mm)	Time (min:s)
ax Deep Resolve T2 TSE	2.0	0	2:18
cor Deep Resolve PD FS TSE	2.0	0.1	1:52
cor Deep Resolve PD FS TSE	2.0	0.1	1:33
cor Deep Resolve T2 TSE	2.0	0.1	2:27

Table 2: Hand imaging

Sagittal and coronal thumb (Figure 4)

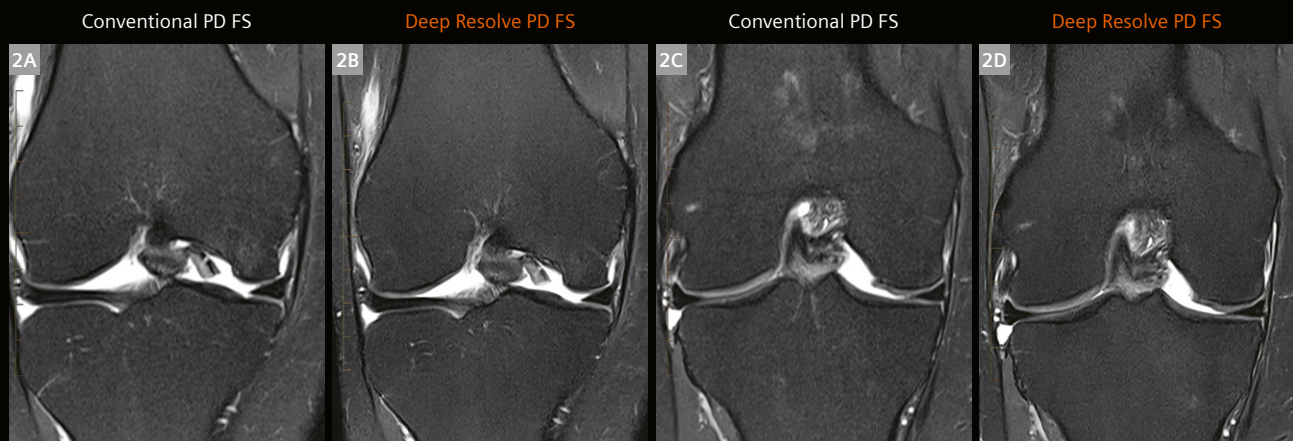
(4A) and (4B) show improved signal and contrast on the Deep Resolve image. There are also significant time savings. Scan time: conventional 3:39 minutes, Deep Resolve 1:22 minute.

(4C) and (4D) are from the same patient. Tear and retraction of the ulnar collateral ligament are shown nicely with both techniques. There is improved delineation of the adductor aponeurosis and articular cartilage using Deep Resolve. Scan time: conventional 2:53 minutes, Deep Resolve 2:07 minutes.

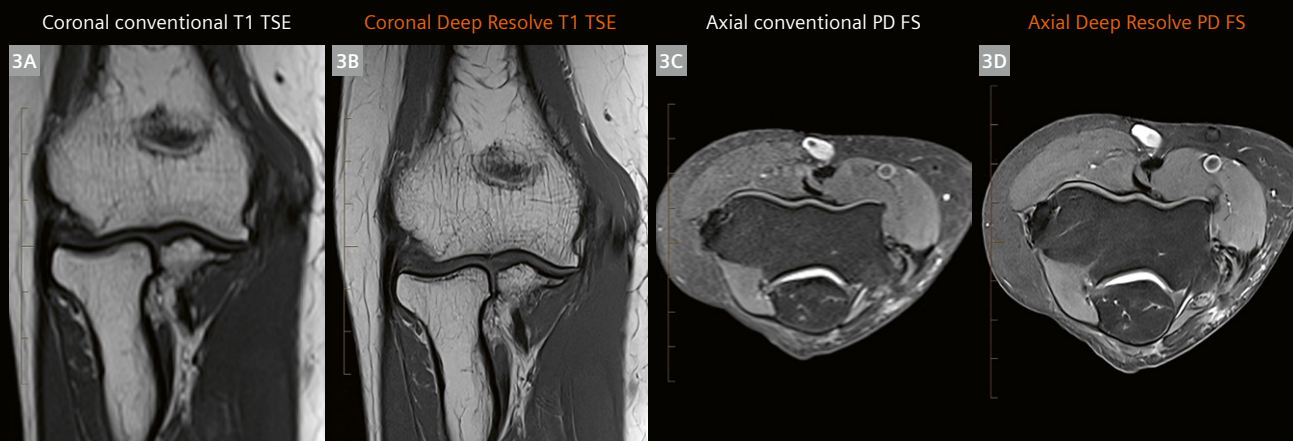
Shoulder imaging

The shoulder arthrogram protocol is run with a FOV of around 150 mm, depending on slice orientation and the size of the patient. A 16-channel dedicated shoulder coil is used for image acquisition. Shoulder imaging is known to be full of motion artifacts due to patient discomfort and respiratory motion. Shorter scan times can be helpful when scanning claustrophobic, elderly, or pediatric² patients, or patients in significant discomfort. Optimized shoulder imaging involves high-quality images with minimal other troublesome artifacts, such as magic angle artifacts. Both our routine shoulder and shoulder arthrogram protocols have been converted to Deep Resolve, with significant time savings.

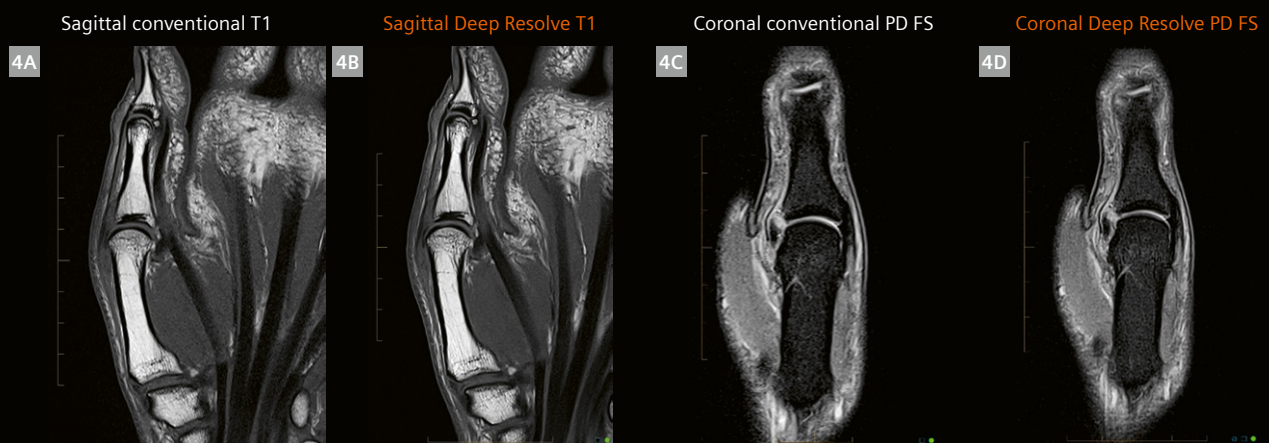
²MR scanning has not been established as safe for imaging fetuses and infants less than two years of age. The responsible physician must evaluate the benefits of the MR examination compared to those of other imaging procedures. Note: This disclaimer does not represent the opinion of the authors.



2 Knee imaging



3 Elbow imaging



4 Thumb imaging

For the routine shoulder protocol, our acquisition time is around 9 minutes, down from 15 minutes. NRGH runs the following sequences:

Sequence	Slice thickness (mm)	Gap (mm)	Time (min:s)
ax Deep Resolve PD FS TSE	3.0	0.3	1:36
cor Deep Resolve PD FS TSE	3.0	0.3	1:21
sag Deep Resolve PD FS	3.0	0.3	1:20
cor Deep Resolve T1 FS TSE	3.0	0.3	1:24
ax 3D T1 VIBE	0.6		

Table 3: Shoulder imaging

For the routine shoulder arthrogram protocol, our acquisition time is 9 minutes, down from 15 minutes. NRGH runs the following sequences:

Sequence	Slice thickness (mm)	Gap (mm)	Time (min:s)
ax Deep Resolve T1 FS TSE	3.0	0.3	1:22
cor Deep Resolve T1 FS TSE	2.5	0.1	1:24
cor Deep Resolve PD FS TSE	3.0	0.3	1:05
sag Deep Resolve T1 FS TSE	3.0	0.3	1:28
ax 3D T1 VIBE	0.6		

Table 4: Shoulder arthrogram

Axial and coronal shoulder arthrogram (Figure 5)

(5A, 5B) Note the improved edge sharpness of the cortical bone and labrum, and the improved depiction of articular cartilage. We do not routinely use abduction and external rotation (ABER) positioning, although a faster sequence would make scanning in the ABER position more attractive. (5A) has a base matrix of 212×304 . The image was acquired with a voxel size of $0.75 \times 0.53 \times 3.0 \text{ mm}^3$ and interpolated to $0.26 \times 0.26 \times 3.0 \text{ mm}^3$, with 2 averages, 3 concatenations, GRAPPA 3, and an echo spacing of 10.9 ms.

(5B) is from the same patient with medium denoising and Deep Resolve Sharp options, interpolated to a reconstructed voxel of $0.28 \times 0.28 \times 3.0 \text{ mm}^3$ with a base matrix of 201×288 . The image was acquired with a voxel size of $0.79 \times 0.53 \times 3.0 \text{ mm}^3$, 2 averages, 3 concatenations, GRAPPA 3, and an echo spacing of 10.9 ms. Both sequences have a TR of 635 ms and a TE of 11 ms. Scan time: conventional 3:32 minutes, Deep Resolve 2:18 minutes.

(5C) and (5D) include coronal PD FS TSE arthrographic images. The images demonstrate a full-thickness supraspinatus tendon tear with fraying and delamination of the tendon. The membranes within the bursa are better demonstrated with Deep Resolve. (5C) has a base matrix of 224×320 acquired in 3 minutes. The image was acquired with a voxel size of $0.71 \times 0.71 \times 3.0 \text{ mm}^3$ reconstructed to $0.25 \times 0.25 \times 3.0 \text{ mm}^3$, with 2 averages, 1 concatenation, GRAPPA 3, and an echo spacing of 10.2 ms.

(5D) was acquired from the same patient with medium denoising and sharp edge options, interpolation, and a reconstructed voxel of $0.26 \times 0.26 \times 3.0 \text{ mm}^3$ with a base matrix of 213×304 . The sequence was acquired with a voxel size of $0.75 \times 0.53 \times 3.0 \text{ mm}^3$, 2 averages, 1 concatenation, GRAPPA 3, and an echo spacing of 10.2 ms. Both sequences have a TR of 2750 ms and a TE of 41 ms. Scan time: conventional 3:00 minutes, Deep Resolve 2:02 minutes.

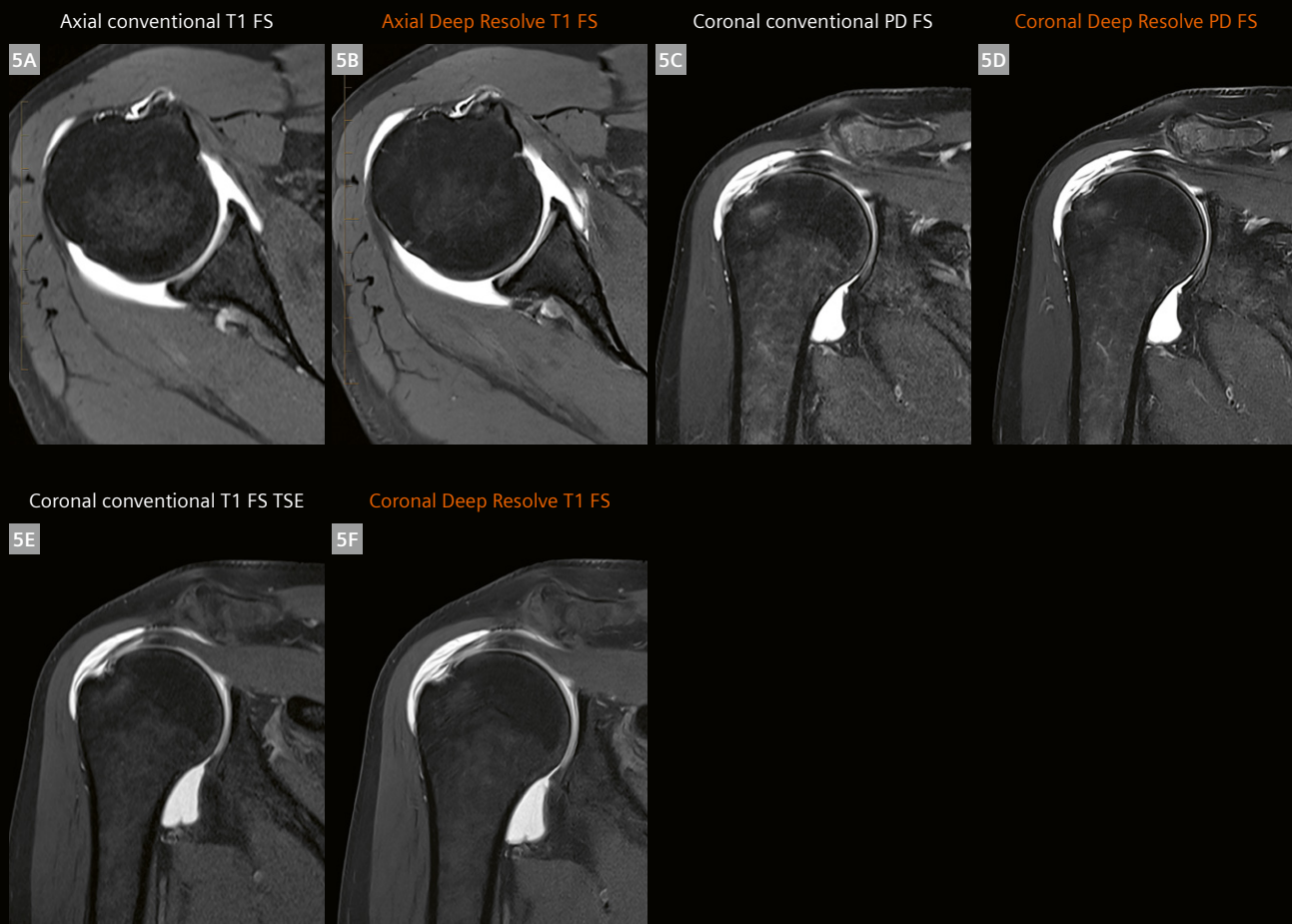
(5E) and (5F) show coronal T1 FS images from the same patient. Again, the tear and membranes are better graded using Deep Resolve. Also note the improved delineation of articular cartilage with Deep Resolve. Scan time: conventional 2:56 minutes, Deep Resolve 1:58 minute.

(5E) was acquired with a base matrix of 212×304 . The image was acquired with a voxel size of $0.75 \times 0.53 \times 2.5 \text{ mm}^3$ and reconstructed to $0.26 \times 0.26 \times 2.5 \text{ mm}^3$; 2 averages, 3 concatenations, GRAPPA 2, and an echo spacing of 9.7 ms. (5F) was collected with medium denoising and sharp edge options, interpolation, and a reconstructed voxel of $0.28 \times 0.28 \times 2.5 \text{ mm}^3$ with a base matrix of 201×288 , acquired in 1:58 minute. The sequence was acquired with a voxel size of $0.79 \times 0.56 \times 2.5 \text{ mm}^3$, 2 averages, 3 concatenations, GRAPPA 3, and an echo spacing of 9.6 ms. Both sequences have a TR of 580 ms and a TE of 9 ms.

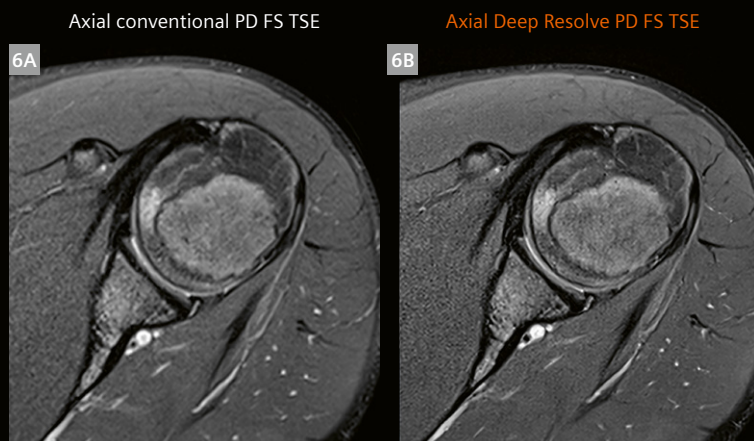
Axial shoulder (Figure 6)

(6A, 6B) The subscapularis tendon and posterior labral tear are equally assessed. There is improved depiction of articular cartilage and cortical bone on the Deep Resolve image. There is an overall improvement in signal and resolution on the Deep Resolve image.

(6A) and (6B) are identical with the same imaging parameters, but Deep Resolve was applied in (6B). Both are acquired with a base matrix of 256×256 and an acquired voxel size of $0.63 \times 0.63 \times 3.0 \text{ mm}^3$. Both sequences have 1 average and 1 concatenation, a turbo factor of 7, and echo spacing of 11.6 ms. (6A) is our conventional sequence with no acceleration and no interpolation. (6B) has an acceleration factor of GRAPPA 3, Deep Resolve Boost with medium denoising and sharp edge options. The conventional sequence took 3:59 minutes. The Deep Resolve sequence took 1:36 minute, and is now part of our routine shoulder protocol.



5 Shoulder arthrogram



6 Shoulder imaging

Foot imaging

Imaging of the feet and toes can be challenging due to the small structures being assessed. Evaluating the phalanges and metatarsophalangeal (MTP) joints in particular demands both high-resolution and high-contrast images. Our routine foot protocol varies depending on the clinical reason for referral, but generally consists of multiplanar PD FS with at least a single plane T1-weighted sequence. Scanning of the toes and MTP joints requires thinner slices, generally 2 to 3 mm.

The 16-channel receive foot/ankle coil is used for routine image acquisition. We have adopted Deep Resolve sequences for routine foot sequences. At NRGH, the routine foot protocol consists of the following TSE sequences, and the acquisition time is down from 17 minutes to 10 minutes with Deep Resolve:

Sequence	Slice thickness (mm)	Gap (mm)	Time (min:s)
sag Deep Resolve PD FS TSE	3.0	0.3	1:56
cor Deep Resolve PD FS TSE	3.0	0.3	1:58
ax Deep Resolve PD FS TSE	2.0	0.2	2:06
ax Deep Resolve T1 TSE	2.0	0.2	2:05
cor Deep Resolve T1 TSE	3.0	0.3	1:45

Table 5: Foot imaging

Sagittal and axial foot (Figure 7)

(7A) is a sagittal conventional PD FS and (7B) is a sagittal Deep Resolve PD FS of the first MTP joint. The Deep Resolve image demonstrates improved image resolution. Scan time: 2:50 minutes for (7A) and 1:56 minute for (7B). Slice thickness is 3 mm. Both have a reconstructed voxel size of $0.2 \times 0.2 \times 3.0 \text{ mm}^3$ but differ in the acquired matrix (307×384 for conventional; 294×368 for the Deep Resolve sequence). The acceleration factor on the conventional sequence is GRAPPA 2, vs. GRAPPA 3 on the Deep Resolve sequence.

(7C) is an axial conventional T1 TSE and (7D) is an axial Deep Resolve T1 of the forefoot. Note the improved assessment of muscles, trabecular pattern, and cortical bone. The components of the Lisfranc ligament complex are also better seen using Deep Resolve.

(7C) and (7D) are the same sequence but with Deep Resolve applied to (7D). Imaging parameters are as follows: a fairly close reconstructed voxel size ($0.2 \times 0.2 \times 2.0 \text{ mm}^3$ for the conventional versus $0.21 \times 0.21 \times 2.0 \text{ mm}^3$ for the Deep Resolve sequence); a lower acquisition matrix for Deep Resolve (336 versus 352 for the conventional), and a higher acceleration for Deep Resolve (GRAPPA 3 versus

GRAPPA 2 for the conventional sequence). Scan time: conventional 3:06 minutes, Deep Resolve 2:03 minutes. The images nicely demonstrate the benefits of AI technology: the Deep Resolve sequences use raw data from a data-reduced scan. Through iterative processes, they produce a final image with significantly reduced noise and high SNR in a shortened acquisition time.

Neurological imaging focus

Pituitary imaging

The pituitary gland examination is one area where the NRGH radiologists have made it a priority to attain high resolution scans. For the Deep Resolve images currently in our pituitary protocol, we have aimed to use as square a voxel as possible (90%–100%) and the improved signal from the AI sequences helps to facilitate the improved phase resolution without adding a time penalty. The Deep Resolve sequence shown below has a 90% phase resolution compared to the 75% phase resolution in the conventional sequence.

We used Deep Resolve with success for both pre-contrast T1 and T2, as well as post-contrast T1 imaging. We have adopted Deep Resolve sequences for our routine pituitary sequences. The total time with Deep Resolve sequences is 13:51 minutes compared to 13:32 minutes with our conventional sequences, and the image quality has significantly improved, as illustrated in the following examples. Our routine pituitary protocol consists of:

Sequence	Slice thickness (mm)	Gap (mm)	Time (min:s)
sag Deep Resolve T1 TSE	2.0	0.2	2:43
cor Deep Resolve T1 TSE	2.0	0.2	2:38
cor Deep Resolve T2 TSE	2.0	0.2	2:10
cor Dynamic T1 TSE			
sag Deep Resolve T1 TSE post contrast	2.0	0.2	2:43
cor Deep Resolve T1 TSE post contrast	2.0	0.2	2:38

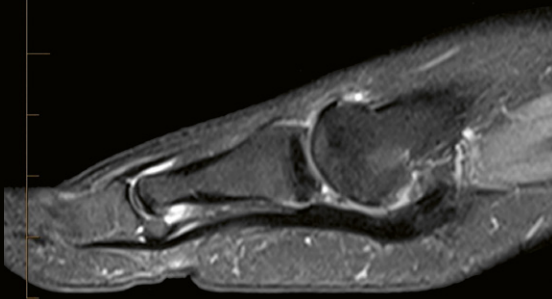
Table 6: Pituitary imaging

Pituitary imaging (Figure 8)

(8A) sagittal conventional T1 pre-contrast and (8B) sagittal Deep Resolve T1 pre-contrast imaging of the sella demonstrates improved edge sharpness but also exposes higher noise levels due to shorter scan time and increased resolution of Deep Resolve. Improved depiction of the infundibulum is apparent with Deep Resolve. Both images are acquired with a matrix of 192×256 and 2 averages.

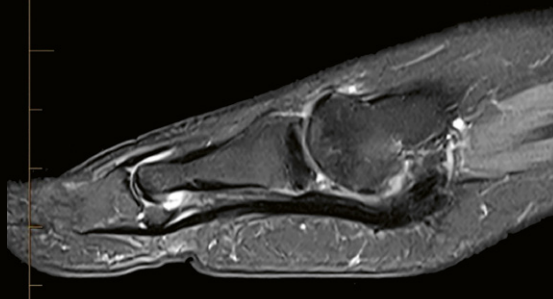
Sagittal conventional PD FS TSE

7A



Sagittal Deep Resolve PD FS TSE

7B



Axial conventional T1 TSE

7C



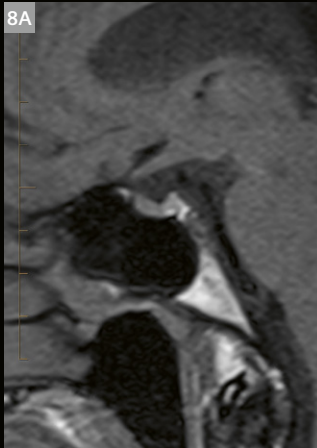
Axial Deep Resolve T1 TSE

7D

**7** Foot imaging

Sagittal conventional T1 TSE

8A



Sagittal Deep Resolve T1 TSE

8B

**8** Pituitary gland imaging

An acceleration factor of GRAPPA 2 was used on the Deep Resolve image, and no acceleration on the conventional image. Scan time: 3:29 minutes for the conventional image and 1:49 minute for the Deep Resolve image.

The Deep Resolve image is noisier than what we currently use in our Deep Resolve protocol because it is highly resolved. This resolution and speed would not be possible without Deep Resolve.

Coronal and sagittal pituitary gland (Figure 9)

(9A, 9B) are from the same patient. The Deep Resolve image demonstrates improved delineation of the pituitary adenoma with overall higher resolution. Note the exquisite detail of cranial nerves within the left cavernous sinus.

(9A) has a base matrix of 192×256 (75% phase) acquired in 2:26 minutes. The sequence was acquired with a voxel size of $0.94 \times 0.7 \times 2.0 \text{ mm}^3$ and interpolated to $0.35 \times 0.35 \times 2.0 \text{ mm}^3$. Four averages, 1 concatenation, and GRAPPA 2 were used. Both sequences have a 2 mm slice thickness, a FOV of 180 mm, echo spacing of 10.9 ms, and a TE of 11 ms. The conventional sequence has a TR of 741 ms and the Deep Resolve sequence has a TR of 622 ms.

(9B) is the Deep Resolve Boost sequence with medium denoising and sharp edge options on, a 272×304 acquired matrix (90% phase), and a reconstructed voxel of $0.3 \times 0.3 \times 2.0 \text{ mm}^3$ collected over 2:20 minutes. The sequence has an acquired voxel size of $0.66 \times 0.59 \times 2.0 \text{ mm}^3$, 3 averages, 1 concatenation, and GRAPPA 2.

(9C, 9D) were acquired in the same patient. There is much better definition of the margins of the pituitary gland, adenoma, and infundibulum using Deep Resolve. Also note the cystic change within the adenoma, which is not apparent on the conventional sequence.

(9C) is a conventional sagittal T1 TSE post-contrast sequence with a base matrix of 192×256 (75% phase) acquired in 3:12 minutes. The sequence was acquired with a voxel size of $0.97 \times 0.74 \times 2.0 \text{ mm}^3$ and interpolated to $0.4 \times 0.4 \times 2.0 \text{ mm}^3$ with 2 averages, 1 concatenation, and no acceleration factor. Both sequences have a FOV of 190 mm, a TR of 550 ms, a TE of 11 ms, and echo spacing of 10.9 ms.

(9D), which is the Deep Resolve sequence, has medium denoising and sharp edge options, a 259×288 matrix (90% phase), and a reconstructed voxel size of $0.3 \times 0.3 \times 2.0 \text{ mm}^3$. It runs for 2:43 minutes. The sequence was acquired with a voxel size of $0.73 \times 0.76 \times 2.0 \text{ mm}^3$ with 2 averages and 1 concatenation. The Deep Resolve sequence required 120% phase oversampling, compared to 80% phase oversampling with the conventional sequence. The Deep Resolve sequence was acquired with a 90% phase resolution, compared to 75% phase resolution in the conventional sequence.

(9E) is from the same patient as in the example above. (9E) used medium denoising and sharp edge options, a reconstructed voxel size of $0.3 \times 0.3 \times 2.0 \text{ mm}^3$, with a base matrix of 259×288 (90% phase), an acquired voxel size of $0.69 \times 0.63 \times 2.0 \text{ mm}^3$, and a scan time of 2:10 minutes. The sequence also has 2 averages, 1 concatenation, a FOV of 180 mm, GRAPPA 2, a TR of 3800 ms, a TE of 82 ms, a turbo factor of 17, and echo spacing of 10.3 ms.

Whole-brain imaging

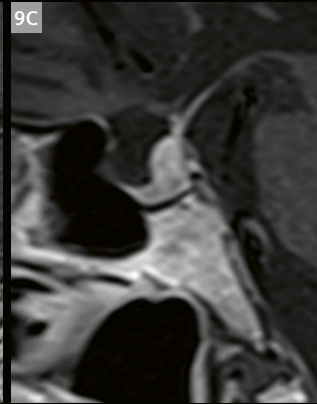
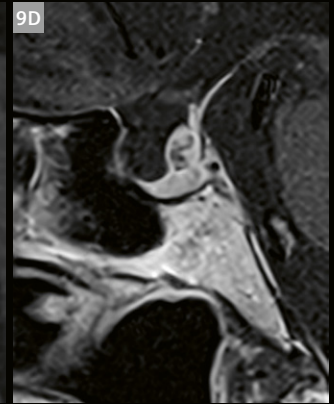
At NRGH, our previous standard axial was a 5 mm BLADE sequence, acquiring 26 slices with a 30% gap (1.5 mm) over 1:51 minute. The sequence is lacking spatial resolution, although it had a fairly high-resolution matrix of 320×320 and a FOV of 230 mm (which was not rectangular due to the BLADE option).

The results of the optimized axial Deep Resolve T2 TSE sequence are stunning and shown in Figures 10B and 10D. In a scan time of 2:39 minutes, a very high-resolution square voxel sequence is acquired with 46 slices of 3 mm thickness with a 20% gap (0.6 mm). Spatial resolution is increased as slice thickness is 3 mm instead of 5 mm, the acquisition matrix has increased to 400×400 from 320×320 , and the slice gap has decreased by over 50%, so more of the brain tissue is being imaged. The resolution advantage can be demonstrated in cranial nerves 7 and 8, with the individual nerves clearly resolved in Figure 10B. The normal flow voids appear similar in both the standard and Deep Resolve versions of the axial T2 TSE sequence. We first adopted the sequence as part of our seizure protocol, and the slightly shorter axial Deep Resolve T2 TSE is now part of our routine brain imaging.

Axial T2 TSE brain (Figure 10)

In Figure 10, we see axial T2 images of the posterior fossa from a whole-brain exam. (10A) is conventional BLADE, while (10B) is a Deep Resolve image from the seizure protocol. Scan time: 1:51 minute for the BLADE sequence and 2:59 minutes for the Deep Resolve sequence. Both sequences have a TR of 4500 ms, and a TE of 88 and 95 ms respectively. (10A) is an axial T2 TSE BLADE with a base matrix of 320×320 , an acquired voxel size of $0.72 \times 0.72 \times 5.0 \text{ mm}^3$ with no interpolation, 2 concatenations, GRAPPA 2, 26 slices with a 30% gap (1.5 mm), and an echo spacing of 5.5 ms.

(10B) is the axial Deep Resolve T2 sequence and part of the seizure protocol. 46 slices of 3 mm thickness are collected over 2:59 minutes with medium denoising and sharp edge options. The base matrix is square at 400×400 , the acquired voxel is $0.57 \times 0.57 \times 3.0 \text{ mm}^3$ and is reconstructed to $0.29 \times 0.29 \times 3.0 \text{ mm}^3$. The slice gap is 20% (0.6 mm), and 1 average, 2 concatenations,

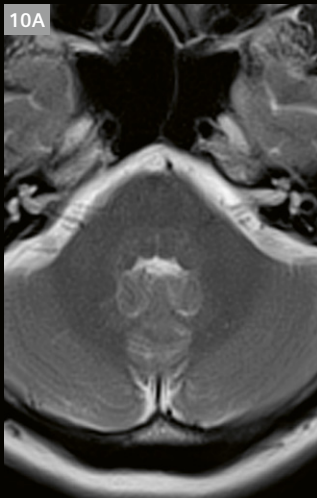
Coronal conventional
T1 post-contrastCoronal Deep Resolve
T1 post-contrastSagittal conventional
T1 post-contrastSagittal Deep Resolve
T1 post-contrast

Coronal Deep Resolve T2 TSE

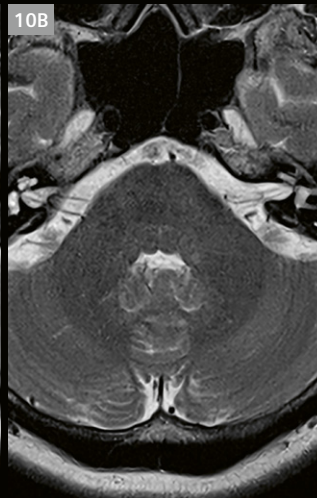


9 Pituitary gland imaging

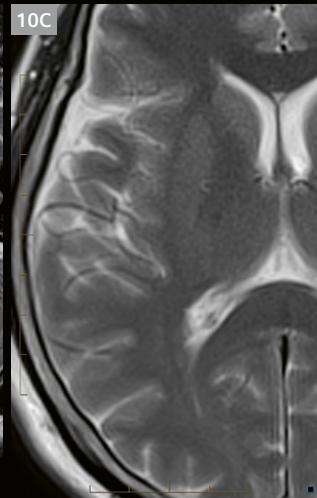
Axial conventional T2 TSE BLADE



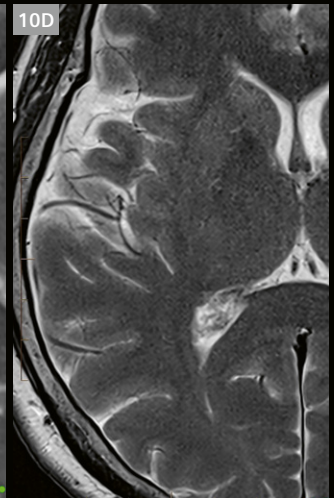
Axial Deep Resolve T2 TSE



Axial conventional T2 TSE BLADE



Axial Deep Resolve T2 TSE



10 Brain imaging

GRAPPA 2, 50% phase oversampling, and an echo spacing of 10.6 ms are used. Note the significantly improved resolution on the Deep Resolve image with excellent delineation of cranial nerves 7 and 8, the inner ear structures, and the cerebrospinal fluid (CSF)/parenchymal interfaces. Improved assessment of the basilar artery is seen. (Another axial Deep Resolve T2 sequence, now part of the routine brain protocol, takes 2:39 minutes, uses 3 concatenations, and a higher TR. All other parameters are the same as the Deep Resolve seizure sequence above.)

(10C, 10D) are from the same patient and sequence as above. Both images are zoomed to illustrate the significant improvement in spatial resolution. Note the improved grey/white matter differentiation and depiction of the CSF/parenchymal interfaces, and that the preservation of the normal vascular flow voids is apparent.

Our previous standard axial FLAIR at NRGH was a 5 mm sequence, acquiring 26 slices with a 30% gap (1.5 mm) over 3:54 minutes. The sequence had a spatial resolution of 240×320 (70% phase), was not interpolated, and yielded a $0.7 \times 0.7 \times 5.0 \text{ mm}^3$ voxel size. The sequence was adequate but long and the phase resolution was not near the 90% to 100% we are aiming for in neuro imaging. Our routine brain protocol now includes a 3 mm Deep Resolve FLAIR sequence. We illustrate two Deep Resolve options below and compare them to our conventional FLAIR sequence. The first is a 5 mm Deep Resolve FLAIR sequence and the second is a 3 mm Deep Resolve FLAIR sequence. The 5 mm Deep Resolve FLAIR has a scan time of 2:42 minutes and the 3 mm Deep Resolve FLAIR is taken directly from the protocol tree of Siemens Healthineers and has a scan time of 2:39 minutes. We have added the 3 mm Deep Resolve FLAIR to our routine brain protocol, but please note that we do see CSF-related flow artifact in the ventricles with the thin slice sequence.

Axial FLAIR brain (Figure 11)

(11A) is a conventional axial FLAIR with a base matrix of 240×320 (70% phase) and acquired in 3:56 minutes. The image was acquired with a voxel size of $0.7 \times 0.7 \times 5.0 \text{ mm}^3$, 1 average, 2 concatenations, and GRAPPA 2 with no interpolation.

(11B) is an axial Deep Resolve FLAIR sequence with medium denoising and sharp edge options, an acquired voxel size of $1.2 \times 0.9 \times 5.0 \text{ mm}^3$ reconstructed to $0.4 \times 0.4 \times 5.0 \text{ mm}^3$, and acquired in 2:26 minutes. The matrix is 192×256 (75% phase) and was acquired with 1 average, 2 concatenations, and an increased GRAPPA factor of 3. Both (11A) and (11B) have a slice thickness of 5 mm, a TR of 9000 ms, a TE of 86 ms, and 40% phase oversampling.

In (11A) and (11B), there is minor ischemic change within the periventricular region. Resolution is improved

on the Deep Resolve image, with improved edge definition and grey/white matter differentiation.

(11C) is the 3 mm Deep Resolve FLAIR sequence that is now part of our routine brain imaging. The sequence collects 50 slices of 3 mm thickness, has a 10% slice gap (0.3 mm), a base matrix of 272×272 (100% phase), a reconstructed voxel size of $0.4 \times 0.4 \times 3.0 \text{ mm}^3$, and is acquired in 2:39 minutes. The sequence has Deep Resolve high denoising and sharp edge options, 1 average, 2 concatenations, and GRAPPA 2. The image demonstrates flow void artifact within the ventricle seen with this 3 mm Deep Resolve FLAIR sequence. The sequence replaced our previous FLAIR sequence, which had 5 mm slice thickness and took 3:54 minutes (shown in (11A)).

The combination of Deep Resolve sequences, a slightly longer axial T2 TSE, and a shorter axial FLAIR allows the department to perform highly resolved brain imaging. In our previous protocol, the conventional 5 mm axial T2 TSE BLADE and the 5 mm axial FLAIR had a cumulative acquisition time of 4:55 minutes. With the Deep Resolve sequences, the protocol has a cumulative acquisition time of 5:19 minutes, however, with thinner 3 mm slices for both the axial Deep Resolve T2 TSE and the axial Deep Resolve FLAIR sequences.

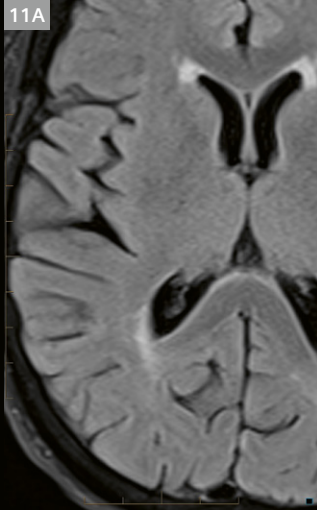
Cervical spine imaging

In the first example of the cervical spine, we compare the standard SMS protocol to Deep Resolve sequences, for which different percentages of phase data are acquired. The Deep Resolve option, with its inherent SNR advantage from AI technology, was used to decrease acquisition time while improving contrast and spatial resolution. The routine sagittal T2 TSE sequence is run with a resolution of 240×320 with 75% of the base matrix in the phase direction, a slice thickness of 2.5 mm, a 10% gap (0.25 mm), and is acquired in 3:05 minutes. The sagittal Deep Resolve T2 cervical spine images demonstrate a two-step decrease in base resolution, decreased averages (from 5 to 2), in-plane parallel imaging GRAPPA (instead of SMS acquisition), and an increase in phase oversampling from 100% to 140% to prevent phase-wrapping artifact from the higher PAT factor. We ran the Deep Resolve sequences with 75% and 85% phase resolution and compared the results with our routine sequence. The results were improved contrast, higher reconstructed resolution, less flow artifact, and acquisition times for the Deep Resolve sequences that were 38% less than the conventional sequence for the sagittal T2 TSE.

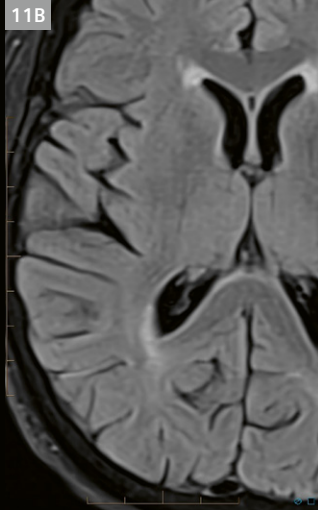
Sagittal cervical spine (Figure 12)

(12A–12C) show images of the cervical spine from the same patient. There is improved resolution and contrast on the Deep Resolve images. There is slightly improved

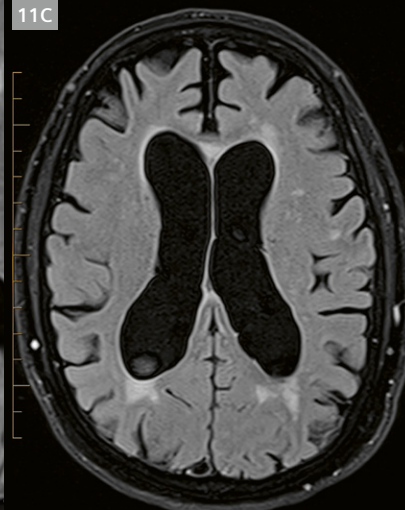
Axial conventional FLAIR 5 mm



Axial Deep Resolve FLAIR 5 mm



Axial Deep Resolve FLAIR 3 mm

**11** FLAIR brain imaging

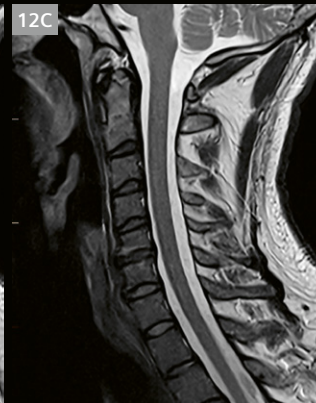
Routine sagittal conventional T2 TSE



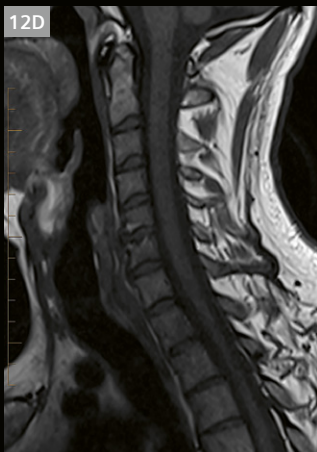
Deep Resolve T2 TSE 75% phase



Deep Resolve T2 TSE 85% phase



Conventional T1 TSE



Deep Resolve T1 TSE, phase 80%



Deep Resolve T1 TSE, phase 90%

**12** Cervical spine imaging

sharpness on the sagittal Deep Resolve T2 TSE 85% phase image. Scan time: conventional sagittal T2 acquired in 3:05 minutes, sagittal Deep Resolve T2 TSE 75% phase resolution acquired in 1:56 minutes, and sagittal Deep Resolve T2 TSE 85% phase resolution acquired in 2:05 minutes.

Increasing the number of phase steps collected (from 75% to 85%) raised image resolution slightly and the penalty was an increased data collection time of 9 seconds. Both Deep Resolve sequences have 140% phase oversampling, GRAPPA 3, a TR of 4630 ms, a TE of 81 ms, medium denoising, and sharp edge enhancement. All three of the sagittal T2 sequences have a FOV of 240 mm, an echo time of 11.5 ms, and a turbo factor of 16.

(12A) is a conventional sagittal T2 TSE with a base matrix of 240×320 (75% phase), an acquired voxel size of $1.0 \times 0.75 \times 2.5 \text{ mm}^3$ interpolated to $0.75 \times 0.75 \times 2.5 \text{ mm}^3$, 5 averages, 1 concatenation, an SMS factor of 2, a TR of 2310 ms, a TE of 81 ms, and an acquisition time of 3:05 minutes.

(12B) is a sagittal Deep Resolve T2 TSE with 75% phase collection that was acquired with a voxel size of $1.18 \times 0.88 \times 2.5 \text{ mm}^3$ reconstructed to $0.44 \times 0.44 \times 2.5 \text{ mm}^3$. (12C) is a sagittal Deep Resolve T2 TSE with 85% phase collection. It has a slightly smaller acquired voxel at $1.04 \times 0.88 \times 2.5 \text{ mm}^3$, reconstructed to $0.44 \times 0.44 \times 2.5 \text{ mm}^3$. The reconstructed data from the Deep Resolve sequences have almost twice the resolution compared to our routine sequence, and were collected in significantly less time. The slightly improved detail and signal seen in (12C) is due to the higher percentage of phase data collected.

In the next cervical spine example, we again compare the standard SMS protocol to Deep Resolve sequences with different percentages of phase data acquired in the pursuit of improving resolution while decreasing scan time. (12D) shows a conventional sagittal T1 TSE with 80% phase resolution, (12E) is a sagittal Deep Resolve T1 TSE with 80% phase resolution, and (12F) is a sagittal Deep Resolve T1 TSE with 90% phase resolution of the cervical spine. They were all collected from the same patient. The Deep Resolve images demonstrate improved resolution and contrast. There is slightly improved sharpness and signal on the Deep Resolve image with more phase data collected (12F, 90% phase). In terms of scan time, the conventional sagittal T1 is acquired in 2:32 minutes, while the sagittal Deep Resolve T1 with 80% phase is acquired in 2:32 minutes, and the sagittal Deep Resolve T1 TSE with 90% phase is acquired in 2:51 minutes. Increasing the number of phase steps (from 80% to 90%) slightly decreased SNR and improved the image resolution minimally, although the time penalty was 20 seconds. The interpolated data for (12D) and (12E) are the same voxel size ($0.47 \times 0.47 \times 2.5 \text{ mm}^3$), demonstrating significant improvement in spatial and

contrast resolution when moving from a conventional sequence to a sequence with AI technology.

(12D) is a conventional sagittal T1 TSE with a base matrix of 205×256 (80% phase resolution), an acquired voxel size of $1.17 \times 0.94 \times 2.5 \text{ mm}^3$ interpolated to $0.47 \times 0.47 \times 2.5 \text{ mm}^3$, with 5 averages, 1 concatenation, an SMS factor of 2, a TR of 412 ms, and a TE of 9.9 ms. The acquisition time is 2:32 minutes.

(12F) is a sagittal Deep Resolve T1 TSE with 90% phase resolution, with a base resolution of 230×256 , a slightly smaller acquired voxel at $1.04 \times 0.94 \times 2.5 \text{ mm}^3$ reconstructed to $0.47 \times 0.47 \times 2.5 \text{ mm}^3$, and a scan time of 2:51 minutes. Both Deep Resolve sequences have 140% phase oversampling, GRAPPA 3, a TR of 645 ms, a TE of 12 ms, medium denoising, and sharp edge enhancement. All of the sagittal T1 sequences have a FOV of 240 mm, an echo time of 9.9 ms, and a turbo factor of 3.

(12D–12F) demonstrate findings similar to the previous example. There is improved resolution and contrast on the Deep Resolve images, and increased signal on the Deep Resolve sequence with the highest phase resolution (most square voxel imaging). Increasing the number of phase steps (from 80% to 90%) increases image resolution but the penalty is a longer data collection time and reduced SNR. Images acquired with a square or 100% phase would have more resolution but would suffer a higher time penalty and reduced SNR. Clinical decisions are used to justify the tradeoffs of added time, SNR, and resolution. We can see from the images above that there is only minor benefit when moving from a phase of 80% to 90%.

Thoracic spine imaging

High-quality imaging of the thoracic spine can at times be challenging due to respiratory motion and CSF flow artifact. Deep Resolve was used to decrease scan times and improve SNR, spatial resolution, and contrast resolution. Imaging of the thoracic spine was challenging with Deep Resolve, yet we achieved acceptable thoracic spine images when increased phase FOV was used in combination with phase oversampling. The sagittal Deep Resolve T2 sequence is now part of our routine thoracic spine protocol.

Sagittal and axial thoracic spine (Figure 13)

(13A, 13B) Demonstrate improved contrast and SNR, decreased artifact, and increased conspicuity of the thoracic disc with Deep Resolve. Scan time: routine sagittal T2 acquired in 2:29 minutes; sagittal Deep Resolve T2 acquired in 2:16 minutes.

(13A) is a conventional sagittal T2 TSE with a base matrix of 307×384 (80% phase resolution) and an acquired voxel size of $1.14 \times 0.9 \times 3.0 \text{ mm}^3$ interpolated to $0.91 \times 0.91 \times 3.0 \text{ mm}^3$, with 3 averages, 1 concatenation, an SMS factor of 2, a TR of 2110 ms, a TE of 86 ms, and an acquisition time of 2:29 minutes.

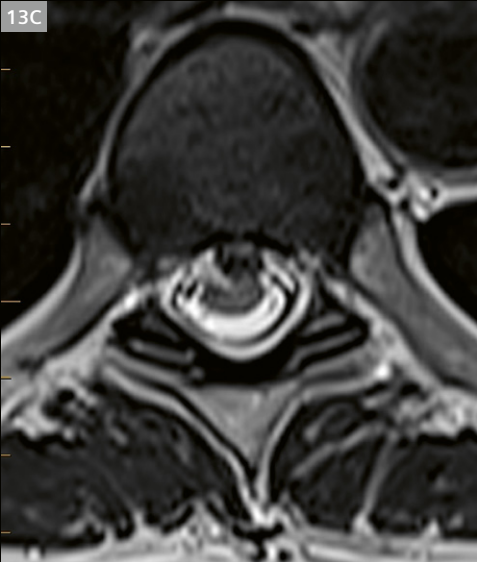
Sagittal conventional T2 TSE



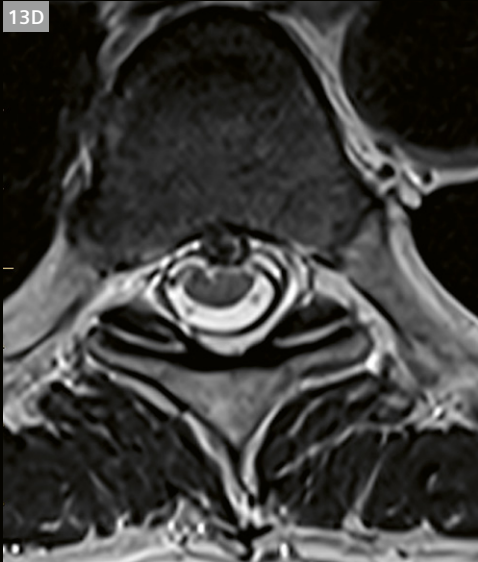
Sagittal Deep Resolve T2 TSE



Axial conventional T2 TSE



Axial Deep Resolve T2 TSE



13 Thoracic spine imaging

(13B) is a sagittal Deep Resolve T2 TSE sequence acquired in 2:16 minutes. The sequence is a rectangular FOV with 150% FOV phase, an FOV of 230 mm, and 150% phase oversampling. The base resolution is 346×256 (90% phase resolution) and the acquired voxel is $1.0 \times 0.9 \times 3.0 \text{ mm}^3$, reconstructed to $0.45 \times 0.45 \times 3.0 \text{ mm}^3$. A GRAPPA 2 acceleration was used with high denoising and sharp edge enhancement. The base matrices of both sequences are similar, but the Deep Resolve produces a sequence with twice the spatial resolution when reconstructed.

(13C, 13D) demonstrate similar findings in the axial plane (improved contrast and SNR, decreased artifact) and increased conspicuity of the thoracic disc with Deep Resolve, with improved depiction of the disc protrusion. Scan time: routine axial T2 acquired in 4:08 minutes; axial Deep Resolve T2 acquired in 3:13 minutes.

Both sequences have a FOV of 190 mm, 36 slices, a 15% gap, and a slice thickness of 3.5 mm. (13C) has a base matrix of 202×288 (70% phase resolution), an acquired voxel size of $0.94 \times 0.66 \times 3.5 \text{ mm}^3$, 3 averages, GRAPPA 2, and 30% phase oversampling. (13D) has a base matrix of 205×256 (80% phase resolution) and an acquired voxel size of $0.93 \times 0.74 \times 3.5 \text{ mm}^3$ reconstructed to $0.37 \times 0.37 \times 3.5 \text{ mm}^3$. It used GRAPPA 2, as well as 2 averages and 70% phase oversampling.

Axial upper thoracic spine imaging can often be suboptimal due to the changing spinal curvature in the area and the inability of the block of slices to be perpendicular to each disc. Depending on the curvature of the spine, data can be collected at acute angles to the vertebrae, which yields suboptimal images. In our experience, axial Deep Resolve imaging seems to resolve this problem somewhat and can produce improved axial imaging in the upper thoracic spine when block axial acquisitions are collected.

Lumbar spine imaging

Similar to the imaging attempts in the cervical and thoracic spine areas, Deep Resolve was used to optimize imaging in the lumbar spine. Imaging of the spine was challenging and rewarding with Deep Resolve. We experienced acceptable sagittal thoracic and lumbar spine images when extended phase FOV was used in combination with phase oversampling. The sagittal Deep Resolve T2 and T1 TSE sequences and the axial Deep Resolve T2 TSE sequences are now part of our routine protocol for both the thoracic and lumbar spine. Based on the findings and optimization of Deep Resolve sequences, NRGH has done the following:

- Implemented a 13-minute T-spine protocol, which took almost 18 minutes without Deep Resolve
- Implemented a 9-minute L-spine protocol, which took 13 minutes without Deep Resolve

Lumbar spine imaging (Figure 14)

(14A) Is a conventional sagittal T2 TSE sequence with a FOV of 280 mm and 100% oversampling. The sequence uses a base matrix of 280×400 , has an acquired voxel size of $1.0 \times 0.7 \times 3.0 \text{ mm}^3$ reconstructed to $0.7 \times 0.7 \times 3.0 \text{ mm}^3$, 2 averages, and 1 concatenation.

(14B) Is a sagittal Deep Resolve T2 TSE sequence with a rectangular FOV of 190 mm with a 150% FOV, and 150% phase oversampling. The base resolution is 280×208 (90% phase) with an acquired voxel size of $1.0 \times 0.9 \times 3.0 \text{ mm}^3$, reconstructed to $0.46 \times 0.46 \times 3.0 \text{ mm}^3$. GRAPPA 2 acceleration was used with high denoising and sharp edge enhancement.

The Deep Resolve images demonstrate increased signal with improved delineation of vertebral endplates and nerve roots, with decreased motion and pulsation artifact. Scan time: conventional sagittal T2 TSE acquired in 2:59 minutes; sagittal Deep Resolve T2 TSE acquired in 1:12 minute.

(14C, 14D) Illustrate improved resolution and contrast with decreased artifact using Deep Resolve. Scan time: conventional sagittal T1 TSE acquired in 2:36 minutes; sagittal Deep Resolve T1 TSE acquired in 1:57 minute.

(14C) A conventional sagittal T1 TSE sequence with an FOV of 280 mm and 70% oversampling. The sequence uses a base matrix of 268×384 , an acquired voxel size of $1.0 \times 0.7 \times 3.0 \text{ mm}^3$ reconstructed to $0.7 \times 0.7 \times 3.0 \text{ mm}^3$, with 2 averages and 2 concatenations.

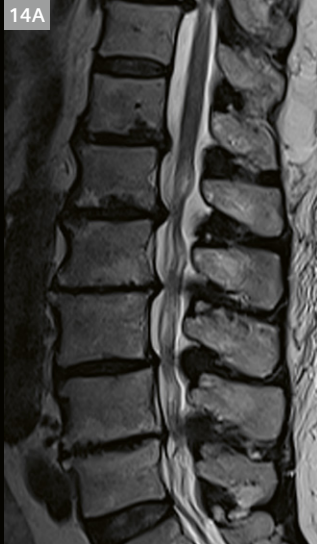
(14D) A sagittal Deep Resolve T1 TSE sequence that uses a rectangular FOV of 190 mm with a 150% FOV phase and 120% phase oversampling. The base resolution is 270×208 (90% phase) with an acquired voxel of $1.01 \times 0.91 \times 3.0 \text{ mm}^3$ reconstructed to $0.46 \times 0.46 \times 3.0 \text{ mm}^3$. Deep Resolve with high denoising and sharp edge enhancement was used, as well as 1 average and 1 concatenation.

The axial Deep Resolve T2 TSE sequence had a base resolution of 205×256 (80% phase resolution) with an acquired voxel of $0.93 \times 0.74 \times 3.5 \text{ mm}^3$, reconstructed to $0.37 \times 0.37 \times 3.5 \text{ mm}^3$. Two averages, 1 concatenation, medium denoising, and sharp edge enhancement were also used. The reconstructed spatial resolution in the Deep Resolve imaging has doubled, as seen in the image comparison below.

Both sequences collect 3 mm slices and use an acceleration factor of GRAPPA 2. (14E) and (14F) demonstrate increased signal and sharpness of visualized nerve roots. Scan time: 4:08 minutes for (14E) and 3:13 minutes for (14F).

Both sequences collected 36 slices at 3.5 mm slice thickness using a FOV of 190 mm. On the conventional axial T2 TSE sequence, the base resolution was 202×288 (70% phase resolution) with an acquired voxel of $0.94 \times 0.66 \times 3.5 \text{ mm}^3$. The images are not interpolated. Three averages, 1 concatenation and an acceleration factor of GRAPPA 2 were also used.

Conventional sagittal T2 TSE



Sagittal Deep Resolve T2 TSE



Sagittal conventional T1 TSE



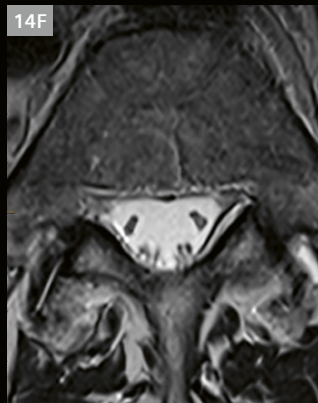
Sagittal Deep Resolve T1 TSE



Axial conventional T2 TSE



Axial Deep Resolve T2 TSE

**14** Lumbar spine imaging

Body imaging focus

Pelvis imaging

Early on, a decision was made to optimize prostate imaging with Deep Resolve. The standard prostate protocol at NRGH consists of the following sequences:

Sequence	Slice thickness (mm)	Gap (mm)	FOV	Time (min:s)
cor T2 TSE prostate	3.0	0	200	3:58
sag T2 TSE prostate	3.0	0	200	3:22
ax T2 TSE prostate and entire pelvis	3.0	0	200	2:49
ax T1 TSE entire pelvis	6.0	1.2	300	2:00
ax T1 GRASP pre- and post-contrast (dynamic)				
ax DWI ZOOMit, small FOV prostate				

Table 7: Prostate imaging

The standard rectal cancer protocol is:

Sequence	Slice thickness (mm)	Gap (mm)	FOV	Time (min:s)
ax T2 TSE	5.0	0.5	230	3:23
sag T2 TSE	3.0	0	200	2:59
cor T2 TSE	3.0	0	200	3:40
ax oblique T2 TSE	3.0	0	200	3:02
ax T1 TSE	5.0	0.5	230	2:23

Table 8: Rectal cancer imaging

As a result of previous success with Deep Resolve for rectal and prostate imaging, it was felt that using Deep Resolve would offer even more advantages. One of the challenges we observed with Deep Resolve, however, is the susceptibility to peristaltic motion artifacts, which can be explained by the reduced motion averaging effect with the lower number of averages acquired in Deep Resolve protocols.

As we do not use antiperistaltics routinely we were not able to consistently obtain high quality, high-resolution images required for these anatomic regions and consequently have not adopted Deep Resolve for our default protocol. Sites that routinely use antiperistaltics for rectal imaging may have a different experience: Image quality may be improved and scan time shortened with the application of Deep Resolve. Another countermeasure may be to balance out motion with more averages, which partially counteracts the time savings gained with Deep Resolve and has not been systematically tested in our setting.

One other area where Deep Resolve may be of benefit is in the evaluation of organ-at-risk (OAR) prostate spacer gel prior to radiation therapy in prostate cancer. These exams do not require high-resolution imaging.

Sagittal and axial prostate (Figure 15)

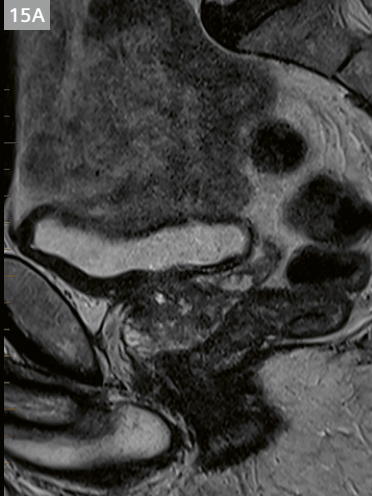
Figures (15A) and (15B) from a prostate exam demonstrate less motion and improved delineation of the rectal and bladder wall with Deep Resolve. However, the posterior peripheral zone cancer is slightly less conspicuous on Deep Resolve imaging.

(15C) and (15D) from a different patient show the following: While the margins of the prostate are more distinct on the Deep Resolve image, the apical cancer is more conspicuous and better defined on the conventional sequence in this particular case, potentially caused by motion effects as described before.

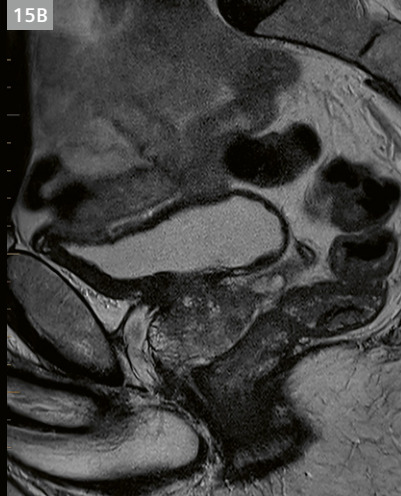
One area in prostate imaging that may benefit from Deep Resolve is in the evaluation of OARS spacer gel. The exam is performed to document the position of the gel spacer relative to the prostate and does not require high resolution. A shorter scan time would be attractive in these patients. Figures (15E) and (15F) show the position of the gel spacer, with improved signal on the Deep Resolve image. Scan time: (15E) conventional is 3:09 minutes and (15F) Deep Resolve is 2:40 minutes.

(15E) has a base resolution of 336, and (15F) has a base resolution of 320. Both sets of images reconstruct to $0.31 \times 0.31 \times 3.0 \text{ mm}^3$ voxel size. The Deep Resolve image demonstrates the power of AI when voxel sizes are directly compared.

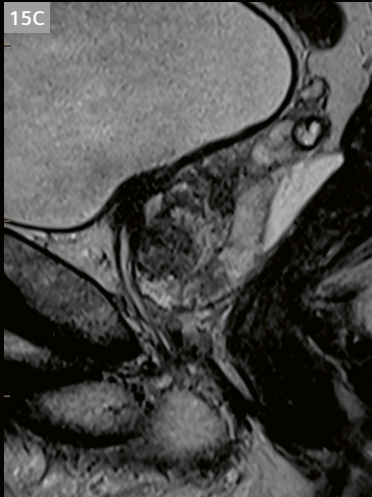
Sagittal conventional T2 TSE



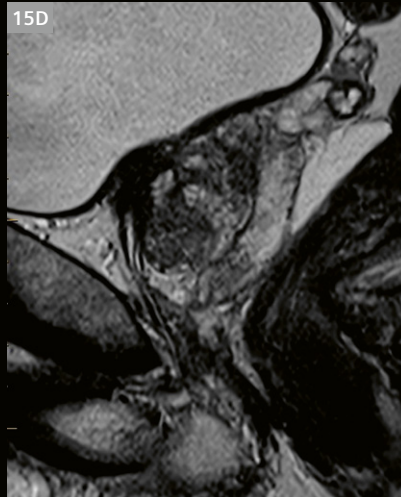
Sagittal Deep Resolve T2 TSE



Sagittal conventional T2 TSE



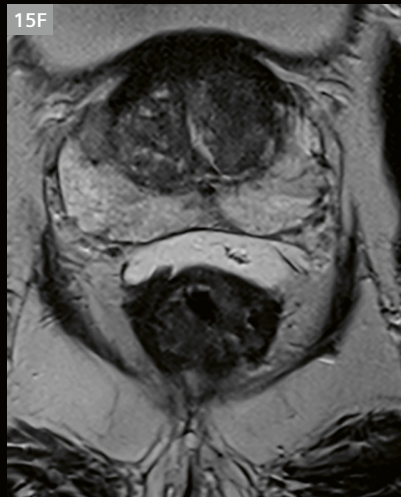
Sagittal Deep Resolve T2 TSE



Axial conventional T2 TSE



Axial Deep Resolve T2 TSE



Female pelvis imaging

The standard female pelvis protocol at NRGH consists of the following sequences:

Sequence	Slice thickness (mm)	Gap (mm)	Time (min:s)
cor Deep Resolve STIR Pelvis	4.0	0.8	1:11
sag T2 TSE uterus	4.0	0.4	2:58
ax T2 TSE pelvis	5.0	0.5	3:10
ax T1 TSE pelvis	5.0	0.5	2:23
ax T1 FS TSE pelvis	5.0	0.5	3:20
sag Deep Resolve T1 FS TSE	4.0	0.4	2:22
ax T1 TSE FS pre- and post-contrast	5.0	0.5	3:20
ax DWI pelvis	5.0	0.5	3:15

Table 9: Female pelvis

Coronal, axial, and sagittal pelvic imaging (Figure 16)

(16A) and (16B) demonstrate similar conspicuity of the uterine fibroids on Deep Resolve and conventional images. The scan time for the conventional sequence was 2:27 minutes and for the Deep Resolve sequence it was 1:11 minute. Fat saturation is uniform and equivalent. Note the improved edge definition of the hip joints and the bladder wall with Deep Resolve.

(16A) is a conventional coronal STIR with a base matrix of 288×384 , a 380 mm FOV, and a scan time of 2:27 minutes. The image was acquired with a voxel size of $0.99 \times 0.99 \times 4.0 \text{ mm}^3$, no interpolation, 1 average, 1 concatenation, and GRAPPA 2. (16B) is the Deep Resolve sequence with medium denoising and sharp edge enhancement options, interpolation, a reconstructed voxel of $0.59 \times 0.59 \times 4.0 \text{ mm}^3$, a 380 mm FOV acquired in 1:11 minute. The image was acquired with a voxel size of $1.58 \times 1.19 \times 4.0 \text{ mm}^3$, 1 average, 1 concatenation, and GRAPPA 4. The 1-minute coronal STIR is now part of the routine protocol for female pelvic imaging.

(16C) and (16D) also demonstrate equivalent image quality on axial T2 TSE. (16C) was acquired with a base matrix of 256×320 and a 230 mm FOV in 3:10 minutes. The image was acquired with a voxel size of $0.7 \times 0.7 \times 5.0 \text{ mm}^3$, no interpolation, 1 average, and 1 concatenation.

(16D) is the axial Deep Resolve T2 TSE sequence with medium denoising and sharp edge enhancement options, interpolation, a reconstructed voxel of $0.42 \times 0.42 \times 5.0 \text{ mm}^3$, and a 230 mm FOV acquired

in 2:25 minutes. The image was acquired with a voxel size of $0.94 \times 0.85 \times 5.0 \text{ mm}^3$, 1 average, 2 concatenations, and GRAPPA 2. The conventional sequence had a TR of 3940 ms and a TE of 101 ms, and the Deep Resolve sequence had a TR of 3580 ms with a TE of 103 ms.

(16E, 16F) The Deep Resolve image demonstrates slightly improved edge definition. Note the improved conspicuity of the right ovarian T1 hyperintensity with Deep Resolve. (16E) was acquired with a base matrix of 240×320 and a 230 mm FOV in 2:23 minutes. The image was acquired with a voxel size of $0.7 \times 0.7 \times 5.0 \text{ mm}^3$, no interpolation, 1 average, and 3 concatenations.

(16F) is the axial Deep Resolve T1 TSE sequence with medium denoising and sharp edge enhancement options, interpolation, a reconstructed voxel of $0.4 \times 0.4 \times 5.0 \text{ mm}^3$, and a 230 mm FOV acquired in 2:38 minutes. The image was acquired with 1 average, 3 concatenations, GRAPPA 2, and 120% phase oversampling. The conventional sequence had a TR of 555 ms and a TE of 19. The Deep Resolve sequence had a TR of 578 ms and a TE of 20 TE ms.

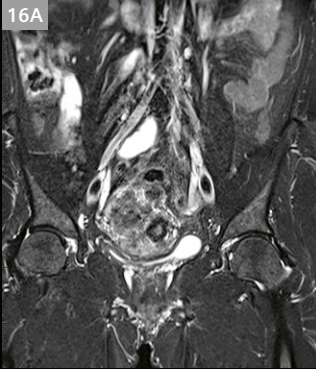
(16G, 16H) demonstrate improved resolution and diminished motion artifact related to vascular pulsation and peristalsis using Deep Resolve. Note the improved delineation of the left ovary, as well as increased conspicuity of the right ovarian hyperintensity.

(16G) is the conventional axial T1 TSE FS post-contrast with a base matrix of 240×320 acquired in 3:20 minutes. The image was acquired with a voxel size of $0.7 \times 0.7 \times 5.0 \text{ mm}^3$, no interpolation, 1 average, and 4 concatenations.

(16H) is the axial post-contrast Deep Resolve T1 TSE FS with high denoising and sharp edge options, interpolation, a reconstructed voxel of $0.4 \times 0.4 \times 4.0 \text{ mm}^3$ with a base matrix of 288×320 . The image was acquired with 1 average, 5 concatenations, GRAPPA 4, and 140% phase oversampling. Extended phase oversampling was required to ameliorate the aliasing effects of a higher acceleration GRAPPA. A TR of 576 ms, a TE of 19 ms, and 40 slices of 5 mm thickness were used on the conventional sequence, compared to a TR of 611 ms, a TE of 8.4 ms, and 50 slices at 4 mm thickness for the Deep Resolve sequence.

Figure (16I) illustrates the lack of motion artifact and excellent fat saturation on the sagittal Deep Resolve T1 FS. This is a reliable and robust sequence, which has been adopted as part of our endometriosis protocol. The sagittal Deep Resolve T1 FS was acquired with high denoising and sharp edge enhancement options, interpolation, a reconstructed voxel of $0.4 \times 0.4 \times 4.0 \text{ mm}^3$ with a base matrix of 288×320 . The image was acquired with a voxel size of $0.8 \times 0.7 \times 4.0 \text{ mm}^3$, 1 average, 4 concatenations, GRAPPA 4, and 140% phase oversampling. A TR of 550 ms and a TE of 8.4 ms were used.

Coronal conventional STIR



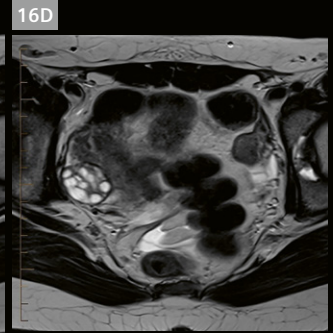
Coronal Deep Resolve STIR



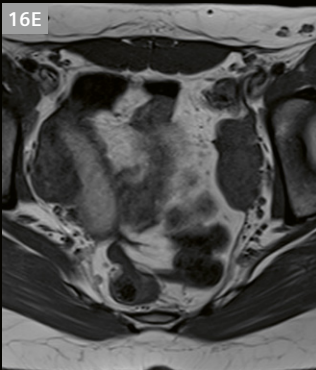
Axial conventional T2 TSE



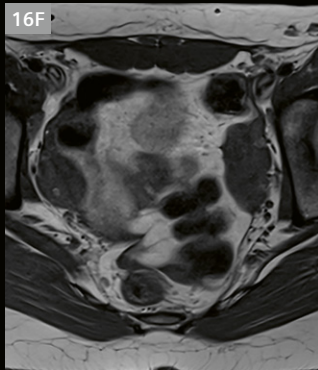
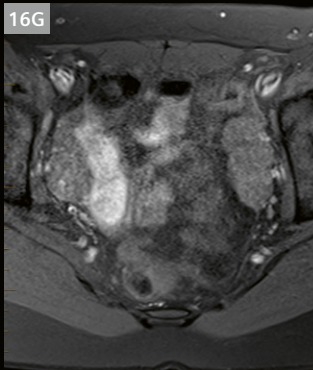
Axial Deep Resolve T2 TSE



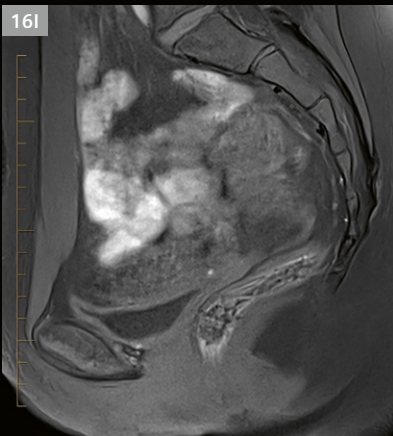
Axial conventional T1 TSE



Axial Deep Resolve T1 TSE

Axial conventional T1 FS
post-contrastAxial Deep Resolve T1 FS
post-contrast

Sagittal Deep Resolve T1 FS TSE



16 Pelvic imaging

Cardiac imaging

Our final assessment of Deep Resolve was for TSE imaging of the heart. This is a common technique for turbo inversion recovery magnitude (TIRM) and TSE anatomical and morphologic assessment of the cardiac muscle. TIRM is commonly employed in the arrhythmogenic right ventricular cardiomyopathy (ARVC) protocol, the myocarditis protocol, and in the cardiac mass protocol.

Deep Resolve performance was compared to standard TIRM in the short axis. TIRM is a common sequence for assessment of myocardial edema in myocarditis. Figures (17A) and (17B) show that the Deep Resolve image has significantly improved resolution and signal. Motion artifacts are minimized. Deep Resolve also allows for a shorter breath-hold, approximately 13 seconds compared to 19 seconds for the conventional sequence. Since changing our default protocol to Deep Resolve, we feel that Deep Resolve facilitates improved detection of myocardial edema.

Short-axis dark-blood cardiac imaging (Figure 17)

(17A) is the conventional T2 short-axis dark-blood (DB) inversion recovery with a base matrix of 154×192 and an FOV of 360 mm acquired in a 19-second breath-hold. The image was acquired with a voxel size of $1.8 \times 1.8 \times 10 \text{ mm}^3$, no interpolation, 1 average, and no acceleration. (17B) is the Deep Resolve sequence with medium denoising and sharp edge options, a reconstructed voxel of $0.63 \times 0.63 \times 6.0 \text{ mm}^3$, and a 400 mm FOV (with an 84% phase FOV) acquired in a 13-second breath-hold. The image was acquired with a voxel size of $1.67 \times 1.25 \times 6.0 \text{ mm}^3$, 1 average, and GRAPPA 3.

Ultrafast imaging

Scanner efficiency and patient care can be improved by using ultrafast sequences on selected populations, such as pediatric, anesthetized, or claustrophobic patients. We provide two examples of ultrafast imaging performed with Deep Resolve at our site: head and knee imaging.

Ultrafast brain and knee imaging (Figure 18)

(18A) is the 3 mm Deep Resolve FLAIR sequence now part of our routine brain imaging. Scan time is 2:39 minutes compared to 1:06 minute for (18B), which is the ultrafast 3 mm FLAIR. Gibbs (or truncation) artifact is evident on the ultrafast image and can be corrected by increasing the matrix, but that would also increase the acquisition time.

Both sequences collect 50 slices of 3 mm thickness, have a 10% slice gap (0.3 mm), and use high denoising and sharp edge options. (18A) has a base matrix of 272×272 (100% phase) compared to a matrix of 141×176

(80% phase) in (18B). (18B) uses the highest possible acceleration factor of GRAPPA 4 while (18A) uses GRAPPA 2. (18C) is the axial Deep Resolve T2 TSE 3 mm sequence now part of our routine brain imaging. Scan time is 2:39 minutes compared to 1:03 minute for (18D), the ultrafast 3 mm axial Deep Resolve T2.

Both axial T2 TSE 3 mm sequences collect 50 slices of 3 mm thickness, have a 10% slice gap (0.3 mm), with high-level denoising and sharp edge options. (18C) has a base matrix of 400×400 (100% phase) compared to a matrix of 212×352 (60% phase) with the ultrafast scan in (18D). (18C) uses the highest possible acceleration factor of GRAPPA 4, while (18D) uses GRAPPA 2. Note the resolved detail in the ultrafast minute-long sequence.

Using ultrafast sequences, a complete knee exam can be acquired in 4:31 minutes. The approach was to take the Deep Resolve sequences in our current protocol and maximize the acceleration factor, decrease the frequency matrix, and use a reduced-phase FOV where possible with as little phase oversampling as possible. Parameters of the ultrafast knee protocol are:

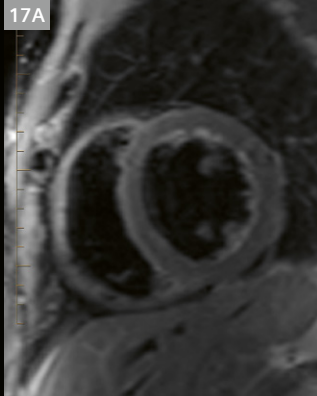
Sequence	Slice thickness (mm)	Gap (mm)	Time (min:s)
sag Deep Resolve PD FS ultrafast	2.5	0.3	1:07
cor Deep Resolve PD FS ultrafast	2.5	0.3	0:59
cor Deep Resolve T1 ultrafast	2.5	0.3	1:16
ax Deep Resolve T2 FS ultrafast	2.5	0.3	1:08

Table 10: Ultrafast knee imaging

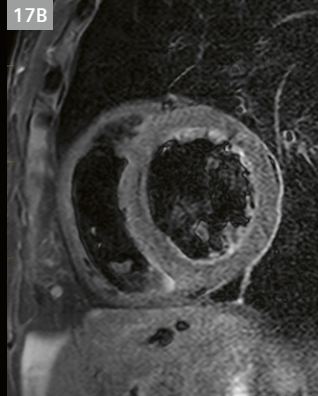
Images (18E–18H) demonstrate the difference in time and image quality between the sagittal Deep Resolve PD FS sequence in our routine Deep Resolve protocol and the ultrafast sagittal Deep Resolve PD FS sequence. Image quality is clearly superior using standard Deep Resolve parameters, although the ultrafast scan is deemed diagnostic.

Images (18E) and (18F) demonstrate a partially torn meniscus. (18G) and (18H) demonstrate the ACL surrounded by fluid. Both sequences collected 38 slices of 2.5 mm thickness, with a 10% gap (0.3 mm) and used 90% phase oversampling; medium denoising and sharp edges were applied to both sequences. The Deep Resolve PD FS sequence used a matrix of 202×288 , SMS 2, and 2 averages. The ultrafast Deep Resolve PD FS sequence used a matrix of 134×192 , GRAPPA 4, and one average. Scan time: Deep Resolve PD FS was 1:55 minute, and the ultrafast Deep Resolve PD FS was 1:07 minute.

Conventional SA TIRM DB

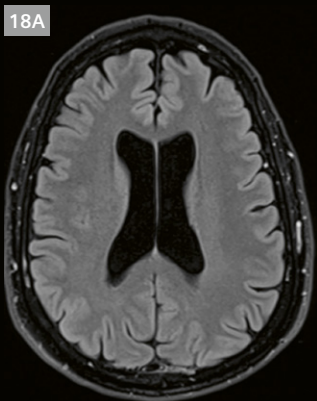


Deep Resolve SA STIR DB

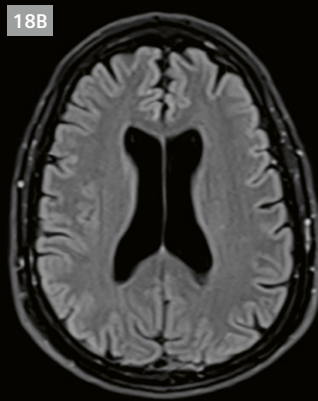


17 Short-axis dark-blood cardiac imaging

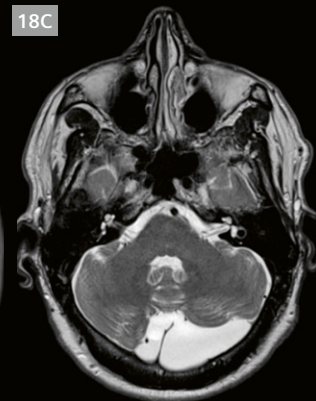
Axial Deep Resolve FLAIR 3 mm



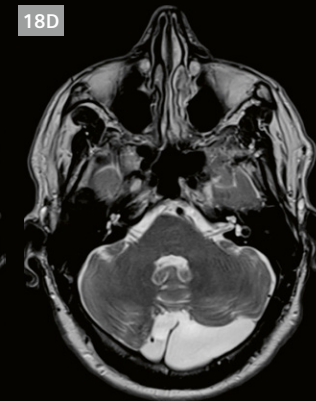
Axial Deep Resolve FLAIR ultrafast 3 mm



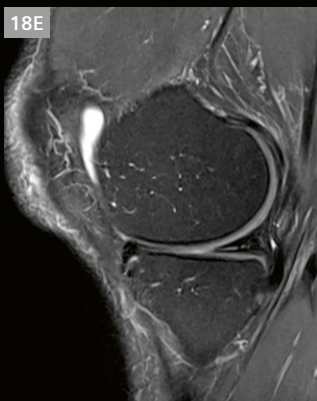
Axial Deep Resolve T2 TSE 3 mm



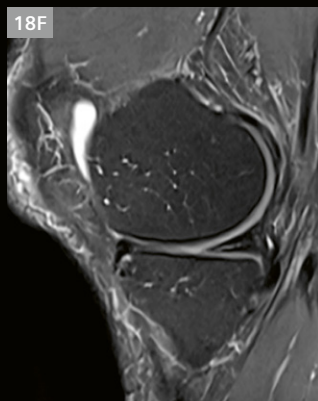
Axial Deep Resolve T2 TSE ultrafast



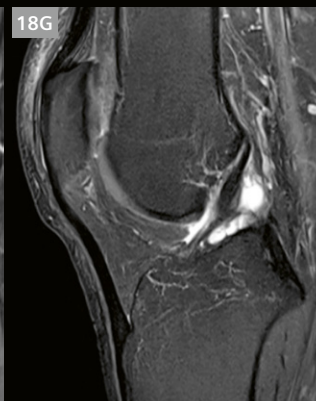
Sagittal Deep Resolve PD FS TSE



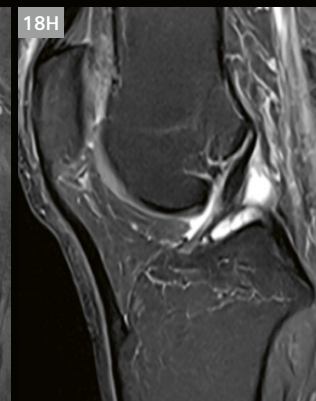
Sagittal Deep Resolve PD FS TSE ultrafast



Sagittal Deep Resolve PD FS TSE



Sagittal Deep Resolve PD FS TSE ultrafast



18 Ultrafast brain and knee imaging

Aside from being advantageous in sedated, pediatric, and claustrophobic patients, ultrafast techniques might be usefully applied in exams requiring lower resolution, such as in patients deemed nonsurgical due to underlying arthritis. Ultrafast sequences might also allow for limited dynamic imaging in certain orthopedic applications.

Observations

The most obvious benefits of Deep Resolve are the resolution enhancement, decreased acquisition time, and apparent SNR boost. Application to virtually all MSK imaging was fairly easy. Spine imaging and body imaging were more challenging as fold-over artifacts may occur in regions with large anatomies and small FOVs, in particular when applying higher PAT factors. To avoid such, an increase of phase oversampling was required for many sequences to compensate for the higher GRAPPA values. When first using Deep Resolve, we were very aggressive with increasing the matrix and averages while increasing GRAPPA, and learned to provide enough phase oversampling to prevent aliasing artifacts, at times up to 200%. After making adjustments and working to optimize the sequences, many of these issues were resolved. The presence of motion poses challenges to MRI, and Deep Resolve acquisitions are no exception, but many of the challenges can be ameliorated with shorter acquisitions or patient coaching. The issue with the phase oversampling requirements being more sensitive to wrap and phase aliasing were resolved by keeping the oversampling at acceptable levels, specific to the area being imaged.

The images included in this report are a sample of the variety of applications that we trialed with the Deep Resolve technology. It appears that more can be achieved in other areas of the body, such as the orbits, IACs, cranial nerves, and other small structures. Vessel wall imaging may also be an interesting area to focus on for future efforts.

Clinical results

In our opinion, Deep Resolve excels the most at musculoskeletal imaging. AI and deep learning generate opportunities that allow for a quantum shift in scheduling and can potentially increase throughput of MSK exams. Decreasing scan times by up to 50% will allow new booking models to increase capacity, which is particularly important in the Canadian system, where limited access is an issue. Future projects could evaluate these changes and how application might affect volumes, efficiency, and wait times. Shorter

scan times will also translate into a more satisfactory patient experience, particularly for claustrophobic and pediatric patients.

As we have seen, Deep Resolve technology allows for a significant increase in spatial resolution and contrast, which is particularly important in small joints. Slice thickness can be reduced while maintaining signal without a significant time penalty, particularly when evaluating fingers, toes, and potentially the temporomandibular joint (TMJ).

Deep Resolve performs well with TSE sequences in the brain. In regard to T2 and FLAIR whole-brain imaging, there is a modest decrease in scan time with an overall improvement in image quality. However, it is particularly advantageous in pituitary imaging, allowing for a decrease in acquisition time and a significant improvement in resolution. Potential future applications might include imaging of the globe and for diagnosis of vasculitis.

Advantages are seen in spinal imaging. Again, these concern shorter scan times, and improved SNR and resolution. An attractive future development would be a Deep Resolve sequence compatible with the Dixon technique for pre- and post-contrast spine work.³

In view of our experience with Deep Resolve, we anticipated that Deep Resolve would excel at pelvic work. Though significant improvements in terms of image quality and time savings were reported in the literature [3] we, unfortunately, were not able to reproduce this in our practice due to the waiver of antiperistaltics. Accordingly, exams requiring high-resolution, small-FOV sequences such as prostate, rectal, and cervical exams were very susceptible to motion, particularly peristalsis but also bladder filling. At this time we have not adopted Deep Resolve protocols in these applications. We do not routinely administer antiperistaltics in these cases, but sites that do would likely have more success. However, full FOV STIR in the pelvis performed well, both for MSK and intrapelvic pathology. In addition, T1 FS was very robust, with excellent fat saturation and a decrease in both motion and flow artifacts compared to conventional T1 FS. The Deep Resolve T1 FS has become our default sequence for evaluation of endometriosis and post-contrast imaging in the pelvis.

There are a few niche situations where Deep Resolve might be advantageous. In pre-radiation MR of the prostate to confirm OARS gel spacer position, high-resolution scanning is not required. Deep Resolve technology also results in very short examinations, so another application is in the use of ultrafast MSK protocols. The ability to perform exams in scan times of less than 5 minutes provides obvious benefits for pediatric and claustrophobic patients.

³Work in progress. Available as a research sequence.

However, while higher resolution images as provided by routine Deep Resolve would be preferred for most patients, a lower resolved but diagnostic scan may be advantageous in selected patients. This technique might be applied in older patients undergoing knee MRI who are unlikely to be surgical candidates. With scan times of approximately a minute, there might be opportunity to perform dynamic imaging through a limited range of motion. Ultrafast techniques requiring lower resolution could be developed for non-MSK applications, such as for documenting cord compression prior to radiation therapy.

Overall, we have been very happy with the performance of Deep Resolve. It has become our method of choice for essentially all MSK protocols, small-FOV neurological brain, spine, and selected body applications. While Deep Resolve for TSE sequences already covers a huge scope of applications and clinical use-cases we are excited to evaluate and clinically implement new and upcoming deep learning algorithms for more sequences in the very near future.

Conclusion

NRGH spent a great deal of time carefully optimizing and refining the protocols with the Deep Resolve sequences on clinical patients. Many of the improvements were made on the fly with clinical patients presenting with a range of common concerns and imaging challenges. Frontline MRI departments face a variety of scenarios and challenges in clinical imaging protocols. Building capacity and improving access to MRI for the future in a sustainable way is critical. The use of deep learning methods with new algorithms to gather high-quality data in shortened acquisition times will be a way forward. Deep learning can optimize and streamline imaging protocols to enhance patient care and reduce the cycle time spent acquiring image data.

References and further reading

- 1 Kim M, Yun J, Cho Y, Shin K, Jang R, Bae HJ, et al. Deep Learning in Medical Imaging. *Neurospine*. 2019;16(4):657–668.
- 2 Parmar R. Training Deep Neural Networks. Medium. Published September 11, 2018. Accessed October 4, 2023. Available from: <https://towardsdatascience.com/training-deep-neural-networks-9fdb1964b964>
- 3 Gassenmaier S, Afat S, Nickel D, Mostapha M, Herrmann J, Othman AE. Deep learning-accelerated T2-weighted imaging of the prostate: Reduction of acquisition time and improvement of image quality. *Eur J Radiol*. 2021;137:109600.
- 4 Almansour H, Herrmann J, Gassenmaier S, Afat S, Jacoby J, Koerzdoerfer G, et al. Deep Learning Reconstruction for Accelerated Spine MRI: Prospective Analysis of Interchangeability. *Radiology*. 2023;306(3):e212922.
- 5 Kim EH, Choi MH, Lee YJ, Han D, Mostapha M, Nickel D. Deep learning-accelerated T2-weighted imaging of the prostate: Impact of further acceleration with lower spatial resolution on image quality. *Eur J Radiol*. 2021;145:110012.
- 6 Herrmann J, Keller G, Gassenmaier S, Nickel D, Koerzdoerfer G, Mostapha M, et al. Feasibility of an accelerated 2D-multi-contrast knee MRI protocol using deep-learning image reconstruction: a prospective intraindividual comparison with a standard MRI protocol. *Eur Radiol*. 2022;32(9):6215–6229.
- 7 Herrmann J, Wessling D, Nickel D, Arberet S, Almansour H, Afat C, et al. Comprehensive Clinical Evaluation of a Deep Learning Accelerated, Single-Breath-Hold Abdominal HASTE at 1.5 T and 3 T. *Acad Radiol*. 2023;30(1):93–102.
- 8 Shanbhogue K, Tong A, Smereka P, Nickel D, Arberet S, Anthopolos R, et al. Accelerated single-shot T2-weighted fatsuppressed (FS) MRI of the liver with deep learning-based image reconstruction: qualitative and quantitative comparison of image quality with conventional T2-weighted FS sequence. *Eur Radiol*. 2021;31(11):8447–8457.
- 9 Bae SH, Hwang J, Hong SS, Lee EJ, Jeong J, Benkert T, et al. Clinical feasibility of accelerated diffusion weighted imaging of the abdomen with deep learning reconstruction: Comparison with conventional diffusion weighted imaging. *Eur J Radiol*. 2022;154:110428.
- 10 Afat S, Herrmann J, Almansour H, Benkert T, Weiland E, Hölldobler T, et al. Acquisition time reduction of diffusion-weighted liver imaging using deep learning image reconstruction. *Diagn Interv Imaging*. 2022:S2211–5684(22)00220-0.
- 11 Lee EJ, Chang YW, Sung JK, Thomas B. Feasibility of deep learning *k*-space-to-image reconstruction for diffusion weighted imaging in patients with breast cancers: Focus on image quality and reduced scan time. *Eur J Radiol*. 2022;157:110608.



Contact

Trina V. Gulay, RTR, RTMR
Manager, Medical Imaging, Geo 1/2
Island Health, MRI Department
1200 Dufferin Crescent
Nanaimo, BC V9S 2B7
Canada
Tel.: +1 250.716.7740
trina.gulay@islandhealth.ca

Initial Experiences Using Deep Resolve Boost to Accelerate Whole-Body Diffusion MRI

Andrea Ponsiglione^{1,2}; Will McGuire²; Marie Fennessy²; Anwar R. Padhani²

¹Department of Advanced Biomedical Sciences, University of Naples Federico II, Naples, Italy

²Paul Strickland Scanner Centre, Mount Vernon Cancer Centre, Northwood, Middlesex, United Kingdom

Introduction

In the last decade, whole-body MRI (WB-MRI) has become established as a non-invasive imaging technique for staging and response assessment of cancers with a predilection to spread to the bone [1–3], with emerging indications for screening and inflammatory conditions [4, 5].

Diffusion-weighted imaging (DWI) represents a core sequence [1, 4, 6] achieving on modern MRI scanners spatial resolutions able to detect small lesions up to 5 mm in size with good image quality. The sequence is sensitive to tissue cellularity and water diffusivity while enabling quantification of the apparent diffusion coefficient (ADC; unit: $\mu\text{m}^2/\text{s}$), which aids in lesion characterization and treatment response evaluations [7].

WB-DWI is performed through a series of sequential imaging stations, usually from the head to the mid-thighs, with each station consisting of 30–50, 5-mm thick axial sections and images generally acquired by using two diffusion weightings (50–800/1000 s/mm^2) [8]. Because scanning each station takes approximately 3 minutes, WB-DWI accounts for approximately half of the total acquisition time of a WB-MRI study.

Due to the increasing demand for WB-MRI exams, reducing acquisition times while maintaining image quality would enable greater adoption in clinical routine and improve patient experience [9].

Deep Resolve Boost (DRB) is a raw data-to-image deep-learning reconstruction technology by Siemens Healthineers that enables accelerated image acquisition with high signal-to-noise (SNR) images by increasing parallel imaging acceleration (PAT) factors and/or reducing the number of acquired averages [10].

In this case-based review, we share our initial experience with the DRB WB-DWI sequence in comparison with the sequence that we use routinely, focusing on quantitative and qualitative findings assessed on axial b900 and the corresponding MIP images. The conventional and DRB WB-DWI acquisition protocols for our 1.5T MAGNETOM Sola machine are listed in Table 1.

	Conventional whole-body DWI	DRB whole-body DWI
Scan plane	Axial	Axial
Diffusion mode	3-scan trace	3D diagonal
Diffusion scheme	Bipolar	Monopolar
TR (ms)	6170	5370
TE (ms)	74	63
FOV (mm)	430	430
Phase FOV (% of FOV)	87.5	90.6
Slices	40	40
Slice thickness (mm)*	5	5
Matrix (interpolated matrix)	128 × 128 (256 × 256)	128 × 128 (256 × 256)
Fat suppression method (inversion time, ms)	Inversion recovery (180)	Inversion recovery (180)
Phase encoding direction	A > P	A > P
iPAT	2	3
b-values (s/mm^2)	50–900	50–900
Averages (3D diagonal equivalence)	2, 6 (6, 18)	3, 8 (3, 8)
Bandwidth (Hz/pixel)	2298	1954
Adjustment strategy	SliceAdjust	SliceAdjust
DL reconstruction	N/A	DRB
Denoising strength	N/A	Normal
Acquisition time (min:s)	2:48 (× 5 stations)	1:17 (× 5 stations)

Table 1: Technical parameters of the whole-body DWI acquisition protocols.

*without spacing; DRB: Deep Resolve Boost, TR: repetition time, TE: echo time, FOV: field of view, iPAT: integrated parallel acquisition technique, DL: deep learning

Case 1

A 66-year-old postmenopausal woman presented with bone and lung metastases from breast carcinoma (HER2-positive) on trastuzumab emtansine therapy. She was referred for WB-MRI to assess her disease status (Figures 1 and 2).

Quantitative assessment

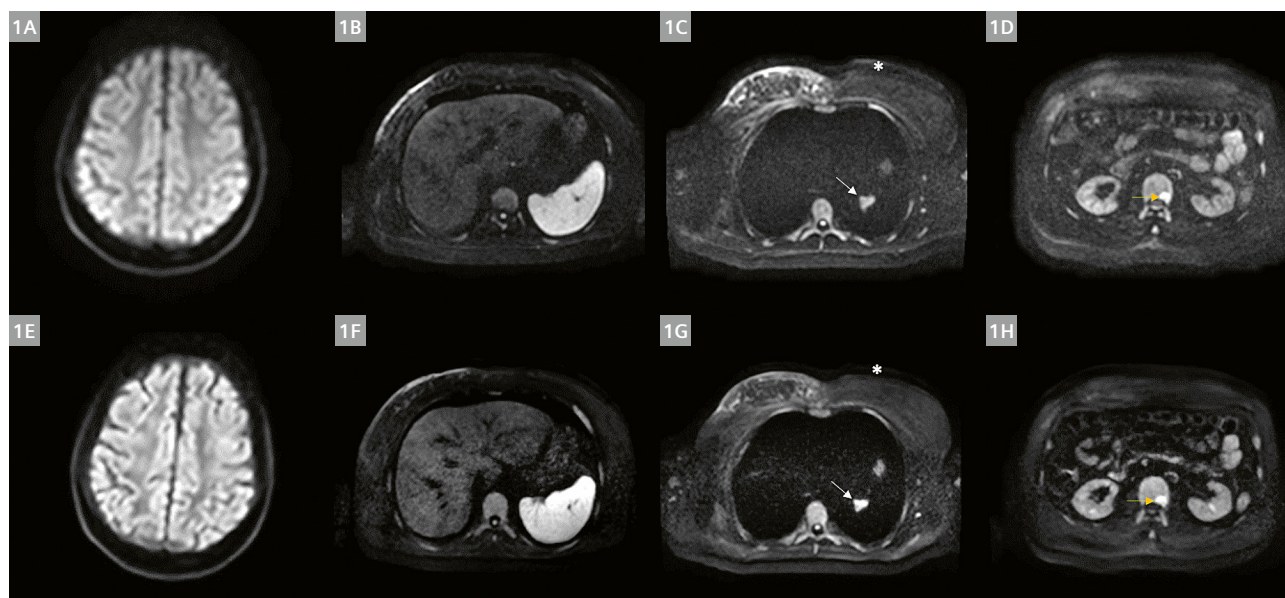
Axial b900 DRB-DWI shows a higher SNR (calculated as signal intensity divided by standard deviation of background air noise adjacent to the lateral chest wall) than the conventional sequence at different anatomical sites, including the parietal cerebral white matter (251 vs. 189 AU), third lumbar vertebral body (91 vs. 33 AU), and spleen (171 vs. 51 AU).

Two different metastatic lesions are chosen for further assessment: within the left lung and at the level of the second lumbar vertebra. The SNR results are higher for DRB-DWI (151 and 178 vs. 48 and 111 AU, respectively), whereas the mean ADC values ($\mu\text{m}^2/\text{s}$) are similar (1457 and 1194 vs. 1463 and 1221 $\mu\text{m}^2/\text{s}$).

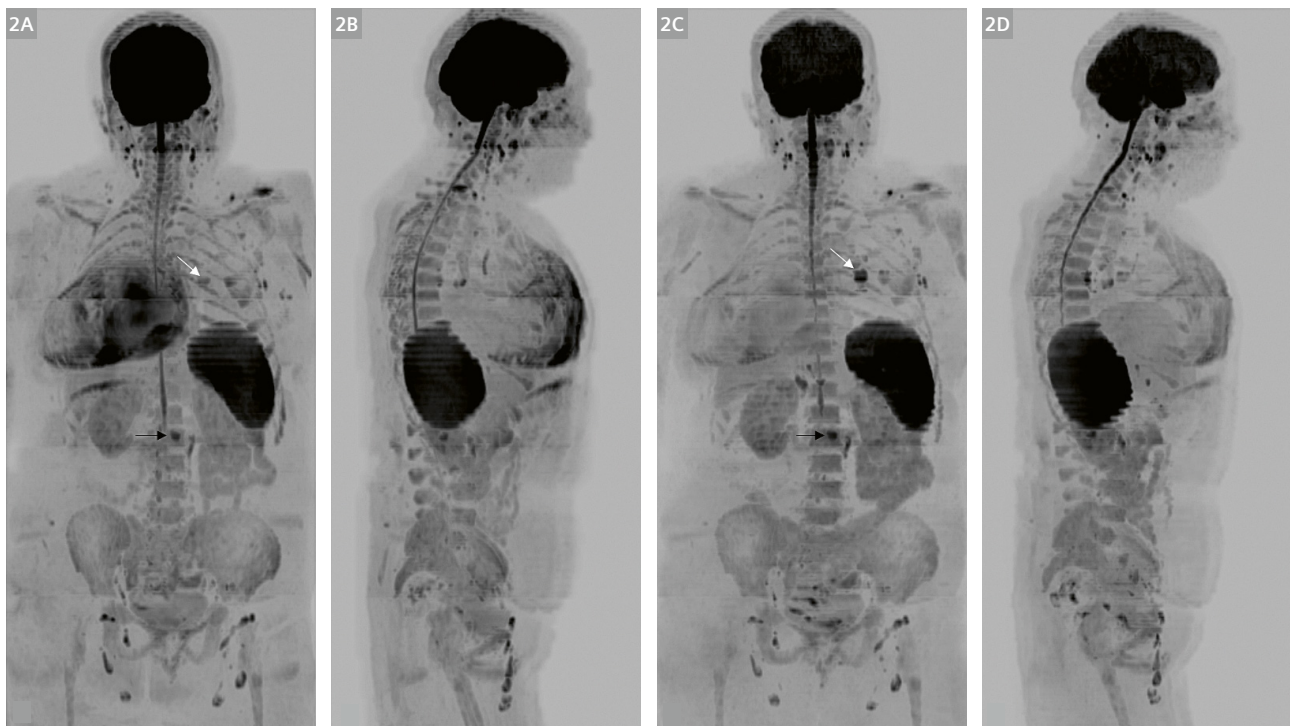
Qualitative assessment

Axial b900 DRB-DWI shows better white/gray matter zone differentiation, with an overall greater signal intensity for visceral organs and bones. When assessing the metastatic lesions, both are visualized with higher conspicuity in the axial DRB sequence. When evaluating the presence of artifacts, axial b900 DRB-DWI shows fewer near-field artifacts.

As for MIP images (Fig. 2), the DRB exhibits a more homogenous background fat suppression in both the frontal and lateral views, with fewer artifacts from the edematous right breast, which compromises the visibility of the chest lesions on the projections for the conventional images. The transitions between different stations are also less evident in the DRB MIP images, whereas striping artifacts are equally visible in both protocols (upper spleen on the conventional images and lower spleen on the DRB images). Both the lung and spine deposits are better depicted on DRB MIP images.



1 Axial b900 DW images in conventional (1A–D) and DRB protocols (1E–H) from a 66-year-old postmenopausal woman presenting with bone and lung metastatic breast carcinoma (HER2-positive) and increased bilirubin, on trastuzumab emtansine. The DRB images show better white/gray matter zone differentiation, with higher signal intensity for the liver, spleen, and lumbar spine compared to the conventional ones. Greater near-field artifacts (*) are present in the conventional images, whereas lung and lumbar spine metastatic lesions (arrows) are visualized with higher conspicuity in the axial DRB sequence.



2 Frontal and lateral views of whole-body b900 3D MIP (inverted greyscale) of conventional (**2A, B**) and DRB protocols (**2C, D**). The DRB MIP shows a more homogenous background fat suppression on both projections, with fewer artifacts from the right breast area. The transition between different stations is less evident on the DRB MIPs while striping artifacts are equally visible in both protocols (upper spleen on the conventional images and lower spleen on the DRB images). Lung and lumbar spine metastatic lesions (arrows) are better depicted on the DRB MIP.

Case 2

A 67-year-old man presented with diffuse bone metastatic prostate cancer and increased serum prostate-specific antigen (PSA) levels on anti-androgen therapy. He was referred for WB-MRI to assess his disease status (Figures 3 and 4).

Quantitative assessment

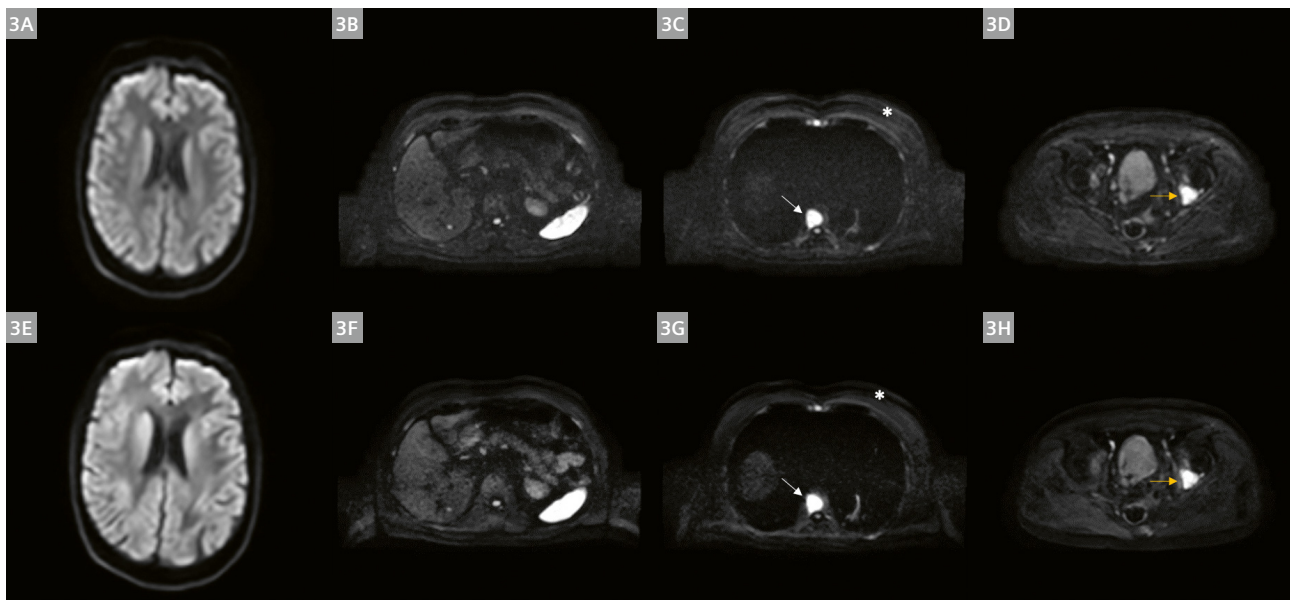
Both axial b900 DWI sequences show similar SNR at the level of parietal brain white matter (104 vs. 101 AU), while DRB exhibits a higher SNR than the conventional sequence when assessing the spleen (166 vs. 99 AU).

Regarding the two metastatic lesions chosen as targets in the 9th thoracic vertebra and the left posterior acetabulum, the SNR results are higher for DRB-DWI (201 and 239 vs. 151 and 143 AU, respectively), whereas the mean ADC values are similar (765 and 780 vs. 750 and 734 $\mu\text{m}^2/\text{s}$, respectively).

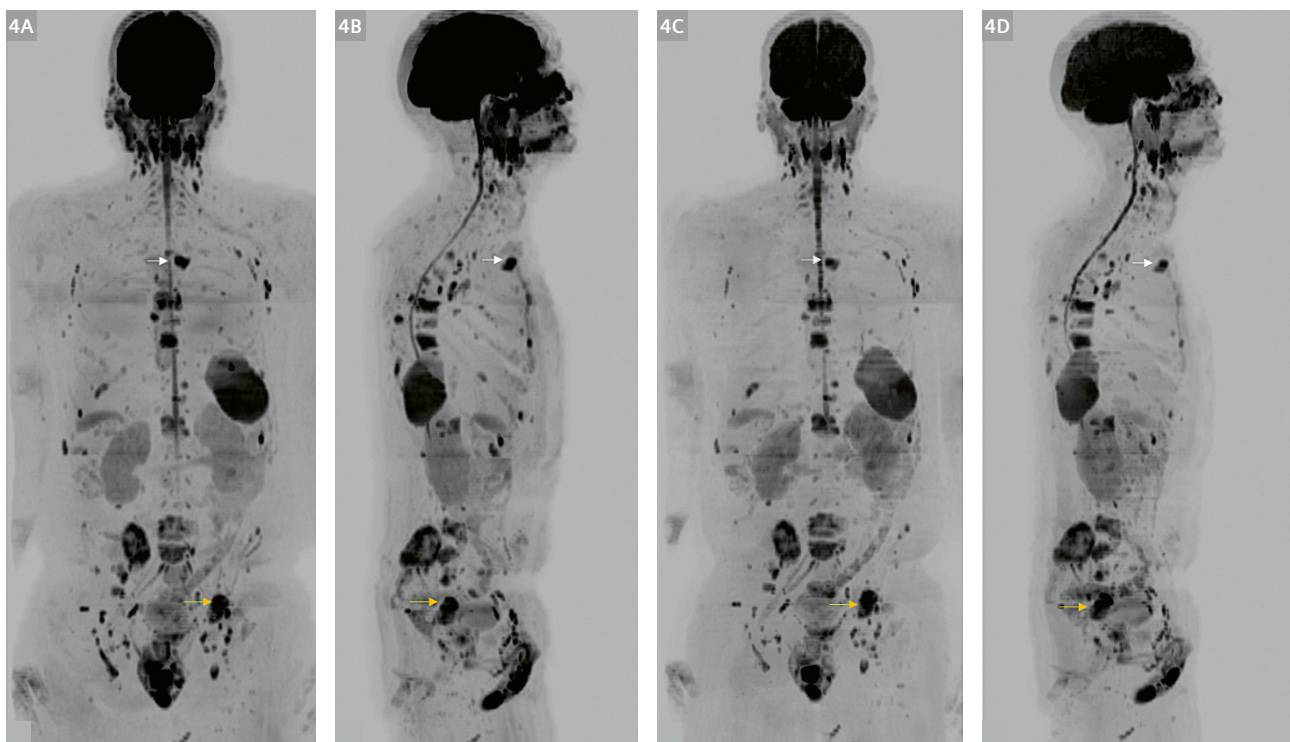
Qualitative assessment

Axial b900 DRB-DWI exhibits improved white/gray matter zone differentiation, with an overall higher image contrast for visceral organs and bone. Notably, both liver lobes and the pancreas show greater signal intensity compared to conventional acquisition. The conspicuity of metastatic lesions is equivalent. As for the presence of artifacts, axial b900 DRB-DWI shows fewer near-field artifacts than the conventional sequence.

Regarding MIP images, DRB shows more uniform background fat suppression on both frontal and lateral projections. Transitions between the image block stations are slightly more evident in conventional DWI, whereas striping artifacts in the abdominal stations are more evident in the DRB images. The conspicuity of target metastatic lesions is equivalent.



3 Axial b900 DW images in conventional (**3A–D**) and DRB protocols (**3E–H**), from a 67-year-old man presenting with diffuse bone metastatic prostate cancer, with rising PSA values on androgen deprivation therapy. The DRB images exhibit a greater white/grey matter zone differentiation, with improved sharpness for the liver, pancreas as well as lumbar spine compared to the conventional ones. Near-field artifacts (*) are less evident in the DRB image, while the conspicuity for both the 9th thoracic vertebra and left posterior acetabulum metastatic lesions (arrows) is the same across different protocols.



4 Frontal and lateral view of whole-body b900 3D MIP (inverted scale) in conventional (**4A, B**) and DRB protocols (**4C, D**). The DRB MIP shows better background fat suppression either on frontal or lateral views, with the transition between different stations being slightly less evident. Striping artifacts within abdomen stations are more evident in the DRB sequence. Multiple bone metastases can be appreciated, in particular, both the 9th thoracic vertebra and left posterior acetabulum deposits chosen as targets show similar conspicuity across protocols (arrows).

Case 3

An 84-year-old woman presented with lung, bone, and liver metastatic breast carcinoma (ER-positive and HER2-negative) after receiving palbociclib and hormonal therapy. She was referred for worsening overall performance status accompanied by breathlessness, and for a WB-MRI scan to assess the extent of her disease (Figures 5 and 6).

Quantitative assessment

Axial b900 DRB-DWI shows a higher SNR than the conventional sequence at different anatomical sites, including the brain white matter (235 vs. 188 AU), third lumbar vertebra (38 vs. 22 AU), and spleen (129 vs. 44 AU).

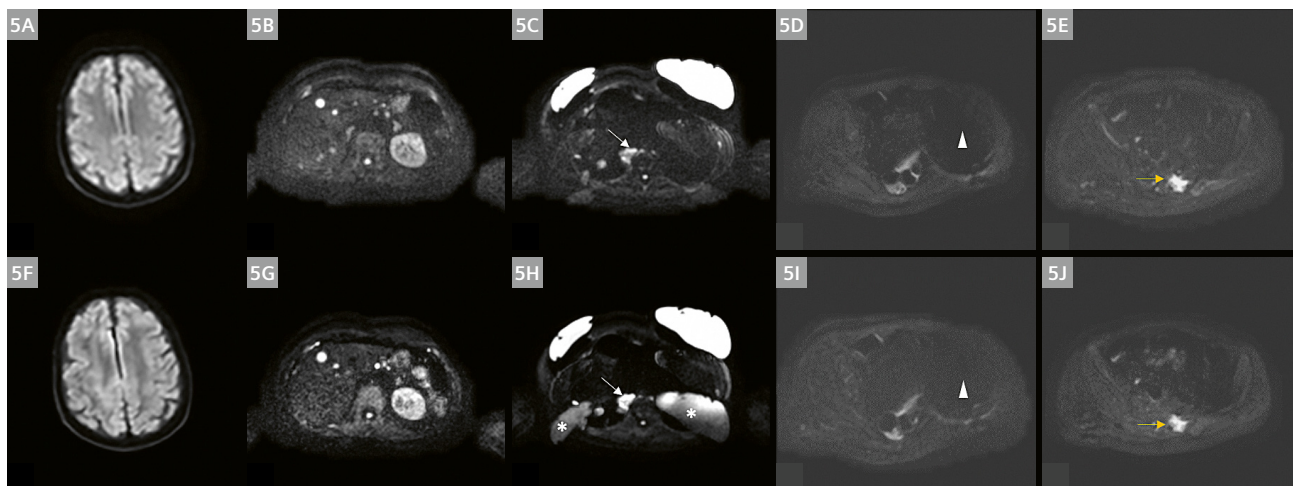
Two metastatic lesions are chosen as targets: one in the right subpleural lung base and one in the left sacrum. In the axial DRB-DWI, they show higher SNR (152 and 201 vs. 54 and 137 AU, respectively), with minimally lower mean ADC values (915 and 977 vs. 1130 and 1091 $\mu\text{m}^2/\text{s}$) compared to the conventional sequence. The difference in the ADC values is within the repeatability coefficient limits for ADC values [11].

Qualitative assessment

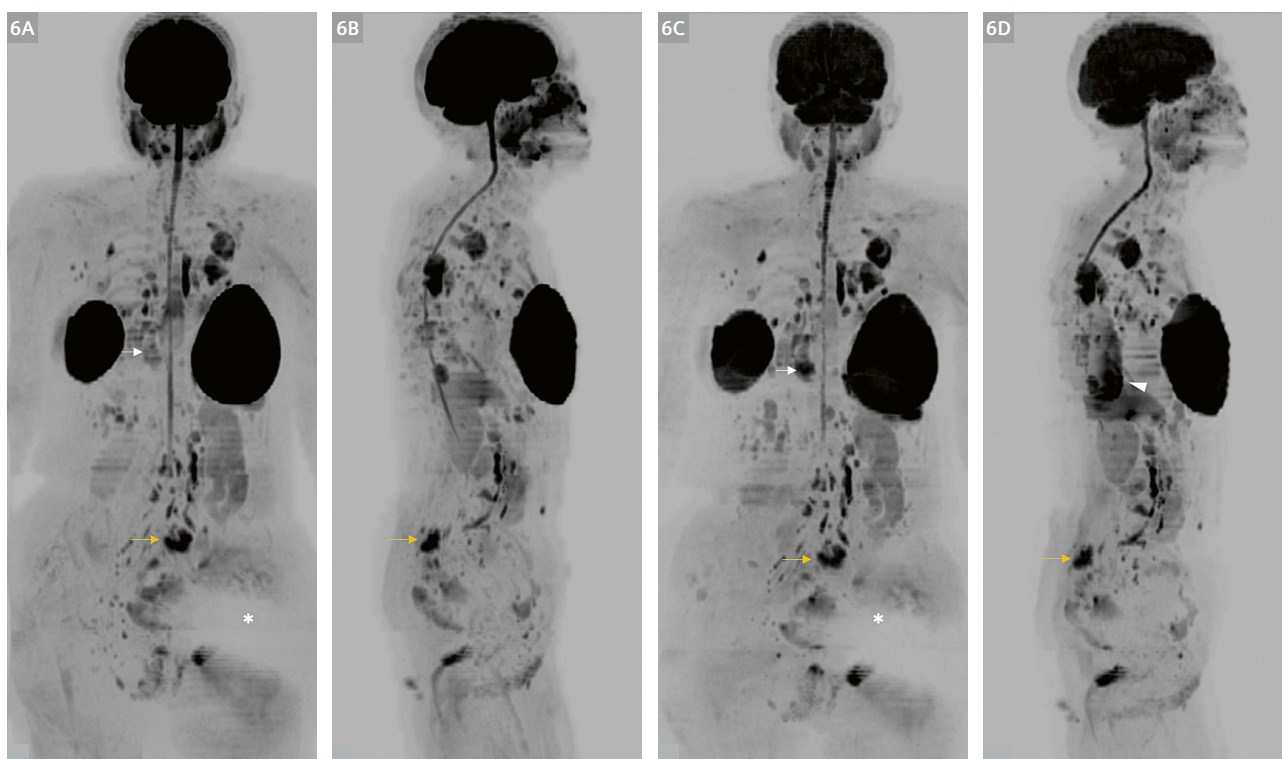
Axial b900 DRB-DWI shows better white/gray matter zone differentiation, with overall similar visualization quality for visceral organs, and slightly better sharpness for the spine.

The conspicuity of the right subpleural lesion is higher for the DRB sequence, whereas that of the left sacrum is equivalent. When evaluating the presence of artifacts, axial b900 DRB-DWI shows larger artifacts through the thorax related to breast implants. However, in this case, where deposits are widespread in both lungs, artifacts do not compromise the overall diagnostic assessment. Furthermore, the patient underwent a left hip replacement, and the related artifacts are equivalent in both sequences.

Regarding the MIP images, DRB shows similar background fat suppression in frontal and lateral views. Similarly, the transition between different stations is also equivalent, whereas striping artifacts are slightly more evident in the DRB sequence. Bilateral breast implants cause larger artifacts in the lateral MIP for the DRB sequence; however, artifacts related to the metallic left hip prosthesis are the same. Finally, the conspicuity of the right lung lesion is slightly higher for the DRB sequence, whereas that of the left sacrum deposit is equivalent across the protocols.



5 Axial b900 DW images in conventional (5A–E) and DRB protocols (5F–J), from an 84-year-old woman presenting with extensive lung, bone, and liver metastatic breast carcinoma (HR-positive and HER2-negative) on palbociclib. The DRB images exhibit greater white/gray matter zone differentiation, with similar sharpness for visceral organs and the lumbar spine. Axial b900 DRB-DWI shows greater artifacts through the thorax station related to bilateral breast implants (asterisks) compared to the conventional sequence, although the diagnostic assessment of the widespread lung deposits is maintained. Artifacts from left hip replacement (arrowheads) are equivalent across protocols. The conspicuity of the right lung subpleural lesion is higher for the DRB sequence (white arrows) compared to the conventional one, while that of the left sacrum is equivalent (orange arrows).



6 Frontal and lateral projections of whole-body b900 3D MIP (inverted scale) in the conventional (**6A, B**) and DRB protocols (**6C, D**). The DRB MIP showed similar fat background suppression on both the frontal and lateral views compared to the conventional MIP. The transition between different stations is equivalent while stripping artifacts within abdominal stations are slightly more evident in the DRB sequence. Artifacts from the bilateral breast implants are greater in the lateral AI MIP (arrowhead), while those related to the left hip prosthesis are the same (asterisks in frontal projections). The conspicuity of the right subpleural lesion is higher for the DRB sequence (white arrows in the frontal projections) than for the conventional sequence, while that of the left sacrum deposit is equivalent (orange arrows).

Conclusion

Our experience with 50 head-to-head comparisons of DRB-DWI with a conventional sequence in the context of WB imaging shows that the optimized DRB sequence from Siemens Healthineers produces high-quality axial images resulting in improved MIP projections, while at the same time reducing the acquisition time by more than half. DRB-DWI is superior or equivalent to the conventional sequence in terms of overall SNR and lesion conspicuity on axial images, with more uniform background fat suppression on MIP projections. However, increased striping artifacts in the abdomen, and artifacts related to silicone breast implants should be further investigated for their clinical impact. The time-saving with preserved image quality allowed us to incorporate a modified DRB-DWI sequence into our clinical routine to increase patient throughput.

References

- 1 Messiou C, Hillengass J, Delorme S, Lecouvet FE, Mouloupoulos LA, Collins DJ, et al. Guidelines for Acquisition, Interpretation, and Reporting of Whole-Body MRI in Myeloma: Myeloma Response Assessment and Diagnosis System (MY-RADS). *Radiology*. 2019;291(1):5-13.
- 2 Ahlawat S, Debs P, Amini B, Lecouvet FE, Omoumi P, Wessell DE. Clinical Applications and Controversies of Whole-Body MRI: AJR Expert Panel Narrative Review. *AJR Am J Roentgenol*. 2023;220(4):463-475.
- 3 Cruz IAN, Fayad LM, Ahlawat S, Lederman HM, Nico MAC, Ormond Filho AG, et al. Whole-Body MRI in Musculoskeletal Oncology: A Comprehensive Review with Recommendations. *Radiol Imaging Cancer*. 2023;5(3):e220107.
- 4 Petralia G, Koh DM, Attariwala R, Busch JJ, Eeles R, Karow D, et al. Oncologically Relevant Findings Reporting and Data System (ONCO-RADS): Guidelines for the Acquisition, Interpretation, and Reporting of Whole-Body MRI for Cancer Screening. *Radiology*. 2021;299(3):494-507.
- 5 Kraus MS, Yousef AA, Cote SL, Greer MC. Improving protocols for whole-body magnetic resonance imaging: oncological and inflammatory applications. *Pediatr Radiol*. 2023;53(7):1420-1442. Epub 2022 Aug 19.

- 6 Padhani AR, Lecouvet FE, Tunariu N, Koh DM, De Keyzer F, Collins DJ, et al. METastasis Reporting and Data System for Prostate Cancer: Practical Guidelines for Acquisition, Interpretation, and Reporting of Whole-body Magnetic Resonance Imaging-based Evaluations of Multiorgan Involvement in Advanced Prostate Cancer. *Eur Urol*. 2017;71(1):81-92.
- 7 Tunariu N, Blackledge M, Messiou C, Petralia G, Padhani A, Curcean S, et al. What's New for Clinical Whole-body MRI (WB-MRI) in the 21st Century. *Br J Radiol*. 2020;93(1115):20200562.
- 8 Petralia G, Padhani AR. Whole-Body Magnetic Resonance Imaging in Oncology: Uses and Indications. *Magn Reson Imaging Clin N Am*. 2018;26(4):495-507.
- 9 Evans RE, Taylor SA, Beare S, Halligan S, Morton A, Oliver A, et al. Perceived patient burden and acceptability of whole-body MRI for staging lung and colorectal cancer; comparison with standard staging investigations. *Br J Radiol*. 2018;91(1086):20170731.
- 10 Siemens Healthineers. Deep Resolve Boost [Internet]. Erlangen, Germany: Siemens Healthcare GmbH [Accessed on June 7, 2023]. Available from: <https://www.siemens-healthineers.com/magnetic-resonance-imaging/options-and-upgrades/clinical-applications/deep-resolve-boost>
- 11 ElGendy K, Barwick TD, Auner HW, Chaidos A, Wallitt K, Sergot A, et al. Repeatability and test-retest reproducibility of mean apparent diffusion coefficient measurements of focal and diffuse disease in relapsed multiple myeloma at 3T whole body diffusion-weighted MRI (WB-DW-MRI). *Br J Radiol*. 2022;95(1138):20220418.

Contact

Dr. Andrea Ponsiglione, Ph.D.
Post-doctoral Research Fellow
Department of Advanced
Biomedical Sciences
University of Naples Federico II
Via Pansini 5
Napoli, 80131
Italy
Tel.: +39 (0)817 464 857
a.ponsiglione@gmail.com



Will McGuire
Deputy Superintendent Radiographer
Paul Strickland Scanner Centre
Rickmansworth Road
Northwood, Middlesex HA6 2RN
United Kingdom
Tel.: +44 (0)1923 886 310
will.mcguire@stricklandscanner.org.uk



Prof. Anwar R. Padhani,
MB, BS, FRCP, FRCR
Consultant Radiologist and
Professor of Cancer Imaging
Paul Strickland Scanner Centre
Mount Vernon Cancer Centre
Rickmansworth Road
Northwood, Middlesex HA6 2RN
United Kingdom
Tel. (PA): +44 (0)1923 844 751
anwar.padhani@stricklandscanner.org



Marie Fennessy
MRI Superintendent Radiographer
Paul Strickland Scanner Centre
Rickmansworth Road
Northwood, Middlesex HA6 2RN
United Kingdom
Tel.: +44 (0)1923 886 310
marie.fennessy@stricklandscanner.org.uk



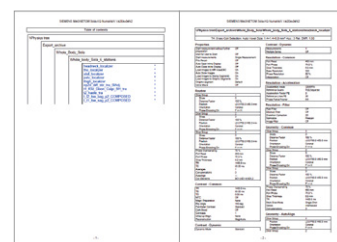
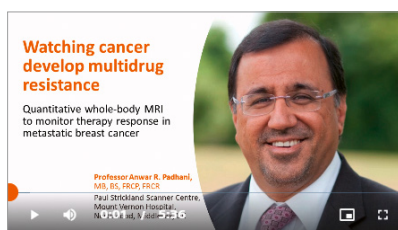
Advertisement

Learn more about quantitative whole-body MRI



For protocols, step-by-step videos,
application tips, clinical talks and
articles please visit

www.magnetomworld.siemens-healthineers.com/hot-topics/quantitative-whole-body-mri



Whole-Body MRI at 1.5T in the Era of Deep Resolve

Will McGuire; Marie Fennessy; Anwar R. Padhani

Paul Strickland Scanner Centre, Mount Vernon Hospital, Northwood, Middlesex, UK

Until recently it could take up to an hour to perform a whole-body MRI (WB-MRI). But what if you could cut that in half and make it better? Buckle up.

Around six years ago we shared a how-to guide hosted on the Siemens Healthineers *WB-MRI website*. Hopefully, many of you found this helpful in designing and refining your protocols to meet the increasing demand for WB-MRI for clinical indications including the diagnosis of multiple myeloma, the surveillance of patients with cancer predisposition syndromes, and for patients with bone predominant metastatic disease from prostate and breast cancer. Over the past few years several technological and software developments have improved access to this technique by significantly reducing scan times (TA) while maintaining (and in many cases improving) image quality.

In this article, we share our experience in developing WB-MRI protocols on the 1.5T MAGNETOM Sola emphasising how we have harnessed the power of Deep Resolve and the XA platform. For reference, previous guides and resources remain available online and as such we won't touch on the older software platforms and instead focus on how things have changed.

XA platform

The latest generation MAGNETOM scanners feature the new XA-platform scanner software. Previous-generation systems may also be offered upgrades (dependent on individual support agreements) enabling access to the library of the latest scanning techniques.

Sequence/ stations	TR (ms)	TE (ms)	FOV (mm)	Phase FOV (%)	Slice	Slice thick- ness (mm)	Gap (%)	Matrix (inter- polation)	Phase enc. direction (over- sampling)	iPAT / DRB / DRS / DRG	b- values (s/mm ²)	Aver- ages	TA (min:sec)
FastView	n/a	n/a	n/a	n/a	Range 1350 mm	n/a	n/a	n/a	n/a	n/a	n/a	n/a	00:38
STIR spine sag (x2)	3500	89	380	100	15	4	20	272×218 (on)	H>F (80%)	2 / off / on / on	n/a	1	02:24 total
T1 spine sag (x2)	266	8.6	380	100	15	4	20	256×204 (on)	H>F (80%)	0 / off / on / on	n/a	1	02:08 total
T1 Dixon VIBE axial (x6)	6.8	2.39 / 4.77	430	93.8	44	5	0	256×204 (off)	A>P (PE – 0% SL – 45.5%)	CAIPI 4 (2×PE2×SL)	n/a	1	01:36 total
DWI axial (x6)	5370	63	430	90.6	40	5	0	128×128 (on)	A>P (0%)	2 / on / on / off	50, 900	3D diagonal 3, 8	07:42 total
T2 HASTIRM cor (x4)	1000	95	450	100	38	6	10	384×346 (off)	R>L (50%)	3	n/a	1	02:32
T2 HASTE axial (x6)	1000	96	430	93.8	40	5	0	320×240 (off)	A>P (0%)	3	n/a	1	02:48
Total measurement time													19:48

Table 1: Key sequence parameters for MET-RADS [1] core sequences on 1.5T MAGNETOM Sola – excluding adjustment times.

Evolution, not revolution

This updated protocol relies heavily on the utilization of **Deep Resolve Boost (DRB)**, **Gain (DRG)** and **Sharp (DRS)** which are available to current owners and new purchasers of the various Deep Resolve packages. DRB for DWI¹ will become available upon future upgrades to syngo MR XA60/61 – contact your local product specialist for details. Cases demonstrating the clinical use of DRB in whole-body DWI can be found in the article “*Initial experiences using DRB to accelerate whole-body diffusion MRI*” presented in this edition of MAGNETOM Flash.

Procedurally, many aspects of executing a whole-body examination remain the same as were set out in the previous guide – Table 1, detailing parameter selections, shows the familiar structure of the examination.

Software compatibility

A downloadable *.exar1 file from the syngo MR XA51 platform is available at www.siemens.com/wb-mri. Due to the inability to perform sequence conversion to an older software platform, *.pdf files are also available. Please note that, at the time of publishing, these files do not include the DRB DWI sequence – updates will be posted online as this becomes available.

¹Work in progress. The product is still under development and not commercially available. Its future availability cannot be ensured.

Managing changes

As changes in quantitative measurements such as ADC values and bone marrow fat fraction are increasingly relied on by radiologists to assess the success of anticancer treatments [1], scan parameters must remain as consistent as possible between patient visits – we recommend this should include ensuring patients are scanned on the same hardware each time. Those managing a fleet of different scanner models will be familiar with the difficulties around standardization of acquisition in this context. Naturally, as scanners are replaced and upgrades are performed,

it can be difficult to match exactly what was done before and this may mean the advantages of new techniques are overlooked in the pursuit of reproducibility.

Utilize the resources available to you, whether that be through the expertise of the Siemens Healthineers MR Applications team or via assistance from expert colleagues. You should ensure that whatever changes to image appearance manifest as a result of system upgrades, everyone in the team knows how to identify and interpret the effect of those changes.

You may find **teamplay Protocols** useful if managing more than one Siemens Healthineers MR system. This service allows you to distribute protocol changes remotely.

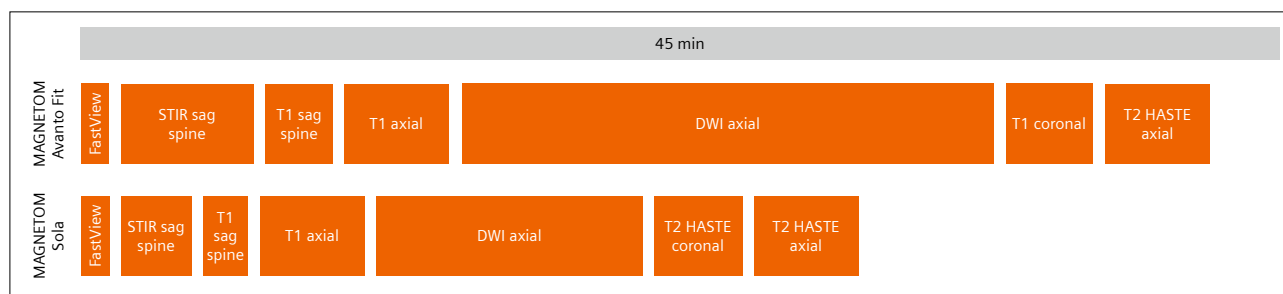
Minimum equipment requirements

- Spine 32
- BioMatrix Head/Neck 20
- Body 18 coils as required for coverage to knees (3× recommended)
- Optional: Peripheral Angio 36 if full-leg coverage is required without patient repositioning

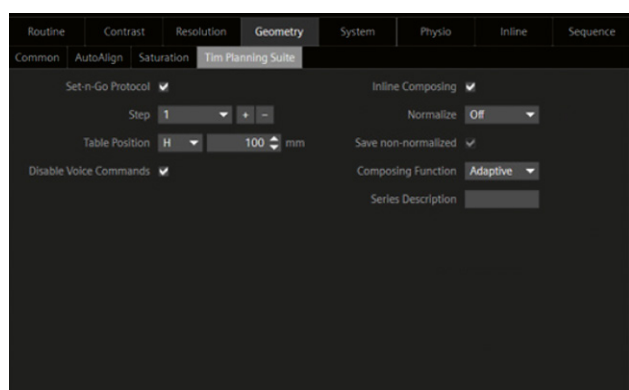
Protocol set-up

As pointed out in the introduction, little has changed in the set-up for whole-body MRI examinations. However, as acquisition times become shorter, inefficient workflows can have a greater impact on the total examination time. Some sites will find the features of **MyExam Whole-Body Assist** useful particularly when designing user friendly protocols for less experienced operators.

The sequences presented here are ordered in such a way that ensures any post-processing (MIPs, MPRs) can be completed while the patient is being examined. Due to the decreased TAs, adjustments can occupy a greater proportion of the examination length (Fig. 1). Use the shim mode “Tune up” where appropriate for spine and HASTE sequences that do not require a comprehensive adjustment strategy to reduce the impact on examination duration.



1 Comparison of example examination times on the MAGNETOM Avanto Fit (top) versus MAGNETOM Sola (bottom) scanners with approximate adjustment times included.



2 Location of disable voice commands tick box – this can be set on a per-step basis.



3 A colleague demonstrating vertex to knee coil coverage with three Body 18 coils.

During initial protocol setup, disable breath-hold instructions on slice groups positioned in the head, lower body and leg regions as there are minimal breathing artifacts in these anatomical regions (**Geometry: Tim Planning Suite: Disable Voice Commands** tick box, Fig. 2).

You may choose to have the T2 HASTE/HASTIRM sequences run without breath-holds as standard – the single-shot nature of the acquisition effectively eliminates motion artifact, however, there may be some slice-to-slice positional mismatch if this approach is selected. Including extras such as a fast FLAIR brain sequence using Deep Resolve is optional but can serve as early asymptomatic lesion detection for some patient groups.

Patient and equipment set-up

It is important to ensure patients are as comfortable as possible so that they can tolerate the full examination without interruption. Use foam pads, pillows and knee supports where required for comfort and to protect patients from possible injury from a conductive loop or RF proximity burns. Changing patients into hospital gowns or other suitable clothing can help reduce the likelihood of discovering non-implanted metallic objects once the scan has begun.

Use of the anterior part of the Head/Neck 20 will improve image quality in the anterior head and neck region. All of the sequences in this protocol are fairly tolerant to the removal of these coil elements, so you can afford to be led by patient preference. Remember

that BioMatrix Head/Neck 20 coil can be tilted to 9 or 18 degrees, enabling closer posterior coil positioning for kyphotic patients and thus greatly improving both patient comfort and image quality in the head and neck region. Place Body 18 and/or Peripheral Angio 36 coils as required to cover the desired length of scan (Fig. 3) – ensure the first Body 18 coil is positioned to cover the patient's shoulders superiorly.

If regularly used together you can prepare two of your Body 18 coils for whole-body placement using loosely connected Velcro straps – being careful not to damage the coils.

Depending on the height of the patient and the range of motion of your scanner table you may be able to achieve full head-to-toe coverage with the Peripheral Angio 36 coil. With this coil you may notice signal drop posteriorly which can be countered by positioning an upside-down Body 18 coil longways in the recess the removable table padding occupies. Ensure that excess pressure is not placed on this Body 18 coil by strategic placement of the foam pads supplied with your system.

AutoCoilSelect is now managed on a per-sequence basis (further details in Table 2) and you should set group graphics to ON before you start. If patients are unable to hold their breath remember to disable any automatic voice commands. Using the positioning laser, set the start position to a patient's chin and the FastView localizer will begin acquisition from above the skull vertex. You're now ready to scan – read on for sequence-specific tips and follow along with the video at www.siemens.com/wb-mri.

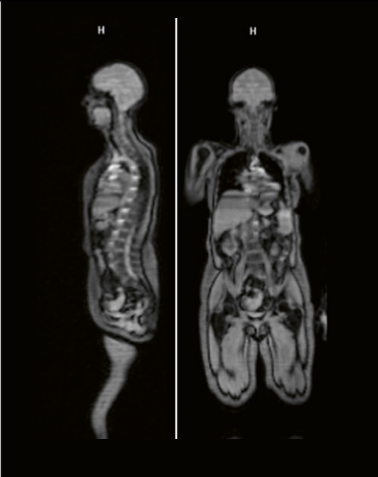
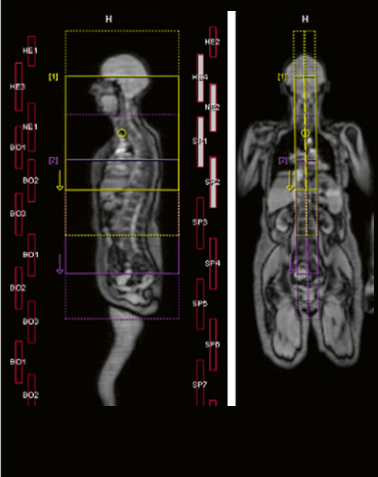
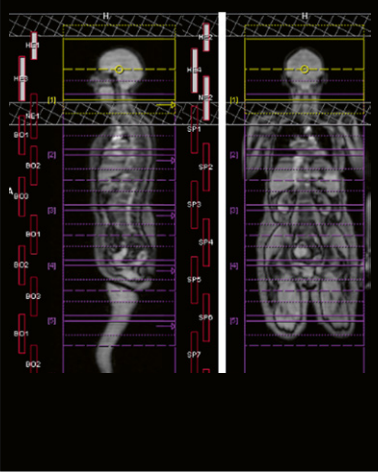
Sequence details	Positioning and ranges	Acquisition tips	Adjustable parameters	Notes
Step 1 FastView localizer Range: Vertex to knees Plane: Axial (MPRs are generated automatically)		Set the acquisition range required for your study – the maximum range will vary depending on the table movement limits of your scanner		As before you should allow this localizer to fully complete before planning further. When complete your anterior elements will display on screen
Step 2 STIR and T1 spine Range: Whole spine Plane: Sagittal to patient's anatomy Method: Set-n-Go		Enable spine or adaptive composing in the Geometry: Tim Planning Suite tab Ensure H>F coverage from skull base to at least S3 Angle to cover all vertebral bodies R>L for best fit Reduce artifact by setting AutoCoilSelect to "Restricted" and allowing only posterior elements to be used	Increase the number of slices to cover vertebral bodies R>L Increase phase FOV to a maximum of 120% to accommodate taller patients while maintaining resolution If this is still insufficient, add an additional slice group	Experiment with the amount of overlap required to maintain the quality of the composed images – be mindful that shorter bore scanners may have a more limited region of homogeneity
Step 3 T1 Dixon CAIPI VIBE Range: Vertex to knees Plane: Axial Method: Set-n-Go with automated breath-hold instructions		Position the Set-n-Go stack so that the first step has "spare" slices proud of the vertex – this ensures the DWI and HASTE axial series have the correct coverage Disabling breath-holds on those steps not affected by breathing motion can reduce TA and improve the patient experience	Add further steps if required for taller patients You may increase FOV for larger patients but be aware you will gain little additional anatomical coverage R>L due to edge-of-field artifact	Stacked 3D VIBE images benefit from a small amount of overlap – this is why the VIBE has 44 slices versus the 40 for DWI/HASTE which do not require overlap

Table 2: Step-by-step sequence positioning and acquisition tips (steps 4–6 on the next page).

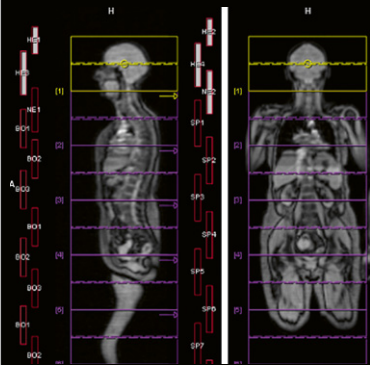
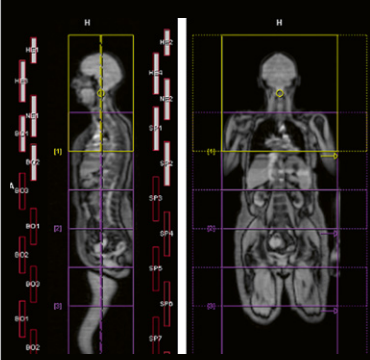
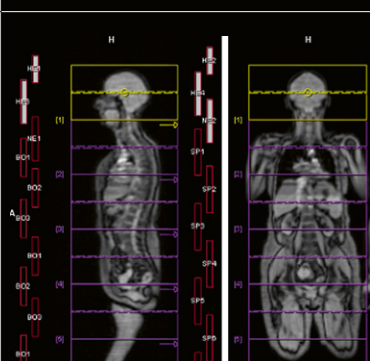
Sequence details	Positioning and ranges	Acquisition tips	Adjustable parameters	Notes
Step 4 DWI Range: Vertex to knees Plane: Axial Method: Set-n-Go		<p>Applying copy reference functions to the DWI and HASTE axial sequences will ensure slice position match between series</p> <p>Experiment with setting the AutoCoilSelect range to “Generous” – you may find this improves SNR by activating additional receiver elements</p>	<p>Limit parameter changes to this sequence as the ADC values produced are increasingly relied on for quantitative response assessment – altering acquisition parameters may impact the ADC and make serial comparison more challenging</p>	<p>Removing b900 averages from the signal-rich head step and adding them to the abdomen steps can reduce stepping artifacts through the liver and spleen</p>
Step 5 T2 HASTIRM Range: Vertex to knees Plane: Coronal Method: Set-n-Go		<p>Leave some space above the level of the vertex – without this, the head will be affected by edge-of-field artifact</p> <p>If desired this sequence can be performed with breath-holds but typically motion artifact is not significant using this single-shot technique</p>	<p>Vary the inversion time (TI) to achieve the desired level of fat suppression</p> <p>For a HASTE, TR controls the spacing between shots rather than having a significant impact on image contrast – be wary of going too fast however as you can increase SAR issues and introduce artifact if the TR is too short</p>	<p>Where available, applying DRB will compensate for noise introduced by using an increased GRAPPA factor – this shortens the echo train and sharpens HASTE images</p>
Step 6 T2 HASTE Range: Vertex to knees Plane: Axial Method: Set-n-Go		<p>Use the copy reference function to ensure slice positions match with the DWI and T1 VIBE axial images</p> <p>As with step 5, this sequence can be performed with breath-holds if required</p>	<p>As above</p>	<p>In addition to the above, where available increase the interleaving step size to reduce any artifact from shorter TRs on image quality</p>

Table 2: Step-by-step sequence positioning and acquisition tips.

Spine sequences (STIR and T1-weighted)

These sequences are used to evaluate bone lesions and reveal any lesions threatening the spinal canal. STIR remains the recommended approach for fat-suppressed whole-spine imaging due to its robustness against artifacts, and ability to tailor the degree of fat suppression by varying the inversion time (TI). The CoilShim feature, integrated into the BioMatrix Head/Neck 20 coil, improves local field homogeneity and has a role to play where spectral fat-suppression techniques are preferred, reducing or eliminating bright-fat artifact in the cervical and upper thoracic spine.

For T1-weighted imaging, setting a low TR can improve the contrast between normal and tumour-infiltrated bone marrow, spinal cord, and cerebrospinal fluid. When set to only activate posterior elements, the new per-sequence AutoCoilSelect setting "Restricted" allows operators the freedom to move scan volumes without inadvertent activation of anterior artifact-creating elements during spinal imaging.



4 STIR and T1 sagittal composed whole-spine images demonstrating improvements in image quality between conventional (**4A, 4C**) and DRG+DRS (**4B, 4D**) sequences.

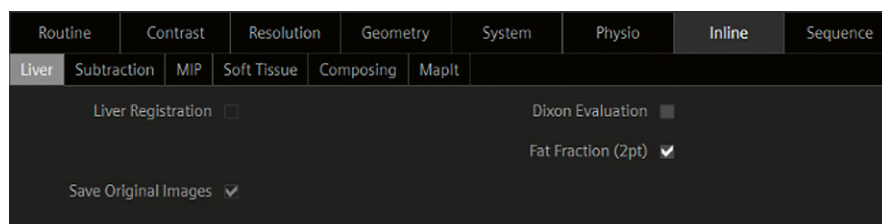
Deep Resolve for TSE can facilitate marked reductions in TA while maintaining or improving image quality (Fig. 4). You may find DRB less useful for spine imaging due to infolding (SENSE) artifacts when an H>F phase encoding direction is selected. This protocol uses the image-based denoising technique DRG which (while less effective at denoising) avoids such infolding artifacts. DRG has several settings which require trialling using the retro-recon function to find the best balance for your readers. DRS permits a lower base resolution to be selected for equivalent or better reconstructed image resolution.

Utilizing simultaneous multi-slice (SMS) can allow you to quickly acquire large volume T1 and T2 TSE axial spine series in regions of concern (for example if impending cord compression is seen). If thinner slice resolution is required you might consider using Compressed Sensing (CS) on a SPACE axial sequence to reduce the comparatively lengthy TA.

Whole-body sequences (T1 Dixon, T2 HASTE, and HASTIRM)

T1 Dixon imaging allows the creation of quantitative fat-fraction images which are used to assess tumor response or progression. Previously, the creation of these images was a manual procedure involving the addition and division of image series but can now be generated inline (**Inline: Liver: Fat Fraction (2pt)** tick box, Fig. 5) and will be composed along with the chosen Dixon contrasts.

If enabled, DRB can improve the sharpness of HASTE images by compensating for noise introduced with the use of higher acceleration factors, reducing the echo train length and thus reducing blurring.



5 Tick box for automatic fat-fraction reconstruction.

Diffusion-weighted imaging

Previously, WB diffusion sequences were affected by broken spine artifacts, which were countered with awkward manual frequency-fixing techniques. This is now a thing of the past with the advent of SliceAdjust – a slice-by-slice shimming technique available on BioMatrix scanners. SliceAdjust should be used when acquiring and composing multiple large-volume DWI blocks.

Acquiring liver-lesion sensitive b-value images (between b500-b600 s/mm²) was previously recommended by the MET-RADS and MY-RADS guidelines. However, improvements in the signal-to-noise ratio enabled by the XA platform now allow good-quality b500-b600 s/mm² to be calculated rather than acquired, saving you time. Setting a calculated b value is straightforward – simply enable it in the **Diff**: tab on each DWI step.

DWI-SNR can be optimized by setting the bandwidth to allow minimum echo spacing, permitting the selection of an optimally minimized TE.

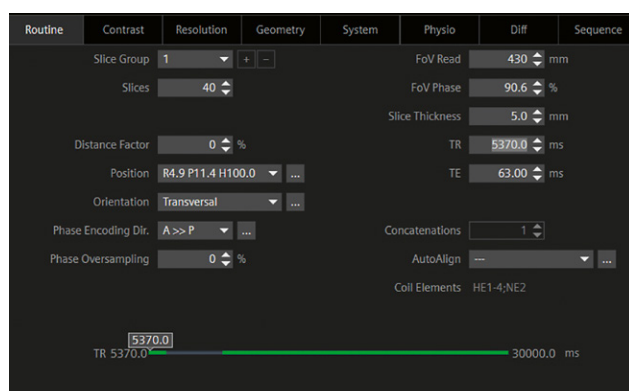
The diffusion parameters should be set to your team's preferred balance of SNR versus geometric distortion. Typically a 3D diagonal acquisition maximizes gradient performance resulting in greater SNR compared to the 3-scan-trace method. It's important to note that if the single-diffusion-direction 3D diagonal mode is selected, averages should be multiplied by 3 to reach an equivalent number of averages to a 3-directional 3-scan-trace. Additionally, the selection of a monopolar diffusion scheme will allow a shorter TE (and thus increased SNR) at the cost of increased geometric distortion.

When optimizing the sequence you may find a TR gap between a range of shorter, more SAR-intensive TRs and the next selectable TR (Fig. 6). Usually it is optimal

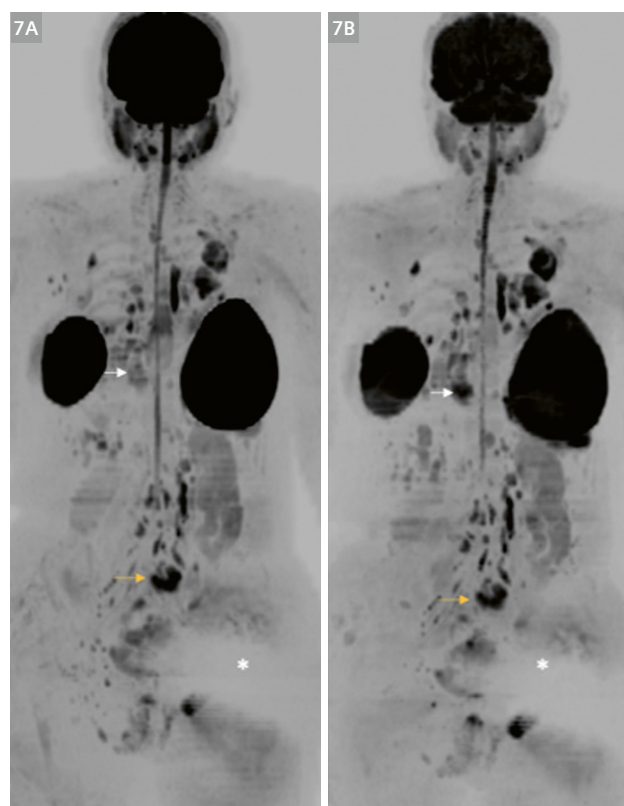
to select the lowest TR however if SAR is an issue (e.g., if you are attempting to replicate this technique at 3T) an effective tactic is to select the minimum TR of the second "window" – reducing heating while minimizing TA.

Currently, SMS is an ineffective acceleration technique for WB-DWI. To maximize time-saving, one must either select a much shorter TR (which may have a significant negative impact on image contrast / DWI-SNR) or acquire more slices per step risking straying into the region of ADC drop-off as demonstrated by Winfield et al. [2]. SMS may however have a role to play in addressing the TA implications of a large TR "gap" as discussed above.

Deep Resolve Boost performs excellent denoising, enabling the selection of fewer averages per b-value resulting in a much shorter total TA versus conventional DWI (Fig. 7). Asymmetric averaging ensures the majority of time is spent acquiring high b-value data. Additionally, step-based averaging (e.g., more on the liver, fewer on the brain) helps to reduce the more conspicuous stepping artifact which can be seen in the liver and spleen with these shorter duration/fewer average sequences.



6 TR selection demonstrating interval between selectable TRs.



7 b900 inverted coronal MIP projections of conventional (7A) and DRB (7B) DWI.

Embrace the potential

Re-learning the relationships between SNR, scan time, and sequence parameters in the era of Deep Resolve has been a fascinating journey. Ultimately, you'll need to take that journey yourself to find what works best for you and your team.

By leveraging the power of these acceleration techniques, we've seen that patients' experience and image quality can be improved while allowing greater utilization of these often-limited resources.

While we'll always have fond memories of the MAGNETOM Avanto Fit, we've aimed to show that you too can make a huge impact for your patients by embracing the future of MRI. Good luck!

Visit www.siemens.com/wb-mri to watch the video tutorial.

References

- 1 Padhani AR, Lecouvet FE, Tunariu N, et al. METastasis Reporting and Data System for Prostate Cancer: Practical Guidelines for Acquisition, Interpretation, and Reporting of Whole-body Magnetic Resonance Imaging-based Evaluations of Multiorgan Involvement in Advanced Prostate Cancer. *Eur Urol*. European Association of Urology; 2017;71:81–92.
- 2 Winfield JM, Collins DJ, Priest AN, et al. A framework for optimization of diffusion-weighted MRI protocols for large field-of-view abdominal-pelvic imaging in multicenter studies. *Med. Phys*; 2016;43:95–110.



Contact

Will McGuire, MSc MRSO (MRSC™)
Deputy Superintendent Radiographer
Paul Strickland Scanner Centre
Northwood, UK
will.mcguire@stricklandscanner.org.uk

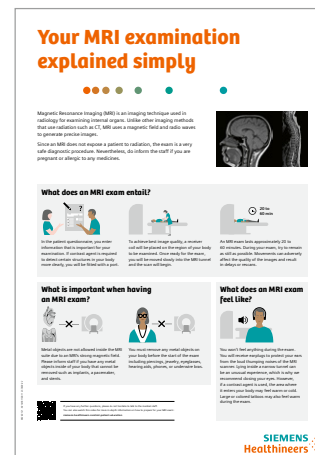
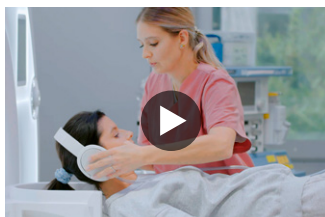
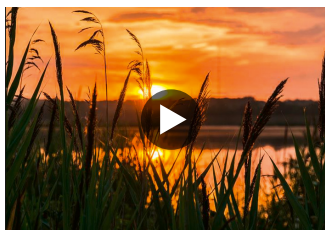
Advertisement

Prepare your patients mentally for their MRI exam

Most patients who undergo an MRI exam, experience some level of anxiety. As a result, some move so much that they cause motion artifacts, cannot complete the scan, or do not even show up for the exam. Up to 75%¹ of all unsatisfactory scan outcomes can be eliminated by educating patients on the MRI exam.

Tap the full potential of your facility by preparing your patients for the scan with our patient education toolkit. A **video**, **poster**, **meditation**, and a **book for children** explain the process of an MRI exam in simple words and answer common questions:

- What does an MRI exam entail?
- What is important when having an MRI exam?
- What does an MRI exam feel like?



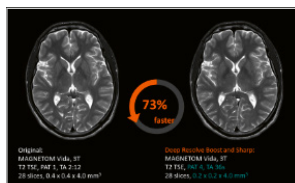
Download the patient education toolkit in your preferred language here:
siemens-healthineers.com/mri-patient-education



¹Törnqvist, E., Månsson, A., Larsson, E.-M., & Hallström, I. (2006). Impact of extended written information on patient anxiety and image motion artifacts during magnetic resonance imaging. *Acta Radiologica*, 47(5), 474–480. <https://doi.org/10.1080/02841850600690355>.

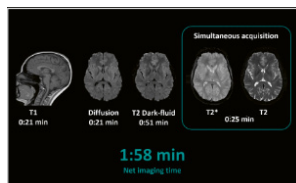
Try them on your system

Trial licenses for many of the applications featured in this issue of MAGNETOM Flash are available as a trial license free of charge for a period of 90 days.



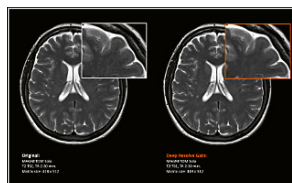
Deep Resolve Boost

Deep Resolve Boost uses raw-data-to-image deep learning reconstruction technology.



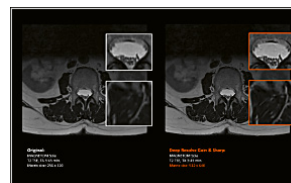
Deep Resolve Swift Brain

Deep Resolve Swift Brain is an ultra-fast brain imaging protocol leveraging the fastest available imaging sequence together with a deep learning reconstruction.



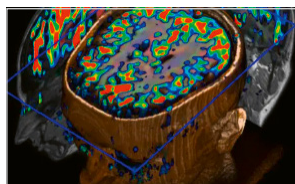
Deep Resolve Gain

Deep Resolve Gain is an advanced image reconstruction technology that achieves intelligent denoising.



Deep Resolve Sharp

Deep Resolve Sharp is an AI-powered image reconstruction technology with a deep neural network at its core that increases the sharpness of the image.



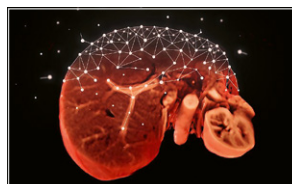
ASL 2D and ASL 3D

ASL is an MR technique using the water in arterial blood as an endogenous contrast agent to evaluate perfusion.



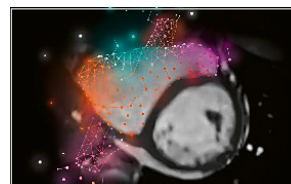
Simultaneous Multi-Slice

Setting the pace in MRI acceleration for TSE and DWI.



Compressed Sensing Grasp-VIBE

Beyond speed.
Beyond motion.



Compressed Sensing Cardiac Cine

Beyond speed.
Beyond breathholds.

Additional technical prerequisites may apply. Upon receiving your request, your local Siemens Healthineers representative will clarify whether your system meets the requirements.



For further details, product overviews, image galleries and general requirements please visit us at:

www.siemens-healthineers.com/magnetic-resonance-imaging/options-and-upgrades

The following software may not be available for trial on all systems. Trials are limited to software applications only and are available free of charge for a single 90-day period to Siemens Healthineers customers with a service contract only. Trials may not be available should required hardware and/or software prerequisites not be available on the local system. Please contact your local Siemens Healthineers representative for more information.

MR Elastography Using the Gravitational Transducer

Omar Isam Darwish^{1,2}; Vitali Koch³; Thomas Joseph Vogl³; Marcos Wolf⁴; Katharina Schregel⁵; Arnie Purushotham⁶; Valerie Paradis^{7,9}; Valerie Vilgrain^{8,9}; Radhouene Neji¹; Ralph Sinkus^{1,10}

¹School of Biomedical Engineering and Imaging Sciences, King's College London, United Kingdom

²MR Predevelopment, Siemens Healthineers, Erlangen, Germany

³Department of Diagnostic and Interventional Radiology, University Hospital Frankfurt, Frankfurt am Main, Germany

⁴Centre for Medical Physics and Biomedical Engineering, Medical University of Vienna, Austria

⁵Department of Neuroradiology, Heidelberg University Hospital, Heidelberg, Germany

⁶School of Cancer & Pharmaceutical Sciences, King's College London, United Kingdom

⁷Department of Pathology, Hôpital Beaujon, Clichy, France

⁸Department of Radiology, Hôpital Beaujon, Clichy, France

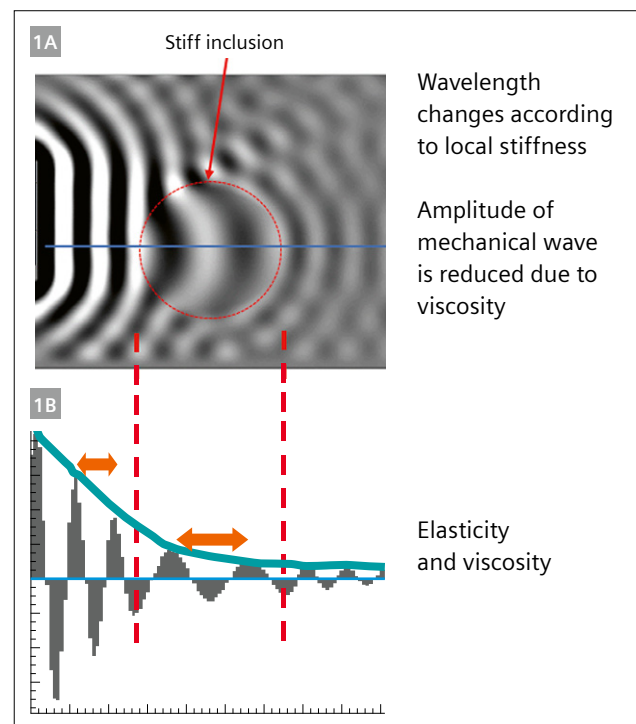
⁹Université Paris Cité, INSERM, Centre de recherche sur l'inflammation, Paris, France

¹⁰Laboratory for Vascular Translational Science (LVTS), INSERM U1148, Paris, France

Introduction

Biomechanical integrity is at the heart of the body's homeostasis. Many pathologies manifest themselves by impacting tissue stiffness. These include chronic liver diseases, which cause inflammatory and fibrotic processes that lead to a "stiff liver". For a long time, liver palpation was used to estimate liver size, feel for liver stiffness, and possibly local masses to find signs of liver disease. However, the development of ultrasound elastography (USE) [1] and MR elastography (MRE) [2, 3] changed this radically by providing quantitative maps of tissue stiffness, and even tissue viscosity when done in 3D [4]. MRE has demonstrated its ability to non-invasively assess chronic liver disease [5, 6] and characterize breast cancer lesions [4, 7] and brain tumors [8, 9]. Currently, hepatic MRE is the most applied elastography technique in the clinic, where it is used to quantify liver fibrosis by measuring the shear stiffness [10] or the shear wave speed [6]. In addition, it has shown promise in grading liver inflammation by measuring the loss modulus [6].

In general, elastography utilizes the intricate link between the properties of propagating mechanical shear waves, i.e., their amplitude, phase, and local wavelength, to uncover the underlying mechanical properties of tissue. Importantly, soft tissue is quasi-incompressible since it consists of 70% water, sometimes even more. Thus, the typical physician's notion of tissue being "more or less compressible" is based on the wrong terminology: Tissue can be sheared to a certain extent given an exerted force, but it does not change its volume as water is incompressible. The spatially varying constitutive material properties result



1 **Dependence of shear wavelength on local stiffness**
(1A) Finite element simulation of a wavefield with a homogeneous background and a hard inclusion. **(1B)** The corresponding line profile shows that the local wavelength (orange arrows) changes depending on the underlying stiffness. Additionally, the amplitude of the wave drops due to intrinsic loss mechanism (viscosity). "Imaging" the shear wave allows hence in return to recover the local biomechanical properties.

in shear waves propagating faster or slower depending on whether tissue is locally stiff or soft, respectively (Fig. 1). For a fixed vibrational frequency, this translates into a longer or shorter wavelength, which can be imaged via phase contrast-based MRI sequences [3, 4, 11, 12].

Overall, MRE necessitates three essential steps:

- I) Efficient wave generation and penetration in a patient-friendly way
- II) Wave image acquisition using phase-locked and motion-sensitized MRI sequences that yield high spatial fidelity
- III) Recovery of the underlying biomechanics in the most unbiased fashion

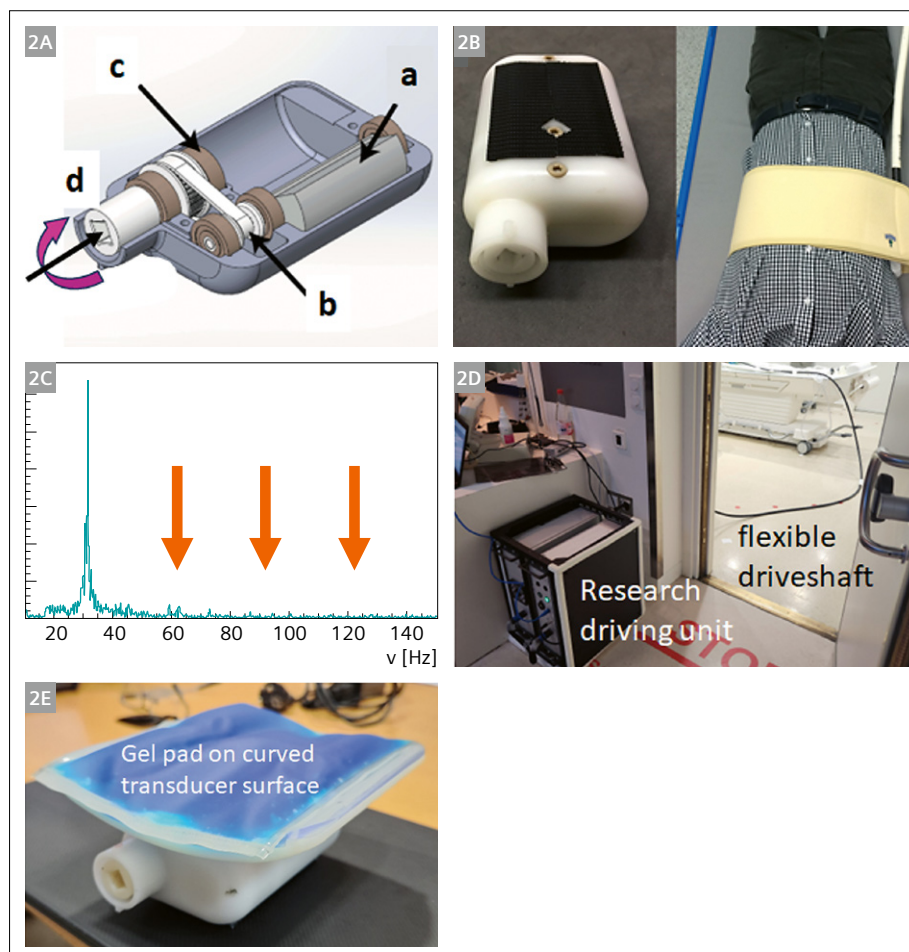
Shear wave generation: MR Elastography transducer

The generation of monofrequent shear waves with sufficient amplitude and phase stability within the MRI environment is a non-trivial task. To date, several MRE transducer concepts have been proposed [19] with very different driving approaches:

- I) Current-driven electromagnetic coils that oscillate due to the Lorentz force in the main B_0 -field [4, 13, 20]
- II) A pneumatic approach connecting an active driver with a membrane via a flexible tube [21]
- III) A pulse-density modulated approach using compressed air [22]
- IV) A gravitational transducer approach [23]

For MRE to yield high-quality maps of biomechanical properties, the transducer needs to transmit a pure frequency spectrum. Otherwise, parasite frequencies (upper harmonics) impact in particular the quality of the viscous biomechanical properties [24]. Each transducer concept has pros and cons, which relate to flexibility, strength, pureness of the frequency spectrum, and the ability to transmit waves even under the application of external mechanical load, e.g., when the transducer is positioned at the back of the patient. Here we focus on the description of the gravitational transducer approach and discuss its properties.

A gravitational transducer utilizes the generic equivalence of acceleration to force with a rotating eccentric mass for the generation of vibrations, similar



2 Gravitational transducer concept

(2A) The gravitational transducer consists of a casing that hosts a spinning eccentric mass (a), which is connected via a gearbox (b, c) to an external flexible driveshaft (d). (2B) The closed transducer is very compact and, for abdominal applications, is strapped to the patient's body via a belt. (2C) When operated at 30 Hz, the frequency response spectrum shows no upper harmonics. (2D) The research prototype of the gravitational MRE concept had the driving unit outside the MRI room, with the flexible driveshaft going through the waveguide toward the patient table. The picture shows the installation at University Hospital Frankfurt am Main, Germany. (2E) To improve patient comfort for abdominal applications, the transducer has a curved contact plate with a gel pad. The curvature and size of the contact plate are easily adaptable to different applications.

to those found in a mobile phone's vibrating alert motor. Figure 2A shows a sketch of the transducer design: The eccentric mass (a) is connected via a gearbox (b, c) to an external flexible driveshaft (d). The presence of the gearbox allows to reduce the friction on the external drive-shaft. A rotating eccentric mass has the advantage that the generated force grows with increasing frequency quadratically, which leads to a vibrational amplitude independent of frequency [23]. This is in stark contrast to acoustically driven (pneumatic) approaches, which always experience a reduction in amplitude with increasing frequency. The compact design of the transducer enables various abdominal or cerebral applications (Fig. 2B) as the mass rotates independently of whether any external load is applied to the casing of the transducer.

Typically, the loss in amplitude for acoustically driven approaches is compensated by an increase in driving power, which leads in turn to a non-linear system response, i.e., the presence of upper harmonics. This leads to a degradation of data quality. The gravitational approach – by contrast – represents a linear system with a frequency response spectrum devoid of any upper harmonics (Fig. 2C). This concept, which was developed within an EU-funded Horizon 2020 project (FORCE) at St Thomas' Hospital (part of King's College London), had the driving unit outside the MRI scanning room with the flexible driveshaft reaching through the waveguide and finally connecting to the transducer at the patient bed (Fig. 2D). To ensure patient comfort, the transducer has a curved contact plate cushioned with a gel pad. The gel pad allows compressional waves to pass without any attenuation into the patient's body, while shear vibrations of the transducer are dampened, which increases patient comfort. This flexible design allows for easy adaption to other organs such as kidney, breast, and brain.

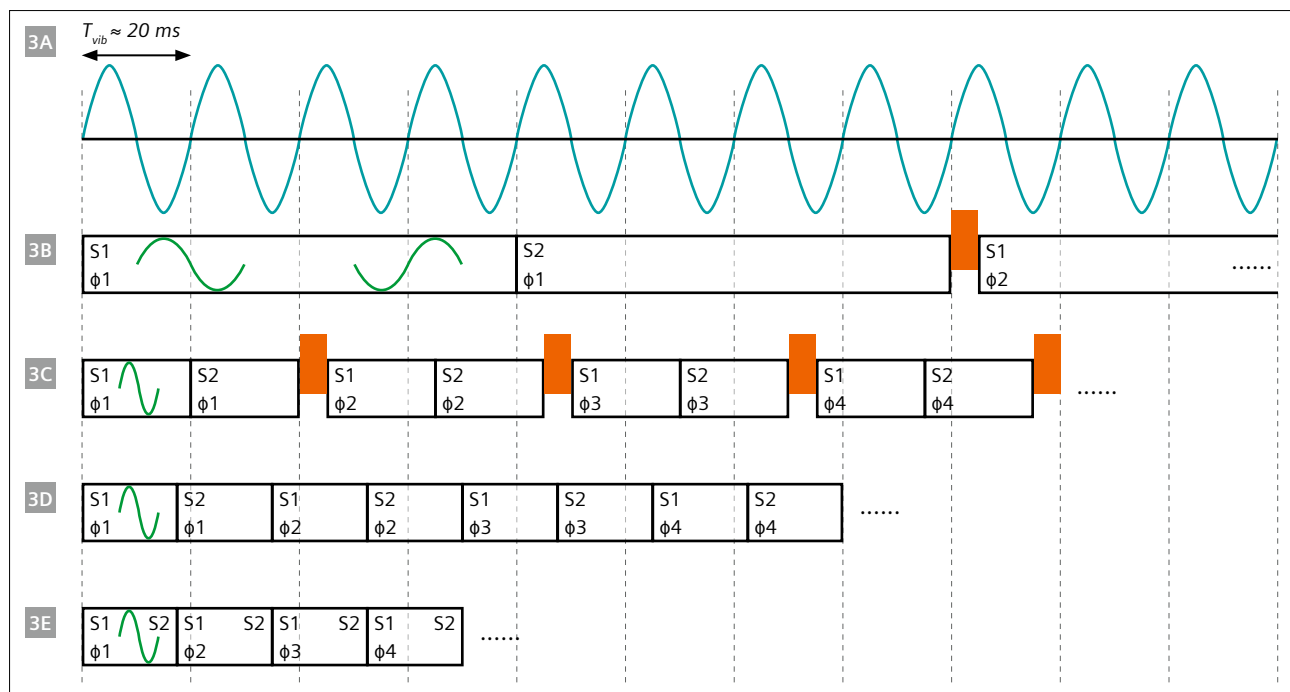
MR Elastography sequence

MRE and diffusion-weighted imaging (DWI) sequences share many properties: They both are intended to quantify motion of moving water molecules using motion-sensitized sequences. The fundamental difference between the concepts is that in diffusion we do not know when the individual water molecules are jumping in time due to the Brownian motion. Hence, DWI is based on the concept of signal destruction without any impact on the net phase of the MR image [25]. In MRE, however, time is controlled via the vibration of the mechanical transducer. Hence, it is possible to use a phase-locked approach to visualize the micron-level vibrations within the phase of the MR image [4, 13]. Many phase-contrast MRI sequences can be used for MRE; however, gradient-echo (GRE) and spin-echo echo-planar imaging (SE-EPI) sequences are the ones most frequently employed. The fundamental concept of the

phase-locking is shown in Figure 3. The frequency of the motion-encoding gradient (MEG) should be identical with the mechanical vibration frequency to obtain the largest sensitivity to motion. At 60 Hz, this leads to very long echo times (TE), which requires the utilization of SE sequences to recover sufficient signal-to-noise ratio (SNR), especially when operating at 3T. Consequently, a single SE-based excitation-readout block spawns over approximately 50–66 ms (Fig. 3B). Temporal delays (orange blocks in Fig. 3B) allow to shift the MR acquisition relative to the mechanical vibration, providing images of the wave propagation at another timepoint (wave phase) throughout the oscillatory period of one mechanical vibration. Typically, 4 to 8 of such wave phases equally spaced over one oscillatory cycle are acquired to recover later – during the MRE reconstruction process – the complex-valued displacement field. The long TE results in prohibitively long acquisition times, which can be counterbalanced via EPI readout approaches. Depending on echo spacing, phase field of view (FOV), and off-resonance, EPI leads to geometrical distortions, which in turn will impact the recovery of the biomechanical properties, because higher-order spatial derivatives of the wavefields are necessary for solving the wave equation. GRE-based sequences using MEGs at the mechanical vibration frequency are one way to shorten acquisition time [26]. However, the long TE of ~20 ms results in very poor SNR. The use of fractional MEGs overcomes this limitation by sacrificing sensitivity to motion by shortening the MEG, which therefore no longer operates at the mechanical vibrational frequency [11]. The corresponding loss in phase-to-noise ratio for wave propagation imaging can be partially recovered by more advanced motion-encoding concepts such as Hadamard encoding [27]. Initial approaches used excitation readout blocks with durations that were still integer multiples of one mechanical oscillation period (Fig. 3C) [28]. More advanced approaches incorporated the temporal delays into the duration of each individual shot, leading to a further shortening of the scan time (Fig. 3D) [12]. Now, simultaneous multi-slice (SMS) excitation [29] has opened the gateway to shortening acquisition time even more, by enabling the capture of 3D datasets within one single breath-hold (Fig. 3E) [30]. Spiral readout concepts have also been proposed for brain MRE [31], including self-navigation for motion correction. Here again, due to the long readout, B_0 inhomogeneities and eddy-current effects need to be properly compensated to avoid any impact on the fidelity of space.

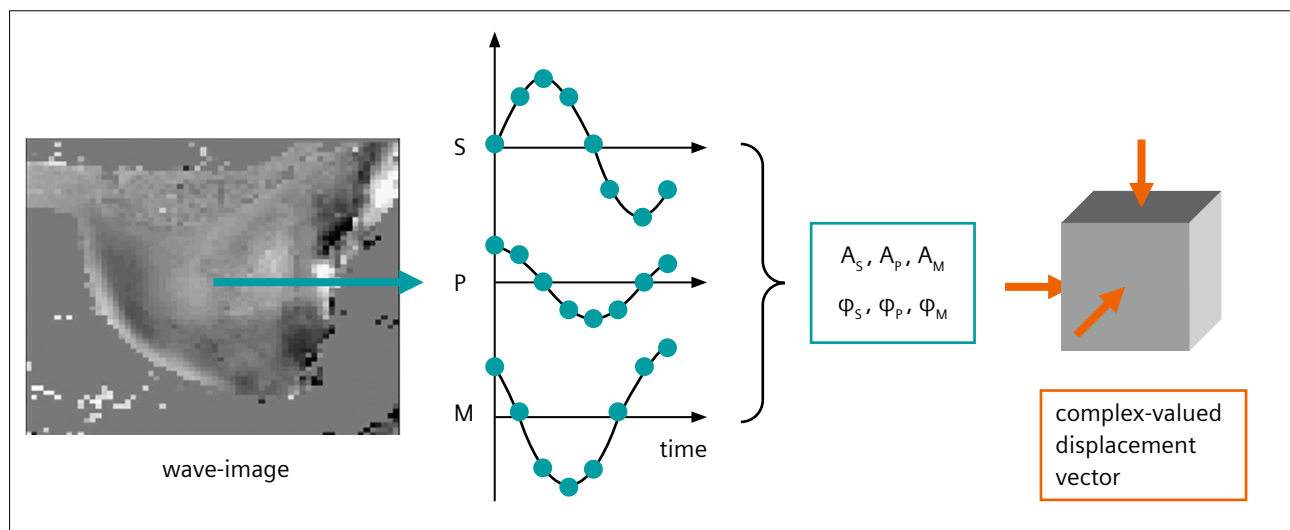
MR Elastography reconstruction

The MRE sequence provides snapshots of the wavefield at different timepoints (wave phases) throughout an oscillatory cycle (Fig. 4). Thus, when presented as a function of



3 MRE sequence concepts

(3A) Sinusoidal mechanical vibration generated by the MRE transducer is for clinical applications typically in the 40–60 Hz range. Thus, one period corresponds to roughly $T_{vib} \sim 20$ ms. (3B) SE-based sequences typically use MEGs (green) that operate at the vibration frequency. This leads to a long shot duration, i.e., the time interval encompassing excitation and readout. Temporal delays (orange rectangles) are used to shift to the next wave phase ϕ_j ($j \in [1, 2, 3 \dots M]$, M = number of wave phases) once all slices S_i have been acquired ($i \in [1, 2, 3 \dots N]$, N = # of slices). (3C) Fractional motion-encoding concepts enable significant scan-time reduction at the cost of a loss of motion sensitivity. Initial approaches still had the temporal delays separate from each shot, thereby perturbing the eddy-current steady state [12]. (3D) More sophisticated concepts overcame this by incorporating the delays into each shot, further reducing scan time. (3E) SMS finally provided a straightforward way to acquire 3D MRE datasets within a single breath-hold.

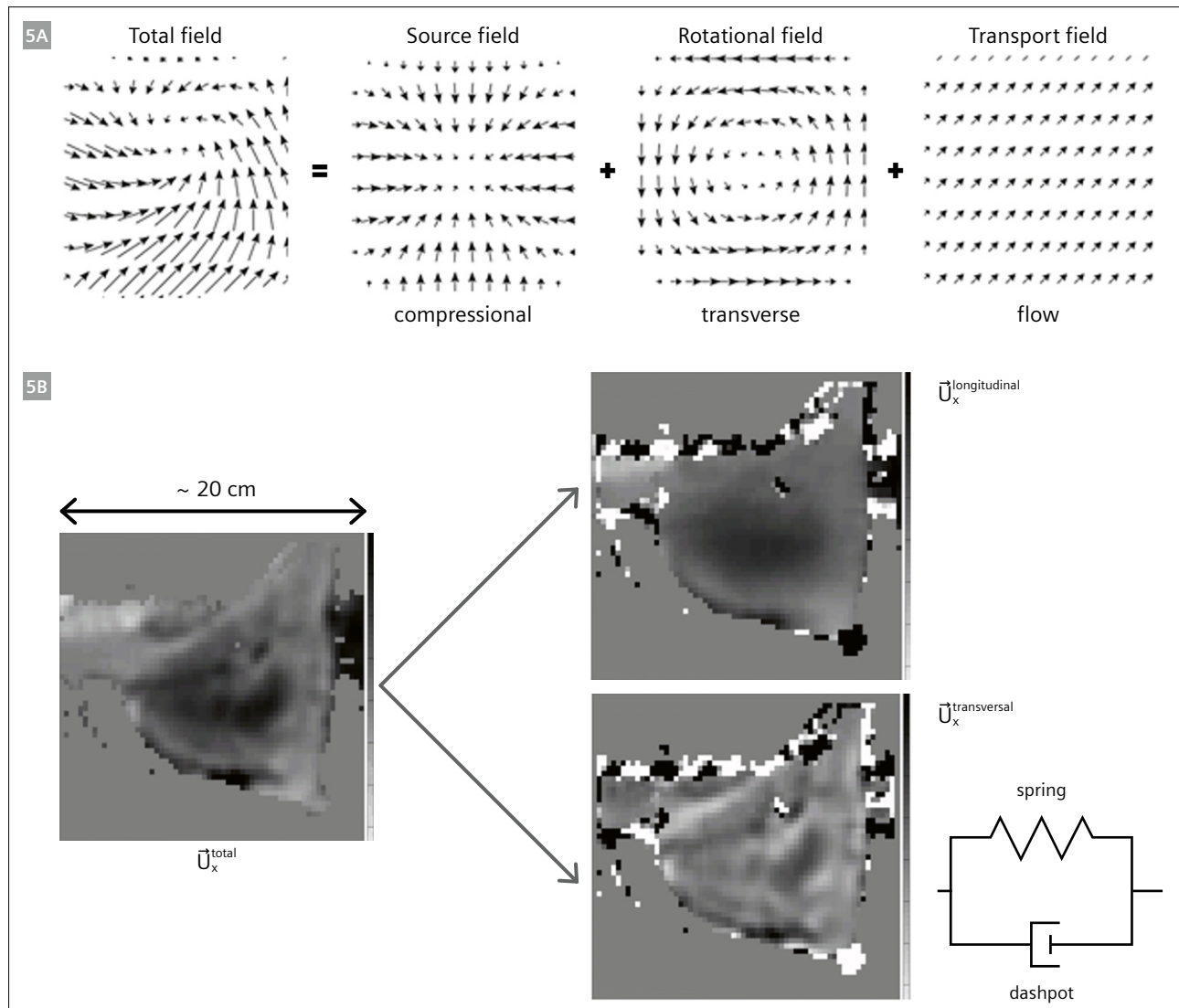


4 From MRE raw data to wavefield displacement vector

The MRE data acquisition provides snapshots of the propagating wave. When looked at pixel-wise, a sinusoidal modulation of the MRI phase is observed for each of the three encoding directions (readout [M], phase-encoding [P], slice direction [S]). A temporal Fourier transform yields the corresponding amplitudes A_i and phases ϕ_i of the complex-valued displacement vector of the wavefield in direction $i \in (M, P, S)$. This approach assumes temporal steady state, i.e., there are no transient effects, and the time component is purely described by sinusoidal temporal modulation at the driving frequency.

wave phase, each encoding direction will show for each single pixel a sinusoidal temporal MRI-phase modulation. A temporal Fourier transform then yields the corresponding amplitudes A_i and phases ϕ_i of the wavefield, which constitute the steady-state solution to the problem.

The wave propagation is in general a 3D problem and can only, under specific boundary conditions, be simplified to 2D or even 1D [1]. The beauty of the MRE approach is that the measured displacement field constitutes the underlying wave solution of the problem at hand. Certainly, boundary



5 Mathematical foundations of MRE reconstruction

(5A) In general, any wavefield is the sum of three fields that exhibit very different mathematical properties: a source field, a rotational field, and a transport field. In our case, the total displacement vector is the sum of the compressional (source) and the transverse (rotational, shear) wave, because there are no transport effects in our experiments. (5B) Both waves exhibit very different mathematical properties and different wavelengths since they are coupled to different mechanical properties of tissue, shown here for in vivo data in breast tissue. The compressional wave in our frequency domain has a very long wavelength (\sim cm) as it is linked to the bulk modulus. Remember that tissue is incompressible, leading to a bulk modulus in the order of GPa. Conversely, the shear wave is relatively short (\sim cm) as it is linked to the shear modulus (\sim kPa). Note that both moduli differ by six orders of magnitude! The solution of the complex-valued shear modulus can now be interpreted in many ways: One possibility is to view tissue as if shear stiffness (elasticity, spring) and shear loss (viscosity, dashpot) were organized as spring and dashpot connected in a parallel fashion (Voigt model). In reality, tissue exhibits a more complex mechanical response function, leading to fractal-like mathematical representations due to its hierarchical organization.

conditions do impact the details of the wavefield due to reflections and scattering. Since the underlying physics is local, except under specific quantum mechanical conditions [32], all we need to do is invert the 3D wave propagation equation [33]. Mathematically, any continuous vector field can be decomposed into three different components which carry very different mathematical properties:

- I) One field that has sources (curl-free)
- II) One field that – similar to the magnetic field – has no start and no end (divergence-free)
- III) One field that relates to transport effects (curl- and divergence-free, Fig. 5A) [34]

In our case, due to the absence of any transport effects (there is no flow of tissue present in the data), the total displacement field is the sum of the compressional and the transverse (shear) wavefield (Fig. 5B). These two fields probe very different properties of tissue: The compressional wavefield is linked to the bulk modulus of tissue and propagates at the speed of sound in water, i.e., at 1550 m/s. Hence, it exhibits very long wavelengths, which are around ~30 m at frequencies of around 50 Hz. This is mathematically very challenging to handle, given the typical SNR in MRE data. The transverse wave, by contrast, travels at speeds of around 1–10 m/s resulting in wavelength of around 2–20 cm! Given typical pixel-sizes of ~3–4 mm, such wavelengths can properly be resolved and used to calculate spatial derivatives of a higher order. For a correct inversion of the wave equation, it is necessary to first remove the compressional field. Using, for instance, its mathematical properties of “carrying” the sources of the mechanical wavefield, it is possible to mathematically remove it via the “curl operator”. Certainly, this is at the cost of an additional spatial derivative [17]. Other approaches try to remove the compressional component via high-pass filters in the Fourier domain [18], or via integration [35]. A combination of both utilizes divergence-free basis functions in the context of finite element modelling [24]. Once the compressional field has been removed, the remaining equation is basically expressing Hooke’s law: Stress and strain are related via the shear modulus [33]. The beauty in MRE is that the approach to solve for the complex-shear modulus is independent of any assumptions of the underlying rheological properties of tissue [17, 36]. The single most important assumption is that the material is isotropic and linear. Thus, shear modulus (elasticity) and loss modulus (viscosity) of the complex-valued shear modulus can be interpreted a posteriori in terms of the Voigt model, which assumes tissue

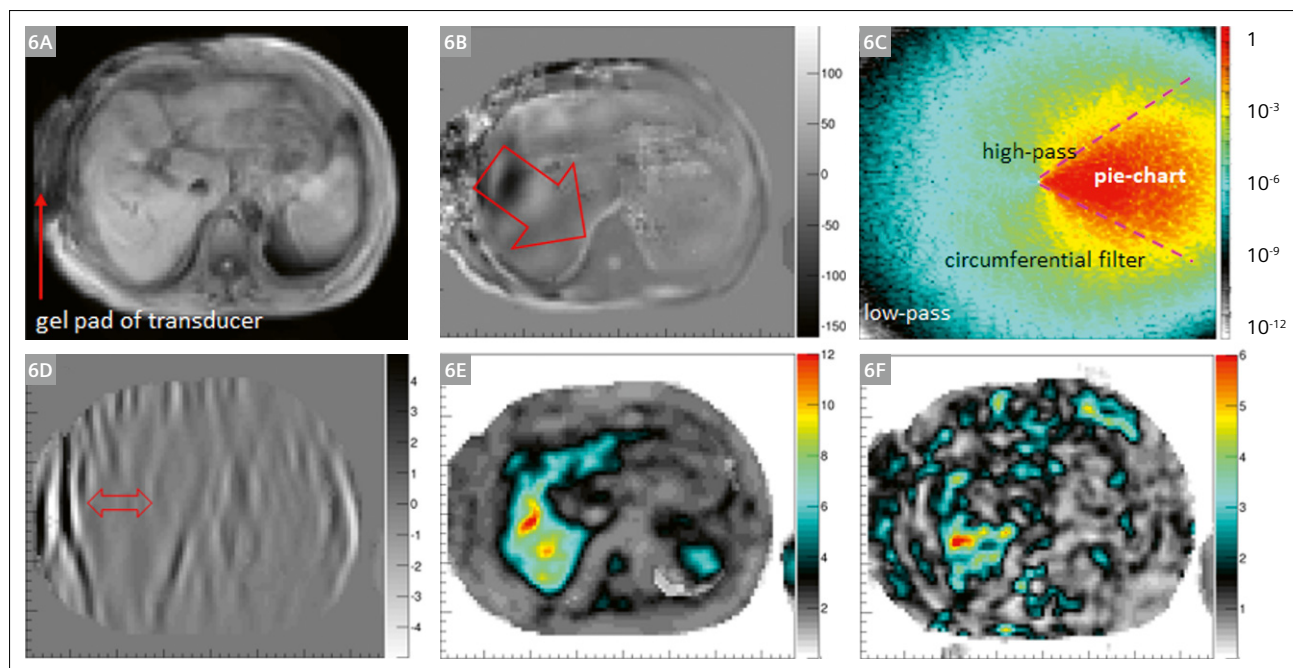
to behave as a spring and a dashpot in parallel (Fig. 5B). In reality, tissue exhibits far more complex dispersion (i.e., frequency-dependent) properties, which are likely to carry valuable diagnostic information [37, 38].

It is important to stress that both elasticity and viscosity relate to the solid shear properties of the material, and the loss describes the ability of the material to extract energy from the propagating wave. The origin of this energy loss can be true absorption (i.e., conversion to heat) or scattering (leading to a redistribution of the wave’s energy in space). Scattering-induced effects within tissue impact the frequency dependence of tissue and lead to an intricate mixture of constitutive and apparent effects governing the dispersion properties [39].

Figure 5 shows the overarching mathematics and physics governing the 3D wave propagation. Under certain assumptions, however, it is possible to simplify the 3D equation, which after all necessitates the measurement of the 3D displacement vector within a volume and the calculus of third-order spatial derivatives, which puts high demands on the SNR of the data. Another approach assumes that the total wavefield is composed of independent plane waves, and cuts out in Fourier space a “pie-chart” section to virtually recover the individual plane waves (Figs. 6A–6C) [18]. Additionally, low-pass and high-pass filters are utilized to suppress noise and compressional wave components, respectively. The resulting wave is a quasi-plane-shear-wave, which allows to recover local stiffness values without needing to measure all wave components within a volume (Figs. 6D, 6E). Clearly, this method relies on several assumptions which are not always met. It is nonetheless a rather robust technique which enables quantification of liver stiffness within a single breath-hold [40]. However, recovery of tissue viscosity requires the full solution of the 3D wave equation since the previous mathematical operations impact too strongly on the imaginary part of the wave equation to obtain reliable values (Fig. 6F).

MR Elastography examples using the gravitational transducer Ultrasound gel phantom

Quality control in MRE is essential to ensure correct performance of the intricate interplay between MRI data acquisition and mechanical vibration. Figure 7A shows results from an ultrasound (US)-based phantom (Ultragel 2000 Hungary, GUS5LT) that exhibits at 60 Hz a shear modulus of ~0.9 kPa and has few dispersive properties. The semi-rigid plastic-based surface of the phantom leads to a grid-like pattern of shear waves



6 Directional wave filtering for 2D MRE and viscosity

(6A) Magnitude image of the liver in transverse orientation. The gravitational liver transducer is located on the right-hand side of the patient with the gel pad visible (arrow). **(6B)** The pattern of the wavefield in through-slice direction shows mainly a plane wave propagating toward the center of the patient (arrow, [mm]). **(6C)** Amplitude of the Fourier transform of the wave image shown in 6B segmented in a pie-chart fashion with additional low-pass, high-pass, and circumferential filters to generate a virtual plane shear wave in image space after inverse Fourier transform. Note that the Z-scale is logarithmic. **(6D)** Corresponding plane-shear wave image showing longer wavelengths within the liver when compared to regions of subcutaneous fat (arrow). **(6E)** Result of the 2D approximation depicting an elevated shear stiffness of the liver in a patient with severe liver fibrosis (grade F4) [kPa]. **(6F)** Corresponding map of the shear viscosity resulting from a full 3D inversion of the wavefield [kPa]. Data from University Hospital Frankfurt am Main, Germany.

within the US gel (Fig. 7B). The directional filter is capable of extracting the individual plane waves, with Figure 7C showing one of the waves travelling from left to right (arrow). The corresponding 2D inversion yields a stiffness of

$$|G^*| = 0.9 \pm 0.1 \text{ kPa}$$

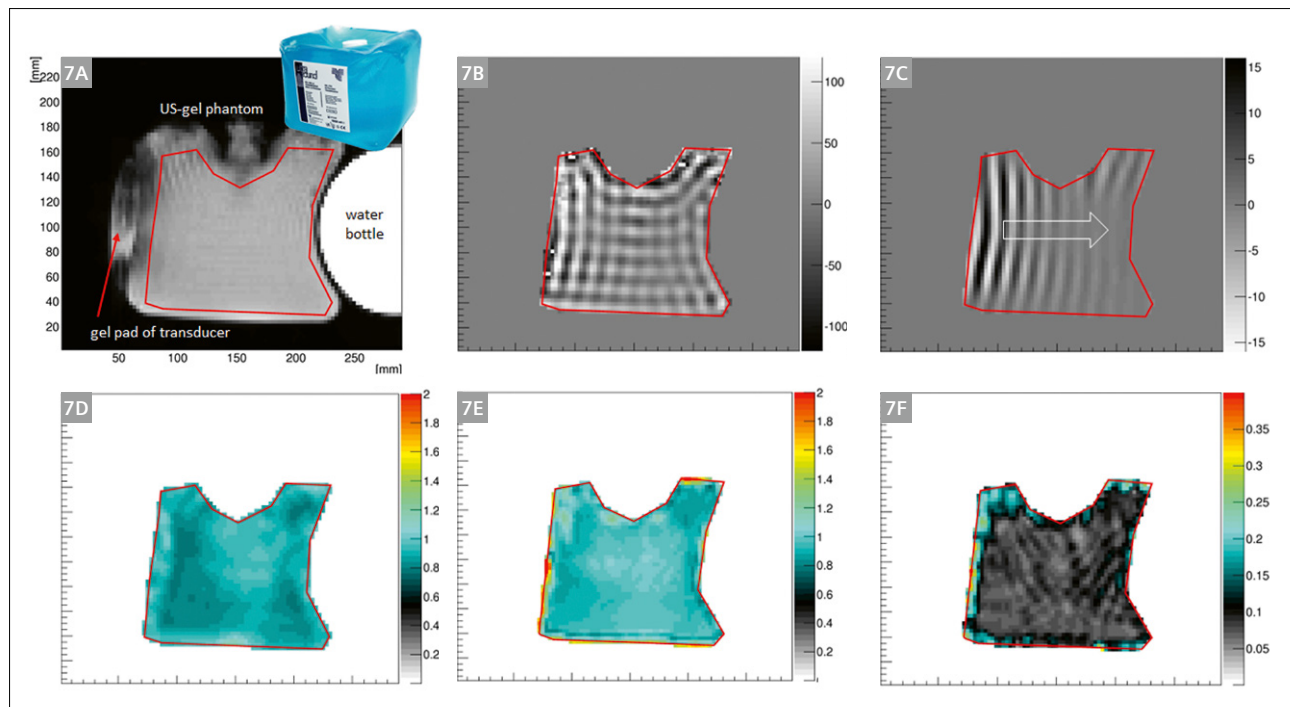
which is confirmed by the 3D inversion (Figs. 7D, 7E). The 3D inversion additionally allows quantification of the shear viscosity (G_v), which is very low for such a gel, naturally. A very homogeneous phase angle of

$$\gamma = 0.1 = \frac{2}{\pi} \arctan\left(\frac{G_v}{G_d}\right)$$

is retrieved, and is indicative of a material that is mostly spring-like with few absorptive properties.

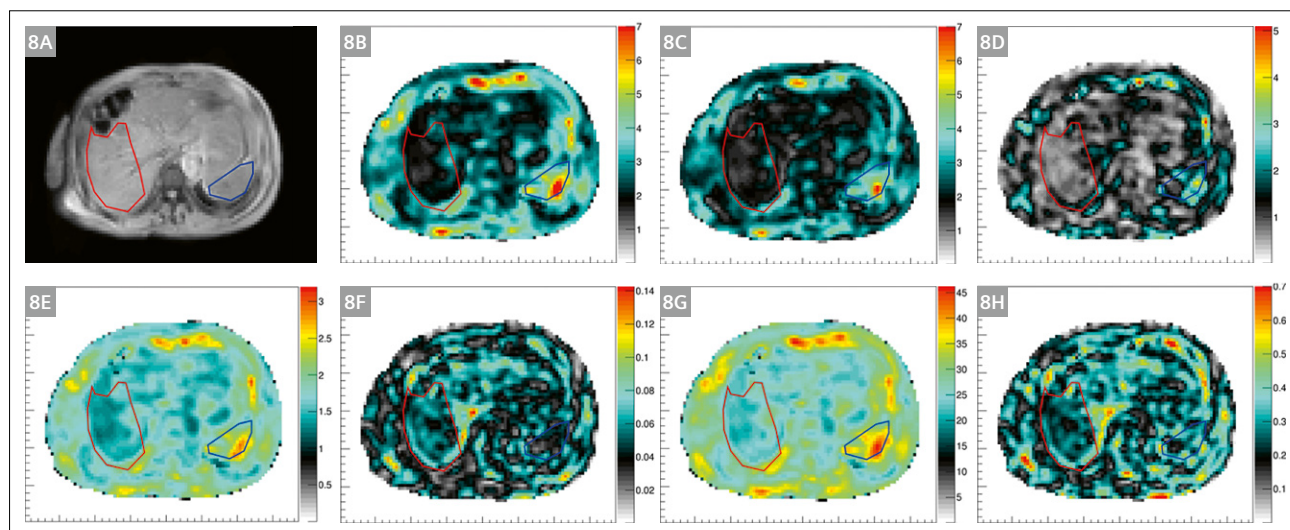
Liver

The mechanical integrity of the liver can be affected by a broad spectrum of diseases, including viruses, drugs, alcohol, or the metabolic syndrome. Metabolic dysfunction-associated steatotic liver disease (MASLD), formerly called non-alcoholic fatty liver disease (NAFLD), is the most common chronic liver disease in Western populations and is continuously increasing in prevalence due to lifestyle changes, obesity, and type 2 diabetes mellitus [41]. Metabolic dysfunction-associated steatohepatitis (MASH), formerly called non-alcoholic steatohepatitis (NASH), is generally considered the advanced type of MASLD. It is characterized by hepatic inflammation, hepatocellular injury, and fibrogenesis [41]. Lipotoxicity with ongoing inflammation is considered the major pathogenic driver of MASH, aggravating liver injury and promoting liver fibrosis [42]. In approximately 20% of cases, MASH



7 Ultrasound gel phantom results

(7A) Magnitude image of the experimental setup. A water bottle is attached to the US phantom to increase its weight. (7B) The real part of the displacement field in through-slice direction showing a grid-like pattern, which originates from the boundary conditions of the phantom, i.e., its semi-flexible plastic surface. (7C) One of the plane waves that was extracted from the directional filter approach here is travelling from left to right in the image. (7D) Magnitude of the complex shear modulus recovered from the 2D approach. The mean value agrees very well with the corresponding gauge obtained via the 3D inversion (7E). (7F) Phase angle $Y \in [0, 1]$ of the phantom as obtained from the 3D inversion indicating that the material is exhibiting mainly spring-like properties.



8 3D MRE results in the liver

(8A) Magnitude image of a liver patient with low-grade fibrosis related to metabolic dysfunction-associated steatohepatitis (MASH). (8B) Magnitude image of the complex shear modulus $|G^*|$ [kPa]. (8C) Shear elasticity G_d [kPa]. (8D) Shear viscosity G_l [kPa]. (8E) Shear speed C_s [m/s]. (8F) Shear absorption a [1/mm]. (8G) Shear wavelength λ [mm]. (8H) Shear phase angle Y [0-1]. Data from University Hospital Frankfurt am Main, Germany.

progresses to cirrhosis with increased overall mortality and sometimes the need for liver transplantation [43]. Early identification and initiation of targeted therapy are important to improve patient prognosis. Given the invasive nature of liver biopsy, which carries the risk of numerous complications, MRE emerges as a precise and non-invasive method for evaluating viscoelastic tissue characteristics at first presentation and during follow-up. Due to its ability to evaluate a substantial portion of the liver, MRE can detect focal viscoelastic disparities in all liver segments, in contrast to liver biopsy or transient elastography. Figure 8 shows an example of gravitational 3D wave-encoded MRE applied to a patient with low-grade fibrosis related to MASH. The liver (red region of interest, ROI, in Figure 8B) appears soft with an average value of the magnitude of the complex shear modulus

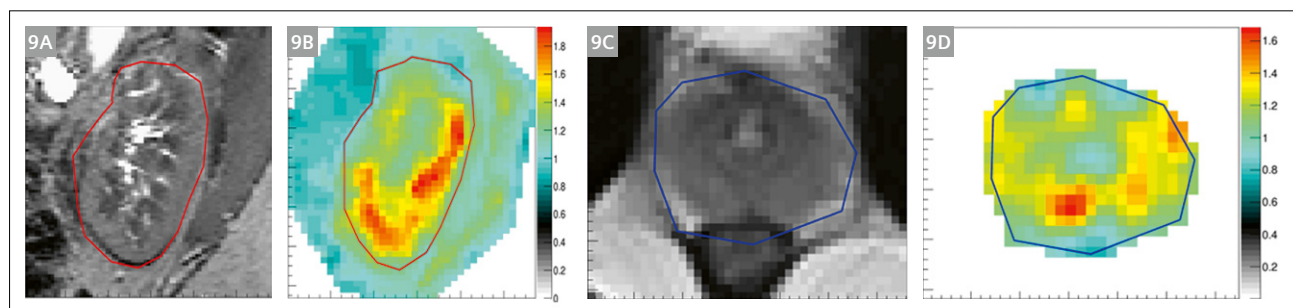
$$|G^*| = \sqrt{Gd^2 + G_l^2}$$

of around 2 kPa. Conversely, the spleen (blue ROI in Figure 8B) shows values of around 4.5 kPa, indicating considerably higher stiffness. This difference is similarly reflected in the elasticity G_d (Fig. 8C) as well as in the viscosity (Fig. 8D). While both elasticity and viscosity express the biomechanics from the point of view of the material, it is equally possible to express it from the point of view of the propagating wave. Numbers can thereby be matched to ultrasound elastography when properly considering dispersive effects, since US-based concepts using acoustic radiation force to generate shear waves are operating at a higher central excitation frequency (~150 Hz). Figure 8E shows the corresponding image of the shear wave speed with the wave propagating faster in the spleen than in the liver. Intriguingly,

the wave absorption is higher in the liver than in the spleen (Fig. 8F). The most simple and robust quantity which can be extracted from the wave equation is the shear wavelength (Fig. 8G). As expected, the shear wavelength is short in this patient's liver, while larger in the spleen, reflecting the corresponding soft and stiff material properties (Fig. 1). The last biomarker which carries great potential in quantifying subtle changes in tissue mechanics is the shear phase angle γ , which reports the ratio of shear viscosity to shear elasticity scaled to the range [0–1]. A value close to zero indicates a mainly elastic behavior (spring-like) of the material, while a value close to one is indicative of viscous dashpot-like behavior. Clearly, the spleen is exhibiting a higher phase angle, which shows that its overall behavior is more dashpot-like than that of the liver. Current research is focusing on exploring which biomarker carries which diagnostic value. We have so far seen a linear behavior of shear speed with liver fibrosis grade, and a non-linear relationship between viscosity and inflammation [6, 30]. Intriguingly, the phase angle γ has shown very little to no dependence on the underlying pathology.

Kidney and prostate

Figures 9A and 9B depict an example of 3D wave-encoded MRE applied to the kidney. The gravitational transducer is located on the posterior-lateral abdominal wall of the patient and is emitting waves in AP direction. Cortex, medulla, and central liquid zone are all well distinguishable in the corresponding maps of the shear speed. Note that liquid is extremely soft in terms of shear, while very stiff regarding compression due to its incompressible nature. Also, shear wave speed is well aligned with the anatomical image, as the renal sinus is reaching into the cranial part of the kidney. Figures 9C and 9D show an example of the application to the prostate with the transducer strapped



9 3D wave-encoded MRE results in the kidney and the prostate

(9A, 9B) T2-weighted anatomical image of the kidney and corresponding image of the shear wave speed [m/s].

Data from University Hospital Vienna, Austria.

(9C, 9D) T2-weighted anatomical image of the prostate and corresponding image of the shear speed [m/s].

Data from University Hospital Frankfurt am Main, Germany.

against the pubic bone and the patient in supine position. The urethra as well as the different zones within the prostate are well delineated in the speed map.

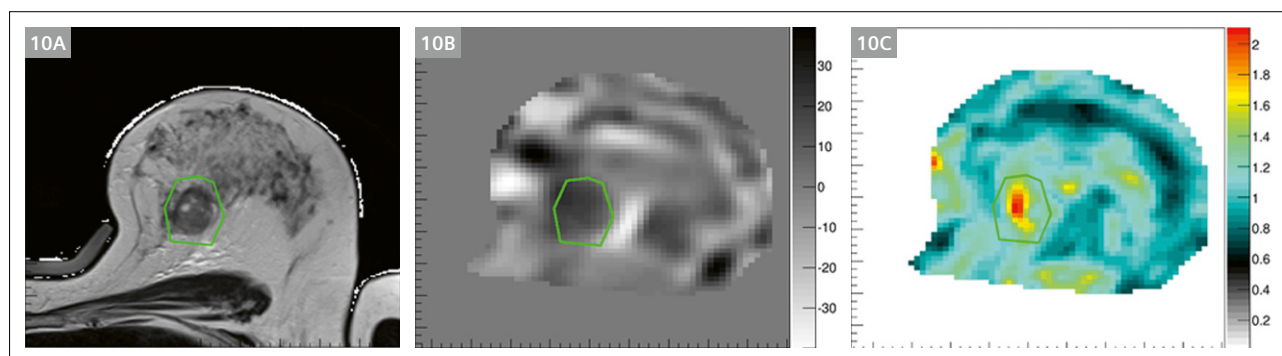
Breast

The application of MRE to the breast [48] necessitates adaptation of the gravitation transducer to the anatomical constraints of the breast coil [49, 50]. This was done in the context of the EU-funded Horizon 2020 project (FORCE at King's College London), in which the transducer was incorporated into the breast MRI biopsy coil. Figure 10 shows results from a breast cancer patient, where the presence of the tumor is well depicted within the shear wave speed image. The corresponding Z-component of the curl field shows that wave propagation is complex, similar to the case of brain MRE (Fig. 11), hence the plane-wave assumption for performing 2D reconstruction approaches might

be challenged. MRE is currently under investigation in women undergoing neoadjuvant chemotherapy for breast cancer to determine response or resistance of the tumor early during treatment. Should MRE prove to be a useful biomarker of response or resistance, it will enable oncologists to switch patients who are not responding to a particular drug regimen of neoadjuvant chemotherapy to an alternative drug regimen or guide the patient to early surgical intervention. This can minimize unnecessary toxicity due to an ineffective chemotherapeutic regimen and thereby improve quality of life.

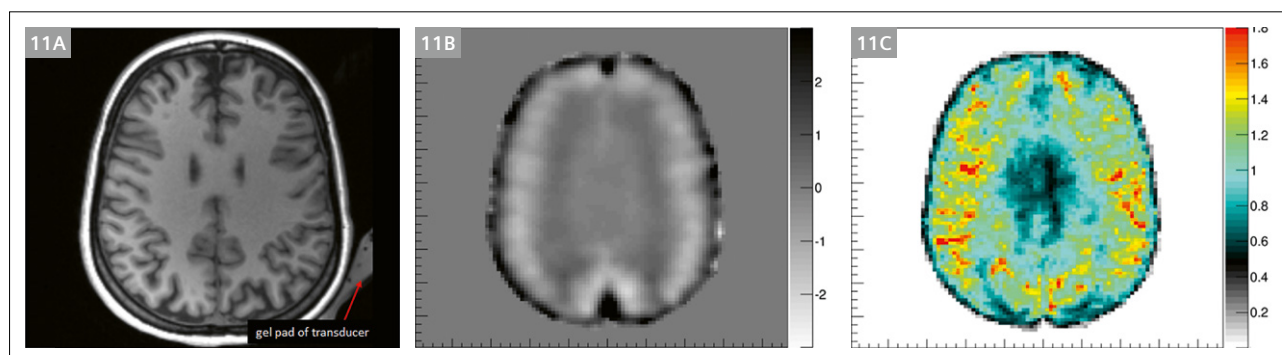
Brain

The application of MRE to the human brain is challenging due to the protective nature of the skull. The transducer is located within the head coil, transmitting waves in an inclined fashion to generate wave motion in all three



10 3D wave-encoded MRE results in the breast

(10A) T1-weighted anatomical image of the breast depicting a tumor within the green ROI. (10B) Corresponding Z-component of the curl field demonstrating that the wave propagation is not in a plane-wave fashion due to the very complex boundary conditions. (10C) Resulting shear wave speed image showing the tumor as a stiff object within the otherwise rather soft breast tissue. Data from King's College London, UK.



11 3D wave-encoded MRE results in the brain

(11A) Axial reformation of a T1-weighted 3D MPAGE structural image of the brain. (11B) Corresponding image of the Z-component of the curl field showing the complex and intricate shear wave pattern within the brain. (11C) The resulting image of the shear wave speed shows a very high level of symmetry within the brain parenchyma and low values within the lateral ventricles, as expected [m/s]. Data from Heidelberg University Hospital, Germany.

directions (Fig. 11A). The corresponding Z-component of the curl field shows that the shear waves are propagating in a rather complex manner through the brain (Fig. 11B). The resulting shear wave speed image (Fig. 11C) depicts a high level of symmetry, as expected, from a healthy volunteer's brain. The subcortical white matter exhibits higher values of shear wave speed than cortical grey matter. Shear wave speed drops within the ventricles since cerebrospinal fluid cannot be sheared and hence exhibits very low values. The non-invasive evaluation of cerebral biomechanics is of high interest and has the potential to improve diagnosis and monitoring of various brain diseases. An obvious application is neuro-oncology as information on stiffness could not only guide the surgical approach, but also help to characterize the tumor in more depth [8]. To this end, initial clinical studies demonstrated an association between glioma stiffness and genetic features that are prognostically relevant [44, 45]. Further areas of interest include neurodegeneration, dementias, and neuroinflammation [46, 47].

Conclusions

The gravitational transducer concept, combined with advanced and fast MRI sequences and robust inversion algorithms, enables non-invasive, high-quality, and versatile assessment of biomechanics, leading to better diagnosis and staging of several clinical conditions, in particular liver fibrosis and inflammation in MASLD.

References

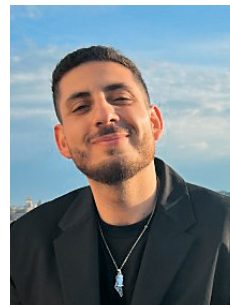
- Ophir J, Céspedes I, Ponnekanti H, Yazdi Y, Li X. Elastography: a quantitative method for imaging the elasticity of biological tissues. *Ultrason Imaging*. 1991;13(2):111–134.
- Lewa GJ. Elastic properties imaging by periodical displacement NMR measurements (EPMRI). *Proceedings of the Ultrasonics Symposium IEEE*, 1994;2:691–694.
- Muthupillai R, Lomas DJ, Rossman PJ, Greenleaf JF, Manduca A, Ehman RL. Magnetic resonance elastography by direct visualization of propagating acoustic strain waves. *Science*. 1995;269(5232):1854–1857.
- Sinkus R, Lorenzen J, Schrader D, Lorenzen M, Dargatz M, Holz D. High-resolution tensor MR elastography for breast tumour detection. *Phys Med Biol*. 2000;45(6):1649–1664.
- Allen AM, Shah VH, Therneau TM, Venkatesh SK, Mounajjed T, Larson JJ, et al. The Role of Three-Dimensional Magnetic Resonance Elastography in the Diagnosis of Nonalcoholic Steatohepatitis in Obese Patients Undergoing Bariatric Surgery. *Hepatology*. 2020;71(2):510–521.
- Sinkus R, Lambert S, Abd-Elmoniem KZ, Morse C, Heller T, Guenther C, et al. Rheological determinants for simultaneous staging of hepatic fibrosis and inflammation in patients with chronic liver disease. *NMR Biomed*. 2018;31(10):e3956.
- McKnight AL, Kugel JL, Rossman PJ, Manduca A, Hartmann LC, Ehman RL. MR elastography of breast cancer: preliminary results. *AJR Am J Roentgenol*. 2002;178(6):1411–1417.
- Bunevicius A, Schregel K, Sinkus R, Golby A, Patz S. REVIEW: MR elastography of brain tumors. *Neuroimage Clin*. 2020;25:102109.
- Fløgstad Svensson S, Fuster-Garcia E, Latysheva A, Fraser-Green J, Nordhøy W, Isam Darwish O, et al. Decreased tissue stiffness in glioblastoma by MR elastography is associated with increased cerebral blood flow. *Eur J Radiol*. 2022;147:110136.
- Glaser KJ, Manduca A, Ehman RL. Review of MR elastography applications and recent developments. *J Magn Reson Imaging*. 2012;36(4):757–774.
- Rump J, Klatt D, Braun J, Warmuth C, Sack I. Fractional encoding of harmonic motions in MR elastography. *Magn Reson Med*. 2007 Feb;57(2):388–395.
- Guenther C, Sethi S, Troelstra M, Dokumaci AS, Sinkus R, Kozerke S. Ristretto MRE: A generalized multi-shot GRE-MRE sequence. *NMR Biomed*. 2019 May;32(5):e4049.
- Muthupillai R, Rossman PJ, Lomas DJ, Greenleaf JF, Riederer SJ, Ehman RL. Magnetic resonance imaging of transverse acoustic strain waves. *Magn Reson Med*. 1996 Aug;36(2):266–274.
- Bercoff J, Tanter M, Fink M. Supersonic shear imaging: a new technique for soft tissue elasticity mapping. *IEEE Trans Ultrason Ferroelectr Freq Control*. 2004;51(4):396–409.
- Kruse SA, Smith JA, Lawrence AJ, Dresner MA, Manduca A, Greenleaf JF, et al. Tissue characterization using magnetic resonance elastography: preliminary results. *Phys Med Biol*. 2000;45(6):1579–1590.
- Van Houten EE, Paulsen KD, Miga MI, Kennedy FE, Weaver JB. An overlapping subzone technique for MR-based elastic property reconstruction. *Magn Reson Med*. 1999 Oct;42(4):779–786.
- Sinkus R, Siegmann K, Xydeas T, Tanter M, Claussen C, Fink M. MR elastography of breast lesions: understanding the solid/liquid duality can improve the specificity of contrast-enhanced MR mammography. *Magn Reson Med*. 2007;58(6):1135–1144.
- Manduca A, Lake DS, Kruse SA, Ehman RL. Spatio-temporal directional filtering for improved inversion of MR elastography images. *Med Image Anal*. 2003;7(4):465–473.
- Uffmann K, Ladd M. Actuation systems for MR elastography: design and applications. *IEEE Eng Med Biol Mag*. 2008;27(3):28–34.
- Van Houten EE, Doyley MM, Kennedy FE, Weaver JB, Paulsen KD. Initial in vivo experience with steady-state subzone-based MR elastography of the human breast. *J Magn Reson Imaging*. 2003;17(1):72–85.
- Yin M, Talwalkar JA, Glaser KJ, Manduca A, Grimm RC, Rossman PJ, et al. Assessment of hepatic fibrosis with magnetic resonance elastography. *Clin Gastroenterol Hepatol*. 2007;5(10):1207–1213.e2.
- Dittmann F, Tzschätzsch H, Hirsch S, Barnhill E, Braun J, Sack I, et al. Tomoelastography of the abdomen: Tissue mechanical properties of the liver, spleen, kidney, and pancreas from single MR elastography scans at different hydration states. *Magn Reson Med*. 2017;78(3):976–983.
- Runge JH, Hoelzl SH, Sudakova J, Dokumaci AS, Nelissen JL, Guenther C, et al. A novel magnetic resonance elastography transducer concept based on a rotational eccentric mass: preliminary experiences with the gravitational transducer. *Phys Med Biol*. 2019;64(4):045007.

- 24 Fovargue D, Kozerke S, Sinkus R, Nordsletten D. Robust MR elastography stiffness quantification using a localized divergence free finite element reconstruction. *Med Image Anal.* 2018;44:126–142.
- 25 Wochner P, Schneider T, Stockmann J, Lee J, Sinkus R. Diffusion phase-imaging in anisotropic media using non-linear gradients for diffusion encoding. *PLoS One.* 2023;18(3):e0281332.
- 26 Venkatesh SK, Yin M, Ehman RL. Magnetic resonance elastography of liver: technique, analysis, and clinical applications. *J Magn Reson Imaging.* 2013;37(3):544–555.
- 27 Guenther C, Runge JH, Sinkus R, Kozerke S. Hadamard encoding for magnetic resonance elastography. In: *Proceedings of the 25th Annual Meeting ISMRM.* 2017. Honolulu.
- 28 Garteiser P, Sahebjavaher RS, Ter Beek LC, Salcudean S, Vilgrain V, Van Beers BE, et al. Rapid acquisition of multifrequency, multislice and multidirectional MR elastography data with a fractionally encoded gradient echo sequence. *NMR Biomed.* 2013;26(10):1326–1335.
- 29 Barth M, Breuer F, Koopmans PJ, Norris DG, Poser BA. Simultaneous multislice (SMS) imaging techniques. *Magn Reson Med.* 2016;75(1):63–81.
- 30 Darwish OI, Gharib AM, Jeljeli S, Metwalli NS, Feeley J, Rotman Y, et al. Single Breath-Hold 3-Dimensional Magnetic Resonance Elastography Depicts Liver Fibrosis and Inflammation in Obese Patients. *Invest Radiol.* 2023;58(6):413–419.
- 31 Johnson CL, McGarry MD, Van Houten EE, Weaver JB, Paulsen KD, Sutton BP, et al. Magnetic resonance elastography of the brain using multishot spiral readouts with self-navigated motion correction. *Magn Reson Med.* 2013;70(2):404–412.
- 32 Einstein A, Podolsky B, Rosen N. Can Quantum-Mechanical Description of Physical Reality Be Considered Complete? *Phys Rev.* 1935;47(10):777–780.
- 33 Landau LD, Lifshitz EM. *Course of Theoretical Physics: Theory of Elasticity.* 2nd English ed. Oxford: Pergamon Press; 1970. p. 165.
- 34 Bhatia H, Norgard G, Pascucci V, Bremer P T. The Helmholtz-Hodge Decomposition – A Survey. *IEEE Transactions on Visualization and Computer Graphics.* 2013;19(8):1386–1404.
- 35 Van Houten EE, Miga MI, Weaver JB, Kennedy FE, Paulsen KD. Three-dimensional subzone-based reconstruction algorithm for MR elastography. *Magn Reson Med.* 2001;45(5):827–837.
- 36 Verdier C. Rheological Properties of Living Materials. From Cells to Tissues. *Journal of Theoretical Medicine.* 2003;5(2):67–91.
- 37 Schiessel H, Blumen A. Mesoscopic Pictures of the Sol-Gel Transition: Ladder Models and Fractal Networks. *Macromolecules.* 1995;28(11):4013–4019.
- 38 Holm S. *Waves with Power-Law Attenuation.* New York: Springer; 2019.
- 39 Lambert SA, Näsholm SP, Nordsletten D, Michler C, Juge L, Serfaty JM, et al. Bridging Three Orders of Magnitude: Multiple Scattered Waves Sense Fractal Microscopic Structures via Dispersion. *Phys Rev Lett.* 2015;115(9):094301.
- 40 Gidener T, Ahmed OT, Larson JJ, Mara KC, Therneau TM, Venkatesh SK, et al. Liver Stiffness by Magnetic Resonance Elastography Predicts Future Cirrhosis, Decompensation, and Death in NAFLD. *Clin Gastroenterol Hepatol.* 2021;19(9):1915–1924.e6.
- 41 Sheka AC, Adeyi O, Thompson J, Hameed B, Crawford PA, Ikramuddin S. Nonalcoholic Steatohepatitis: A Review. *JAMA.* 2020;323(12):1175–1183.
- 42 Rada P, González-Rodríguez Á, García-Monzón C, Valverde ÁM. Understanding lipotoxicity in NAFLD pathogenesis: is CD36 a key driver? *Cell Death Dis.* 2020;11(9):802.
- 43 Loomba R, Adams LA. The 20% Rule of NASH Progression: The Natural History of Advanced Fibrosis and Cirrhosis Caused by NASH. *Hepatology.* 2019;70(6):1885–1888.
- 44 Pepin KM, McGee KP, Arani A, Lake DS, Glaser KJ, Manduca A, et al. MR Elastography Analysis of Glioma Stiffness and IDH1-Mutation Status. *AJNR Am J Neuroradiol.* 2018;39(1):31–36.
- 45 Svensson SF, Halldórsson S, Latysheva A, Fuster-Garcia E, Hjørnevik T, Fraser-Green J, et al. MR elastography identifies regions of extracellular matrix reorganization associated with shorter survival in glioblastoma patients. *Neurooncol Adv.* 2023;5(1):vda021.
- 46 Hiscov LV, Schwarb H, McGarry MDJ, Johnson CL. Aging brain mechanics: Progress and promise of magnetic resonance elastography. *Neuroimage.* 2021;232:117889.
- 47 Wuerfel J, Paul F, Beierbach B, Hamhaber U, Klatt D, Papazoglou S, et al. MR-elastography reveals degradation of tissue integrity in multiple sclerosis. *Neuroimage.* 2010;49(3):2520–2525.
- 48 Bohte AE, Nelissen JL, Runge JH, Holub O, Lambert SA, de Graaf L, et al. Breast magnetic resonance elastography: a review of clinical work and future perspectives. *NMR Biomed.* 2018;31(10):e3932.
- 49 Jurrius P, Darwish O, Shifa B, Bell J, Spence J, Fovargue D, et al. Measuring the tumour IFP using MRE: a mechanical biomarker for the prediction of metastatic potential in women with invasive breast cancer. Abstract #1436 in: *Proceedings of the 30th Annual Meeting ISMRM.* 2021.
- 50 Jurrius P, Darwish O, Fovargue D, Shifa B, Welsh K, Bell J, et al. Magnetic Resonance Elastography for Early Assessment of Response to Neoadjuvant Chemotherapy in Women with Breast Cancer. Abstract #1591 in: *Proceedings of the 31st Annual Meeting ISMRM.* 2022.

Contact



Ralph Sinkus, Ph.D.
Professor of Biomedical Engineering
at King's College London, UK,
and Research Director CNRS
at INSERM, Paris, France
King's College London
School of Biomedical Engineering &
Imaging Sciences
Rayne Institute, 4th Floor, Lambeth Wing
St. Thomas' Hospital
Westminster Bridge Road
London SE1 7EH, United Kingdom
ralph.sinkus@kcl.ac.uk



Omar Darwish
Siemens Healthineers
SHS DI MR RCT CLS BODY
Allee am Roethelheimpark 2
91052 Erlangen
Germany
omar.darwish@siemens-healthineers.com

Expert Insights: Hidden Gems from Application Specialists at Siemens Healthineers

Khaled Khames on the Trigger Delay parameter

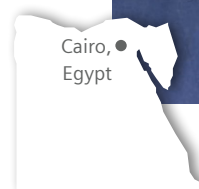
Khaled Khames

Khaled Khames is a physicist in Cairo, Egypt. He is passionate about training clinical staff on new MR technologies to help build MR expertise and practices that achieve the best outcomes for patients and optimal performance for healthcare providers.

Khaled enrolled in a Bachelor of Science in 2006, at the Department of Physics at Ain Shams University in Cairo. He went on to work as a physicist in a diagnostic nuclear medicine unit. When he discovered MRI, however, he was fascinated by the evolving technology and the challenges it solved, all of which inspired him to embark on a career in the MR field.

This path eventually led him to Siemens Healthineers, where he became Senior Application Specialist for Egypt, Sudan, Libya, Eritrea, and Djibouti in 2015. He is also an instructor at the Siemens Healthineers Academy in Egypt, where he teaches basic and advanced MR courses for physicians and technologists.

Khaled received the Learn Passionately Award 2023 at the Egypt Mid-Year townhall meeting. Outside of work, he loves spending time with his three daughters and going fishing.



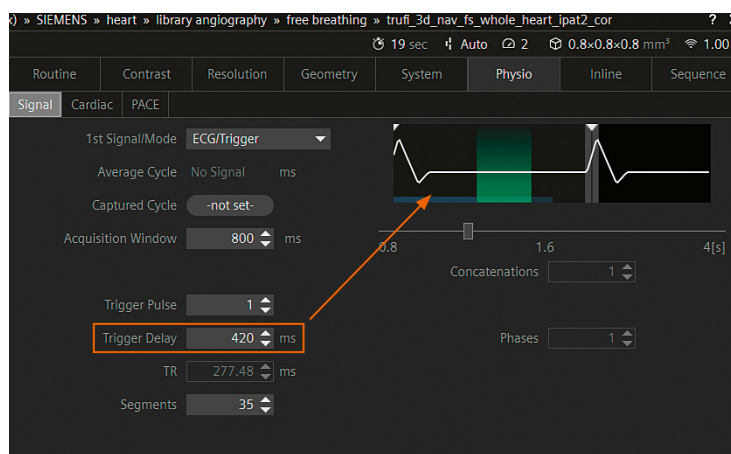
Contact

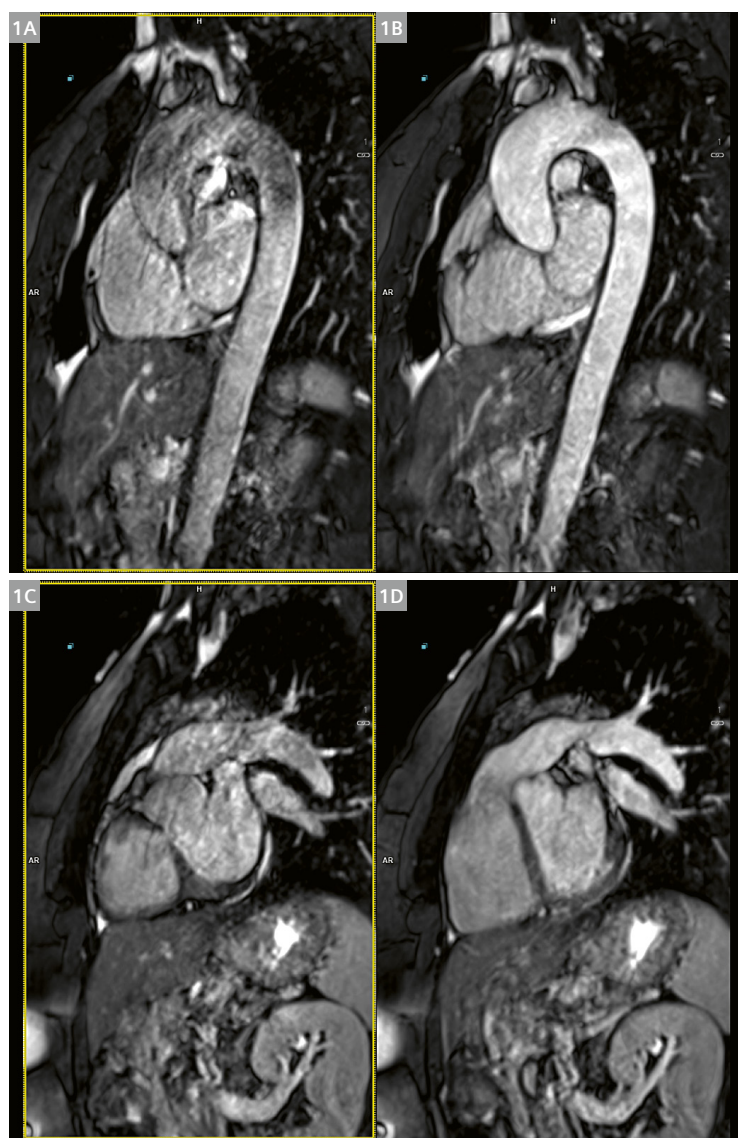
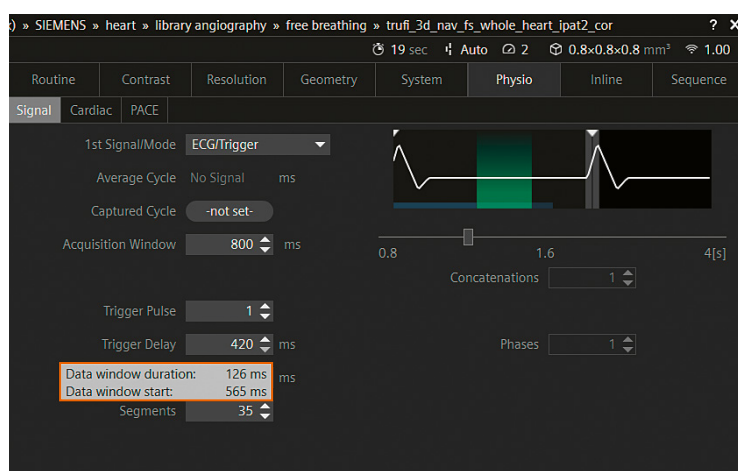
Khaled Khames
Siemens Healthcare S.A.E.
SHS EMEA MESA EGY CS 1
Etisalat Club Rd
11435 al-Qahirah
Postbox 17631 Maadi
Cairo
Egypt
khaled.khames@siemens-healthineers.com

My favorite feature ...

... is the Trigger Delay parameter, to achieve motion artifact free images in the heart region. You can use it to optimize image quality in noncontrast-enhanced MR angiography when using a triggered 3D TrueFISP or FLASH sequence – to image the whole heart, coronaries, or the aorta.

The Trigger Delay should be set in such a way, that the region of interest is in a quiet phase, i.e., not much heart motion or flow happening during data acquisition.





1 Noncontrast triggered 3D TrueFISP
(1A) Suboptimal Trigger Delay time, **(1B)** Appropriate Trigger Delay time,
(1C) Suboptimal Trigger Delay time, **(1D)** Appropriate Trigger Delay time

This quiet phase can be identified by a visual assessment of cine or flow images from the corresponding region. Scroll through the cine images and identify the quiet phase, ideally with starting and end point and the length in ms. The TT (Trigger Time) can be found in the image text on the left side.

With this knowledge you can now individually optimize the parametrization of the 3D sequence to the patients' condition on the parameter card Physio/Signal.

Before you start editing, hover with the mouse cursor over the Trigger Delay parameter to visualize the information of the Data window start and the Data window duration.

Adapting the Trigger Delay shifts your Data window start. (Cave: Additional Prep Pulses are added to the Trigger Delay for the Data window start point, such that the shown Trigger Delay in the user interface (UI) is not corresponding to the Data window start).

Adapting the number of segments modifies the Data window length. Modifying the number of segments has an impact on the Data window duration and the total acquisition time.

Number of segments ↑
 Data window duration ↑
 Total acquisition Time ↓

Number of segments ↓
 Data window duration ↓
 Total acquisition Time ↑

It is recommended to use a Data Window duration between 100 and 180 ms to keep motion and flow artifacts minimal.

Cave: Use a consistent trigger source. If you use e.g., Beat Sensor for cine imaging, make sure to use Beat Sensor for 3D imaging, too.

Acknowledgments

I would like to acknowledge the fruitful conversations with Manuela Rick, Senior Applications Developer, Erlangen, Germany.

3D Whole-Heart Imaging: An Innovative Collaborative Solution

Karl P. Kunze^{1,2}, Jens Wetzl³, Seung Su Yoon³, Radhouene Neji², Gaia Banks³, Rene Botnar^{2,4,5}, Claudia Prieto^{2,4}, Michaela Schmidt³

¹MR Research Collaborations, Siemens Healthcare Limited, Camberley, United Kingdom

²School of Biomedical Engineering and Imaging Sciences, King's College London, United Kingdom

³Cardiovascular MR Predevelopment, Siemens Healthineers, Erlangen, Germany

⁴Escuela de Ingeniería, Pontificia Universidad Católica de Chile, Santiago, Chile

⁵Institute for Biological and Medical Engineering, Pontificia Universidad Católica de Chile, Santiago, Chile

Clinical need

A broad spectrum of clinical use cases for cardiovascular magnetic resonance imaging (CMR) profit from high isotropic resolution in three dimensions to show thoracic vasculature including the small and tortuous coronary artery vessels and fibrosis/myocardial viability using the late gadolinium enhancement (LGE) measurement technique. Recent clinical studies have demonstrated the value of free-breathing, high-isotropic-resolution CMR to diagnose ischemic heart disease using coronary artery and vein [1, 2] or LGE imaging [3], cardiomyopathy [4], congenital [5] and structural [6] heart disease, and ablation lesion assessment [7].

Challenges

One challenge of using a high isotropic resolution in the range of 1 mm³ to 1.3 mm³ in the context of CMR exams is the prolonged scan time when compared to other imaging methods. Although CMR has several benefits including high tissue contrast and no need for radiation, it remains a comparatively slow imaging modality. For whole-heart coverage with high isotropic resolution, a novel imaging strategy is required to complete scans in 5 to 10 minutes.

Ideally, these measurements should be acquired in free breathing. Hence, cardiac and respiratory motion must be addressed. To minimize cardiac motion, scanning should be performed during a time in the cardiac cycle when the heart is in its quiescent phase, usually at end-diastole with a window of 80–160 ms, depending on the heart rate. To find the still phase of the heart, a 4-chamber cine is usually acquired. An experienced operator needs to manually define it and then enter it correctly in the 3D measurement protocol.

To account for respiratory motion, navigators are typically used to scan during free breathing. The frequently used 1D cross-paired diaphragm navigators are manually placed on the liver dome, and imaging data are accepted only in end-expiration. Depending on the breathing pattern, the acceptance rate can be between 20% and 60%. Therefore, scan time is unpredictable upfront, and a drift in breathing pattern during the scan may further decrease acquisition efficiency.

Moreover, accepting data only in end-diastole and in end-expiration makes data sampling very inefficient. Long scan times result in high institutional costs and are a discomfort for sick patients, meaning they can result in patient movement (reduced patient compliance) and non-diagnostic images.

One method to overcome this hurdle is the “free-running” acquisition approach, which samples and uses all data irrespective of the breathing and cardiac-motion states, with separation of these during image reconstruction [8, 9]. While this single-click method has numerous benefits that have been shown in multiple publications, it has not yet been widely distributed and tested clinically because it requires high-end computing, long reconstruction times, and often the use of contrast agent.

Another way to account for respiratory motion is to use image-based navigators [10] combined with non-rigid motion-compensated reconstruction. This enables predictable scan times and an acceptance rate of 100% of data irrespective of the breathing position. When combined with novel undersampling strategies [11, 12], a scan time of 5 to 8 minutes is possible, while the reconstruction only needs to address respiratory-motion compensation and *k*-space undersampling.

3D Whole Heart is work in progress. The application is still under development and not commercially available. Its future availability cannot be ensured.

A third challenge for 3D imaging is the workflow, including positioning of multiple objects like navigators, saturation bands, and imaging volume, and determining the appropriate resting phase in the cardiac cycle as mentioned above. For the LGE measurements, correctly estimating inversion time (TI) to null healthy myocardium is yet another task for operators.

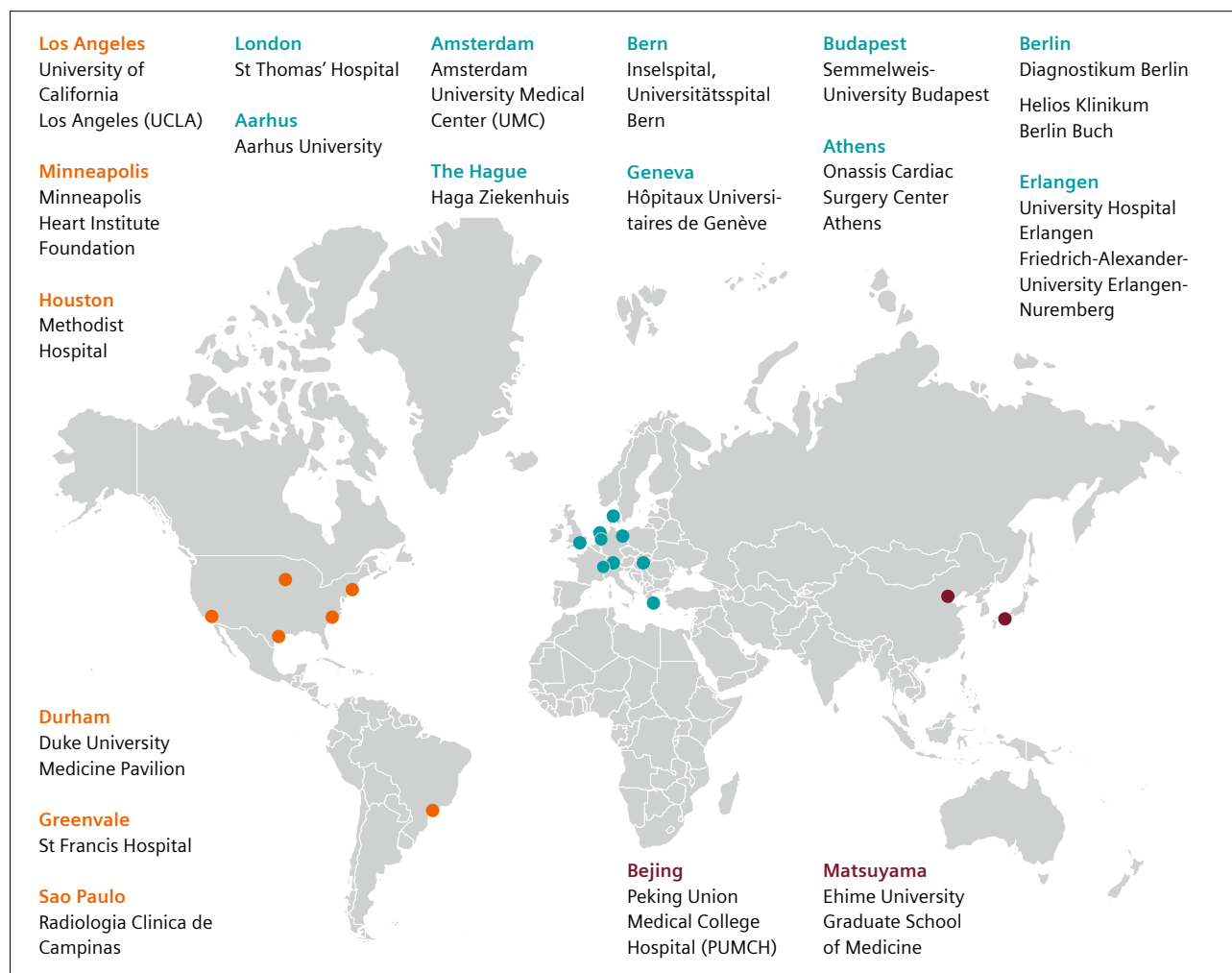
Finally, robust fat saturation is key for high-contrast display of the coronary arteries, as they are embedded in epicardial fat. For certain LGE applications, the separation of fat and water is also essential, e.g., in patients with pericarditis or small endomyocardial fibrosis, where it can be difficult to distinguish between fat and lesion.

The solution

To overcome the limitations of 1D diaphragmatic navigators, 2D image navigators (iNAV) have been proposed to

enable direct tracking of the impact of respiratory motion on the heart [9]. With iNAV imaging, it is possible to derive accurate quantitative motion information in two spatial dimensions. This enables retrospective motion correction rather than prospective gating, resulting in 100% respiratory scan efficiency and predictable scan times.

While iNAV imaging allows for direct correction of beat-to-beat translational respiratory motion in a predefined image region, accounting for non-rigid motion during the breathing cycle requires a more complex, non-rigid motion-compensated reconstruction framework. A first step in such approaches is often data binning, followed by reconstruction of different bin images representing the different respiratory motion states present in the data. As each bin image only contains a small fraction of the already undersampled 3D acquisition, reconstruction of the individual bin images requires a well-designed interplay of acquisition patterns and reconstruction algorithms.



1 Clinical partners for validating the 3D Whole-Heart application

Our clinical partners helped us by sharing their experience so we could improve the research sequence and make it robust for a wide range of clinical questions and settings.

The variable-density Cartesian trajectory with spiral profile order sampling (VD-CASPR) [11, 12] provides high overall undersampling factors while maintaining favorable undersampling properties when data is split up into respiratory bins, enabling regularized reconstruction of artifact-free respiratory bin images [13]. These bin images can then be used to estimate 3D non-rigid motion between the motion states they represent, and motion information can be used in a final, non-rigid motion-compensated reconstruction of all data [14, 15]. Despite the large number of steps involved, the computational burden in the form of reconstruction time can be minimized to orders of 1 to 2 minutes using implementations with modern GPU technology [16].

In addition to standard chemical shift-based fat saturation methods, the described approach can be combined with Dixon-based fat-water separation. This provides a means to achieve robust elimination of fat from the final water-only image [17, 18], while also providing a fat-only image that can enable, e.g., discrimination between bright myocardial scar signal and fatty infiltration (Figure 2). Dixon fat-water separation enables improved visualisation of the coronary arteries [18], especially at 3T.

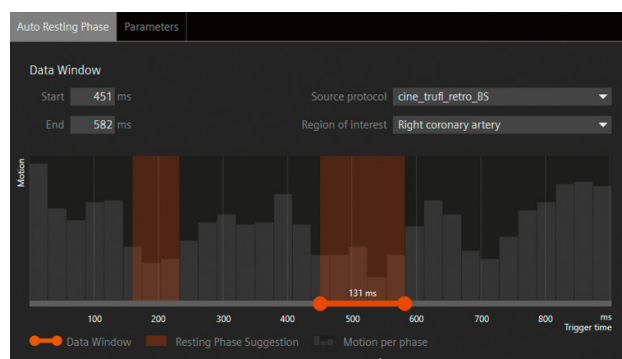
Workflow automation

As previously described, whole-heart imaging has typically increased the workload and requires more experienced operators given the need for precise positioning of saturation bands, image navigator, resting phase, and potentially TI. Together with the novel whole-heart sequence, we now offer workflow support for many of the planning steps that previously required manual user input.

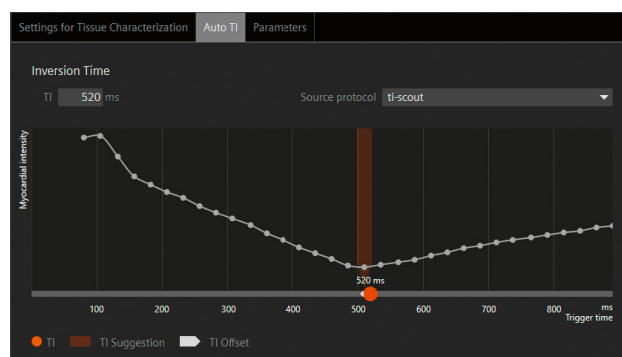
In the following, we describe three modules for automating common planning tasks: **AutoPositioning** (for placement of graphical objects, e.g., the imaging volume, navigator, saturation bands) [19]; **AutoRestingPhase** (to determine a suitable acquisition window during the quiescent period in the cardiac cycle) [20]; and **AutoTI** (to set the proper inversion time for subsequent LGE imaging) [21].

AutoPositioning is based on localizer scans in coronal and transversal orientations. It uses deep learning to detect multiple anatomical structures, including the location and size of the heart and left ventricle, as well as the location of the liver dome and the arms. These are used to automatically perform the subsequent planning steps. Based on an initial localizer, the heart is placed into the isocenter, and further localizers centered on the heart can be acquired. Slices for thorax overview imaging and the AutoAlign scout can be positioned. For the whole-heart sequence, the imaging volume including slice coverage and position of the image navigator and saturation bands can be set automatically.

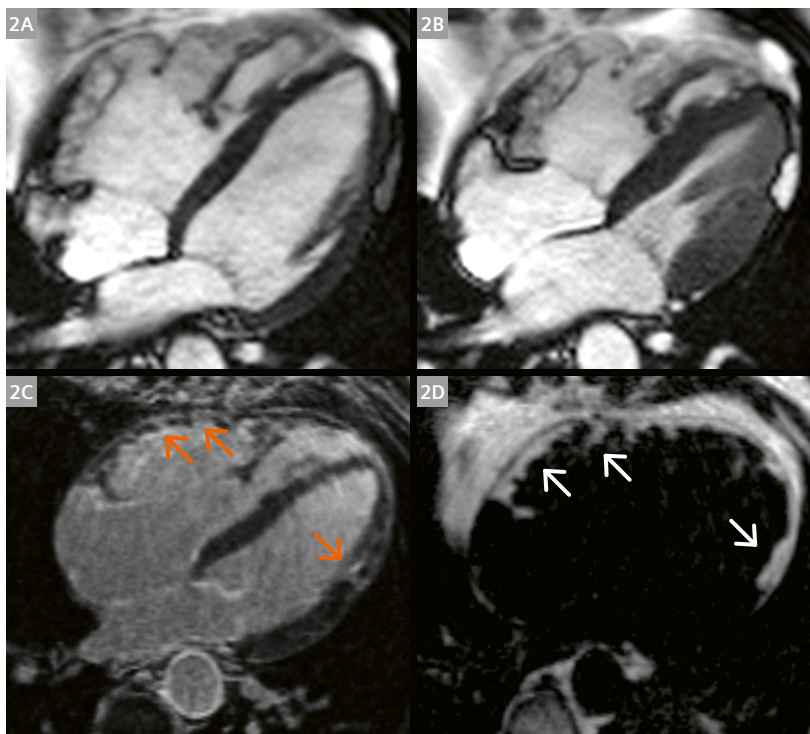
AutoRestingPhase is based on a 4-chamber-view cine to determine the quiescent phases of different cardiac structures within the cardiac cycle. First, the right coronary artery (RCA) and the four chambers of the heart are automatically detected. Subsequently, their motion throughout the cardiac cycle is tracked via image registration and then quantified and displayed as a motion curve. The valleys in this motion curve serve as suggestions for the whole-heart acquisition window. Different types of whole-heart acquisition can use the resting phase results of different anatomies of interest, e.g., the RCA for T2-prepared angiography or the left ventricle for 3D LGE.



AutoTI is based on a TI scout in short-axis orientation, which is segmented to find the myocardial and blood-pool intensity values at each inversion time. The minimum of the myocardial intensity curve is first used to determine a TI with optimal myocardial nulling, then refined by finding an adjacent TI time with improved blood-myocardium contrast in case both have their zero crossings at similar times. An offset can then be applied automatically to subsequent LGE acquisitions to account for the time between TI scout and LGE acquisitions. This is applicable both to conventional 2D LGE and the novel 3D LGE acquisition.



The combination of these modules significantly reduces the complexity and workload involved in performing high-quality whole-heart acquisitions, and simplifies or even improves the entire scan workflow.

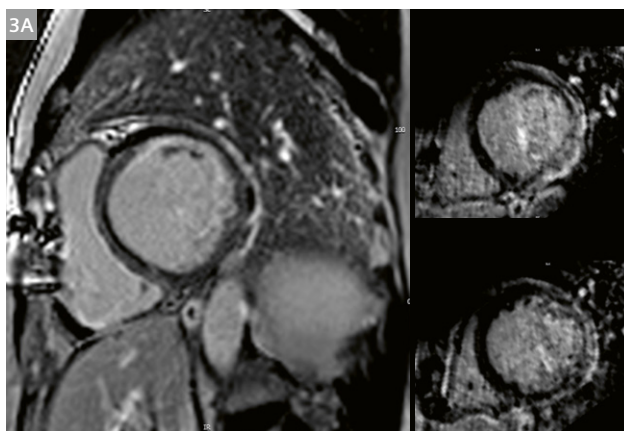


- 2** A 60-year-old male patient with fibrofatty replacement in LGE of the free wall of the RV and LV. Cine imaging 4-chamber view in a diastolic phase (2A) and systolic phase (2B). The 3D whole-heart technique allows a differentiation between fibrosis (2C) in water-only LGE images and fat deposits (2D) in fat-only images. Fat deposition is depicted by the white arrows. Fibrosis is depicted by the orange arrows.

CMR imaging was performed on a 1.5 Tesla scanner (MAGNETOM Avanto fit, Siemens Healthcare, Erlangen, Germany) using cine imaging steady-state free precession (SSFP). After application of gadolinium-based contrast media (gadoteridol 0.2 mmol/kg), image-based navigated 3D whole-heart LGE sequence with fat–water separation was performed.

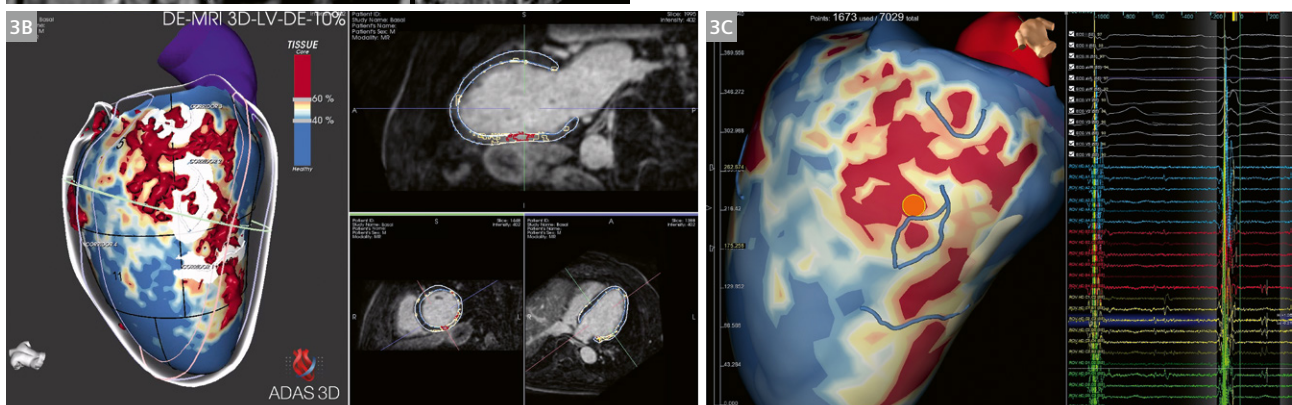
Images courtesy of Edyta Blaszczyk, MD^{1,2,3}, and Jeanette Schulz-Menger, MD^{1,2,3,4}.

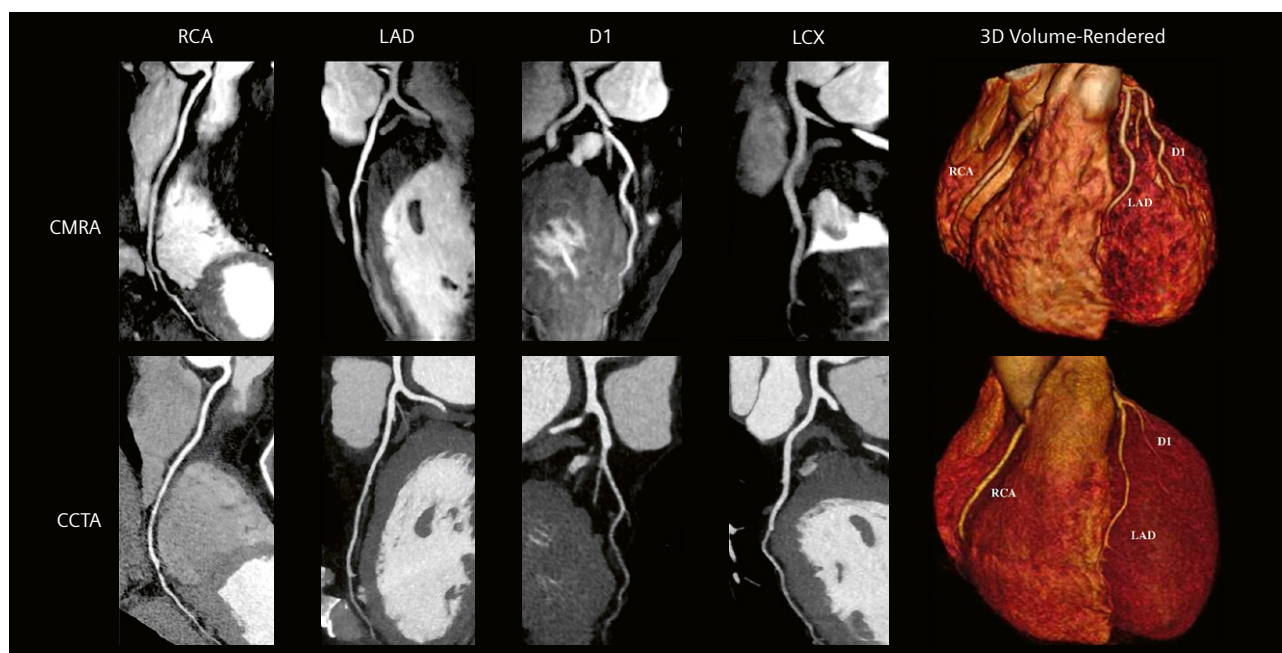
¹Charité – Universitätsmedizin Berlin, corporate member of Freie Universität Berlin and Humboldt-Universität zu Berlin, ECRC Experimental and Clinical Research Center, Berlin, Germany. ²Working Group on Cardiovascular Magnetic Resonance, Experimental and Clinical Research Center, a joint cooperation between Charité Medical Faculty and the Max-Delbrück Center for Molecular Medicine. ³DZHK (German Centre for Cardiovascular Research), partner site Berlin, Germany. ⁴HELIOS Hospital Berlin-Buch, Department of Cardiology and Nephrology, Berlin, Germany.



- 3** 53-year-old male patient. (3A) Sustained VTs, MVR (MVP), DCM like phenotype of HF. (3B) Identify potential ablation targets from 3D corridors of border zone tissue and verify the detected corridors directly with the DICOM images. (3C) Import pre-procedural imaging into any electroanatomic mapping (EAM) system. Agreement of the structural arrhythmogenic substrate detected as corridors by CMR 3D LGE and the sites of electrical channels that may serve as the isthmus of VT. Late potentials and local abnormal ventricular activities at the areas of structural VT corridors. CMR imaging was performed on a 1.5 Tesla MAGNETOM Sola (Siemens Healthcare, Erlangen, Germany).

Images courtesy of Evangelia Nyktari, M.D. (CMR); Athanasios Saplaouras, M.D. (EP lab); Konstantinos Letsas, M.D., Ph.D. (EP lab); Michalis Efremidis, M.D., Ph.D. (EP Lab); P Rozos and S Zarkadoulas (CMR) at Onassis Cardiac Surgery Center, Athens, Greece.





4 Curved multiplanar reformat and 3D volume-rendered non-contrast CMRA and contrast-enhanced CCTA in a 54-year-old male with no significant stenosis.

Abbreviations: CMRA = coronary magnetic resonance angiography; CCTA = coronary computed tomography angiography; RCA = right coronary artery; LAD = left anterior descending artery; D1 = first diagonal artery; LCX = left circumflex artery.

CMR imaging was performed on a 1.5 Tesla MAGNETOM Aera (Siemens Healthcare, Erlangen, Germany).

Images courtesy of Reza Hajhosseiny, M.D.¹; Aurélien Bustin, Ph.D.¹; Imran Rashid, M.D., Ph.D., FRACP¹; Gastao Cruz, Ph.D.¹; Ronak Rajani, M.D., Ph.D., FACC, FRCP²; Claudia Prieto, Ph.D.¹; René M. Botnar, Ph.D.¹; et al.

Adapted and reproduced from Hajhosseiny et al. [22].

¹School of Biomedical Engineering and Imaging Sciences, King's College London, United Kingdom

²School of Cardiovascular Medicine and Sciences, King's College London, United Kingdom

Technical partner for developing the 3D Whole-Heart application

The whole-heart imaging sequence, image navigator, and image reconstruction framework described here were developed in close collaboration with the research groups of Professor René Botnar and Professor Claudia Prieto at King's College London, UK.

Conclusion and outlook

Clinical validation, resp. research studies, and feedback from numerous global sites indicate that implementing the novel 3D Whole-Heart sequence from Siemens Healthineers makes scans with whole-heart coverage and high isotropic resolution routinely possible in 5 to 10 minutes. Given the high level of automation available to support operators and achieve faster scan times, we expect rapid clinical adoption.

References

- Hajhosseiny R, Rashid I, Bustin A, Munoz C, Cruz G, Nazir MS, et al. Clinical comparison of sub-mm high-resolution non-contrast coronary CMR angiography against coronary CT angiography in patients with low-intermediate risk of coronary artery disease: a single center trial. *J Cardiovasc Magn Reson.* 2021;23(1):57.
- Nazir MS, Bustin A, Hajhosseiny R, Yazdani M, Ryan M, Vergani V, et al. High-resolution non-contrast free-breathing coronary cardiovascular magnetic resonance angiography for detection of coronary artery disease: validation against invasive coronary angiography. *J Cardiovasc Magn Reson.* 2022;24(1):26.
- Peters AA, Wagner B, Spano G, Haupt F, Ebner L, Kunze KP, et al. Myocardial scar detection in free-breathing Dixon-based fat- and water-separated 3D inversion recovery late-gadolinium enhancement whole heart MRI. *Int J Cardiovasc Imaging.* 2023;39(1):135-144.
- Bustin A, Hua A, Milotta G, Jaubert O, Hajhosseiny R, Ismail TF, et al. High-Spatial-Resolution 3D Whole-Heart MRI T2 Mapping for Assessment of Myocarditis. *Radiology.* 2021;298(3):578-586.
- Fotaki A, Pushparajah K, Hajhosseiny R, Schneider A, Alam H, Ferreira J, et al. Free-breathing, Contrast Agent-free Whole-Heart MTC-BOOST Imaging: Single-Center Validation Study in Adult Congenital Heart Disease. *Radiol Cardiothorac Imaging.* 2023;5(1):e220146.

- 6 Toupin S, Pezel T, Bustin A, Cochet H. Whole-Heart High-Resolution Late Gadolinium Enhancement: Techniques and Clinical Applications. *J Magn Reson Imaging*. 2022;55(4):967-987.
- 7 Sim I, Razeghi O, Karim R, Chubb H, Whitaker J, O'Neill L, et al. Reproducibility of Atrial Fibrosis Assessment Using CMR Imaging and an Open Source Platform. *JACC Cardiovasc Imaging*. 2019;12(10):2076-2077.
- 8 Di Sopra L, Piccini D, Coppo S, Stuber M, Yerly J. An automated approach to fully self-gated free-running cardiac and respiratory motion-resolved 5D whole-heart MRI. *Magn Reson Med*. 2019;82(6):2118-2132.
- 9 Roy CW, Di Sopra L, Whitehead KK, Piccini D, Yerly J, Heerfordt J, et al. Free-running cardiac and respiratory motion-resolved 5D whole-heart coronary cardiovascular magnetic resonance angiography in pediatric cardiac patients using ferumoxytol. *J Cardiovasc Magn Reson*. 2022;24(1):39.
- 10 Henningsson M, Koken P, Stehning C, Razavi R, Prieto C, Botnar RM. Whole-heart coronary MR angiography with 2D self-navigated image reconstruction. *Magn Reson Med*. 2012;67(2):437-445.
- 11 Prieto C, Doneva M, Usman M, Henningsson M, Greil G, Schaeffter T, et al. Highly efficient respiratory motion compensated free-breathing coronary MRA using golden-step Cartesian acquisition. *J Magn Reson Imaging*. 2015;41(3):738-746.
- 12 Bustin A, Rashid I, Cruz G, Hajhosseiny R, Correia T, Neji R, et al. 3D whole-heart isotropic sub-millimeter resolution coronary magnetic resonance angiography with non-rigid motion-compensated PROST. *J Cardiovasc Magn Reson*. 2020;22(1):24.
- 13 Correia T, Ginami G, Cruz G, Neji R, Rashid I, Botnar RM, et al. Optimized respiratory-resolved motion-compensated 3D Cartesian coronary MR angiography. *Magn Reson Med*. 2018;80(6):2618-2629.
- 14 Batchelor PG, Atkinson D, Irrarrazaval P, Hill DL, Hajnal J, Larkman D. Matrix description of general motion correction applied to multishot images. *Magn Reson Med*. 2005;54(5):1273-1280.
- 15 Cruz G, Atkinson D, Henningsson M, Botnar RM, Prieto C. Highly efficient nonrigid motion-corrected 3D whole-heart coronary vessel wall imaging. *Magn Reson Med*. 2017;77(5):1894-1908.
- 16 Zeilinger MG, Kunze KP, Munoz C, Neji R, Schmidt M, Croisille P, et al. Non-rigid motion-corrected free-breathing 3D myocardial Dixon LGE imaging in a clinical setting. *Eur Radiol*. 2022;32(7):4340-4351.
- 17 Munoz C, Cruz G, Neji R, Botnar RM, Prieto C. Motion corrected water/fat whole-heart coronary MR angiography with 100% respiratory efficiency. *Magn Reson Med*. 2019;82(2):732-742.
- 18 Munoz C, Bustin A, Neji R, Kunze KP, Forman C, Schmidt M, et al. Motion-corrected 3D whole-heart water-fat high-resolution late gadolinium enhancement cardiovascular magnetic resonance imaging. *J Cardiovasc Magn Reson*. 2020;22(1):53.
- 19 Wetzl J, Yoon S, Schmidt M, Haenel A-B, Weißgerber A, Barkhausen J, et al. AI-based Single-Click Cardiac MRI Exam: Initial Clinical Experience and Evaluation in 44 Patients. *International Society for Magnetic Resonance in Medicine* 2023.
- 20 Yoon S, Preuhs E, Schmidt M, Forman C, Chitiboi T, Sharma P, et al. Automated Cardiac Resting Phase Detection Targeted on the Right Coronary Artery. *Machine Learning for Biomedical Imaging*. 2023;2,arXiv:2109.02342:1-26.
- 21 Yoon S, Schmidt M, Rick M, Chitiboi T, Sharma P, Emrich T, et al. Validation of a deep learning based automated myocardial inversion time selection for late gadolinium enhancement imaging in a prospective study. *International Society for Magnetic Resonance in Medicine* 2021.
- 22 Hajhosseiny R, Rashid I, Bustin A, Munoz C, Cruz G, Nazir M.S, et al. Clinical comparison of sub-mm high-resolution non-contrast coronary MRA against coronary CTA in patients with low-intermediate risk of CAD: A single center trial. *J Cardiovasc Magn Reson*. 2021;23(1):57.

Contact

Michaela Schmidt
Siemens Healthineers
SHS DI MR RCT CLS CARD
Allee am Roethelheimpark 2
91050 Erlangen
Germany
michaela.schmidt@siemens-healthineers.com



Karl P. Kunze, Ph.D.
Siemens Healthineers
SHS EMEA GBI DI PI
Riverside Way
Camberley GU15 3YL
United Kingdom
karl-philipp.kunze@siemens-healthineers.com



Free-Breathing Cardiac Cine Magnetic Resonance Imaging with Compressed Sensing Real-Time Acquisition and Respiratory Motion Correction: Initial Clinical Experience at a Single Pediatric Center

Jianing Pang, Ph.D.¹; Pedro Itriago Leon, BS²; Xiaoming Bi, Ph.D.³; Gary R. McNeal, BS¹; Christoph Forman, Ph.D.⁴; Christianne Leidecker, Ph.D.¹; Maria M. Pereyra, BS⁵; Prakash M. Masand, M.D.⁵

¹Siemens Medical Solutions USA Inc., Chicago, IL, USA

²Siemens Medical Solutions USA Inc., Houston, TX, USA

³Siemens Medical Solutions USA Inc., Los Angeles, CA, USA

⁴Siemens Healthcare, Erlangen, Germany

⁵Texas Children's Hospital, Houston, TX, USA

Introduction

Cine MRI is an important diagnostic tool for evaluating cardiac function [1, 2] and an essential part of most cardiac magnetic resonance (CMR) protocols [3]. The current standard technique, 2D segmented acquisition with retrospective electrocardiogram (ECG) gating [4], requires the patient to hold their breath during the multi-heartbeat data acquisition [5]. This breath-holding maneuver is typically repeated 10 to 20 times, with breaks in between, to acquire all desired slice orientations. However, breath-holding is often uncomfortable, and can be difficult for many types of patients such as those with congestive heart failure or chronic obstructive pulmonary disease. Furthermore, for uncooperative patients such as young children¹, reliable breath-holding may only be achieved via mechanical ventilation under general anesthesia, which adds to the cost, risk, and complexity of a CMR exam [6]. Breath-holding also disrupts the exam workflow as the operator must set up or repeatedly give breath-hold commands, check the image quality, and reattempt the scan when necessary. Therefore, free-breathing cine MRI is desirable for improving patient experience, simplifying workflow, and achieving robust image quality in wider patient population.

Previous works have proposed different strategies for free-breathing cardiac cine imaging, which we categorize into three classes.

One class of methods enhances segmented acquisition by adding respiratory monitoring, typically through external monitoring devices [7, 8] or self-navigation [9, 10] since there is no gap in the continuous cine acquisition for inserting conventional MR navigators [11]. These methods then use the respiratory motion information to either reject or correct the acquired k -space data. Such free-breathing, segmented techniques generally maintain the spatiotemporal resolution compared to the conventional breath-hold technique. However, the imaging time is often longer due to respiratory gating. The external respiratory monitoring can be unreliable and time-consuming to set up. And any respiratory pattern drift or errors in the respiratory signal can lead to residual motion artifacts due to inconsistencies between k -space segments.

A second class of methods, real-time imaging, acquires a cine frame in one shot and thus eliminates potential shot-to-shot inconsistencies in segmented acquisition [12–22]. To achieve this goal, these methods use highly accelerated acquisition such as echo-planar imaging [12], view sharing [14], parallel imaging [13, 15], non-Cartesian imaging [16], iterative reconstruction [17–20], and machine learning reconstruction [22]. The spatiotemporal resolution is often reduced compared with segmented techniques, although recent advances in acceleration methods have closed the gap considerably. Furthermore,

¹MR scanning has not been established as safe for imaging fetuses and infants less than two years of age. The responsible physician must evaluate the benefits of the MR examination compared to those of other imaging procedures.

real-time cardiac cine images often require additional steps in post-processing to identify the end-systole and end-diastole phases slice by slice and to ensure the consistency of respiratory phases between slices [23, 24].

Another class of methods extends real-time imaging by introducing retrospective motion processing [25–28]. Based on multi-heartbeat real-time cine acquisition, these methods use image-based metrics to detect respiratory motion, select a subset of heartbeats, perform respiratory motion correction, and then combine motion corrected data through either direct averaging in image space [25, 28] or *k*-space rebinning and a second reconstruction [26, 27]. These motion processing steps effectively suppress respiratory motion artifacts, enhance signal-to-noise ratio (SNR) by exploiting data redundancy after motion correction, and are compatible with established image analysis workflows since the output image series contains only one normalized cardiac cycle and a set number of frames per slice. However, the image reconstruction is often computationally intensive and can take a long time to finish. This can be addressed by running the reconstruction on powerful external hardware connected to clinical scanners [27, 29], yet the associated investment and technical complexity limit the feasibility at most centers.

In this work, we propose a prototype free-breathing cardiac cine imaging technique, real-time compressed sensing cine with motion correction (RTCSCineMoCo)², that runs on existing scanner hardware and combines highly

accelerated real-time acquisition, compressed sensing (CS) reconstruction, and retrospective, fully automated respiratory motion correction. We compare RTCSCineMoCo with the standard breath-hold technique on patients undergoing routine CMR exams at a single pediatric center in terms of quantitative cardiac function measurements and subjective image quality scores.

Materials and methods

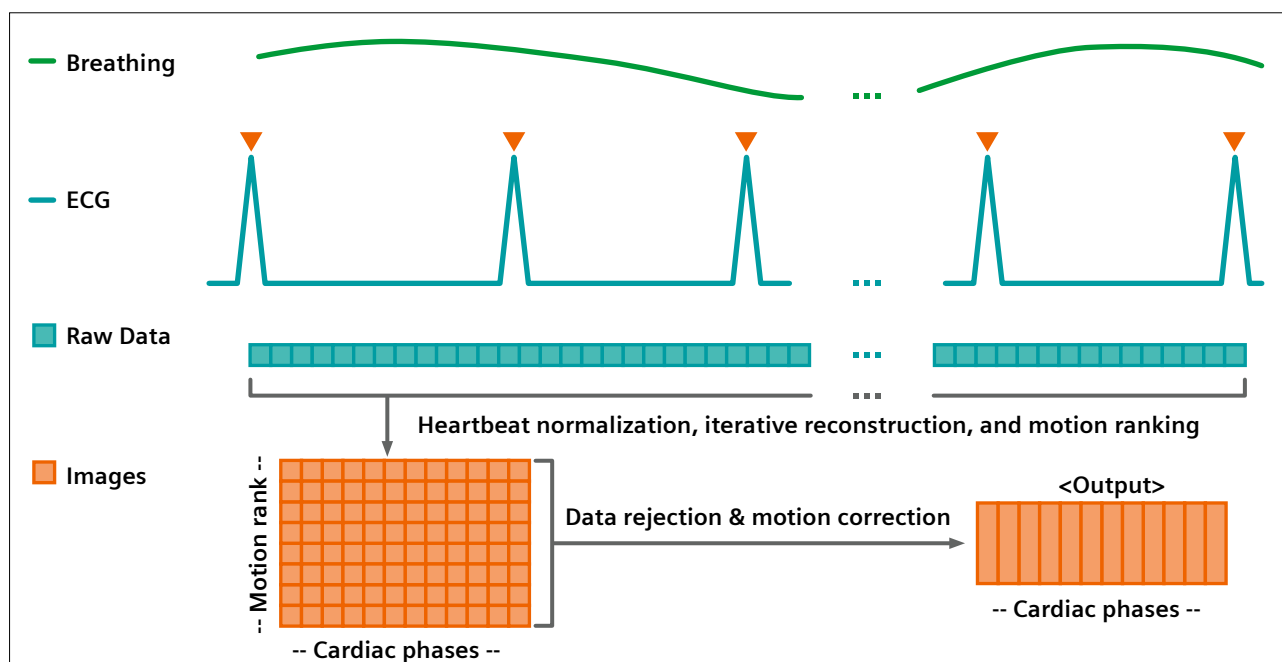
Free-breathing cardiac cine MRI

Overview

Figure 1 shows the RTCSCineMoco acquisition and reconstruction workflow:

- (1) acquiring real-time cine data over multiple heartbeats and respiratory cycles;
- (2) remapping the acquired *k*-space data based on trigger delay so that all heartbeats contain the same number of cardiac phases;
- (3) reconstructing the now normalized heartbeats;
- (4) ranking the heartbeats based on detected respiratory motion and arrhythmia;
- (5) accepting a subset of highly ranked heartbeats;
- (6) performing non-rigid registration of the accepted heartbeats to the top ranked reference heartbeat;
- (7) computing the average of the registered heartbeats as the output. We describe these steps in detail below.

²Work in progress. The product is still under development and not commercially available. Its future availability cannot be ensured.



1 The RTCSCineMoCo acquisition and reconstruction workflow.

Image acquisition

Image acquisition uses a prototype real-time cardiac cine sequence with prospective ECG gating, incoherent Cartesian sampling, and balanced steady-state free precession (bSSFP) readout [19, 20]. The acquisition spans 12 heartbeats for each imaging slice, which we empirically found to be sufficient for covering multiple respiratory cycles and hence capturing the heart in a stationary respiratory phase at least once. The patient specific acceleration factor is set such that the resulting temporal resolution approximately equals to the average RR duration divided by the number of desired cardiac phases. Hence, for a given number of desired cardiac phases, the higher the patient heart rate, the higher the acceleration factor.

Reconstruction of normalized heartbeats

We first remap each acquired k -space line into a cardiac phase based on its relative position within the respective RR duration using a simple linear formula:

$$\text{Cardiac Phase within RR} = \text{ceiling} \left(\frac{\text{Trigger Delay}}{\text{RR Duration}} \times \frac{\text{Desired Number of Phases per RR}}{\text{Desired Number of Phases per RR}} \right)$$

where trigger delay is the time between the current echo and the most recent ECG trigger, and the RR durations are derived from the trigger delay times of all acquired lines. This operation normalizes the heart rate variation and ensures each heartbeat contains the same number of frames, which is necessary in the subsequent motion correction and averaging step. We also discard any data acquired after the last recorded R wave, as they usually do not cover a complete heartbeat. Lastly, we reconstruct all normalized heartbeats jointly using iterative reconstruction with redundant Haar wavelets for spatiotemporal regularization [19, 20].

Heartbeat ranking and motion corrected averaging

After reconstruction, we first perform time-based arrhythmia rejection by rejecting those heartbeats with RR durations more than two standard deviations away from the median RR duration. Then, the remaining normalized heartbeats are ranked by the presence of respiratory motion. Such ranking serves as the basis for selecting the reference heartbeat and deciding which of the heartbeats to keep for further processing. Several previous works proposed deformation-based navigators for detecting respiratory motion from real-time cine images (25–28),

which generally involve first performing non-rigid registration between each real-time frame and an arbitrary reference, and then extracting a scalar, low-pass filtered respiratory navigator signal from the deformation vector fields. In this work, we propose an image-based, one-step alternative, which we describe in detail below.

Consider a real-time, multi-heartbeat cine image series acquired under free-breathing. We observe that an ideal heartbeat should appear as a near perfect loop due to the cyclic nature of cardiac motion. Otherwise, in the presence of respiratory or general bulk motion, the heart and its surrounding anatomy will not return to its original shape and position at the end of the heartbeat, since non-cardiac motion is usually of lower frequency or non-cyclic. To determine the amount of non-cardiac motion in each heartbeat, we therefore define a motion score as the sum of pixel-wise absolute difference between the first and last frame of each heartbeat:

$$\text{Score of Beat} = \sum_{\text{All pixels}} |\text{First Frame of Beat} - \text{Last Frame of Beat}|$$

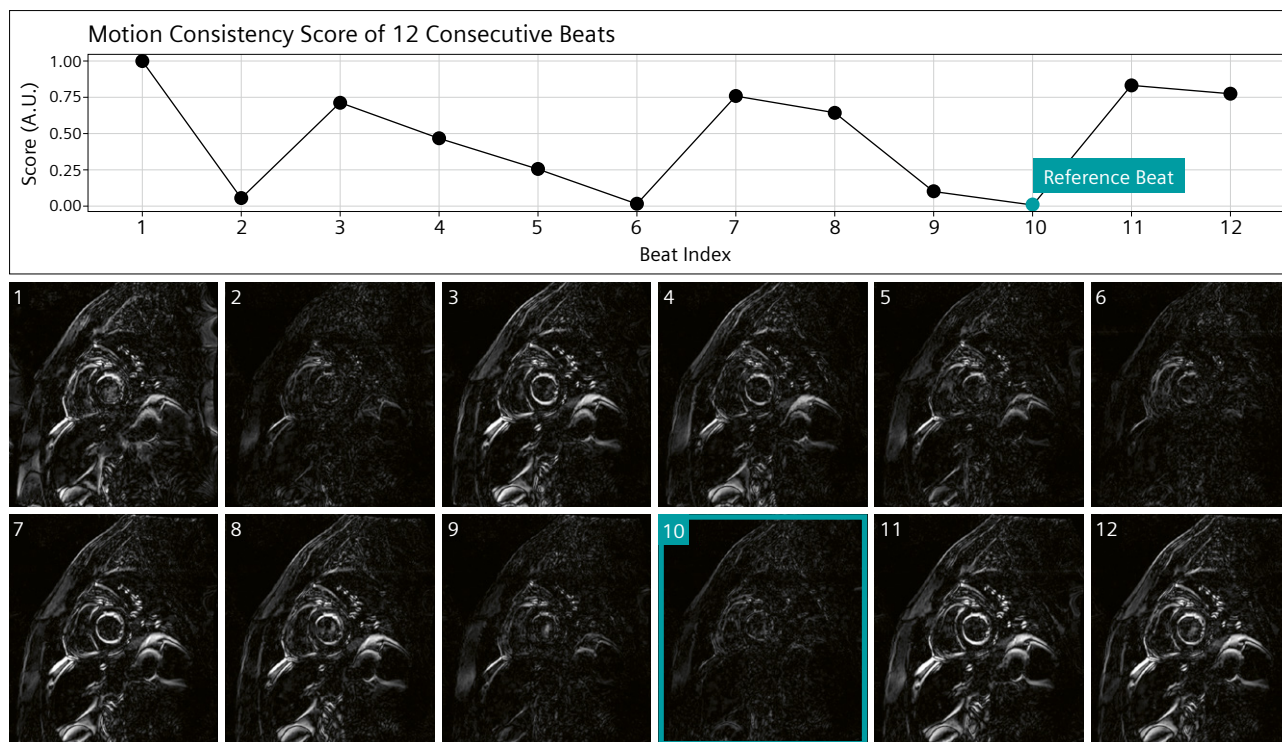
The lower the score is for a given heartbeat, the more similar the first and last cine frames are, and the less non-cardiac motion the heartbeat contains. Figure 2 shows the motion scores and absolute difference images from an example dataset containing 12 consecutive heartbeats.

After calculating the motion scores, we accept a subset (typically one third) of the highest ranked heartbeats for further processing. With the top-ranked heartbeat as the reference, we register each cardiac frame in each accepted heartbeat to the corresponding cardiac frame in the reference beat via non-rigid registration [28], and then compute the average of all registered heartbeats as the final output, which has higher SNR than the original images from individual heartbeats due to averaging.

In vivo study

Study protocol

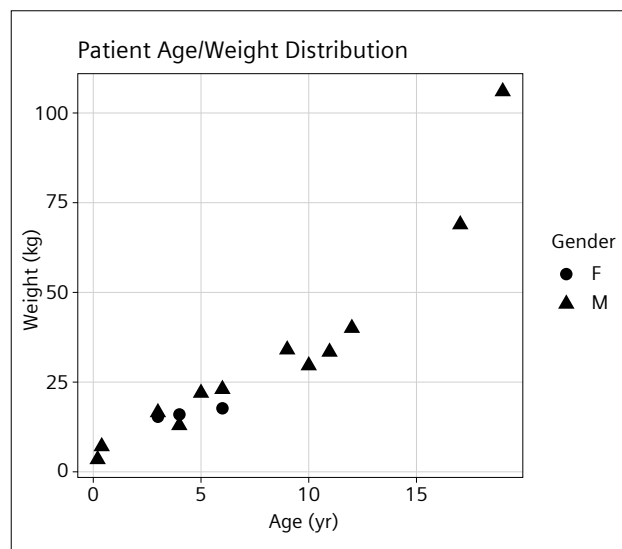
With institutional IRB approval and written consent form (by guardians for underage patients), we acquired both breath-hold segmented cine with retrospective ECG gating (BH) and free-breathing RTCSCineMoCo images, in random order, on 15 patients using a clinical 1.5T MR scanner (MAGNETOM Aera, Siemens Healthcare, Erlangen, Germany). Figure 3 shows the patient demographic data: 7.3 ± 5.4 years, range 11 weeks – 19 years; weight 29.7 ± 25.6 kg, range 3.5–106.0 kg; 12 males. Clinical



2 Visualization of the proposed motion score (pixel sum of the absolute difference between first and last cardiac phases of a given heartbeat) from 12 consecutive heartbeats from an example subject; the bottom figures show the pixel-wise absolute difference for all heart-beats; in this example, beat 10 has the lowest score (highest consistency) and is selected as the reference for respiratory motion correction.

indication of these patients include: ductal origin of pulmonary artery, Fontan (N = 2), Kawasaki with left coronary artery aneurysm, left ventricle dilation, left ventricle non-compaction cardiomyopathy and ventricular ectopy, Marfan syndrome, post COVID-19 myocarditis, right ventricle dominant atrio ventricular septal defect, supraventricular tachycardia, tetralogy of Fallot (N = 2), tetralogy of Fallot post repair (N = 2), total anomalous pulmonary venous return repair, and tricuspid atresia.

The sequence parameters were as follows: 11–14 short axis slices, balanced steady-state free precession readout, flip angle = 58–90°, 25 calculated cardiac phases, in-plane resolution = 1.2–1.8 mm for BH, 1.4–2.0 mm interpolated to 0.7–1.0 mm for RTCSCineMoCo, slice thickness = 5.0–9.0 mm; GRAPPA factor = 2 for BH; CS acceleration factor = 9.6–19.2 for RTCSCineMoCo. In certain subjects we additionally acquired other cardiac views, such as four-chamber (4CH), left ventricle outflow tract (LVOT), right ventricle outflow tract (RVOT), and vertical long axis (VLA).



3 The study population covers a wide range of age (11 weeks¹ to 19 years) and weight (3.5 to 106.0 kg).

¹MR scanning has not been established as safe for imaging fetuses and infants less than two years of age. The responsible physician must evaluate the benefits of the MR examination compared to those of other imaging procedures.

Image analysis

The order of images was randomized prior to analysis. One reader blinded to the underlying technique (MP) manually traced the left ventricle (LV) endocardial contours (QMASS 8.1, Medis Medical System, Leiden, Netherlands), which served as the basis for calculating quantitative LV parameters including end-diastolic volume (EDV), end-systolic volume (ESV), stroke volume (SV), ejection fraction (EF), and cardiac output (CO). In addition, one radiologist experienced in diagnostic CMR (PM, 15 years), blinded to the underlying technique, independently reviewed images from all subjects and scored image quality using a three-point Likert scale (1 = poor image quality and non-diagnostic, 2 = suboptimal image quality but diagnostic, 3 = excellent image quality) in the following categories: (a) myocardial-blood pool contrast, (b) papillary muscle visualization, (c) atrioventricular valve leaflet visualization, (d) wall motion visualization, and (e) visualization of spin dephasing from turbulent flow.

Statistical analysis

We use paired two-tailed t-test and Bland-Altman analysis to compare the quantitative LV parameters (R 3.5.2, R Core Team, www.R-project.org). We define $P = 0.05$ as statistically significant.

Results

Statistical analysis

All patients successfully completed the study without complications. The heart rates during cine exams were 98.9 ± 15.4 beats per minute (BPM) for BH and 100.8 ± 14.7 BPM for RTCSCineMoCo ($P = 0.47$). We found no significant difference between the measured LV function parameters, including EDV (101.1 ± 53.1 ml for BH and 99.0 ± 53.5 ml for RTCSCineMoCo, $P = 0.32$), ESV

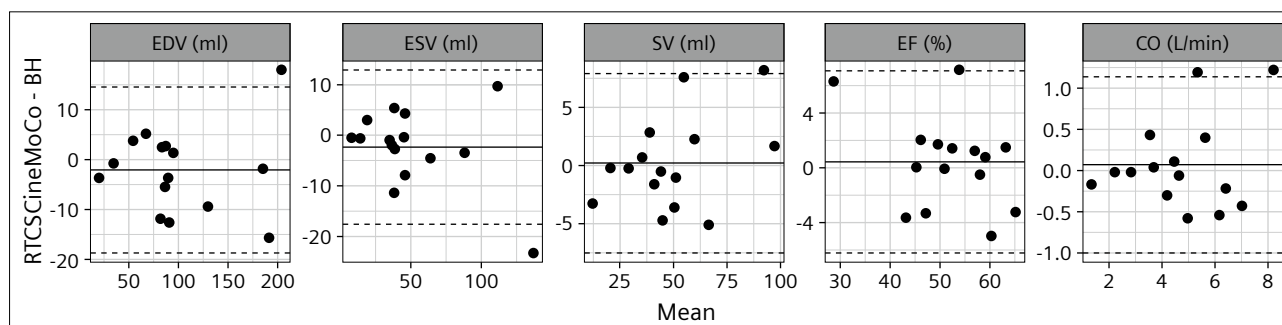
(52.1 ± 36.1 ml for BH, 49.8 ± 33.3 ml for RTCSCineMoCo, $P = 0.27$), SV (49.0 ± 21.8 ml for BH and 49.3 ± 23.4 ml for RTCSCineMoCo, $P = 0.82$), EF ($51.8 \pm 9.7\%$ for BH and $52.2 \pm 8.5\%$ for RTCSCineMoCo, $P = 0.63$), and CO (4.7 ± 1.7 L/min for BH and 4.7 ± 1.9 L/min for RTCSCineMoCo, $P = 0.62$). The two techniques scored identically (3 out of 3) for all five subjective criteria. Figure 4 shows the Bland-Altman plots of the LV function measures. The mean difference, lower limit of agreement, and higher limit of agreement were -2.1 ml, -18.7 ml, and 14.5 ml for EDV, -2.3 ml, -17.6 ml, and 12.9 ml for ESV, 0.2 ml, -7.5 ml, and 7.9 ml for SV, 0.4%, -6.2%, and 7.1% for EF, and 0.1 L/min, -1.0 L/min, and 1.1 L/min for CO. The average acquisition time was 4.0 ± 1.8 min for BH (including all patient rest times in between slices) and 1.7 ± 0.4 min for RTCSCineMoCo ($P < 0.001$). For RTCSCineMoCo, the average reconstruction delay between the end of short axis stack acquisition and all images becoming available was 5.2 ± 1.9 min.

Image examples

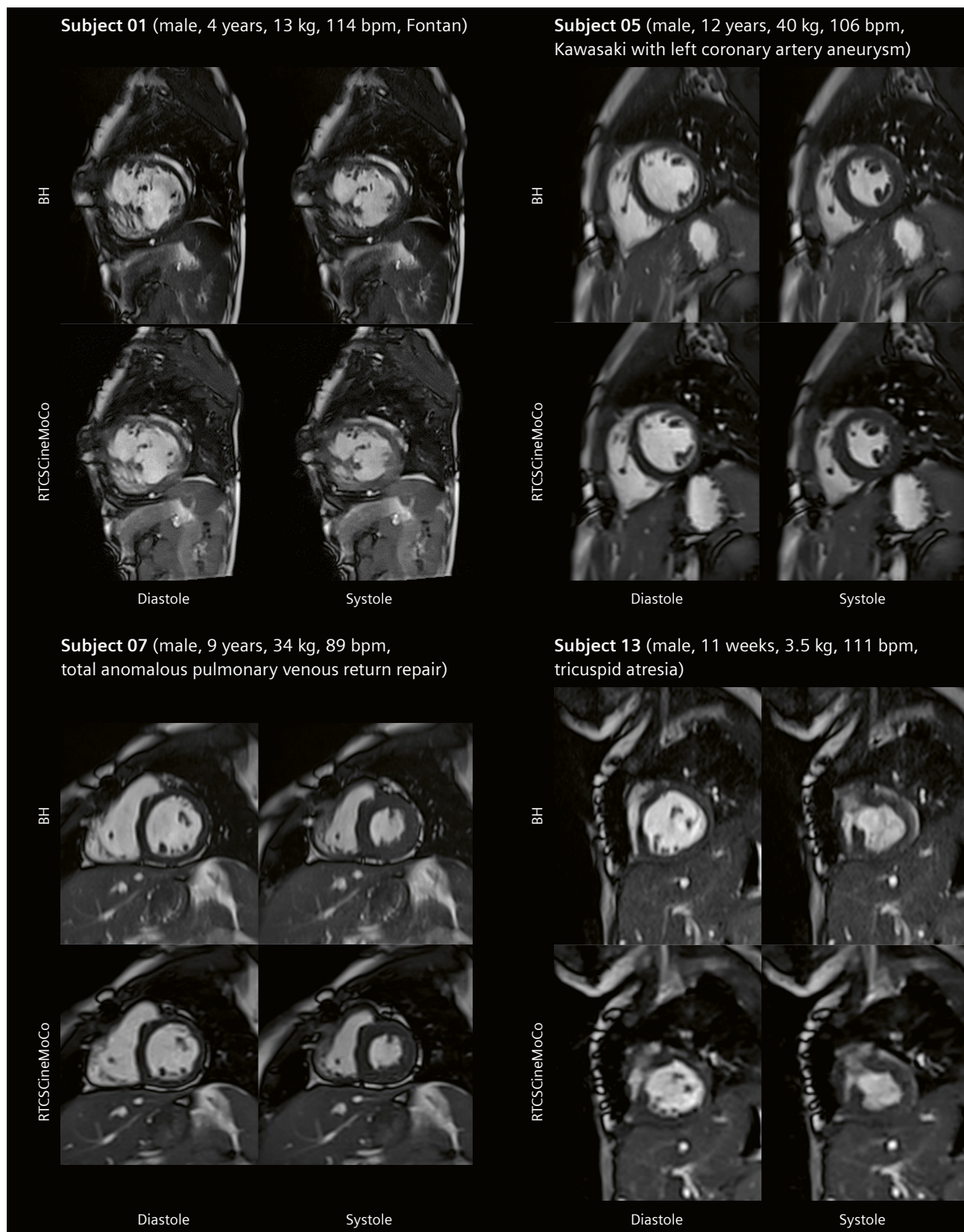
Figure 5 shows example images of both diastole and systole phases at mid-ventricular slice positions from four patients, with ages ranging from 11 weeks to 12 years. Figure 6 shows additional cardiac views obtained with RTCSCineMoCo in one patient.

Discussion

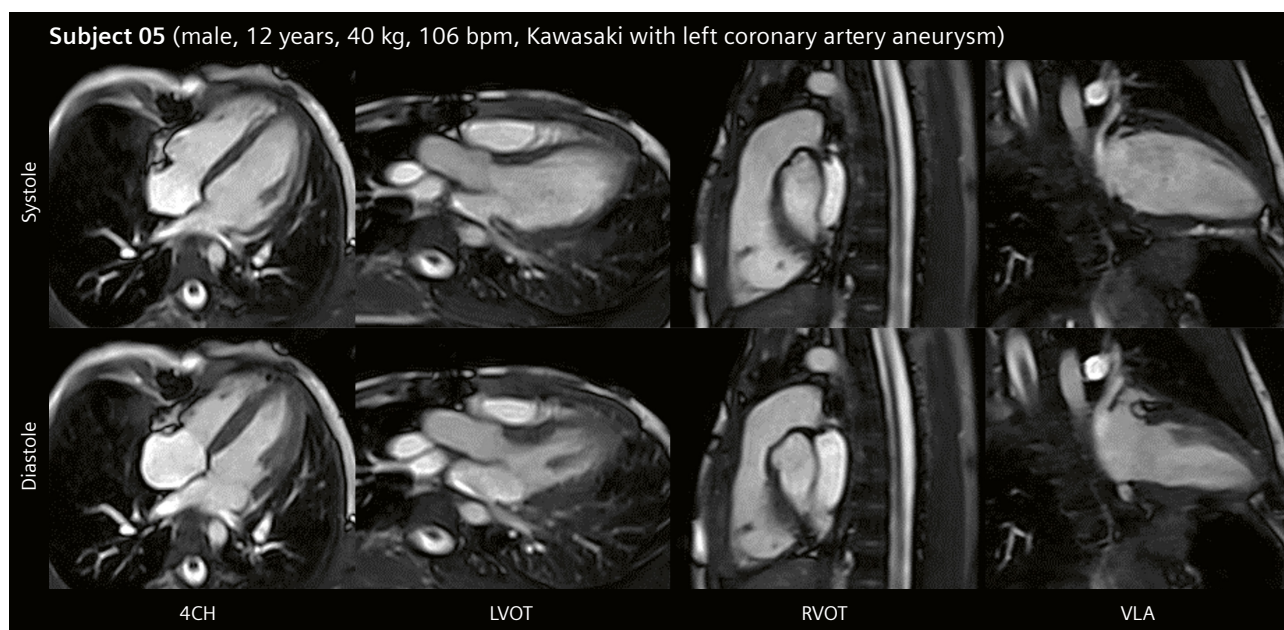
In this work, we proposed a new free-breathing cardiac cine technique, RTCSCineMoCo, which offers several advantages over existing techniques for cardiac cine imaging. First, the free-breathing acquisition considerably improves patient experience and may allow more robust image quality for those who have difficulties holding their breath or uncooperative subjects such as young children.



4 Bland-Altman plot of the left ventricle (LV) end-diastole volume (EDV), end-systole volume (ESV), stroke volume (SV), ejection fraction (EF), and cardiac output (CO). Solid lines indicate the mean difference and dashed lines show the limits of agreement.



5 Example BH and RTCS CineMoCo images from four patients across the age range, showing comparable image quality between the two techniques. Images have been cropped to only show the heart and surrounding anatomy.



6 Additional cardiac views of one subject obtained with RTCSCineMoCo. 4CH: four-chamber. LVOT: left ventricle outflow tract. RVOT: right ventricle outflow tract. VLA: vertical long axis. Images have been cropped to only show the heart and surrounding anatomy.

Second, RTCSCineMoCo achieves comparable spatiotemporal resolution to the current clinical standard, breath-hold segmented acquisition with retrospective ECG gating, by combining highly accelerated real-time acquisition, CS reconstruction, and motion corrected averaging. Third, the inline image reconstruction pipeline is fully automated and runs on existing scanner hardware, making RTCSCineMoCo simple to implement and use. The LV function parameters measured from RTCSCineMoCo, including EDV, ESV, SV, EF, and CO, showed no significant difference versus those derived from the conventional breath-hold technique. Both techniques obtained identical image quality scores across all subjective criteria on all subjects.

The present study contains several limitations. First, although we imaged a wide age range (11 weeks to 19 years), the sample size is small at 15 subjects, which limits the statistical power of our results. Second, we did not evaluate right ventricle (RV) function, which may be more difficult to consistently measure due to the complex shape of the RV [2] but may also be of interest in certain patient populations [30, 31]. Last, not all pulse sequence parameters were matched exactly between BH and RTCSCineMoCo, such as FOV, matrix size, and in-plane interpolation. Such discrepancies should be addressed in future comparisons.

Clinical workflow implications for pediatric subjects

CMR subjects need to remain still for the duration of the exam to minimize bulk motion artifacts and allow consistent slice positioning. Furthermore, conventional CMR

sequences require breath-holding to achieve diagnostic image quality. These requirements are particularly challenging for young children (under 6–8 years of age), and often necessitates general anesthesia, endotracheal intubation, and mechanical ventilation. Free-breathing techniques, such as RTCSCineMoCo and motion corrected late gadolinium enhancement imaging (32, 33), achieve robust image quality without the breath-holding requirement. As a result, such techniques eliminate the need for manually performed breath-holds for patients under general anesthesia, and may also reduce the need for mechanical ventilation in favor of spontaneous breathing under moderate sedation or while fully conscious (34), thereby lowering the complexity, risk, and resource requirement of pediatric CMR [35–41].

Potential utility in imaging patients with arrhythmia

RTCSCineMoCo offers some protection against heart rate variation through time-based arrhythmia rejection, where it rejects the heartbeats with durations outside of an acceptable range. However, dedicated studies on arrhythmia patients are warranted, as are additional considerations for the reconstruction pipeline. For example, more sophisticated RR inclusion/exclusion criteria may be necessary to account for different types of arrhythmias and correctly extract the relevant reference beat for quantitative analysis. It might also be beneficial to additionally output the non-normalized multi-beat real-time images, so that a reader can fully appreciate the changing cardiac rhythm during the acquisition.

Reconstruction time

The RTCSCineMoCo reconstruction is computationally demanding. Despite the use of graphical processing units (GPU) and multithreading, there is still a non-negligible delay between the end of data acquisition and the completion of image reconstruction. For this study, the average delay after a short axis stack was 5.2 ± 1.9 min. This delay may be justified considering that the conventional workflow includes pauses for breath-holding instructions and recovery, during which the scanner sits idle. Meanwhile, the free-breathing workflow needs no such pauses, and during the reconstruction delay the user can already prescribe and execute new scans. Future algorithmic improvements and more powerful scanner hardware may reduce the RTCSCineMoCo reconstruction time further and improve its usability.

Ranking heartbeats

In the proposed motion correction framework, we observe that if a heartbeat is free of non-cardiac motion, its first and last frames will display high similarity due to the cyclical nature of cardiac motion. We further hypothesize that the reverse is also true under most circumstances, and hence rank the acquired heartbeats by the pixel sum of absolute difference between their first and last cine frames. We then use such ranks to inform subsequent reference beat selection and data rejection. This approach is much less computationally intensive than previous approaches that resort to non-rigid registration [25–28], and requires no user input nor empirical parameters such as the respiratory cutoff frequency. Although the proposed strategy has worked robustly in our experience, there are two scenarios where it could produce less than optimal results. First, we do not attempt to measure absolute heart displacement and hence cannot guarantee that the top ranked heartbeat will always correspond to end-expiration. If the respiratory pattern changes dramatically within a multi-slice acquisition, there could be slice-to-slice mismatch of the respiratory phase. Second, we only consider the first and last frames in a heartbeat. Therefore, a heartbeat can in principle contain unwanted motion and be still highly ranked if such motion is contained in the middle frames only. Both scenarios are likely rare in practice but warrant observation in future studies.

Attaching the motion correction pipeline to other accelerated real-time sequences

The RTCSCineMoCo data acquisition employs incoherent Cartesian sampling and iterative reconstruction using redundant Haar wavelets for spatiotemporal regularization [19, 20], which offers the crucial benefit of good image quality even at high acceleration factors. As a result, after beat-to-beat normalization, non-rigid registration can be performed directly on the raw, high temporal resolution

images without the need to start with a lower temporal resolution during the registration step [26]. The image quality is then further improved through motion corrected averaging. We would like to point out, however, that the motion correction pipeline can be readily attached to any other real-time imaging schemes, such as non-Cartesian acquisition with machine learning reconstruction to take advantage of its reconstruction performance [21]. This will be an interesting direction to explore in the future.

Conclusion

In conclusion, we showed that a novel free-breathing cine technique, RTCSCineMoCo, can be implemented in a clinical setting and produce comparable quantitative LV measurements and image quality to the reference breath-hold segmented cine technique.

References

- 1 Grothues F, Smith GC, Moon JC, et al. Comparison of interstudy reproducibility of cardiovascular magnetic resonance with two-dimensional echocardiography in normal subjects and in patients with heart failure or left ventricular hypertrophy. *Am J Cardiol.* 2002;90(1):29-34.
- 2 Grothues F, Moon JC, Bellenger NG, et al. Interstudy reproducibility of right ventricular volumes, function, and mass with cardiovascular magnetic resonance. *Am Heart J.* 2004;147(2):218-23.
- 3 Global Cardiovascular Magnetic Resonance Registry I, Kwong RY, Petersen SE, et al. The global cardiovascular magnetic resonance registry (GCMR) of the society for cardiovascular magnetic resonance (SCMR): its goals, rationale, data infrastructure, and current developments. *J Cardiovasc Magn Reson.* 2017;19(1):23.
- 4 Carr JC, Simonetti O, Bundy J, et al. Cine MR angiography of the heart with segmented true fast imaging with steady-state precession. *Radiology.* 2001;219(3):828-34.
- 5 Kramer CM, Barkhausen J, Bucciarelli-Ducci C, et al. Standardized cardiovascular magnetic resonance imaging (CMR) protocols: 2020 update. *J Cardiovasc Magn Reson.* 2020;22(1):17.
- 6 Fratz S, Chung T, Greil GF, et al. Guidelines and protocols for cardiovascular magnetic resonance in children and adults with congenital heart disease: SCMR expert consensus group on congenital heart disease. *J Cardiovasc Magn Reson.* 2013;15:51.
- 7 Krishnamurthy R, Pednekar A, Atweh LA, et al. Clinical validation of free breathing respiratory triggered retrospectively cardiac gated cine balanced steady-state free precession cardiovascular magnetic resonance in sedated children. *J Cardiovasc Magn Reson.* 2015;17(1):1.
- 8 Ludwig J, Speier P, Seifert F, et al. Pilot tone-based motion correction for prospective respiratory compensated cardiac cine MRI. *Magn Reson Med.* 2020.
- 9 Larson AC, Kellman P, Arai A, et al. Preliminary investigation of respiratory self-gating for free-breathing segmented cine MRI. *Magn Reson Med.* 2005;53(1):159-68.
- 10 Hu P, Hong S, Moghari MH, et al. Motion correction using coil arrays (MOCCA) for free-breathing cardiac cine MRI. *Magn Reson Med.* 2011;66(2):467-75.
- 11 Wang Y, Rossman PJ, Grimm RC, et al. Navigator-echo-based real-time respiratory gating and triggering for reduction of respiration effects in three-dimensional coronary MR angiography. *Radiology.* 1996;198(1):55-60.

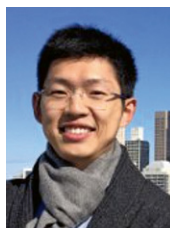
- 12 Nagel E, Schneider U, Schalla S, et al. Magnetic resonance real-time imaging for the evaluation of left ventricular function. *J Cardiovasc Magn Reson*. 2000;2(1):7-14.
- 13 Wintersperger BJ, Nikolaou K, Dietrich O, et al. Single breath-hold real-time cine MR imaging: improved temporal resolution using generalized autocalibrating partially parallel acquisition (GRAPPA) algorithm. *Eur Radiol*. 2003;13(8):1931-6.
- 14 Hori Y, Yamada N, Higashi M, et al. Rapid evaluation of right and left ventricular function and mass using real-time true-FISP cine MR imaging without breath-hold: comparison with segmented true-FISP cine MR imaging with breath-hold. *J Cardiovasc Magn Reson*. 2003;5(3):439-50.
- 15 Breuer FA, Kellman P, Griswold MA, Jakob PM. Dynamic autocalibrated parallel imaging using temporal GRAPPA (TGRAPPA). *Magn Reson Med*. 2005;53(4):981-5.
- 16 Narayan G, Nayak K, Pauly J, Hu B. Single-breathhold, four-dimensional, quantitative assessment of LV and RV function using triggered, real-time, steady-state free precession MRI in heart failure patients. *J Magn Reson Imaging*. 2005;22(1):59-66.
- 17 Feng L, Srichai MB, Lim RP, et al. Highly accelerated real-time cardiac cine MRI using k-t SPARSE-SENSE. *Magn Reson Med*. 2013;70(1):64-74.
- 18 Voit D, Zhang S, Unterberg-Buchwald C, et al. Real-time cardiovascular magnetic resonance at 1.5 T using balanced SSFP and 40 ms resolution. *J Cardiovasc Magn Reson*. 2013;15:79.
- 19 Kido T, Kido T, Nakamura M, et al. Assessment of Left Ventricular Function and Mass on Free-Breathing Compressed Sensing Real-Time Cine Imaging. *Circ J*. 2017;81(10):1463-8.
- 20 Sudarski S, Henzler T, Haubenreisser H, et al. Free-breathing Sparse Sampling Cine MR Imaging with Iterative Reconstruction for the Assessment of Left Ventricular Function and Mass at 3.0 T. *Radiology*. 2017;282(1):74-83.
- 21 Steeden JA, Kowalik GT, Tann O, et al. Real-time assessment of right and left ventricular volumes and function in children using high spatiotemporal resolution spiral bSSFP with compressed sensing. *J Cardiovasc Magn Reson*. 2018;20(1):79.
- 22 Hauptmann A, Arridge S, Lucka F, et al. Real-time cardiovascular MR with spatio-temporal artifact suppression using deep learning-proof of concept in congenital heart disease. *Magn Reson Med*. 2019;81(2):1143-56.
- 23 Bauer RW, Radtke I, Block KT, et al. True real-time cardiac MRI in free breathing without ECG synchronization using a novel sequence with radial k-space sampling and balanced SSFP contrast mode. *Int J Cardiovasc Imaging*. 2013;29(5):1059-67.
- 24 La Gerche A, Claessen G, Van de Bruaene A, et al. Cardiac MRI: a new gold standard for ventricular volume quantification during high-intensity exercise. *Circ Cardiovasc Imaging*. 2013;6(2):329-38.
- 25 Kellman P, Chefd'hotel C, Lorenz CH, et al. Fully automatic, retrospective enhancement of real-time acquired cardiac cine MR images using image-based navigators and respiratory motion-corrected averaging. *Magn Reson Med*. 2008;59(4):771-8.
- 26 Kellman P, Chefd'hotel C, Lorenz CH, et al. High spatial and temporal resolution cardiac cine MRI from retrospective reconstruction of data acquired in real time using motion correction and resampling. *Magn Reson Med*. 2009;62(6):1557-64.
- 27 Xue H, Kellman P, Larocca G, et al. High spatial and temporal resolution retrospective cine cardiovascular magnetic resonance from shortened free breathing real-time acquisitions. *J Cardiovasc Magn Reson*. 2013;15:102.
- 28 Rahsepar AA, Saybasili H, Ghasemiesfe A, et al. Motion-Corrected Real-Time Cine Magnetic Resonance Imaging of the Heart: Initial Clinical Experience. *Invest Radiol*. 2018;53(1):35-44.
- 29 Cross R, Olivieri L, O'Brien K, et al. Improved workflow for quantification of left ventricular volumes and mass using free-breathing motion corrected cine imaging. *J Cardiovasc Magn Reson*. 2016;18:10.
- 30 Scharhag J, Schneider G, Urhausen A, et al. Athlete's heart: right and left ventricular mass and function in male endurance athletes and untrained individuals determined by magnetic resonance imaging. *J Am Coll Cardiol*. 2002;40(10):1856-63.
- 31 te Riele AS, Tandri H, Bluemke DA. Arrhythmogenic right ventricular cardiomyopathy (ARVC): cardiovascular magnetic resonance update. *J Cardiovasc Magn Reson*. 2014;16:50.
- 32 Olivieri L, Cross R, O'Brien KJ, et al. Free-breathing motion-corrected late-gadolinium-enhancement imaging improves image quality in children. *Pediatr Radiol*. 2016;46(7):983-90.
- 33 Xie LJ, Xu R, Xu ZY, et al. Myocardial motion-corrected phase-sensitive inversion recovery late gadolinium enhancement in free breathing paediatric patients: a comparison with single-shot coherent gradient echo ("TrueFISP") phase-sensitive inversion recovery. *Clin Radiol*. 2021;76(6):471 e17- e25.
- 34 Christopher AB, Quinn RE, Zoufagharian S, et al. Motion-corrected cardiac MRI is associated with decreased anesthesia exposure in children. *Pediatr Radiol*. 2020;50(12):1709-16.
- 35 Malviya S, Voepel-Lewis T, Eldevik OP, et al. Sedation and general anaesthesia in children undergoing MRI and CT: adverse events and outcomes. *Br J Anaesth*. 2000;84(6):743-8.
- 36 Morray JP, Geiduschek JM, Ramamoorthy C, et al. Anesthesia-related cardiac arrest in children: initial findings of the Pediatric Perioperative Cardiac Arrest (POCA) Registry. *Anesthesiology*. 2000;93(1):6-14.
- 37 Serafini G, Zadra N. Anaesthesia for MRI in the paediatric patient. *Curr Opin Anaesthesiol*. 2008;21(4):499-503.
- 38 Kalkman CJ, Peelen L, Moons KG, et al. Behavior and development in children and age at the time of first anesthetic exposure. *Anesthesiology*. 2009;110(4):805-12.
- 39 Ramamoorthy C, Haberkern CM, Bhananker SM, et al. Anesthesia-related cardiac arrest in children with heart disease: data from the Pediatric Perioperative Cardiac Arrest (POCA) registry. *Anesth Analg*. 2010;110(5):1376-82.
- 40 Vanderby SA, Babyn PS, Carter MW, et al. Effect of anesthesia and sedation on pediatric MR imaging patient flow. *Radiology*. 2010;256(1):229-37.
- 41 Schiller RM, Allegaert K, Hunfeld M, et al. Analgesics and Sedatives in Critically Ill Newborns and Infants: The Impact on Long-Term Neurodevelopment. *J Clin Pharmacol*. 2018;58 Suppl 10:S140-S50.

Contact

Prakash M. Masand, M.D.
Division Chief of Body Radiology
Vice Chair, Body Radiology and Cardiac Imaging
Department of Radiology
Texas Children's Hospital
6701 Fannin Street, Suite 470
Houston, TX 77030
USA
pmmasand@texaschildrens.org



Jianing Pang, Ph.D.
Siemens Medical Solutions USA Inc.
737 N Michigan Ave Suite 1600
Chicago, IL 60611
USA
jianing.pang@siemens-healthineers.com



Optimizing Brachial Plexus Magnetic Resonance Neurography at 3 Tesla

Yenpo Lin, M.D.¹; Ek T. Tan, Ph.D.¹; Xiaoying Cai, Ph.D.²; Peter Kollasch, M.Sc.²; Alto Stemmer, Dipl.-Phys.³; Marcel Dominik Nickel, Ph.D.³; Guido Buonincontri, Ph.D.³; Andreas Schäfer, Ph.D.³; Tom Hilbert, Ph.D.^{4,5}; Darryl B. Sneag, M.D.¹

¹Department of Radiology and Imaging, Hospital for Special Surgery, New York, NY, USA

²Siemens Healthineers, Malvern, PA, USA

³Siemens Healthineers, Erlangen, Germany

⁴Advanced Clinical Imaging Technology, Siemens Healthineers International AG, Lausanne, Switzerland

⁵LTS5, École Polytechnique Fédérale de Lausanne (EPFL), Lausanne, Switzerland

Introduction

At the Hospital for Special Surgery (HSS), ongoing efforts are made to improve image quality in magnetic resonance neurography (MRN). MRN comprises a specialized set of techniques focused on imaging peripheral nerves, which can be challenging given their small size and non-linear course throughout the body. When utilized in parallel with electrodiagnostic testing, MRN not only facilitates accurate localization of nerve injuries but also offers a comprehensive

assessment of both the injured nerve and the end-organ muscle. MRN of the brachial plexus (BP) presents unique challenges due to inherent field inhomogeneities related to the neck/shoulder curvature and proximity to the lungs [1]. In 2021, the first Siemens Healthineers system was installed at our institution – a MAGNETOM Vida 3T. In this article, we share our experience in optimizing imaging quality for BP imaging on the MAGNETOM Vida.

Three-coil setup:
20-channel HNU +
18-channel UltraFlex +
posterior Spine Coil



Two-coil setup:
18-channel UltraFlex
(anterior: small,
posterior: large)



1 Comparison of coil types for unilateral, left brachial plexus MRN. **(1A)** Imaging with the neck at isocenter and the brachial plexus off isocenter using a combination of a 20-channel neurovascular array for the neck region, an 18-channel UltraFlex flexible coil array, and posterior spine elements. The BioMatrix Respiratory Sensor may be used for respiratory gating. **(1B)** An alternative setup with the left brachial plexus at isocenter, using two 18-channel UltraFlex arrays; the smaller coil is placed anteriorly while the larger coil is placed posteriorly (under the subject). An additional strap may be needed to deploy the respiratory pillow.

Sequence	2D IW-TSE	2D T2w-TSE	SPACE STIR	2D T2w-TSE
Deep Resolve Boost	Y	Y (Prototype) ¹	Y (Prototype) ¹	Y (Prototype) ¹
Orientation	Axial	Coronal	Double oblique-coronal	Oblique sagittal
Field of view, cm	28	32	30	16
TR/TE, ms	4000–6500/35	3000–9000/85	3000/161 (apparent TE = 60)	3000–6000/85
TI, ms	–	–	250	–
Matrix size (frequency × phase)	512 × 410	320 × 240	304 × 168	320 × 240
Pixel resolution (frequency × phase), mm ²	0.5 × 0.7	1.0 × 1.3	1.0 × 1.0	0.5 × 0.7
Slice thickness, mm (no spacing)	3.5	4.0	1.0	2.5
Slices	60	40–50	100–120	24–40
Bandwidth, Hz/Pixel	296	240	382	240
Turbo factor	14	14	130	14
Total acceleration factor (GRAPPA / CAIPIRINHA)	2	2	4	2
Gadolinium contrast	none	none	optional	none
Fat suppression	none	Dixon	STIR	Dixon/Fat saturation
Scan time, min:sec	2:00	3:45	4:40	4:00, variable with respiratory gating

Table 1: Unilateral brachial plexus protocol on MAGNETOM Vida 3T.

IW indicates intermediate-weighted; TSE: turbo spin echo; T2w: T2-weighted; TR: repetition time; TE: echo time; TI: inversion time; GRAPPA: generalized autocalibrating partial parallel acquisition; CAIPIRINHA: controlled aliasing in parallel imaging results in higher acceleration

¹Work in progress. The product is still under development and not commercially available. Its future availability cannot be ensured.

Coil configuration

To maximize signal-to-noise ratio (SNR) for BP MRN, it is vital to use multichannel receiver arrays that cover the large anatomical regions of the neck, shoulder, and axilla, while also minimizing the distance between coil elements and the targeted anatomy [2]. At HSS, the BP is typically imaged unilaterally, rather than bilaterally, to optimize spatial resolution and coverage; if bilateral coverage is required, two unilateral scans are typically acquired. On the MAGNETOM Vida 3T, the preferred three-coil setup includes a combination of either a 20-channel neurovascular array for the neck region, an 18-channel UltraFlex flexible coil array (small or large, depending on coverage needed) over the chest wall/upper arm, and the posterior spine array (Fig. 1). Alternatively, two 18-channel UltraFlex arrays, the smaller version placed anteriorly and the larger

placed posteriorly, can be placed (Fig. 1). The three-coil setup is easier to configure, in our experience, but the two-coil setup provides flexibility for positioning the targeted BP closer to magnet isocenter.

BP protocol – overview and rationale

Our current, unilateral BP protocol comprises acquisitions both longitudinal and orthogonal relative to the course of the nerve segments (Fig. 2). Following localizer scans, a two-dimensional (2D) axial intermediate-weighted (IW)-TSE is acquired to guide plotting of subsequent scans. Next, a large field of view 2D coronal T2-weighted Dixon TSE is acquired to assess the regional musculature. These two TSE sequences are used to plot the remaining nerve-sensitive scans: two, 2D oblique sagittal T2-weighted Dixon acquisitions for orthogonal, high in-plane

resolution and a single, coronal T2-weighted three-dimensional (3D) SPACE-STIR sequence for high through-plane resolution. For the SPACE-STIR, coverage is best optimized with a 'double oblique' prescription, which is first aligned parallel to the clavicle and includes cephalocaudal coverage from the C4 superior endplate to the axilla and anterior-posterior coverage from the chest wall to the posterior scapula. This is followed by a second alignment step, made off the 2D coronal T2-weighted Dixon TSE, from C4 to the axillary region.

Optimized 3D SPACE STIR

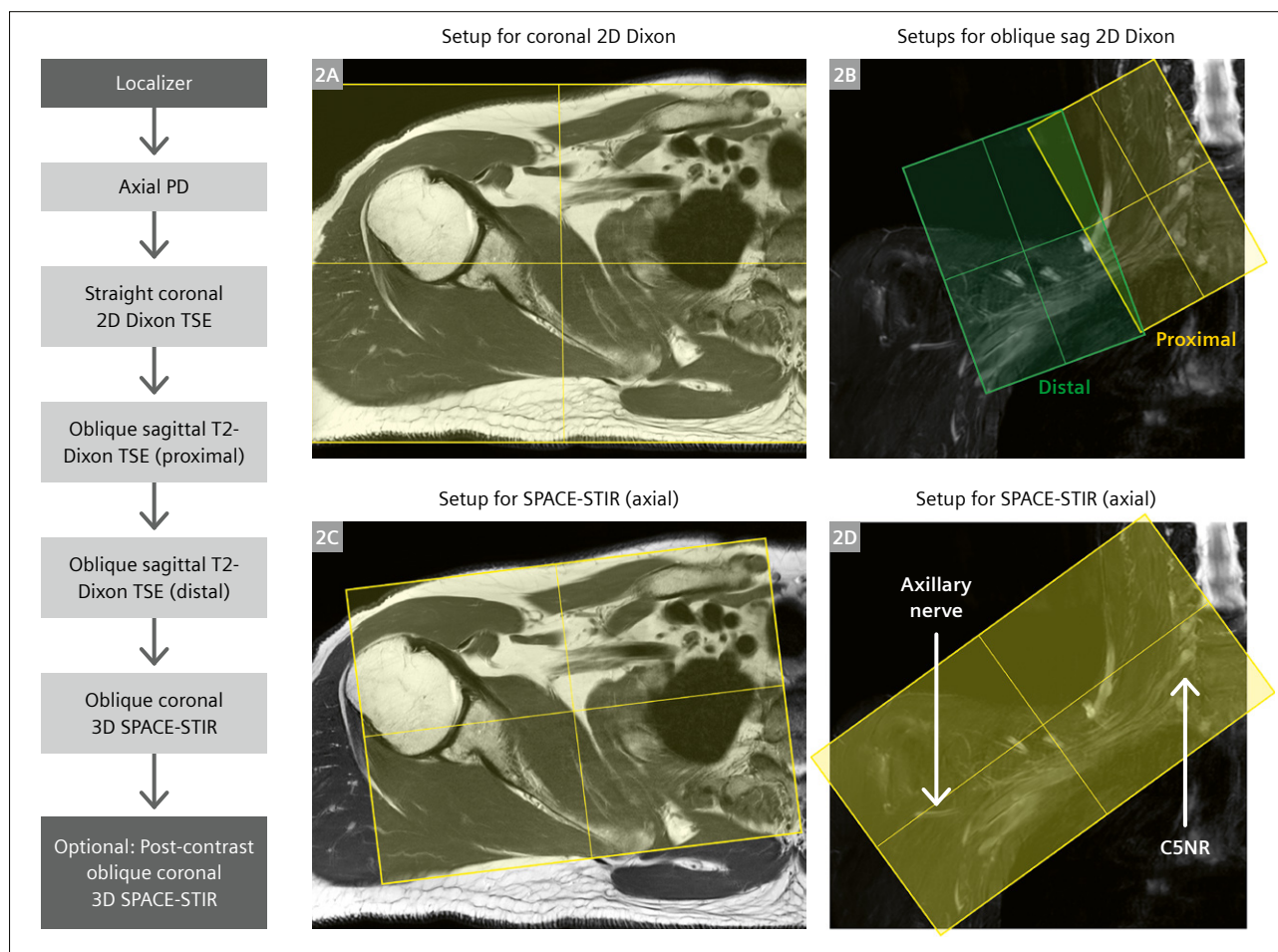
The SPACE sequence offers a significant advantage, compared to 2D imaging, by enabling higher through-plane spatial resolution (0.8–1.0 mm isotropic) and facilitating evaluation in any arbitrary plane without distortion, either

using oblique or curved multiplanar reformations. We use a prototype SPACE-STIR sequence¹ with optimizations to improve B_0 and B_1 robustness. These improvements include:

1. C-shaped frequency offset corrected inversion (C-FOCI) pulse for uniform fat suppression [3, 4],
2. variable flip angle train tailored with consideration of the B_1 inhomogeneity and
3. deep-learning-based 3D reconstruction algorithm tailored for CAIPIRINHA sampling pattern for high-quality reconstruction.

In particular, 3D deep-learning reconstruction now facilitates acquisitions at 0.8 mm resolution, as compared to our default 1.0 mm-isotropic prescription (Fig. 3).

¹Work in progress. The product is still under development and not commercially available. Its future availability cannot be ensured.



- 2** Suggested protocol for unilateral BP MRI, and illustration of prescription boxes. From the unilateral axial intermediate-weighted image (2A), the straight coronal Dixon is plotted to cover 'skin-to-skin' (anterior to posterior) at the level of the subclavian vessels. Then two, 2D oblique sagittal T2-weighted Dixon scans are plotted off the coronal Dixon water image for proximal (yellow) and distal (green) coverages (2B); two scans are needed to ensure the images are orthogonal to the BP. Finally, a double-oblique coronal 3D SPACE-STIR is plotted off the axial IW image, parallel to the clavicle (2C) and off the coronal Dixon, to include from the C5 nerve root to the axillary region (yellow box as shown in 2D).

A SPACE-STIR sequence is sometimes acquired following intravenous gadolinium administration to improve vascular suppression, and to visualize small branch nerves of the plexus that may otherwise be obscured by venous contamination (Fig. 4) [5]. Gadolinium shortens the T1 of blood, thus bringing the blood T1 closer to that of fat, and reduces T2 transverse magnetization.

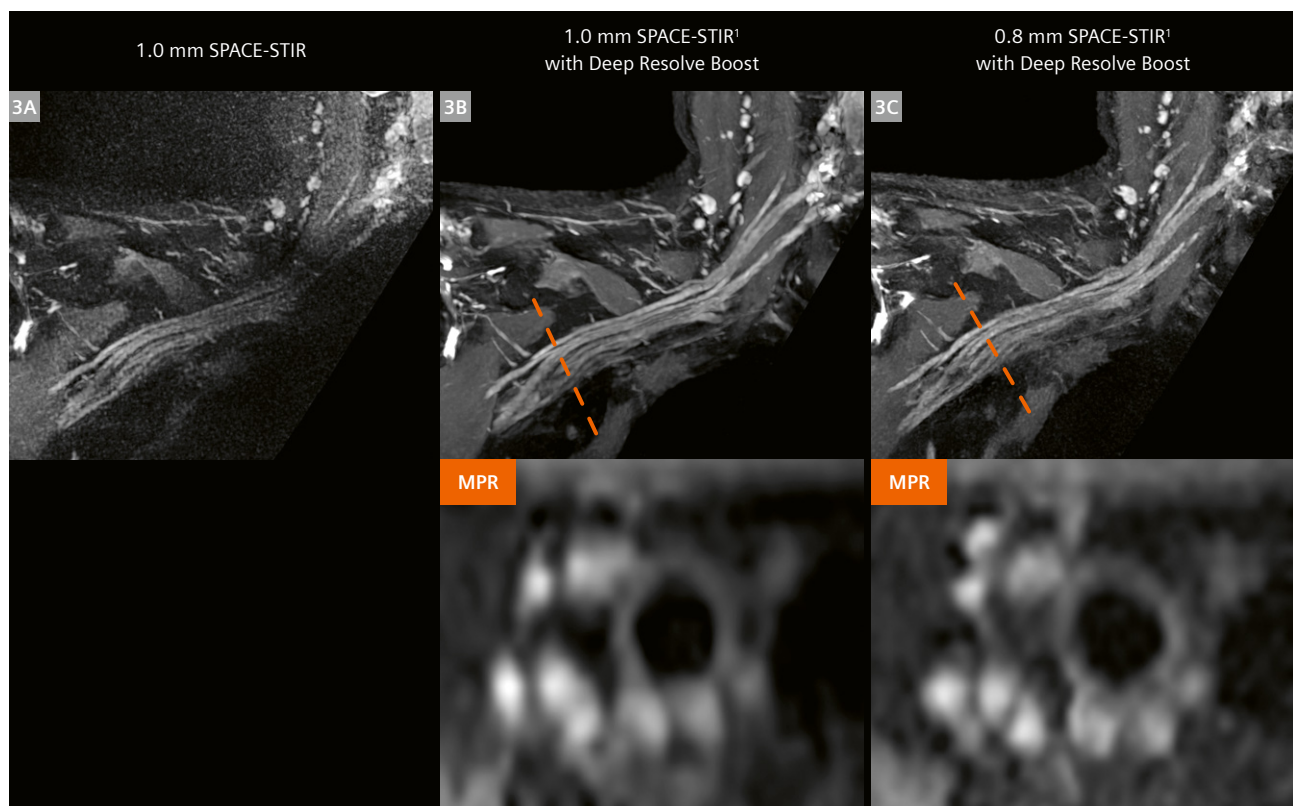
2D MRN

Orthogonal 2D MRN imaging typically provides higher in-plane spatial resolution, compared to 3D sequences, to better evaluate fascicular architecture [6]. However, achieving high in-plane spatial resolution (< 0.5 mm) within a clinically reasonable scan time (to mitigate respiratory motion artifact) while also maintaining adequate SNR poses a significant challenge. The Siemens Healthineers Deep Resolve Boost reconstruction algorithm helps mitigate these challenges by reducing noise amplification or blurring [7], when applying parallel imaging acceleration or partial Fourier acquisition.

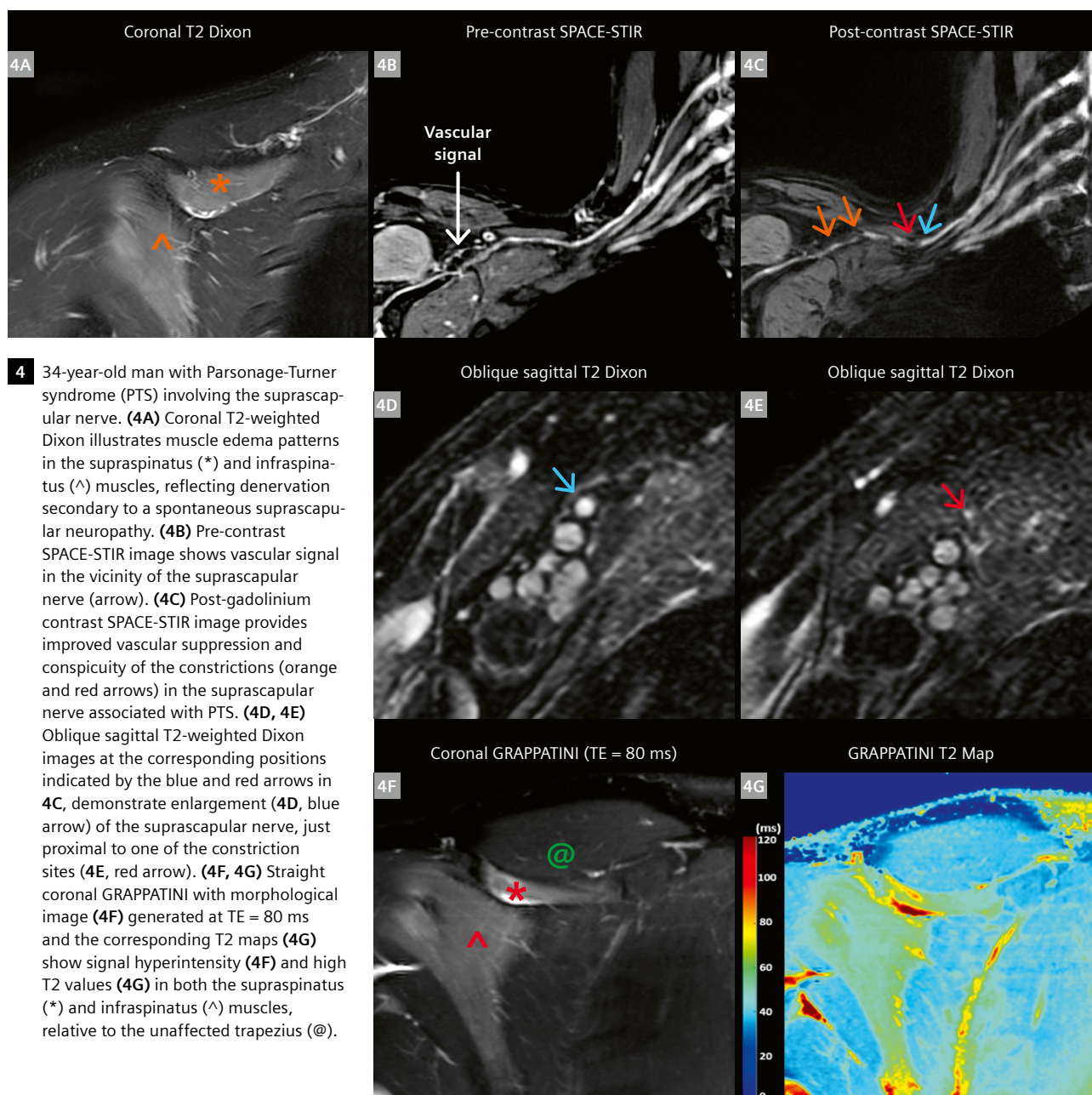
Applying fat suppression techniques is also crucial in 2D MRN to enhance the contrast ratio between the peripheral nerves and surrounding fat. We typically employ the Dixon method in this context due to its ability to simultaneously provide homogenous fat suppression (despite field inhomogeneities) and high SNR efficiency. This is particularly important in the neck-shoulder region, which has high B_0 -variation. For the 2D Dixon sequence on the MAGNETOM Vida system, one can choose between 'strong' and 'weak' fat suppression modes to modulate the degree to which the fat signal contributes to the MR images. Our preference is the 'strong' option to optimize nerve/muscle and nerve/fat contrast.

Respiratory triggering

Orthogonal imaging planes, particularly those through the infraclavicular segments of the BP, are prone to aliasing from respiratory motion due to the proximity of such segments to the lung apex. Respiratory motion artifacts are sometimes severe and may render the exam uninterpretable. Use of prospective respiratory



3 Comparison of SPACE-STIR acquired with standard reconstruction and with Deep Resolve (DR) Boost reconstruction. The top row images are all coronal SPACE-STIR images with 10 mm maximal intensity projection (MIP). **(3A)** Standard reconstruction of a 1.0 mm isotropic acquisition exhibits poor conspicuity of the brachial plexus. **(3B)** With DR Boost, improved conspicuity of the nerves is observed. **(3C)** DR Boost with 0.8 mm acquisition is feasible, providing sharper nerve definition, especially in the oblique-axial multiplanar reformation orthogonal to the brachial plexus at the level of the dashed lines (bottom row).

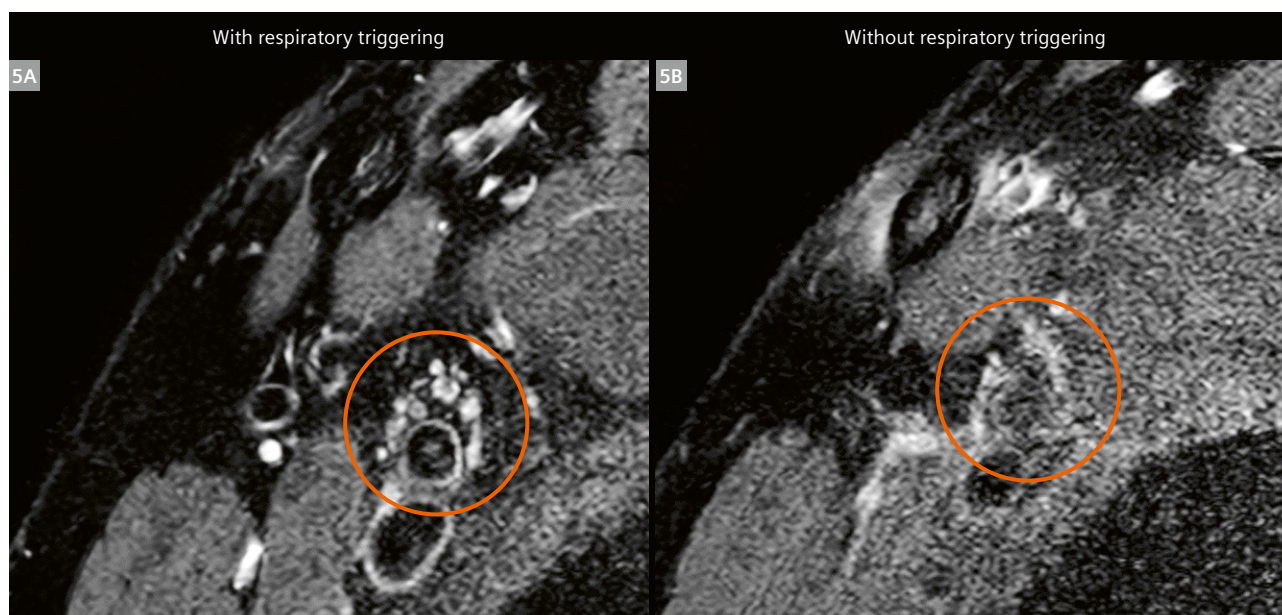


triggering via bellows to enable acquisitions during maximal end-expiration has been shown to improve interobserver agreement and nerve conspicuity [8]. On the MAGNETOM Vida, prospective respiratory gating uses the BioMatrix Respiratory Sensor embedded into the posterior spine array. These sensors automatically detect and record respiratory and head movements once the patient is positioned on the table. This feature enhances workflow efficiency by enabling technologists to perform respiratory-triggered scans without incurring additional setup time (Fig. 5). Alternatively, the respiratory signal may also be obtained using the respiratory cushion

complete with belt setup where an additional posterior phased-array coil is placed between the patient and the table in the two-coil setup.

Future directions

Quantitative MRI techniques, including T2 mapping, perfusion, and diffusion-weighted or diffusion tensor imaging (DWI/DTI), carry the potential to supplement qualitative BP assessment. A study of patients with chronic inflammatory demyelinating polyneuropathy found that not only were nerve root sizes enlarged but also demonstrated elevated



5 Oblique sagittal T2 Dixon imaging through the infraclavicular plexus (distal acquisition), demonstrates improved conspicuity of the cords with prospective respiratory gating (5A, using the imbedded BioMatrix Sensors) compared to the non-gated respiratory acquisition (5B). Note that the gated scan requires approximately two minutes longer to acquire.

T2 relaxation times [9]. A quantitative Siemens Healthineers MRI prototype sequence, generalized autocalibrating partially parallel acquisition with the model-based accelerated relaxometry by iterative nonlinear inversion (GRAPPATINI)¹, can provide accurate T2 estimations and synthetic morphologic images [10, 11]. This technique may enable simultaneous qualitative and quantitative evaluation of both nerves and muscles in MR neurography, thereby shortening overall scan time and reducing registration errors between two separate acquisitions (Fig. 4F–G).

References

- Davidson EJ, Tan ET, Pedrick EG, Sneag DB. Brachial Plexus Magnetic Resonance Neurography: Technical Challenges and Solutions. *Invest Radiol*. 2023;58(1):14-27.
- Sneag DB, Queler S. Technological Advancements in Magnetic Resonance Neurography. *Curr Neurol Neurosci Rep*. 2019;19(10):75.
- Ordidge RJ, Wylezinska M, Hugg JW, Butterworth E, Franconi F. Frequency offset corrected inversion (FOCI) pulses for use in localized spectroscopy. *Magn Reson Med*. 1996;36(4):562-566.
- Wang X, Greer JS, Dimitrov IE, Pezeshk P, Chhabra A, Madhuranthakam AJ. Frequency Offset Corrected Inversion Pulse for B0 and B1 Insensitive Fat Suppression at 3T: Application to MR Neurography of Brachial Plexus. *J Magn Reson Imaging*. 2018;48(4):1104-1111.
- Sneag DB, Daniels SP, Geannette C, Queler SC, Lin BQ, de Silva C, et al. Post-Contrast 3D Inversion Recovery Magnetic Resonance Neurography for Evaluation of Branch Nerves of the Brachial Plexus. *Eur J Radiol*. 2020;132:109304.
- Sneag DB, Rancy SK, Wolfe SW, Lee SC, Kalia V, Lee SK, et al. Brachial plexitis or neuritis? MRI features of lesion distribution in Parsonage-Turner syndrome. *Muscle Nerve*. 2018;58(3):359-366.
- Zochowski KC, Tan ET, Argentieri EC, Lin B, Burge AJ, Queler SC, et al. Improvement of peripheral nerve visualization using a deep learning-based MR reconstruction algorithm. *Magn Reson Imaging*. 2022;85:186-192.
- Sneag DB, Mendapara P, Zhu JC, Lee SC, Lin B, Curlin J, et al. Prospective respiratory triggering improves high-resolution brachial plexus MRI quality. *J Magn Reson Imaging*. 2019;49(6):1723-1729.
- Hiwatashi A, Togao O, Yamashita K, Kikuchi K, Momosaka D, Nakatake H, et al. Simultaneous MR neurography and apparent T2 mapping in brachial plexus: Evaluation of patients with chronic inflammatory demyelinating polyradiculoneuropathy. *Magn Reson Imaging*. 2019;55:112-117.
- Roux M, Hilbert T, Hussami M, Becce F, Kober T, Omoumi P. MRI T2 Mapping of the Knee Providing Synthetic Morphologic Images: Comparison to Conventional Turbo Spin-Echo MRI. *Radiology*. 2019;293(3):620-630.
- Wang F, Zhang H, Wu C, Wang Q, Hou B, Sun Y, et al. Quantitative T2 mapping accelerated by GRAPPATINI for evaluation of muscles in patients with myositis. *Br J Radiol*. 2019;92(1102):20190109.

Contact

Darryl B. Sneag, M.D.
Director of MRI Research & MR Neurography
Hospital for Special Surgery
535 East 70th Street
New York, NY 10021
USA
Tel.: +1 646 714 6043
sneagdb@HSS.EDU



¹Work in progress. The product is still under development and not commercially available. Its future availability cannot be ensured.

Advancing Clinical and Neuroscientific Research Through Accessible and Optimized Protocol Design at 3T

Sriranga Kashyap, Ph.D.¹; Kâmil Uludağ, Ph.D.^{1,2,3,4}

¹BRAIN-TO Lab, Krembil Brain Institute, University Health Network, Toronto, ON, Canada

²Department of Medical Biophysics, University of Toronto, Toronto, ON, Canada

³Center for Neuroscience Imaging Research, Institute for Basic Science, Suwon, Republic of Korea

⁴Department of Biomedical Engineering, Sungkyunkwan University, Suwon, Republic of Korea

Background

Rising concern about healthcare costs and research funding is driving transformative shifts in the field of MR imaging. Collaborative efforts among academics, clinicians, and industry experts are helping dispel outdated notions of MRI as a slow and costly modality. Nevertheless, cutting-edge technological advancements achieved in academia and industry are difficult to translate into a shift in cognitive neuroscience and clinical research and patient care due to a multitude of factors – particularly the availability of technical expertise and time. Clinicians and neuroscientists often rely on colleagues and/or consortia (such as the Human Connectome Project and the Alzheimer's Disease Neuroimaging Initiative) to obtain imaging protocols for their research. This results in a wide variation in imaging protocols used within a single institution, and even by a single researcher for their different

projects. Even sequences considered fairly routine and standard, such as T1w MPRAGE, have a large variation in imaging parameters, and there is no guarantee they will be compatible with post-hoc data analyses. In this article, we detail a strategic approach to developing a set of optimized neuroimaging protocols and present optimized parameters for the 3T MAGNETOM Prisma scanner (Siemens Healthcare, Erlangen, Germany) that are not only faster and more efficient but have also been tested and validated using community-standard MRI post-processing software.

Design principles

When optimizing the BRAIN-TO (Brain Research in Advanced Imaging and Neuromodeling – Toronto) protocols, several overarching principles were applied:

Structural Imaging		Diffusion Imaging			
✓ Standard Sagittal w Axial MPR		20 channel coil			
bto_MPRAGE_2x1_1mm_iso 04:20		Multi-Shell			
bto_SPACE-T2_2x2_CAIP1_1mm_iso 03:17		yes		no	
bto_SPACE-FLAIR_2x2_CAIP1_1mm_... 04:14		Fast		Fast	
bto_MP2RAGE_2x1_1mm_iso_Map1... 07:11		yes		no	
bto_FGATIR_2x1_1mm_iso 05:23		bto_EP2D_DWI_2x2_2mm_iso_64d... 05:33	bto_EP2D_DWI_2x2_2mm_iso_64d... 10:21	bto_EP2D_DWI_2x2_2mm_iso_30d... 03:00	bto_EP2D_DWI_2x2_2mm_iso_64d... 05:33
bto_ME-GRE_largeFoV_2x1_1p0mm 10:35		bto_EP2D_DWI_2x2_2mm_iso_30d... 03:00	bto_EP2D_DWI_2x2_2mm_iso_5b0... 00:45	bto_EP2D_DWI_2x2_2mm_iso_5b0... 00:45	bto_EP2D_DWI_2x2_2mm_iso_5b0... 00:45
		bto_EP2D_DWI_2x2_2mm_iso_5b0... 00:45			
		</			

1 Example BTO imaging strategies laid out using the MAGNETOM Prisma Dot Cockpit interface.

First, the protocols should be built on product sequences from Siemens Healthineers (no work-in-progress packages or C2Ps) to maximize accessibility.

Second, all protocols should have spatially isotropic voxels to reduce partial voluming and voxel volumes. Because the cortex is curved, using anisotropic voxels (as is often the case in patient care) potentially reduces diagnostic value in the dimension with the lowest spatial resolution and should therefore be avoided.

Third, each scan should have a maximum acquisition time of 5 to 6 minutes (exceptions include multi-echo FLASH, multi-shell diffusion, resting-state, and functional MRI) to minimize participant discomfort and motion artifacts.

Fourth, the protocols should be optimized to take advantage of the acceleration capabilities of the head coil (20-channel Head/Neck, 32-channel Head, 64-channel Head/Neck), thus offering higher spatial and/or temporal resolution.

Finally, these optimized protocols should be organized using the Strategy and Decision Tree features in the Dot Cockpit interface from Siemens Healthineers. This means they will offer easy access to the end-users and can be made available to collaborating institutes as .exar1 packages. Unless otherwise specified, the parameters, data, and results illustrated hereafter are for the 20-channel Head/Neck coil.

BRAIN-TO (BTO) protocols

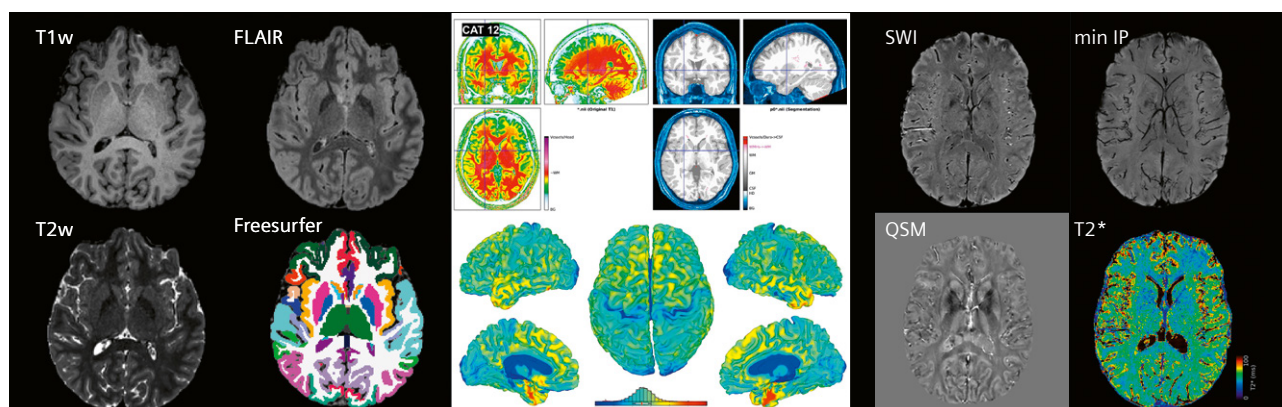
All data acquired from BTO protocols have been tested and validated for clinical and neuroscientific research applications using community-standard tools such as Freesurfer [1], FSL [2], SPM [3], CAT [4], and AFNI [5]. Generalized versions of the code and/or containers, as well as a wiki with recommendations for post-processing, are available through our lab at https://github.com/BRAIN-TO/bto_mri_protocols_info.

Structural imaging

In line with the design principles outlined earlier, the structural imaging component of the BRAIN-TO protocol set constitutes 1 mm isotropic 3D MPRAGE, 3D MP2RAGE, 3D SPACE T2, and 3D SPACE FLAIR sequences. A multi-echo FLASH protocol has also been incorporated. It enables quantitative T2* mapping, susceptibility weighted imaging (SWI) [6], and quantitative susceptibility mapping (QSM) [7] and takes about 10 minutes to acquire in 1 mm isotropic and high-resolution variants (only tested for 32- and 64-channel coils). It is important to point out that clinical research applications have different requirements to diagnostic imaging [8]. In this context, the increase in resolution and savings in time are a good trade-off [9] to enable resolution and field-of-view (FOV) matching of the T1w and FLAIR images and their integration into a post-processing pipeline without resampling artifacts.

	Sequence	Spatial resolution (mm)	Sequence parameters	Acquisition time (min:sec)	Acquisition time difference	Voxel volume difference
Typical T1w	3D MPRAGE	1 × 1 × 1	GRAPPA = 2, TE = 4.1 ms, TR = 2000 ms, IR = non-sel, TI = 899 ms, $\alpha = 8^\circ$, FOV = 256 × 256, 160 axial slices, Inline MPR = off	06:00		
BTO T1w	3D MPRAGE	1 × 1 × 1	GRAPPA = 2, TE = 2.88 ms, TR = 2100 ms, IR = non-sel, TI = 900 ms, $\alpha = 9^\circ$, FOV = 256 × 256, 256 sagittal slices, Inline MPR = tra	04:20	– 28%	0%
Typical FLAIR	IR 2D TSE	0.8 × 0.8 × 4	GRAPPA = 2, TE = 94 ms, TR = 9000 ms, TI = 2500 ms, IR = Slice-sel, $\alpha = 150^\circ$, FOV = 275 × 245, 32 axial slices, distance factor = 25%, Inline MPR = off, interpolation = on	02:44		
BTO FLAIR	3D SPACE	1 × 1 × 1	CAIPIRINHA = 2 × 2, TE = 393 ms, TR = 4500 ms, TI = 1800 ms, IR = non-sel, α = variable, FOV = 256 × 256, 256 sagittal slices, Inline MPR = tra	04:14	+ 55%	– 61%
BTO T1 map	3D MP2RAGE	1 × 1 × 1	GRAPPA = 2, TE = 2.98 ms, TR = 4500 ms, TI ₁ /TI ₂ = 850/2550 ms, IR = non-sel, $\alpha_1/\alpha_2 = 5^\circ/6^\circ$, FOV = 256 × 256, 224 sagittal slices, distance Inline MPR = tra, MapIt = T1 map	07:11	+ 20%	0%
BTO multi-echo	3D GRE	1 × 1 × 1	GRAPPA = 2, TE ₁₋₃ = 12/24/38 ms, TR = 55 ms, $\alpha = 20^\circ$, FOV = 224 × 224, 160 axial slices	10:35		

Table 1: Comparison of typical vs. BTO protocols for structural imaging



2 Example images from the BTO structural protocols and their post-processed results.

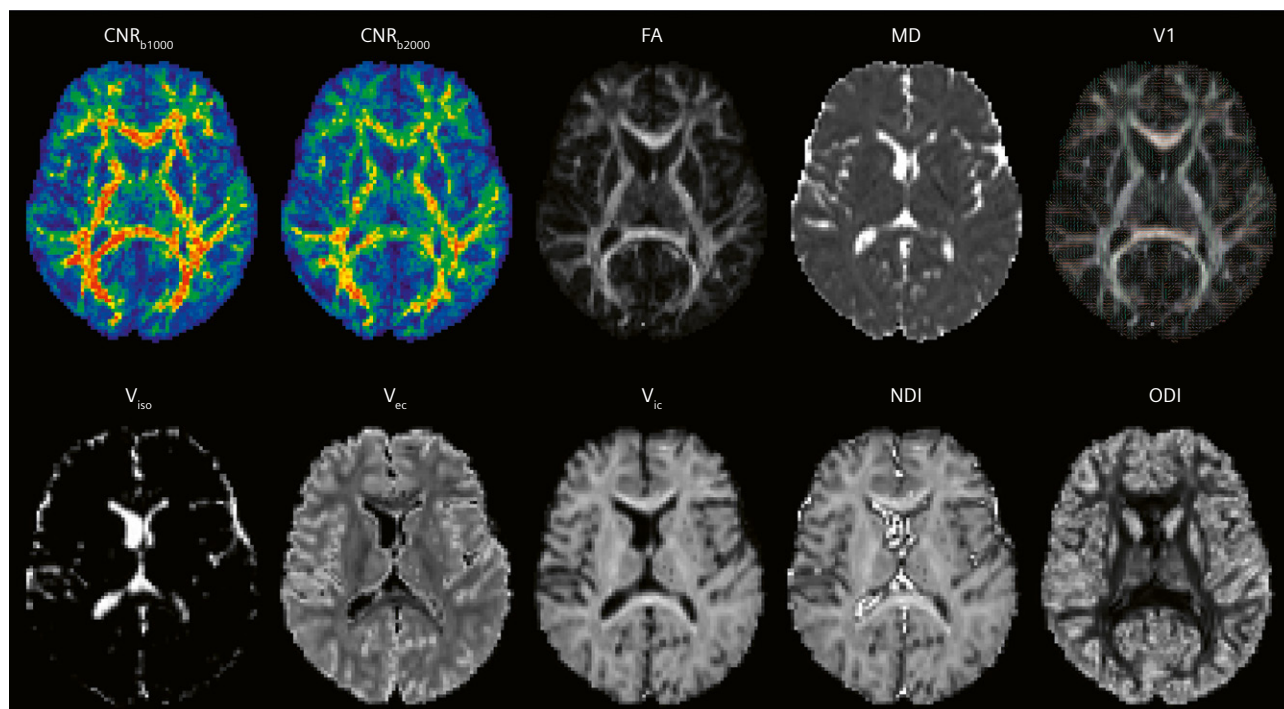
Diffusion imaging

The diffusion imaging component consists of a fast single-shell protocol, a comprehensive single-shell protocol, and a multi-shell protocol for neurite orientation dispersion density imaging (NODDI) [10]. Each protocol has been implemented with two versions: first, with the default diffusion vector set from Siemens Healthineers; second, with a custom diffusion vector set with interspersed b_0 s while ensuring uniform coverage of q-space [11]. The data acquired from BTO protocols were tested, processed, and evaluated for quality using community-standard tools such

as FSL and MRtrix3 [12]. Two example scenarios can be envisioned here. In the first, the investigator is only interested in assessing fractional anisotropy (FA), mean diffusivity (MD), and diffusion tensor (DTI). In that case, they can opt for the BTO single-shell, fast protocol to acquire the data in 3 minutes. In the second scenario, the researcher is also interested in tractography, and can opt for the BTO single-shell protocol to acquire the data in 5.5 minutes. The end-user can make these decisions with the knowledge that the data will be of sufficient quality during

	Sequence	Spatial resolution (mm)	Sequence parameters	Acquisition time (min:sec)	Acquisition time difference	Voxel volume difference
Typical DWI	2D EPI	$2.4 \times 2.4 \times 2.4$	GRAPPA = 2, SMS = 2, TE = 68 ms, TR = 3400 ms, Partial Fourier = 6/8, FOV = 230×230 , echo-spacing = 0.76 ms, bandwidth = 1488 Hz/px, 68 axial slices, diff. directions = 64, $b_1/b_2 = 0/1000$ s/mm ² , averages $b_1/b_2 = 1/2$	07:37		
BTO DWI (single-shell)	2D EPI	$2 \times 2 \times 2$	GRAPPA = 2, SMS = 2, TE = 75 ms, TR = 4500 ms, Partial Fourier = 6/8, FOV = 220×220 , echo-spacing = 0.56 ms, bandwidth = 2164 Hz/px, 84 axial slices, diff. directions = 64, $b_1/b_2 = 0/1000$ s/mm ² , averages $b_1/b_2 = 5/1$	05:33	– 27%	– 42%
BTO DWI (single-shell, fast)	2D EPI	$2 \times 2 \times 2$	GRAPPA = 2, SMS = 2, TE = 75 ms, TR = 4500 ms, Partial Fourier = 6/8, FOV = 220×220 , echo-spacing = 0.56 ms, bandwidth = 2164 Hz/px, 84 axial slices, diff. directions = 30, $b_1/b_2 = 0/1000$ s/mm ² , averages $b_1/b_2 = 5/1$	03:00	– 61%	– 42%
BTO NODDI (multi-shell)	2D EPI	$2 \times 2 \times 2$	GRAPPA = 2, SMS = 2, TE = 75 ms, TR = 4500 ms, Partial Fourier = 6/8, FOV = 220×220 , echo-spacing = 0.56 ms, bandwidth = 2164 Hz/px, 84 axial slices, diff. directions = 30/64, $b_1/b_2 = 0/1000/2000$ s/mm ² , averages $b_1/b_2 = 5/1/1$	08:33 As 2 runs Run 1: 30 dirs, b1000 = 03:00 Run 2: 64 dirs, b2000 = 5:33	+ 12%	– 42%

Table 2: Comparison of typical vs. BTO protocols for diffusion imaging



3 Example images from the BTO diffusion NODDI protocol and its post-processed results.

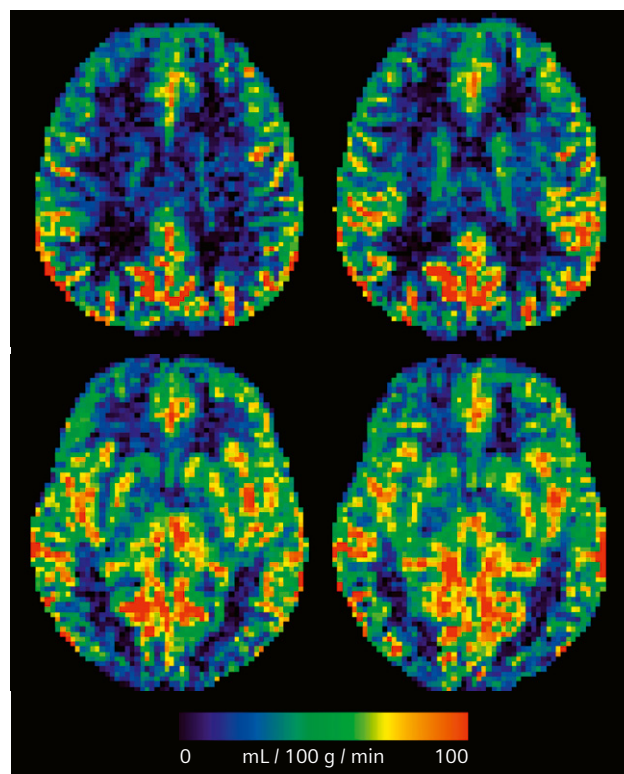
post-processing. It is important to reiterate that these are optimized, general-purpose protocols. They are not designed for bespoke investigations.

Perfusion imaging

Non-invasive perfusion MRI is typically carried out using Arterial Spin Labelling (ASL) sequences that use magnetically labelled arterial blood water as an endogenous tracer to measure blood flow. While community-standard protocols [13] with spatial resolutions of 3 to 4 mm in-plane and 4 to 8 mm slice thickness may suffice for detecting macroscale perfusion patterns in the brain, the anisotropy and increased partial voluming is sub-optimal for clinical and neuroscientific research. The BTO perfusion protocol set consists of whole-brain 3 mm and 2.5 mm isotropic pseudocontinuous ASL (pCASL) and pulsed ASL (PASL) options in a total acquisition time of 4 to 6 minutes. Recently, we pushed this boundary further to evaluate the feasibility of 2 mm isotropic whole-brain ASL and the impact of coil and post-processing choices on the perfusion maps [14].

BOLD imaging (functional MRI)

The functional MRI (fMRI) component that uses the gradient-echo 2D EPI sequence from Siemens Healthineers



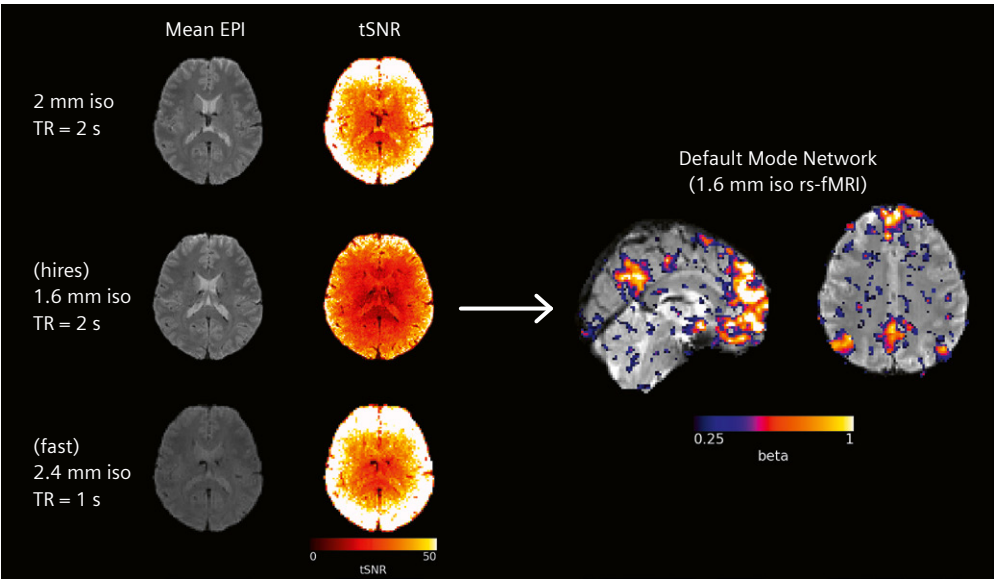
4 Example slices of a single-subject cerebral blood flow map from the BTO 2.5 mm isotropic perfusion protocol.

is by far the most diverse component of the BTO protocol set. Particular emphasis has been placed on providing investigators with a modern fMRI protocol with 2.4 mm isotropic resolution and a community-standard TR of 2.0 seconds employing nominal acceleration factors and applicable for any coil. All BTO fMRI protocols have dedicated variants for 32- and 64-channel coils to make maximum use of the acceleration capabilities. This results in particularly high in-plane resolution and/or Simultaneous Multi-Slice (SMS) factors for higher temporal resolution. For example, the 64-channel coil variant of the standard

BTO BOLD protocol has an increased SMS factor of 4 and a volume TR of 1 second for the same spatial resolution. While staying true to the design principles and generalizability, the BTO BOLD protocols also offer direct decision-making choices without having to worry about the implications of the other parameter choices, as we have assessed the protocols using both resting and task fMRI. We are delighted to report that, over the past year, our protocol offerings have covered a vast array of requirements at our site and did not require case-by-case modifications.

	Sequence	Spatial resolution (mm)	Sequence parameters	Acquisition time (min:sec)	Acquisition time difference	Voxel volume difference
Typical BOLD	2D EPI	3 × 3 × 4	GRAPPA = 2, TE = 30 ms, α = 85°, FOV = 220 × 220, echo-spacing = 0.93 ms, bandwidth = 1184 Hz/px, 40 axial slices	2.0		
BTO BOLD (std)	2D EPI	2.4 × 2.4 × 2.4	GRAPPA = 2, SMS = 2, TE = 30 ms, α = 70°, FOV = 220 × 220, echo-spacing = 0.49 ms, bandwidth = 2470 Hz/px, 68 axial slices	2.0		– 62%
BTO BOLD (std high-res)	2D EPI	2 × 2 × 2	GRAPPA = 2, SMS = 2, TE = 30 ms, α = 70°, FOV = 220 × 220, echo-spacing = 0.53 ms, bandwidth = 2272 Hz/px, 62 axial slices	2.0		– 78%
			32- / 64-channel coils			
BTO BOLD (high-res)	2D EPI	1.6 × 1.6 × 1.6	RAPPA = 2, SMS = 4, TE = 30 ms, α = 70°, FOV = 220 × 220, echo-spacing = 0.61 ms, bandwidth = 1906 Hz/px, 100 axial slices	2.0		– 88%
BTO BOLD (fast)	2D EPI	2.4 × 2.4 × 2.4	GRAPPA = 2, SMS = 4, TE = 30 ms, α = 70°, FOV = 220 × 220, echo-spacing = 0.49 ms, bandwidth = 2470 Hz/px, 68 axial slices	1.0	– 50%	– 62%

Table 3: Comparison of typical vs. BTO protocols for BOLD imaging



5 Example slices of the mean EPI images and temporal signal-to-noise ratio (tSNR) of three BTO BOLD fMRI protocols acquired using the 32-channel Head coil. Illustration of the Default Mode Network obtained from a high-resolution (hi-res) 1.6 mm isotropic resting-state BOLD fMRI acquisition.

Summary

The BRAIN-TO (BTO) protocols present a comprehensive approach to making optimized neuroimaging protocols accessible to clinical and neuroscientific researchers. The BTO protocols are designed based on key principles, utilizing Siemens Healthineers product sequences for accessibility. They incorporate spatially isotropic voxels, efficient scan times, and dedicated variants for using head coils with denser coil arrays. We hold Town Hall sessions to disseminate information about the BTO protocols to our on-site neuroimaging community. To improve the accessibility to advanced neuroimaging, we make the guidelines for processing data acquired with the standard protocols and analysis code available through a dedicated GitHub repository (https://github.com/BRAIN-TO/bto_mri_protocols_info). The BTO protocols not only cover diverse imaging modalities, including structural imaging, diffusion imaging, perfusion, and BOLD imaging, but have also been rigorously tested and validated using community-standard post-processing tools. This enhances their reliability, reassures the end-user, and makes cutting-edge plug-and-play neuroimaging a reality.

References

- 1 Fischl B. FreeSurfer. *NeuroImage*. 2012;62(2):774–81.
- 2 Smith SM, Jenkinson M, Woolrich MW, Beckmann CF, Behrens TEJ, Johansen-Berg H, et al. Advances in functional and structural MR image analysis and implementation as FSL. *NeuroImage*. 2004;23 Suppl 1:S208–19.
- 3 Ashburner J. Computational anatomy with the SPM software. *Magn Reson Imaging*. 2009;27(8):1163–74.
- 4 Eickhoff SB, Stephan KE, Mohlberg H, Grefkes C, Fink GR, Amunts K, et al. A new SPM toolbox for combining probabilistic cytoarchitectonic maps and functional imaging data. *NeuroImage*. 2005;25(4):1325–35.
- 5 Cox RW. AFNI: Software for Analysis and Visualization of Functional Magnetic Resonance Neuroimages. *Comput Biomed Res*. 1996;29(3):162–73.
- 6 Eckstein K, Bachrata B, Hangel G, Widhalm G, Enzinger C, Barth M, et al. Improved susceptibility weighted imaging at ultra-high field using bipolar multi-echo acquisition and optimized image processing: CLEAR-SWI. *NeuroImage*. 2021;237:118175.
- 7 Langkammer C, Bredies K, Poser BA, Barth M, Reishofer G, Fan AP, et al. Fast quantitative susceptibility mapping using 3D EPI and total generalized variation. *NeuroImage*. 2015;111:622–30.
- 8 Kakeda S, Korogi Y, Hiai Y, Ohnari N, Sato T, Hirai T. Pitfalls of 3D FLAIR brain imaging: a prospective comparison with 2D FLAIR. *Acad Radiol*. 2012;19(10):1225–32.
- 9 Kitajima M, Hirai T, Shigematsu Y, Uetani H, Iwashita K, Morita K, et al. Comparison of 3D FLAIR, 2D FLAIR, and 2D T2-Weighted MR Imaging of Brain Stem Anatomy. *AJNR Am J Neuroradiol*. 2012;33(5):922–7.
- 10 Zhang H, Schneider T, Wheeler-Kingshott CA, Alexander DC. NODDI: Practical in vivo neurite orientation dispersion and density imaging of the human brain. *NeuroImage*. 2012;61(4):1000–16.
- 11 Caruyer E, Lenglet C, Sapiro G, Deriche R. Design of multishell sampling schemes with uniform coverage in diffusion MRI: Design of Multishell Sampling Schemes. *Magn Reson Med*. 2013;69(6):1534–40.
- 12 Tournier JD, Smith R, Raffelt D, Tabbara R, Dhollander T, Pietsch M, et al. MRtrix3: A fast, flexible and open software framework for medical image processing and visualisation. *NeuroImage*. 2019;202:116137.
- 13 Alsop DC, Detre JA, Golay X, Gunther M, Hendrikse J, Hernandez-Garcia L, et al. Recommended implementation of arterial spin-labeled perfusion MRI for clinical applications: A consensus of the ISMRM perfusion study group and the European consortium for ASL in dementia. *Magn Reson Med*. 2015;73(1):102–16.
- 14 Kashyap S, Oliveira ÍAF, Uludağ K. Feasibility of high-resolution perfusion imaging using Arterial Spin Labelling MRI at 3 Tesla. *bioRxiv [Internet]*. 2023 [cited 2023 Sep 2]; Available from: <http://biorxiv.org/lookup/doi/10.1101/2023.08.02.551576>

Contact

Sriranga Kashyap, Ph.D.
Research Fellow, BRAIN-TO Lab
Krembil Brain Institute, Toronto Western Hospital
University Health Network
135 Nassau St
Toronto, ON, M5T 1M8
Canada
sriranga.kashyap@uhn.ca



Sriranga Kashyap, Ph.D. Kâmil Uludağ, Ph.D.



Intracranial Vessel Wall MRI

Luigi Cirillo^{*1,2,3}; Arianna Rustici^{*1,3,4}; Tommaso Kaswalder²; Ciro Princiotta²; Massimo Dall'Olio²; Caterina Tonon^{1,3}; Domenico Zacà⁵; Raffaele Lodi^{1,6}

¹Department of Biomedical and Neuromotor Sciences (DIBINEM), University of Bologna, Italy

²UOC di Neuroradiologia, IRCCS Istituto delle Scienze Neurologiche di Bologna, Italy

³Programma Neuroimmagini Funzionali e Molecolari, IRCCS Istituto delle Scienze Neurologiche di Bologna, Italy

⁴UO di Neuroradiologia OM, IRCCS Istituto delle Scienze Neurologiche di Bologna, Italy

⁵Siemens Healthcare Srl, Milano, Italy

⁶IRCCS Istituto delle Scienze Neurologiche di Bologna, Italy

**These authors contributed equally and share first authorship.*

Introduction

To date, MR is the only clinically available imaging modality that allows to image the brain vessels beyond the 'lumen techniques', depicting both the lumen and the vessel walls with high sensitivity and low invasiveness [1]. Besides standard MR angiography (MRA) sequences, some MR sequences for vessel wall imaging have been introduced into clinical practice [2]. These MR sequences allow to depict the vessel walls at high resolution, and are becoming emerging techniques for evaluating cerebrovascular diseases.

Although vessel wall MRI (VW MRI) sequences are widely reported to be effective and efficient [3], there are no commercially available sequences optimized for intracranial imaging. In fact, VW MRI requires a very complex signal because the signal from both the blood inside the lumen and from the outer cerebrospinal fluid (CSF) must be suppressed.

This article describes the technical aspects of our VW MRI sequence¹ so that other institutions can develop their own sequence for the diagnosis and follow-up of cerebrovascular pathologies.

Technique

We developed our optimized protocol on a 3T MAGNETOM Skyra system (Siemens Healthcare, Erlangen, Germany). It is based on a T1-weighted 3D SPACE sequence. Specific parameters have been modified to achieve sufficient signal-to-noise ratio (SNR) and contrast-to-noise ratio (CNR) for vessel wall imaging. Moreover, we set parameters to obtain isotropic 3D imaging, achieve good suppression of CSF and blood, and reduce scan time (to avoid artifacts caused by patient motion) [4, 5]. The total scan time is 7 minutes 10 seconds.

Sequence parameter	
Acquisition time	7:10 min
Orientation	Coronal
Type	3D
Slice for slab	80
Slice oversampling	10.0%
Slice thickness	0.60 mm
FOV read (mm)	160 mm
FOV phase (%)	82.8%
Phase oversampling	20%
Phase resolution	100%
Voxel size	0.3 × 0.3 × 0.6
TR (ms)	1000 ms
TE (ms)	38 ms
ETL	211 ms
Flip angle (°)	T1 variable
Bandwidth (Hz/pixel)	514 Hz/Px
k-space filling	Interpolation with zero-filling
PAT mode	GRAPPA
Accel. factor PE	2
Ref. lines PE	24
Fat suppression	None
Dark blood	Off

Table 1: Our sequence parameters for vessel wall MRI at 3T.

¹Work in progress. The application is still under development and not commercially available. Its future availability cannot be ensured.

Our VW MRI sequence is a 3D multi-slab acquisition (80 slices per slab, each with 0.60 mm slice thickness) acquired in coronal plane, with a rectangular field of view (FOV read = 160 mm; FOV phase = 82.8%) (Table 1). To reduce the slab boundary artifact, we use oversampling in the slice direction (slice oversampling = 10.0%). To avoid the wrap-around artifact, we use phase oversampling (phase oversampling = 20%; phase resolution = 100%).

With spin echo (SE) sequences, it is possible to adjust the TR (repetition time) and TE (echo time) to suit specific needs. We therefore set the TR to 1000 ms and the TE to 38 ms (Table 1), to achieve a CSF darkening effect by tailoring image contrast to T1 weighting and proton-density (PD) weighting (Table 2).

The black-blood effect is achieved by the intravoxel dephasing of moving blood spins within a long echo train length (ETL = 211 ms). A variable refocusing flip angle is used to compensate for the signal decay inherent in the long ETL.

The difference in the precession frequencies of the spins inside the voxels at the extremities of the FOV is set at 514 Hz/Px (bandwidth).

To reduce scan time, a parallel imaging acquisition technique (iPAT) called GRAPPA (Generalized Autocalibrating Partially Parallel Acquisitions) is used, with an acceleration factor (R) of 2, and 24 reference lines in the phase-encoding direction, to compensate for the under-sampling of the *k*-space (Table 1).

With those parameters, there is no need for an inferior outer volume suppression pulse to limit the inflow effects of blood, and no need for a fat-saturation pulse (Tables 1 and 2).

Discussion

Intracranial VW MRI is a complex technique that requires elevated spatial and contrast resolution, and the ability to detect contrast enhancement after the administration of contrast medium.

Correctly visualizing the intracranial vessel walls relies on the suppression of the outer and inner structures. The signal of both the blood inside the lumen and of the outer CSF must therefore be suppressed. Although both structures are fluids, different suppression techniques are required because of their different properties. MR vendors have developed many different fluid-suppression techniques, each with some limitations [6, 7].

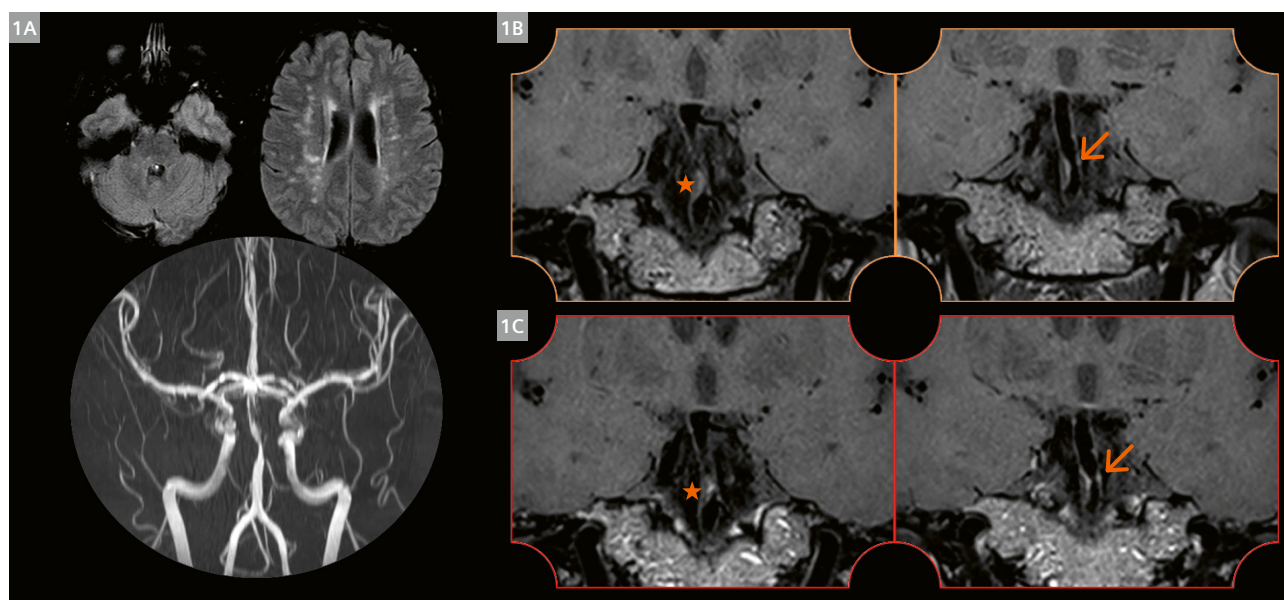
Due to the difficulty of generating one signal while suppressing others, and to the heterogeneity of scanners and coils, no sequences optimized for intracranial imaging are commercially available [8].

The basis of our VW MRI sequence is a 3D SPACE sequence, which is a spin-echo sequence. As all spin-echo sequences are pulsed sequences, they allow us to obtain different weighting based on predefined timing parameters, such as TR and TE. We decided to maintain the contrast of our sequence intermediate between the T1 and PD weighting. This is because the T1-weighted sequences have the advantage of clearer enhancement after the administration of contrast medium, whereas PD-weighted sequences provide a higher SNR [8] (Table 2). Moreover, an intermediate T1/PD weighting achieves the required CSF suppression, due to its long T1 relaxation time (Table 2).

Many different and complex techniques have been developed to suppress flowing blood. Each of them has some limitations [6, 7]. The most commonly used suppression methods are the black-blood techniques [6]. They can be broadly classified as either flow-dependent or flow-independent [7]. Although blood-suppression techniques are not the subject of this paper, it must be noted that the black-blood techniques have several limitations and could lead to artifacts [7], the most common of which is the presence of a residual blood signal, which is due to insufficient blood suppression and can mimic or obscure vascular pathologies. This can occur in cases of stagnant, slow, or retrograde blood flows, and typically with flow-dependent techniques.

	T1-weighted	PD-weighted	T2-weighted
CSF	Dark	Light gray	Bright
Blood inside vessels	Bright	Dark	Dark
Advantages	<ul style="list-style-type: none"> • High anatomical detail • High contrast to Gd • Relatively short lead times 	<ul style="list-style-type: none"> • High SNR • High anatomical detail 	<ul style="list-style-type: none"> • High tissue contrast
Disadvantages	<ul style="list-style-type: none"> • Low tissue contrast 	<ul style="list-style-type: none"> • Reduced contrast enhancement • Reduced suppression of CSF 	<ul style="list-style-type: none"> • Mid-level anatomical detail • Long standard sequences

Table 1: Signal intensity, with advantages and disadvantages, for each MR weighting.



1 (1A) A 55-year-old female patient with recent worsening of chronic headache underwent an MRI study. The FLAIR axial images showed multiple chronic embolic lesions in both the posterior and anterior circulation; the time-of-flight (TOF) sequence showed the presence of multiple caliber alterations in the intracranial arterial circulation, the worst of which was on the basilar artery. (1B, C) Pre- and post-contrast high-resolution vessel wall imaging, with the coronal reconstruction of the 3D acquisition showing a focal atheromatous plaque and wall thickening (arrow), and the absence of wall enhancement after the administration of contrast medium (star).

Regardless of the suppression technique used, VW MRI does have pitfalls that should be noted [7]. For example, it is impossible to assess the presence of wall enhancement in the cavernous segment of the internal carotid artery. This is due to diffuse enhancement inside the cavernous sinus after contrast-agent administration [7].

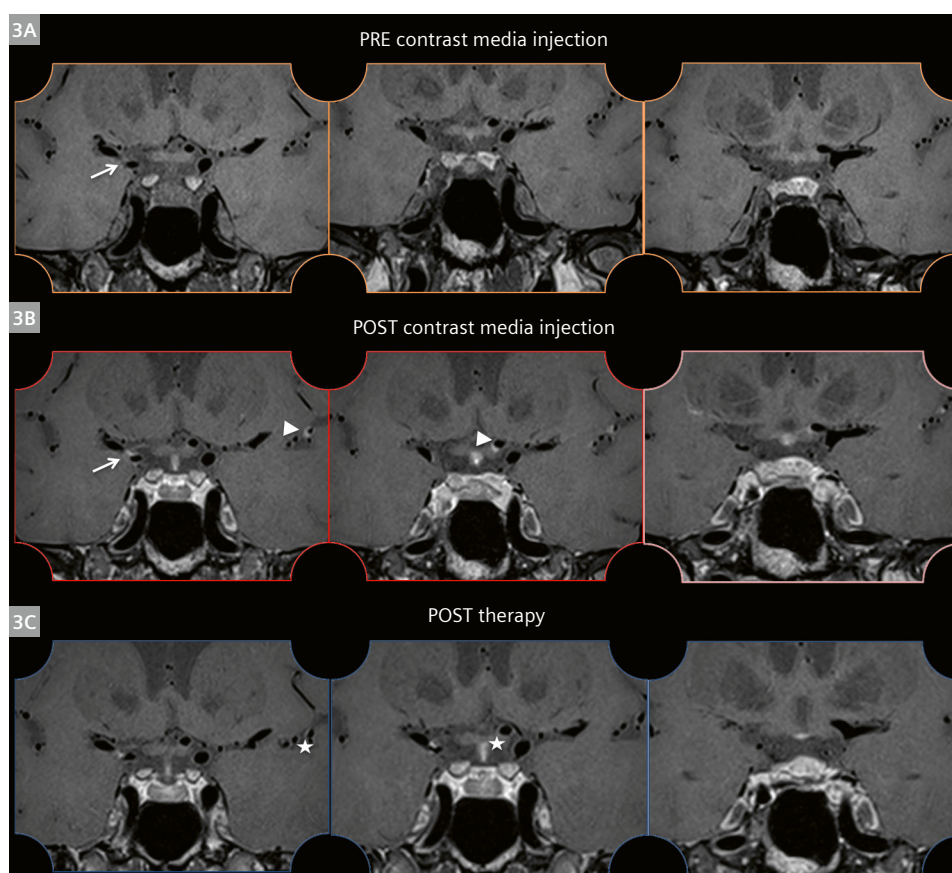
Aside from contrast resolution, the scan time is also important, because using sequences with long acquisition times in clinical practice may cause motion-induced artifacts. It is therefore necessary to reduce the scan time. MR vendors have provided various parallel imaging techniques to achieve this.

We have reported our experience with a VW MRI sequence, a novel imaging tool that has been evolving in recent years. Its purpose is to diagnose and support treatment decisions for various cerebrovascular pathologies, such as CNS vasculitis (Fig. 1), reversible cerebral vasoconstriction syndrome (RCVS), intracranial atherosclerosis (Figs. 2, 3), aneurysms, dissections, moyamoya disease, and moyamoya-like diseases.

After performing more than 200 VW MRI examinations with the aforementioned sequence, we found it to be useful in the diagnosis of more than 97.1% of cases (31.7% of our VW MRI examinations were determined to be positive for vessel wall pathologies, while 65.4% were negative). The VW MRI was inconclusive in less than 3% of cases, due to motion artifacts or blood-suppression artifacts.



2 (2A) A 48-year-old male patient with recent worsening of chronic headache. FLAIR axial images showed multiple chronic embolic lesions. (2B) MR angiography showed a focal stenosis of the right M1 segment at origin (arrow).



3 Vessel wall MRI study before (3A) and after (3B) the administration of contrast media showed the presence of a slight circumferential enhancement in correspondence of the right M1 origin segment (arrow). Other pathological vessel wall enhancements were noticed on the left A1–A2 angle and the M2–M3 segments of the left middle cerebral artery (arrowheads). The laboratory test was positive for a T. pallidum infection, so the final diagnosis is a luetic CNS vasculitis. An MR control performed one month after medical therapy (3C) showed the disappearance of the pathological enhancement at the left A1–A2 angle of the anterior cerebral artery and the M2–M3 segments (stars).

Compared to other VW MRI sequences reported in the literature, ours has the advantage of being as simple as possible, since it uses no blood-suppression techniques, which avoids suppression-related artifacts.

Contact

Luigi Cirillo
Associate Professor of Neuroradiology
Alma Mater Studiorum –
University of Bologna
IRCCS Istituto delle Scienze
Neurologiche di Bologna
Via Altura 3
40133 Bologna
Italy
luigi.cirillo2@unibo.it



References

- 1 Jung SC, Kang DW, Turan TN. Vessel and Vessel Wall Imaging. *Front Neurol Neurosci*. 2016;40:109–123.
- 2 Bhogal P, Uff C, Makalanda HL. Vessel wall MRI and intracranial aneurysms. *J Neurointerv Surg*. 2016;8(11):1160–1162.
- 3 Young CC, Bonow RH, Barros G, Mossa-Basha M, Kim LJ, Levitt MR. Magnetic resonance vessel wall imaging in cerebrovascular diseases. *Neurosurg Focus*. 2019;47(6):E4.
- 4 Rustici A, Merli E, Cevoli S, Donato MD, Pierangeli G, Favoni V, et al. Vessel-wall MRI in thunderclap headache: A useful tool to answer the riddle? *Interv Neuroradiol*. 2021;27(2):219–224.
- 5 Pensato U, Cevoli S, Cirillo L. Vessel Wall Imaging in Thunderclap Headache: A Reversible Cerebral Vasoconstriction Syndrome (RCVS) Case. *Headache*. 2020;60(10):2633–2635.
- 6 Henningson M, Malik S, Botnar R, Castellanos D, Hussain T, Leiner T. Black-Blood Contrast in Cardiovascular MRI. *J Magn Reson Imaging*. 2022;55(1):61–80.
- 7 Lindenholz A, van der Kolk AG, Zwanenburg JJM, Hendrikse J. The Use and Pitfalls of Intracranial Vessel Wall Imaging: How We Do It. *Radiology*. 2018;286(1):12–28.
- 8 Mandell DM, Mossa-Basha M, Qiao Y, Hess CP, Hui F, Matouk C, et al. Intracranial vessel wall MRI: Principles and Expert Consensus Recommendations of the American Society of Neuroradiology. *AJNR Am J Neuroradiol*. 2017;38(2):218–229.

MRI-Guided Thermoablation for Hepatic Malignancies in Clinical Routine

Rüdiger Hoffmann, M.D.; Jens Kübler, M.D.; Antonia Grimm, M.D.; Moritz Winkelmann, M.D.

Department of Diagnostic and Interventional Radiology, University Hospital Tübingen, Germany

Introduction

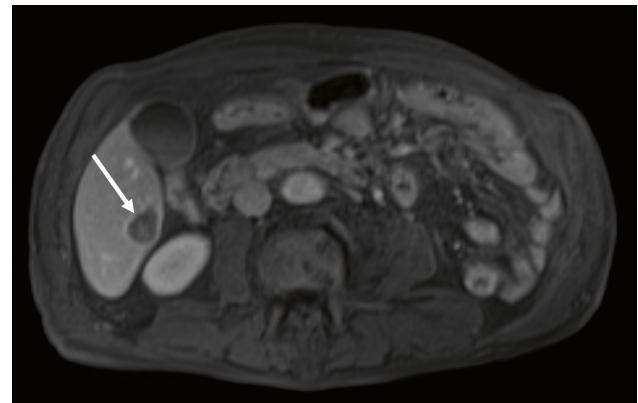
At our institution, MRI-guided interventions have been performed for over 25 years and have gained particular recognition in percutaneous thermoablation of liver and kidney tumors to the extent that we now carry out more than 90% of percutaneous thermoablations with MRI guidance. This is due to the advantages of this technique, such as free slice angulation, the omission of ionizing radiation, applicator placement with MR fluoroscopy, reliable and infinitely repeatable therapy monitoring without intravenous contrast agent [1]. MRI has a particular advantage in the treatment of small lesions because the target tumor can be reliably visualized using different techniques [2]. In this case-based review, we present our experience with MRI-guided thermoablation based on selected cases from recent years conducted on a 1.5T MAGNETOM Aera scanner.

Case 1

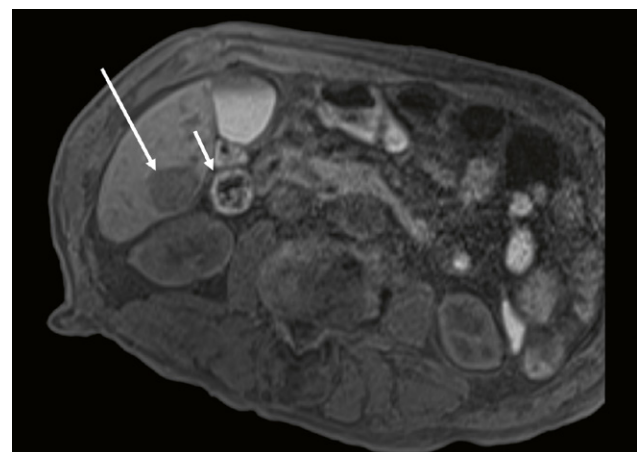
A 63-year-old patient with a hepatic metastasis of a malignant melanoma in segment VI of the right liver lobe. The contrast-enhanced liver MRI performed one month before the planned thermoablation revealed a singular, T1 hypointense lesion with a diameter of 18 mm (Fig. 1). In an interdisciplinary case discussion, the decision was taken to treat the lesion with thermoablation in intubation narcosis.

To plan the access path, at the beginning of the intervention we always conduct a time-optimized short protocol with native planning sequences (Table 1). For this, we not only have the T1-weighted volume interpolated breath-hold exam (VIBE) sequence at our disposal, but now also the T2-weighted half-Fourier acquisition single-shot turbo spin-echo (HASTE) short tau inversion recovery (STIR) sequence that can be acquired within a few breath-holds. In this case, the native planning sequences revealed that the target tumor had considerably increased in size to 27 mm diameter since the image acquired one month before, and as a result now extended right up to the ascending colon (Fig. 2).

To be able to conduct safe ablation without danger of injuring the adjacent colon, we decided to increase the distance between the target tumor and the colon by locally injecting a 5% glucose solution via a 16-G, MR-compatible



1 The axially angled T1 VIBE in the portal venous phase shows a liver metastasis in segment VI with a diameter of 18 mm.



2 The intra-interventionally acquired native T1 VIBE for planning shows that the metastasis is considerably larger than before at 27 mm (long arrow) and is now located close to the ascending colon (short arrow).

puncture cannula ('hydrodissection'). To place the RF applicator and the puncture cannula for hydrodissection, we use an MR fluoroscopic sequence (BEAT_IRTTT). This makes it possible to track the forward movement of a device in three freely selectable planes at an image frame rate of 330 ms, more or less in real time (Fig. 3). The BEAT_IRTTT sequence offers a choice between a spoiled gradient echo (GRE) sequence with T1 contrast and

a balanced steady-state precession (SSFP) sequence with T1/T2 combined contrast [3]. In the case presented here, a pure T1 contrast was chosen to place the RF applicator (Fig. 3), which makes it possible to visualize the applicator reliably and in most cases the target tumor, too.

During local injection of the glucose solution, fluoroscopy was used as an SSFP sequence with T1/T2 combined contrast fluoroscopy (Fig. 4). This allowed to track the

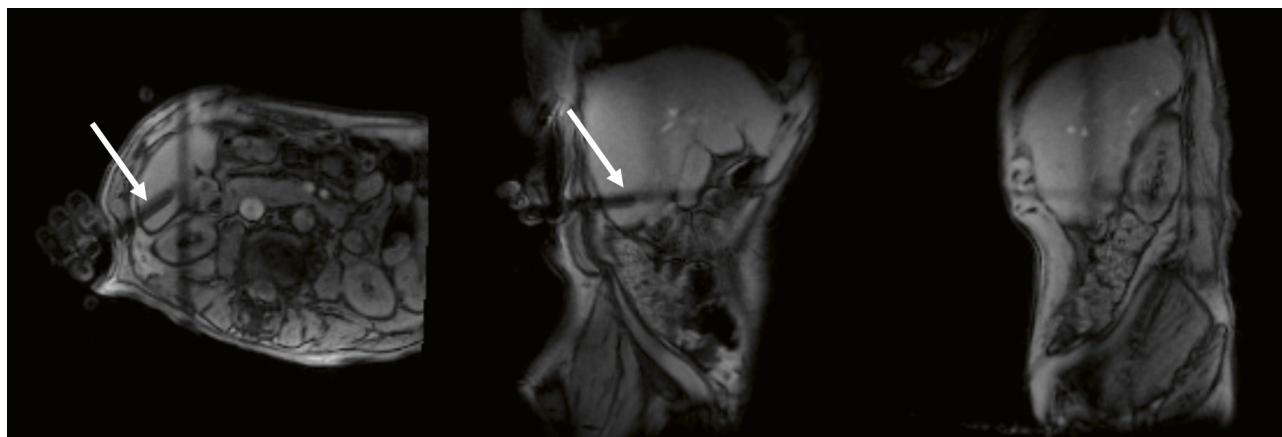
Sequence	TE (ms)	TR (ms)	Slice thickness (mm)	Matrix	Flip angle	Bandwidth (Hz/pixel)
Planning						
T2 HASTE (coronal)	94	1100	4	256 × 120	160	490
T2 HASTE STIR (axial)	81	1400	7	384 × 250	160	450
T1 VIBE e-Dixon (axial)	2.4	6.7	3	320 × 210	10	470
Diffusion* (axial)	62	3000	6	170 × 102	90	1960
CE T1 VIBE*** (axial + coronal)	2.4	6.7	3	320 × 210	10	520
Targeting						
BEAT_IRTTT (GRE)	3.2	460	10	128 × 128	10	500
BEAT_IRTTT (SSFP)	2.2	840	5	220 × 200	50	300
Therapy monitoring						
T1 VIBE (angulated to applicator)	1.4	3.5	2	320 × 210	10	400
Control						
T2 HASTE STIR (axial)	81	1400	7	384 × 250	160	450
CE T1 VIBE** (axial + coronal)	2.4	6.7	3	320 × 210	10	520

Table 1: 1.5T MAGNETOM Aera protocol

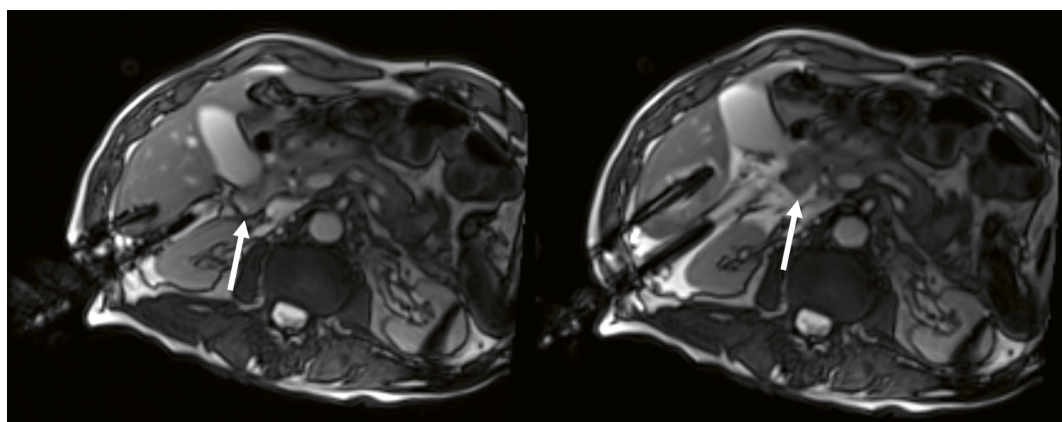
* optional

** contrast-enhanced sequences for planning imaging with extracellular contrast agent, and with hepatocyte-specific contrast agent for control imaging

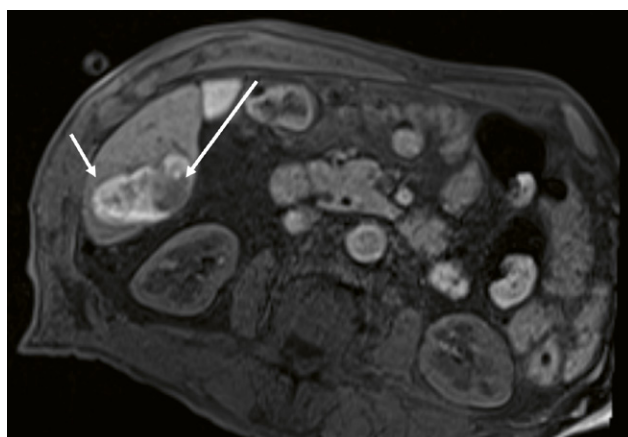
HASTE: half-Fourier acquisition single-shot turbo spin echo, STIR: short tau inversion recovery, Diffusion: echoplanar imaging with b-values of 0 and 800 s/mm², VIBE: volumetric interpolated breath-hold examination, CE: contrast enhanced, GRE: gradient echo, SSFP: steady-state free precession



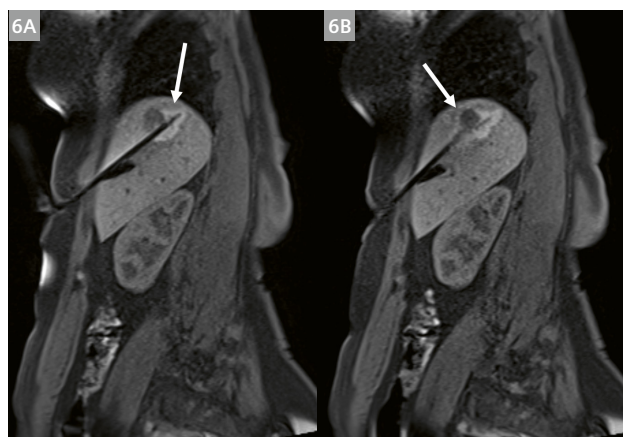
3 MR fluoroscopy (BEAT_IRTTT), as GRE sequence with T1 weighting, shows the forward movement of the applicator (arrow) in real time.



- 4** Using BEAT_IRTTT (SSFP) in T1/T2 combined contrast, the injected glucose solution for distending the cavity between the target tumor and the colon (arrow) can be tracked in real time.



- 5** T1 VIBE is also conducted after ablation as a native sequence. The T1 hyperintense ablation zone (short arrow) is clearly conspicuous against the surrounding liver tissue. The treated target tumor can still be seen inside the ablation zone (long arrow.)



- 6** (6A) The native T1 VIBE shows only partial coverage of the target tumor by the ablation zone with an off-center applicator position (microwave ablation, 5 minutes 100 W.) After repositioning the applicator with MR fluoroscopy to the apical tumor border (not shown) and another five-minute ablation, the ablation zone fully surrounds the tumor (6B).

correct distribution of the fluid and therefore the increasing distension of the cavity between the target tumor and the adjacent colon in real time.

When thermoablation is completed, we acquire a native 3D VIBE sequence as standard across the ablation region. Since the T1 relaxation time of the ablated liver tissue is reduced, the extent of the ablation zone can be estimated reliably and as often as necessary [4]. In this case, the T1 hyperintense ablation zone surrounds the target tumor. As is usually the case, here the target tumor is still recognizable as a hypointense region within the ablation zone, which makes it easier to assess whether ablation has been complete (Fig. 5).

In the case of a 59-year-old patient with metastasis of a neuroendocrine tumor measuring 2.5 cm in liver segment VII, reliable visualization of an insufficient ablation zone can be demonstrated. Due to the off-center placement of the microwave applicator at the bottom edge of the target lesion (Fig. 6A), the T1 hyperintense ablation zone only covered the caudal portion of the tumor after five minutes of ablation at 100 W. Once the applicator had been repositioned in the cranial direction, a sufficiently large ablation zone with full inclusion of the target tumor was achieved (Fig. 6B).

Case 2

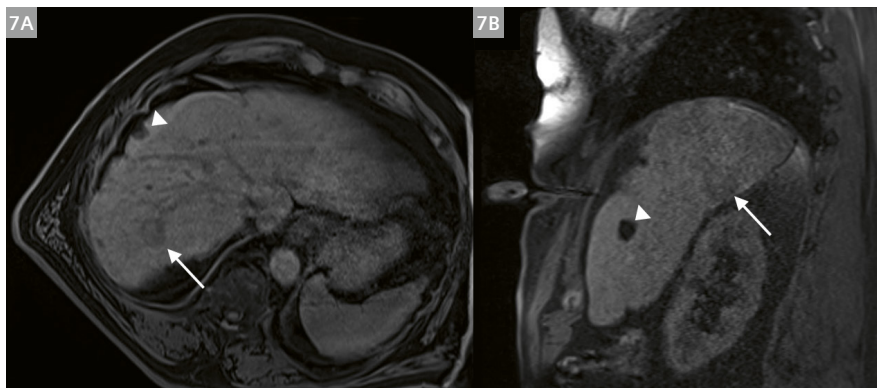
In a 74-year-old patient, alcohol-related liver disease (ARLD) caused a single HCC in liver segment VII. The tumor board recommended local treatment using microwave ablation.

In the native T1-VIBE planning sequence, the liver lesion in segment VII is only shown as being faintly hypointense against surrounding cirrhotic liver tissue (Fig. 7). The lesion had no correlation in the T2-weighted scan.

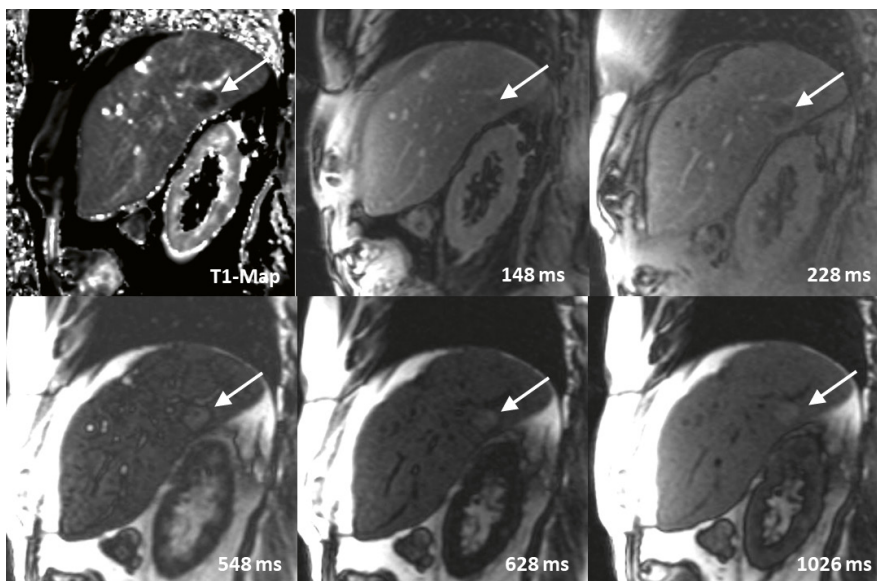
Due to the different T1 relaxation times of liver parenchyma and the liver lesion, the lesion can nevertheless be visualized in the T1 mapping without any significant administration of contrast agent [5]. For this, we use a modified Look-Locker inversion recovery sequence (MOLLI), which originally comes from cardiac MRI (MyoMaps, T1long, 5(3)3, Siemens Healthcare, Erlangen, Germany). The T1 maps are calculated based on different inversion times between approximately 150 and 1700 ms.

The contrast between the lesion and the surrounding liver tissue for some inversion times is greater than in conventional native T1-weighted imaging (Fig. 8). After precise localization of the lesion, the ablation probe can be correctly placed and thermoablation can begin.

This case shows that a standard native sequence is not always sufficient to show the lesion reliably and with good contrast. In such cases, contrast agent containing gadolinium can be administered in the planning sequence as an alternative, if reliable navigation is not possible by any other means [6]. From our experience, however, dispensing with intravenous contrast agent during the intervention has several advantages, including better ability to assess the ablation zone with T1-weighted sequences that can be repeated as often as necessary. That is why we are currently examining the potential of native inversion imaging for improved visualization of liver lesions as shown in this example.



7 T1 VIBE sequences in transversal (**7A**) and sagittal (**7B**) angulation, with only faint hypointense distinction of the HCC lesion in segment VII against the surrounding liver parenchyma (arrow). Liver cysts are an additional finding (arrowhead).

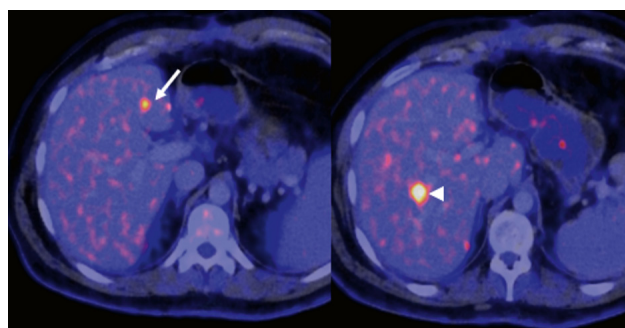


8 T1 mapping and various inversion times. The contrast between the liver lesion (arrow) and the parenchyma changes as a function of the inversion time.

Case 3

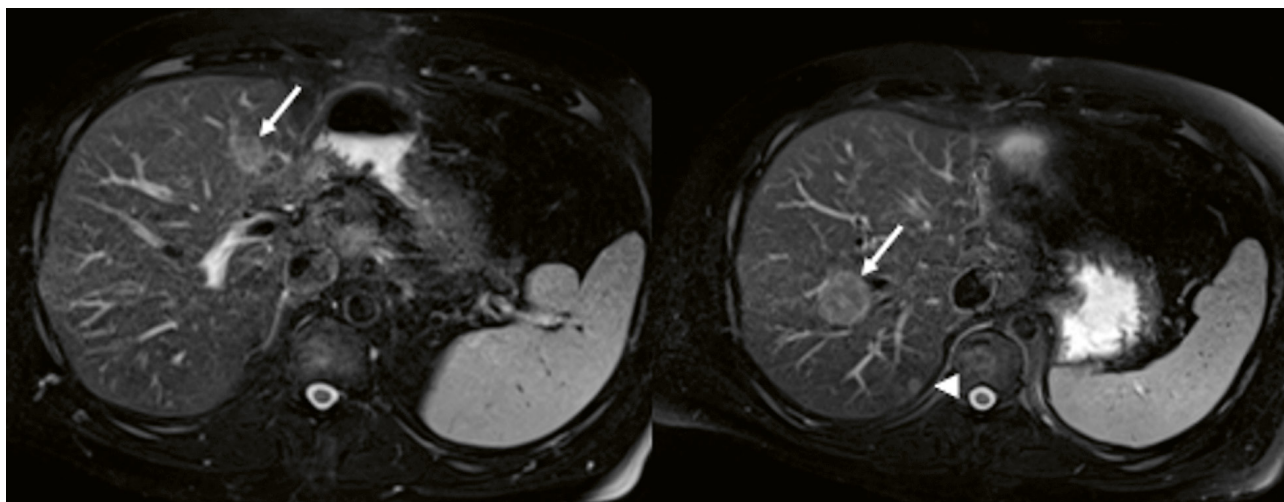
A 42-year-old patient with hepatic metastasized rectal carcinoma presenting after neoadjuvant chemotherapy and left lateral liver portion resection following initial metastasizing in the left liver lobe. An ^{18}F -FDG-PET/CT shows two new conspicuous liver metastases in segments IVa and VIII (Fig. 10), which according to an interdisciplinary tumor board decision are to be treated with MRI-guided percutaneous radiofrequency (RF) ablation.

The two liver lesions in segment IVa and segment VIII were captured in the preprocedural MRI scan (Fig. 10A). Moreover, a further smaller subcapsular liver lesion 5 mm in size, which was not previously conspicuous, was revealed in segment VI (Fig. 10B). Despite the subcapsular position of the metastasis detected for the first time during the intervention, all three metastases were successfully treated during the same procedure (Fig. 11.) Due to its small size, it can be assumed that the third lesion

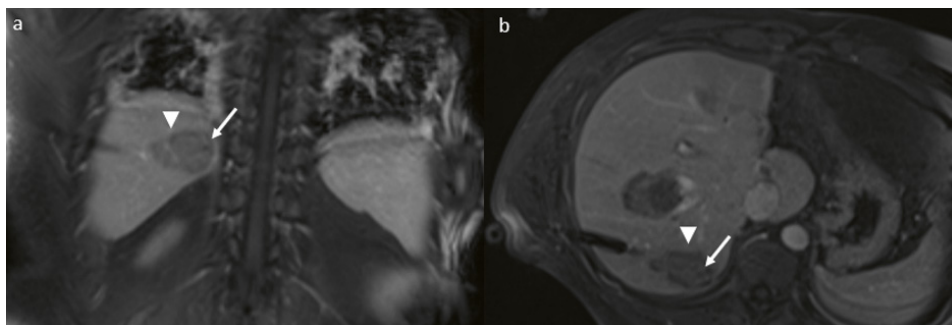


9 In the staging CT scan, two liver lesions with metabolic activity and suspected metastasis are shown in segment IVa (arrow) and VIII (arrowhead).

would have remained undetected in a CT-guided intervention, making a further procedure necessary to prevent progression.



10 In the T2 TSE acquired as part of intra-interventional planning imaging, the two T2-hyperintense liver lesions with suspected metastasis are indicated by arrows in segment IVa and VIII. A further previously non-distinguishable T2 hyperintense lesion with suspected metastasis is located subcapsular in segment VII.



11 A contrast-agent-enhanced final T1 control sequence in the coronal and transversal orientation showing the unenhanced ablation zone surrounding the suspected metastasis in segment VII (arrow).

Discussion

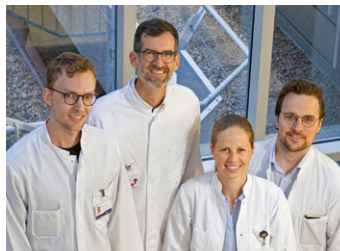
Despite the benefits discussed above, MRI-guided interventions in tumor therapy are only performed at a few specialist centers. Besides limited availability of the required equipment, another reason are the comparatively long intervention times. This is problematic, in particular with respect to the high cost of MRI scan times. Current approaches for reducing intervention times are improving the visualization of applicators and target lesions [5, 7]; reducing the acquisition time is also decisive. It remains to be seen whether new acceleration techniques such as Deep Learning or Simultaneous Multi-Slice will result in increasing acceptance of MRI as an imaging modality for interventions.

References

- 1 Winkelmann MT, Gohla G, Kubler J, Weiss J, Clasen S, Nikolaou K, et al. MR-Guided High-Power Microwave Ablation in Hepatic Malignancies: Initial Results in Clinical Routine. *Cardiovasc Intervent Radiol*. 2020;43(11):1631-8.
- 2 Weiss J, Hoffmann R, Rempp H, Kebetaler DE, Pereira PL, Nikolaou K, et al. Feasibility, efficacy, and safety of percutaneous MR-guided ablation of small (≤ 12 mm) hepatic malignancies. *J Magn Reson Imaging*. 2019;49(2):374-81.
- 3 Rempp H, Loh H, Hoffmann R, Rothgang E, Pan L, Claussen CD, et al. Liver lesion conspicuity during real-time MR-guided radiofrequency applicator placement using spoiled gradient echo and balanced steady-state free precession imaging. *J Magn Reson Imaging*. 2014;40(2):432-9.
- 4 Rempp H, Unterberg J, Hoffmann R, Pereira PL, Schick F, Claussen CD, et al. Therapy monitoring of magnetic resonance-guided radiofrequency ablation using T1- and T2-weighted sequences at 1.5 T: reliability of estimated ablation zones. *Invest Radiol*. 2013;48(6):429-36.
- 5 Kubler J, Krumm P, Martirosian P, Winkelmann MT, Gohla G, Nikolaou K, et al. Improved visualization of hepatic tumors in magnetic resonance-guided thermoablation using T1-inversion-recovery imaging with variable inversion time. *Eur Radiol*. 2023;33(10):7015-24.
- 6 Fischbach F, Lohfink K, Gaffke G, Wybranski C, Mohnike K, Wonneberger U, et al. Magnetic resonance-guided freehand radiofrequency ablation of malignant liver lesions: a new simplified and time-efficient approach using an interactive open magnetic resonance scan platform and hepatocyte-specific contrast agent. *Invest Radiol*. 2013;48(6):422-8.
- 7 Kubler J, Martirosian P, Jacoby J, Gohla G, Winkelmann MT, Nikolaou K, et al. Fluid-based augmentation of magnetic resonance visualization of interventional devices. *J Appl Clin Med Phys*. 2021;22(10):261-9.

Contact

Professor Rüdiger Hoffmann, M.D.
Eberhard Karls University Tübingen
Diagnostic and Interventional Radiology
Hoppe-Seyler-Straße 3
72076 Tübingen
Germany
Tel.: +49 7071 29-86676
Ruediger.Hoffmann@med.uni-tuebingen.de



Celebrating 20 Years of MAGNETOM Avanto

Euan Stokes

Siemens Healthineers, Erlangen, Germany

For Siemens Healthineers, 2023 marks three very important anniversaries in our MR Business Line: MR itself is celebrating 40 years; MAGNETOM Flash, which you are currently reading, is celebrating 30 years of excellent peer-to-peer publications; and MAGNETOM Avanto is celebrating its 20th birthday. MAGNETOM Avanto – more commonly known as “The landmark in 1.5T” – has truly shaped the MR community and defined an entire generation of users. Speak to anyone who has used the system, and you will hear some wonderful reviews. Even in today’s mostly wide-bore markets, the most common thing I hear from customers is, “We love our Avanto.” People often stop me in the corridor at the office to tell me how fondly they think of the Avanto, how nostalgic they are for it, and how excited they are that new technology is still being added to it.

Back in November 2003, we were about to launch a system that was going to set new industry standards and forge a path for all MR systems to follow from then on. We knew it was good, but I don’t think we knew it would still be held as the benchmark system and we would still be talking about it 20 years later.

MAGNETOM Avanto was so successful that there isn’t just one generation of Fit Upgrade; there are two. This means the original magnet can be fitted with the newest types of technology and techniques such as BioMatrix, Deep Resolve, and Compressed Sensing – all things that would have seemed unimaginable back in 2003.

Pioneering change

The world of MR in the early 2000s was very different than the one we have today. Acquisition times were relatively slow, coil changes were clunky and time-consuming, and the community tolerated the very low accessibility to MR as the norm. It would sometimes take over 90 minutes to perform an examination like head and whole spine, pre- and post-contrast, and even that would have been considered speedy. After all, you would “only” have to get the patient on and off the examination table four times.

At Siemens Healthineers we, along with the community as a whole, saw the value in the modality and its potential. So we knew changes had to be made to a new generation of systems to keep up with the increasing demand for and complexity of examinations. We knew that the scan itself was one of the shortest parts of an MR appointment. It was the on-and-off-the-table, the change around, and the positioning that took longer than necessary. Back in 2003, we even knew we had to change the environmental footprint of our systems and protect one of our most precious resources – helium, the liquid gold of MRI.

So we set out on an adventure to create a system that could do it all. A system that had new hardware, new software, and new benchmarks. The result of that adventure was MAGNETOM Avanto.



1 Siemens Healthineers internal launch of Tim technology as part of the MAGNETOM Avanto in late 2003.



2 The MAGNETOM Avanto mock-up being positioned in place at the front of our booth at RSNA.

Tim

For today's technologists, who are highly savvy with extensive knowledge of complex technologies, it's hard to imagine that something as simple as combining individual coils was not as easy as it is nowadays. For example, scanning the entire neuroaxis pre- and post-contrast involved the patient getting on and off the examination table four times because the head coil could not be combined with the spine coil. This was a time-consuming task for even the most agile patients; for those with poor mobility and pain, it was a difficult one, too.

In 1997 with the launch of 1.5T MAGNETOM Symphony, Siemens introduced the IPA (Integrated Panoramic Array) concept to our coils so we were able to create customized arrays by combining different elements from different coils. While preserving the flexibility of the IPA concept, Tim significantly extended the performance. Total imaging matrix, or Tim for short, was introduced with MAGNETOM Avanto and extended and (some would say) perfected the mixing and matching of coils. Now, the head-and-neck coil and the spine coil could be combined easily. And so, quite literally overnight, the problems of having to get a patient on and off the table for a pre-and post-contrast neuroaxis examination were gone. Instead of physically and manually changing coils, users could change them and select elements with just one click. The time saved by eliminating manual coil changes was vast, and brought examination times down to a more realistic 60- or 30-minute slots. The changeover time between patients was also much improved – allowing MAGNETOM Avanto users to increase their patient throughput without adapting their protocols.

Zero Helium Boil-Off

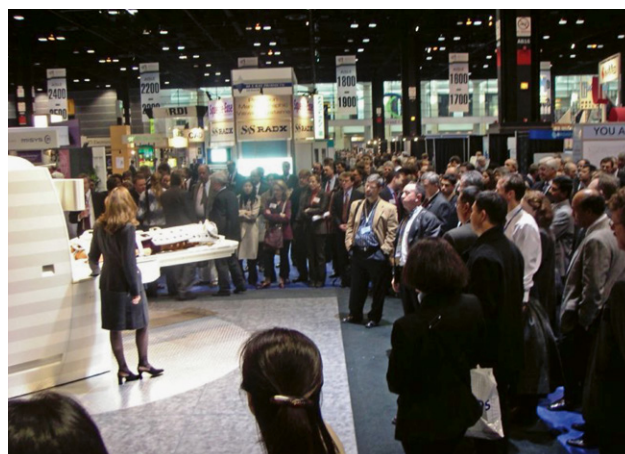
The early 2000s were a time of major change – both medically and environmentally. As a society, we had joined the dots and understood that the human impact on the planet was causing problems with our environment. It is no coincidence, then, that MAGNETOM Avanto introduced new features to preserve our planet's finite resources and safeguard the future of the modality. One of those features was Zero Helium Boil-Off Technology, an innovation that has been included in all our systems since then. Zero Helium Boil-Off stops the MR system from slowly emitting helium from the cryogen chamber, meaning that one fill of helium lasts the lifetime of the system.

Zero Helium Boil-Off reduced recurring costs by hundreds of Euros for users, as they no longer had to regularly top up their systems with helium. It also saved hours of potential scanning as refills were very time intensive. Most modern-day users of MR systems could not even bear to think about closing their scanner for half a day to have Dalek-style dewars of helium arrive in the department to top up their system. But this was common practice in 2003. Closing a system for half a day in 2023 would be very difficult, as MRI is so heavily relied upon.

In our modern-day systems, we have reduced helium requirements even further, and we have solidified our commitment to continue doing so: Thanks to DryCool Technology, MAGNETOM Free.Max and Free.Star require just 0.7 liters of liquid helium, which is a fraction of the amount that earlier systems needed. To put this into perspective: in 2021, we extracted from our reclaimed systems enough helium to fill over 28,000 MAGNETOM Free.Max and Free.Star systems. If every system had DryCool Technology, we could fill more than half of the projected 36,000 global MRI systems with just this reclaimed helium.



3 Teamwork: The MAGNETOM Avanto mock-up being carefully lifted into place. Despite not being an operational system the mock-ups are full life-size replicas of the system.



4 Crowds gather to watch the launch of the system and learn more about what new exciting technology MAGNETOM Avanto brings.

In 2010, Siemens Healthineers introduced MAGNETOM Aera to the market. This was a 70 cm, 1.5T system with an ultra-short bore that once again created a shift that shaped the global MR market. 2010 saw not only the introduction of MAGNETOM Aera and Tim 4G but also of Dot, a real game changer in UI experience, patient workflow, and automation. However, MAGNETOM Avanto users knew their system was steadfast and were not easily persuaded to give up their beloved scanner.

We wanted to bring all the new technology that was available on MAGNETOM Aera to those who had invested in MAGNETOM Avanto systems. After all, the magnet, the heart of the system, was still in perfect working order and an engineering masterpiece. This resulted in us adding something to the MR portfolio that we had never done before: a Fit Upgrade. We could keep the MAGNETOM Avanto magnet and replace everything that surrounds it: the covers, the host computer, the electronic cabinets,

the coils, the operating software. In short, everything that wasn't the magnet would change, essentially creating a 60 cm version of MAGNETOM Aera. We could complete the Fit Upgrade in under 10 working days, as no large-scale construction work or cranes were required. It was a cleaner, faster, cheaper way for users to benefit from everything new but keep the steadfast magnet they loved. The Fit Upgrade was so successful that the concept was developed further, and we now have five Fit Upgrades: MAGNETOM Skyra Fit, MAGNETOM Sola Fit, MAGNETOM Vida Fit, MAGNETOM Cima.X Fit¹, and of course MAGNETOM Avanto Fit, which is now into its second generation.

MAGNETOM Avanto Fit with BioMatrix is a second-generation Fit Upgrade. This means the original system can make two generational steps to our current BioMatrix Technology. MAGNETOM Avanto Fit can now use Deep Resolve to perform complete knee examinations in under three minutes, Compressed Sensing GRASP VIBE to perform free-breathing dynamic liver examinations, and BioMatrix Beat Sensor to perform ECG-free cardiac exams. For the MR community in 2003, these things were mere dreams or not even thought possible.

We are now entering a new and more sustainable era of MRI, with AI-powered acceleration techniques, and hardware specifications so powerful they allow us to see things we never thought possible. Now more than ever, we are able to make a difference to those who need it. And no matter what happens in the future of MRI – whatever is still to be written, achieved, coded, developed, or connected – and wherever we go and whatever we do as a community, we can be sure that it can all be traced back to one system: MAGNETOM Avanto.



5 Original marketing image of the MAGNETOM Avanto with its signature zebra stripes and pale green cover.



6 Marketing images of the MAGNETOM Avanto cover showing the easy position controls.



7 Marketing images showing new Tim Coils, highlighting their ability to be combined together in one FOV.

¹Work in progress. The product is still under development and not commercially available. Its future availability cannot be ensured.



- 8** (8A) The original MAGNETOM Avanto system with its signature zebra stripes and pale green cover.
 (8B) The first generation Fit Upgrade – the MAGNETOM Avanto^{fit}. The design was to replicate the MAGNETOM Aera design.
 (8C) MAGNETOM Avanto Fit with BioMatrix our second-generation Fit upgrade reflecting the newest Siemens Healthineers design. This newest generation of Avanto Fit allows users to benefit from a whole host of new technology.

Personal message

When I was a student, physics was not my forte. So on a fateful Thursday afternoon in the deepest, darkest part of February 2008, when I entered a lecture entitled “An Introduction to MRI Physics,” I was not enthused. The terms T1, T2, relaxation, and decay were all bandied around the room with vigor, and I could feel my eyes slowly close as I adopted my usual position of forearms on the table, pen in hand, and head down pretending to take notes. Secretly, I was having a nap. At the time I thought, “This is not for me.”

Fast-forward 15 years, and I’ve very much had a change of heart. Not on physics (I still feel the same about that), but it is with a profound sense of fulfilment that I write this article as the Global Marketing Manager for Fit Upgrades, including MAGNETOM Avanto Fit. So what changed?

In 2009, I was shipped out of university lecture halls to do an eight-week placement as part of my undergraduate degree. I landed in a department that just months before had had a MAGNETOM Avanto installed. As part of this placement, I spent four weeks in the MRI department. I had a preconceived idea of what MRI was like (see above for a description of the lectures) and I wasn’t particularly

looking forward to it. But on day one, I was introduced to the most enthusiastic team that was so excited about its new scanner. My attitude very quickly changed. I remember distinctly that a cardiac list was scheduled for the afternoon, and as soon as the first short-axis view appeared on the screen, I was hooked. I was watching someone’s heart beating. I could see the blood moving through it, and the valves opening and closing. It was a moment I will never forget. I am truly grateful to the MRI staff of Perth Royal Infirmary. You inspired me.

From that placement on, I knew that MRI was where I was going to end up. I did everything I could to fully understand the modality and made sure I had as much exposure to it as possible. My fourth-year project focused on head injuries – and I was the only person in the group who did not choose CT as their modality. Some would say it was a brave choice, but I would say it was the best one. I got to spend the year deep-diving into MRI and finding out about all the things that made it so exciting to me.

When I graduated, I knew that I would make my way to an MRI scanner – and sure enough, I did. I spent many happy years working clinically with MRI in the NHS. There isn’t an hour of the day I haven’t done a shift in an MRI department, and nothing wakes you up quite like a pediatric general anesthetic examination at 3 a.m. I am now working at Siemens Healthineers with some of the people who were part of the MAGNETOM Avanto development team. It is truly an honor to work together with these people and I look forward to it every day.

MAGNETOM Avanto is a love letter to the MR community, written by all those involved with its development. It is a testament to the passion and devotion of everyone in MR at Siemens Healthineers. I take great pride in looking after the legacy of this system and in ensuring its ongoing success. It is truly a full Fourier transformation from where I began.

Contact

Euan Stokes
 Siemens Healthineers
 Global Marketing Manager MR,
 Installed Base Development
 Karl-Schall-Str. 6
 91052 Erlangen
 Germany
euan.stokes@siemens-healthineers.com



Meet Siemens Healthineers

Siemens Healthineers: Our brand name embodies the pioneering spirit and engineering expertise that is unique in the healthcare industry. The people working for Siemens Healthineers are totally committed to the company they work for, and are passionate about their technology. In this section we introduce you to colleagues from all over the world – people who put their hearts into what they do.

Hyun-Soo Lee, Ph.D.

Hyun-Soo Lee was born in Seoul, Republic of Korea and grew up in Goyang, a neighboring city of the capital. In 2010, Hyun-Soo began studying biomedical engineering at the Korea Advanced Institute of Science & Technology (KAIST) in Daejeon, Republic of Korea. She also earned her master's and her doctorate there, for which she focused on developing new data acquisition schemes for fast MRI sequences. Since 2020, she has been working for Siemens Healthineers as an MR research collaboration scientist and as an onsite MR research scientist at Seoul St. Mary's Hospital. As an MR research collaboration scientist, she plays a vital role in supporting and managing a variety of research projects onsite. She also improves existing MRI techniques, and is currently focusing on ASL and DWI.

Seoul,
South Korea



How did you first come into contact with MRI?

If I recall correctly, I was first exposed to MRI in a signal-processing class given by my advisor in my junior year of college. My advisor spent an entire week introducing MRI and recruited students for summer internships. I didn't apply for the internship then, because I wasn't captivated enough. It wasn't until the following year, when I enrolled in a biomedical imaging course and delved into various medical imaging modalities, that I truly grasped the unique physics of MRI, particularly in terms of signal generation. That was the moment I became genuinely captivated by MRI and decided to pursue a graduate program in the field. This was the beginning of my career as an MRI expert.

What do you find motivating about your job?

As an MR research collaboration scientist and onsite scientist, I have met many clinicians, MR technicians, and physicists, who are all passionate about their work. These encounters allow me to get to know the reality of daily clinical practice. I couldn't fully understand it when I was in academia, but now I believe it's one of the most motivating aspects of my job. Interacting with people from different backgrounds has provided me with invaluable insights into the real-world challenges we have faced. Furthermore, knowing that our research and collaboration activities have great potential to improve diagnosis and treatment options is highly motivating. It's not just about theoretical advancements; it's about making a tangible difference in people's lives.

What are the biggest challenges in your job?

Effective task prioritization and time management. I have a wide array of responsibilities on my plate – including supporting multiple research projects in parallel and developing new techniques – so achieving the right balance can be quite demanding. One of the primary hurdles lies in allocating my attention and resources across these various projects, each with its unique demands and deadlines. Given that I'm responsible for the onsite research projects, which cover every body region, it's tough for me to keep up with all the new research topics and techniques. I also have to somehow find time for implementing the new techniques, which is another challenge.

What are the most important developments in MRI?

It's hard to choose, but I believe one of the most pivotal advancements in MRI is the integration of AI and machine learning. While we've witnessed significant progress in data acquisition and image reconstruction with techniques like parallel imaging and compressed sensing, the recent introduction of deep learning has truly changed the game. Deep learning has revolutionized MRI by dramatically reducing scan times while maintaining or even improving the qualitative and quantitative image quality. Beyond reconstruction, it also benefits post-processing tasks, alleviating the burden on radiologists and technicians. This, in turn, elevates the quality of medical services and patient care. What's truly remarkable is that deep learning can

explore undiscovered territory and come up with entirely new pulse sequences that we could never dream up using our imagination or traditional physics-based approaches. It's essentially opening up a whole new world of possibilities in MRI technology.

What would you do if you could spend a month doing whatever you wanted?

If I could take a one-month vacation, the first thing I'd do is travel abroad, especially to destinations far from Korea. Right now, I'm very interested in Eastern European

countries like Slovenia, the Czech Republic, Croatia, and Hungary. Northern regions of Italy, particularly near Lake Como, could be perfect as well. While it might sound like a cliché, I'd also like to embark on the Camino de Santiago pilgrimage. Additionally, one of my hobbies is doing jigsaw puzzles. Since I'm a huge fan of Harry Potter, I started doing 1,000-piece puzzles featuring the covers of the Harry Potter books three years ago. I've done four so far, leaving just the final three to conquer. So I'd like to spend some of my time doing those puzzles to complete the series.

Dongyeob Han, Ph.D.

Dongyeob Han was born in Seoul, Republic of Korea. In 2005, he began his bachelor's degree at Yonsei University in the Department of Electrical and Electronics Engineering. In his senior year, he began an internship in Professor Dong-Hyun Kim's Medical Imaging Laboratory. Dongyeob began his master's program in 2012 and completed his doctorate in February 2020 at the same university and lab.

Throughout his graduate studies, Dongyeob was actively immersed in research, attending ISMRM nearly every year, receiving both the Summa Cum Laude and Magna Cum Laude awards, and giving poster presentations on numerous occasions. During his Ph.D., he began researching MR fingerprinting (MRF) and developed a high-resolution 3D MRF pulse sequence.

Dongyeob is currently working at Eunpyeong St. Mary's Hospital as an onsite MR scientist, and is collaborating with physicians on various research initiatives, including MRF.

Seoul,
South Korea



How did you first come into contact with MRI?

There were two memorable occasions: One was my first encounter with k -space. It was a project on advanced image processing during the first semester of my senior year of university. My first impression of k -space was that it was like a constellation, and I had no idea how it stored image data. After performing Fourier transform, MR images suddenly appeared, which astonished me. This was my first encounter with MRI data, and it led me to enroll in a graduate lab dealing with MRI physics.

The second occasion occurred in graduate school. I will never forget successfully reconstructing an MR image on the scanner (it was a 3T MAGNETOM Trio) with my first pulse sequence modification. In the gradient echo sequence, I added a simple gradient along the slice direction (also known as the z-shim gradient). At that moment, I was so thrilled that the reconstructed MR image matched my expectations precisely. It was amazing to see my theoretical ideas transformed into the actual world with a few codes and a very complex machine.

What do you find motivating about your job?

I enjoy my job for numerous reasons. The first is unquestionably down to MRI itself. Even though more than ten years have passed since I first encountered MRI, I am still fascinated by its fundamentals, such as magnetization, resonance, and imaging! Occasionally, while operating an MRI scanner, I listen to it carefully and imagine (please don't laugh) what happens to the protons in the human body. I find it endlessly exciting.

I typically work with physicians at the university hospital, with colleagues at headquarters, and with my research team in Korea. All of these people constantly inspire me. For instance, physicians inform me of the clinical significance and their experience of our new techniques. This helps me understand the Korean medical environment, what physicians require, and how we can proceed with our study. And with my colleagues at headquarters and in Korea, we discuss the techniques in depth and exchange ideas. This has most definitely given me a lot of inspiration.

Since I am an onsite scientist at a hospital, I have frequent opportunities to observe patients and some find it difficult to obtain MR images. In the end, with everyone's effort, I do believe that our investigations will ultimately help the patients. This faith inspires me to continue my work.

What are the biggest challenges in your job?

During my research collaborations, I've encountered a variety of obstacles, including most recently the restriction of data sharing as a result of the growth of AI research. Generally, it's difficult to maintain a balance between clinical protocol acquisition and research protocol acquisition. Since Korea has national health insurance, university hospitals and MRI examinations are readily accessible to Korean patients. Therefore, MRI scans are limited in time (around 30 minutes to 1 hour) and it is difficult to add additional scans for research purposes.

What are the most important developments in healthcare?

So many aspects of MRI advances require our attention. However, if I had to choose one, I would prioritize the motion-related solution. Obviously, motion issues can be resolved in a number of ways, including rapid imaging with deep learning-based parallel imaging, prospective/retrospective motion correction, and improving patient comfort.

Throughout my Ph.D. at engineering school, I placed a strong emphasis on learning and developing cutting-edge

techniques. These techniques were typically tested on healthy volunteers to determine their efficacy. Since joining Siemens Healthineers, I have worked as an onsite scientist in a hospital, so I have had numerous opportunities to observe MR imaging with patients in a clinical setting. I've observed that the image quality degrades as a result of motion when applying recent innovative techniques that produce beautiful images of healthy volunteers. In addition, patients who are seriously ill are occasionally unable to obtain MRI scans due to motion. I find this upsetting, and it compels me to help solve the issue as soon as possible.

What would you do if you could spend a month doing whatever you wanted?

A number of thoughts are surfacing in my mind in response to this: I'd like to spend some time on an island with a stunning shoreline – Bali, perhaps, or Hawaii, where I can learn to surf, run along the coast, and watch the sunset from the beach. It would surely rejuvenate and revitalize my mind.

In addition, if I had enough time, I'd like to build an MRI scanner so I could learn how to construct and connect each component – the magnet, gradient coil, RF amplifier, receiver coils, controller computer, everything – on my own. When I envision receiving my first image from that DIY system, it feels extraordinary.

Get to know us



Annemie Steegmans, Ph.D.

Groot-Bijgaarden,
Belgium



Kelvin Chow, Ph.D.

Chicago, USA



Emily Lucchese

Melbourne, Australia



Tom Hillbert, Ph.D.

Lausanne, Switzerland



Find more portraits
of our colleagues
around the world!

www.magnetomworld.siemens-healthineers.com/meet-siemens-healthineers

Not for distribution in the US

On account of certain regional limitations of sales rights and service availability, we cannot guarantee that all products included in this brochure are available through the Siemens sales organization worldwide. Availability and packaging may vary by country and is subject to change without prior notice. Some/All of the features and products described herein may not be available in the United States.

The information in this document contains general technical descriptions of specifications and options as well as standard and optional features which do not always have to be present in individual cases, and which may not be commercially available in all countries.

Due to regulatory reasons their future availability cannot be guaranteed. Please contact your local Siemens organization for further details.

Siemens reserves the right to modify the design, packaging, specifications, and options described herein without prior notice. Please contact your local Siemens sales representative for the most current information.

Note: Any technical data contained in this document may vary within defined tolerances. Original images always lose a certain amount of detail when reproduced.

Siemens Healthineers Headquarters

Siemens Healthineers AG
Siemensstr. 3
91301 Forchheim, Germany
Phone: +49 9191 18-0
siemens-healthineers.com